2018

Branching Fractions and Amplitude Analysis of B± → φKS0π± decays

Alyssa D. Loos
University of South Carolina - Columbia

Branching Fractions and Amplitude Analysis of $B^{\pm} \to \phi K^0_S \pi^{\pm}$ decays

by

Alyssa D. Loos

Bachelor of Science
Manchester University 2013

Submitted in Partial Fulfillment of the Requirements

for the Degree of Doctor of Philosophy in

Physics

College of Arts and Sciences

University of South Carolina

2018

Accepted by:

Milind Purohit, Major Professor

Steffen Strauch, Committee Member

Vishal Bhardwaj, Committee Member

Jeff Wilson, Committee Member

Cheryl L. Addy, Vice Provost and Dean of the Graduate School

Acknowledgments

I would like to thank Prof. Milind Purohit for his support and great assistance during this analysis. He has been a fantastic adviser and teacher through all of my grad school years.

I would also like to thank Prof. Vishal Bhardwaj for his help in getting this analysis started and for his great help along the way. Additionally, I would like to say thank you to my dissertation committee members: Prof. Steffen Strauch, Prof. Vishal Bhardwaj, and Prof. Jeff Wilson.

Abstract

The Belle detector is a particle physics detector that is located around the collision point of the asymmetric-energy e^+e^- collider KEKB. Both detector and collider are located at the KEK international lab in Japan. This thesis uses the full Belle data sample of 772×10^6 $B\bar{B}$ pairs collected at the $\Upsilon(4S)$ resonance.

Decays with large b $\to$ s penguin transitions in the standard model (SM), such as $B^\pm \to \phi K^0_S \pi^\pm$, could be a source of CP violation. This is important in the race to find the mechanism behind the universe's matter-antimatter imbalance. b $\to$ s penguin transitions allow us to search for new particles to appear in virtual loops because they are reliably calculable in the SM thereby providing an opportunity to observe new physics resulting in direct CP violation.

In this thesis we study the branching fractions and CP asymmetries in $B^\pm \to \phi K^0_S \pi^\pm$. Many experiments (such as Belle, CLEO or LHCb) have not made a branching fraction measurement in this decay mode. Other associated modes that need further study are $B^\pm \to \phi K^{*\pm}(892)$, and $B^\pm \to \phi K^{*\pm}_2(1430)$. The fraction of longitudinal polarization of the K^* mesons, f_L, needs to be further studied by Belle and other experiments for $B^\pm \to \phi K^0_S \pi^\pm$ as there is other interest in these measurements.

Table of Contents

Acknowledgments iii

Abstract iv

List of Tables vii

List of Figures x

Chapter 1 Introduction 1

Chapter 2 The KEKB Accelerator 12

Chapter 3 The Belle Detector 14

Chapter 4 Particle Identification 23

Chapter 5 Data Overview 29

Chapter 6 Physics Model 35

Chapter 7 Sources of Background 50

Chapter 8 Efficiency of Selection 70

Chapter 9 Early Fits for Yields and BFs 107

Chapter 10 Full Unbinned Fits for BFs and Amplitudes 114

Chapter 11 The Control Mode 159

Chapter 12 Systematics 163

Chapter 13 Simulated Results 169

Chapter 14 Conclusion 171

Bibliography 172

Appendix A Event Processing Tables 175

Appendix B Additional Efficiency Plots 225

List of Tables

Table 1.1 Properties of the Quarks 1

Table 1.2 Theorectical Predictions 7

Table 1.3 Results for $\mathcal{B}$ for B-meson Decays to $\phi K^0_S\pi$ Final States 8

Table 1.4 Measurements of the Longitudinal Polarization Fraction f_L for B-meson Decays to $\phi K^0_S\pi$ Final States 9

Table 1.5 Properties of Particles in this Decay Analysis 11

Table 2.1 KEKB Machine Parameters 13

Table 6.1 Resonance Parameters for S-, P-, and D-Wave Components . . 40

Table 7.1 Mixed Background With Tight ANN Cuts 60

Table 7.2 Charged Background With Tight ANN Cuts 60

Table 7.3 Charm Background With Tight ANN Cuts 61

Table 7.4 uds Background With Tight ANN Cuts 62

Table 7.5 Mixed RareMC Background With Tight ANN Cuts 65

Table 7.6 Charged Rare MC Background With Tight ANN Cuts 67

Table 7.7 Summary Table Background With Tight ANN Cuts 69

Table 10.1 Parameters for Fits to a'_2 115

Table 10.2 Parameters for Fits to a'_1 and ΔE 116

Table 10.3 Input Values, Bias Means, and Pull RMS for 1x Signal Fits to 320 Toy MC Data Sets 121

Table 10.4 Input Values, Bias Means, and Pull RMS for 10x Signal Fits to 320 Toy MC Data Sets 154

Table 11.1 Yields for Data and MC Signals from the Control Mode Study 162

Table 12.1 Fit Parameters, and Their Input Values, Stat. Errors, and Systematic Shifts for 1x Signal Fits to 320 Toy MC Data Sets . 167

Table 12.2 Fit Parameters, and their Input Values, Stat. Errors, and Systematic Shifts for 10x Signal Fits to 320 Toy MC Data Sets 168

Table 13.1 Fit Parameters, and Their Toymc Input Values, Output Values and Errors for One Set of Toy MC Data 170

Table A.1 Skim and Reconstruction Event Numbers From Real Data Processing 176

Table A.2 Skim and Reconstruction Event Numbers From Full Stream 1 uds Processing 178

Table A.3 Skim and Reconstruction Event Numbers From Full Stream 1 Charm Processing 180

Table A.4 Skim and Reconstruction Event Numbers From Full Stream 1 Mixed Processing 182

Table A.5 Skim and Reconstruction Event Numbers From Full Stream 1 Charged Processing 184

Table A.6 Skim and Reconstruction Event Numbers From Full Stream 2 uds Processing 186

Table A.7 Skim and Reconstruction Event Numbers From Full Stream 2 Charm Processing 188

Table A.8 Skim and Reconstruction Event Numbers From Full Stream 2 Mixed Processing 190

Table A.9 Skim and Reconstruction Event Numbers From Full Stream 2 Charged Processing 192

Table A.10 Skim and Reconstruction Event Numbers From Full Stream 3 uds Processing 194

Table A.11 Skim and Reconstruction Event Numbers From Full Stream 3 Charm Processing 196

Table A.12 Skim and Reconstruction Event Numbers From Full Stream 3 Mixed Processing 198

Table A.13 Skim and Reconstruction Event Numbers From Full Stream 3 Charged Processing 200

Table A.14 Skim and Reconstruction Event Numbers From Full Stream 4 uds Processing 202

Table A.15 Skim and Reconstruction Event Numbers From Full Stream 4 Charm Processing 204

Table A.16 Skim and Reconstruction Event Numbers From Full Stream 4 Mixed Processing 206

Table A.17 Skim and Reconstruction Event Numbers From Full Stream 4 Charged Processing 208

Table A.18 Skim and Reconstruction Event Numbers From Full Stream 5 uds Processing 210

Table A.19 Skim and Reconstruction Event Numbers From Full Stream 5 Charm Processing 212

Table A.20 Skim and Reconstruction Event Numbers From Full Stream 5 Mixed Processing 214

Table A.21 Skim and Reconstruction Event Numbers From Full Stream 5 Charged Processing 216

List of Figures

Figure 1.1 Measurements of branching fractions for B to VV decays from Ref. [4]. 5

Figure 1.2 A penguin diagram of the $B^{\pm} \to \phi K^{*\pm}$ decay. 10

Figure 2.1 Shows the configuration of the two KEKB rings and the collision site at Tsukuba experimental hall where the Belle detector is located [18]. 12

Figure 2.2 Shows the bunches of the beams rotated so that the bunches collide head-on [19]. 13

Figure 3.1 A side view of the Belle Detector and all its subcomponents [20] 15

Figure 3.2 The cross-section of the beam pipe at the interaction point. The crossing angle between beams is ± 11 mrad. . . 16

Figure 3.3 Configuration of the BGO crystals of the extreme forward calorimeter [20]. 17

Figure 3.4 Shows the three ladders or layers of the SVD along the endview and side. A close-up of one of the ends of the SVDI with the double-sided silicon strip detectors (DSSD) is also shown. 18

Figure 3.5 Shows the wires of CDC [22]. 19

Figure 3.6 The layout of the CDC [20]. 19

Figure 3.7 Shows the layout of the ACC. 20

Figure 3.8 Shows a figure of the typical ACC module. 20

Figure 3.9 Shows the overall configuration of the ECL. 21

Figure 3.10 Shows the combined iron and tracking components for the endcap portion of the KLM. 22

Figure 4.1 Coordinates of the Belle detector as shown on the Belle II detector [23] 23

Figure 4.2 The spectrum of the momenta for K^+, K^-, and the π. . . . 24

Figure 4.3 The cos(θ) spectrum for the K^+, K^-, and the π. 24

Figure 4.4 The ϕ spectrum for the K^+, K^-, and the π. 24

Figure 4.5 The K/π efficiency versus momentum for ID rates greater than 0.75. 26

Figure 4.6 The K/π efficiency versus momentum for ID rates greater than 0.8. 26

Figure 4.7 The K/π efficiency versus momentum for ID rates greater than 0.85. 26

Figure 4.8 The K/π efficiency versus momentum for ID rates greater than 0.9. 26

Figure 4.9 The K/π efficiency versus momentum for ID rates greater than 0.95. 26

Figure 4.10 The K/π efficiency versus cos(θ) for ID rates greater than 0.75. 27

Figure 4.11 The K/π efficiency versus cos(θ) for ID rates greater than 0.8. 27

Figure 4.12 The K/π efficiency versus cos(θ) for ID rates greater than 0.85. 27

Figure 4.13 The K/π efficiency versus cos(θ) for ID rates greater than 0.90. 27

Figure 4.14 The K/π efficiency versus cos(θ) for ID rates greater than 0.95. 27

Figure 4.15 The K/π efficiency versus ϕ for ID rates greater than 0.75. . 28

Figure 4.16 The K/π efficiency versus ϕ for ID rates greater than 0.8. . 28

Figure 4.17 The K/π efficiency versus ϕ for ID rates greater than 0.85. . 28

Figure 4.18 The K/π efficiency versus ϕ for ID rates greater than 0.9. . 28

Figure 4.19 The K/π efficiency versus ϕ for ID rates greater than 0.95. . 28

Figure 6.1 Illustration of the three helicity angles given in the rest frame of the parent particles for the $B^+ \to \phi K^{*+}$ decay. Angles are defined similarly for the charge-conjugate decay mode. 37

Figure 6.2 Shows different $m_{K^0_S\pi}$ curves using data from all $K^*(892)$ helicity modes. 46

Figure 6.3 Shows different $m_{K^0_S\pi}$ curves using data from all $K^*(892)$ helicity modes. 47

Figure 6.4 The EvtGen and physics models for $\Phi K^*(892)$ helicity=+1 $m_{K^0_S\pi}$ range. 47

Figure 6.5 The EvtGen and physics models for $\Phi K^*(892)$ helicity=+1 $cos(\theta_{K^0_S\pi})$. 47

Figure 6.6 The EvtGen and physics models for $\Phi K^*(892)$ helicity=+1 $cos(\theta_\Phi)$. 48

Figure 6.7 The EvtGen and physics models for $\Phi K^*(892)$ helicity=+1 ϕ angle. 48

Figure 6.8 The EvtGen and physics models for $\Phi K^*(892)$ helicity=0 $m_{K^0_S\pi}$. 48

Figure 6.9 The EvtGen and physics models for $\Phi K^*(892)$ helicity=0 $cos(\theta_{K^0_S\pi})$. 48

Figure 6.10 The EvtGen and physics models for $\Phi K^*(892)$ helicity=0 $cos(\theta_\Phi)$. 49

Figure 6.11 The EvtGen and physics models for $\Phi K^*(892)$ helicity=0 ϕ angle. 49

Figure 6.12 The EvtGen and physics models for $\Phi K^*(892)$ helicity=-1 $m_{K^0_S\pi}$. 49

Figure 6.13 The EvtGen and physics models for $\Phi K^*(892)$ helicity=-1 $cos(\theta_{K^0_S\pi})$. 49

Figure 6.14 The EvtGen and physics models for $\Phi K^*(892)$ helicity=-1 $cos(\theta_\Phi)$. 49

Figure 6.15 The EvtGen and physics models for $\Phi K^*(892)$ helicity=-1 ϕ angle. 49

Figure 7.1 A background rejection vs signal efficiency plot for various MVA's. 51

Figure 7.2 Output of the first ANN (event shape) for signal and background. 53

Figure 7.3 Comparison of signal and background distributions for the first set of variables that are input to ANN2. 54

Figure 7.4 Comparison of signal and background distributions for the second set of variables that are input to ANN2. 55

Figure 7.5 Comparison of signal and background distributions for the third set of variables that are input to ANN2. 55

Figure 7.6 The correlation matrix for background variables. 56

Figure 7.7 The correlation matrix for signal variables. 56

Figure 7.8 Signal and background output for the binary decision tree (BDTB) classifier. 56

Figure 7.9 Signal and background output for the Fisher classifier. . . . 56

Figure 7.10 Signal and background output for the LikelihoodD classifier. 57

Figure 7.11 Signal and background output for the SVM classifier. 57

Figure 7.12 Signal and background output for the TMlpANN classifier. 57

Figure 7.13 Overtraining check for the BDTB classifier. 58

Figure 7.14 Overtraining check for the Fisher classifier. 58

Figure 7.15 Overtraining check for the LikelihoodD classifier. 58

Figure 7.16 Overtraining check for the SVM classifier. 58

Figure 7.17 Overtraining check for the TMlpANN classifier. 58

Figure 8.1 $\cos(\theta_{K^0_S\pi})$ vs. $m_{K^0_S\pi}$ efficiency for $\Phi K^*(892)$ $h = +1$ trueb_best candidates. 70

Figure 8.2 $\cos(\theta_{K^0_S\pi})$ vs. $m_{K^0_S\pi}$ efficiency for $\Phi K^*(892)$ $h = +1$ bmatch_best candidates 70

Figure 8.3 ϕ vs. $\cos(\theta_\Phi)$ efficiency for Φ $K^*(892)$ $h = +1$ trueb_best candidates. 71

Figure 8.4 ϕ vs. $\cos(\theta_\Phi)$ efficiency for $\Phi K^*(892)$ $h = +1$ bmatch_best candidates. 71

Figure 8.5 $\cos(\theta_{K^0_S\pi})$ vs. $m_{K^0_S\pi}$ efficiency for $\Phi K^*(892)$ $h = 0$ trueb_best candidates. 71

Figure 8.6 $\cos(\theta_{K^0_S\pi})$ vs. $m_{K^0_S\pi}$ efficiency for $\Phi K^*(892)$ $h = 0$ bmatch_best candidates. 71

Figure 8.7 ϕ vs. $\cos(\theta_\Phi)$ efficiency for $\Phi K^*(892)$ $h = 0$ trueb_best candidates. 72

Figure 8.8 ϕ vs. $\cos(\theta_\Phi)$ efficiency for $\Phi K^*(892)$ $h = 0$ bmatch_best candidates. 72

Figure 8.9 $\cos(\theta_{K^0_S\pi})$ vs. $m_{K^0_S\pi}$ efficiency for $\Phi K^*(892)$ $h = -1$ trueb_best candidates. 72

Figure 8.10 $\cos(\theta_{K^0_S\pi})$ vs. $m_{K^0_S\pi}$ efficiency for $\Phi K^*(892)$ $h = -1$ bmatch_best candidates. 72

Figure 8.11 ϕ vs. $\cos(\theta_\Phi)$ efficiency for $\Phi K^*(892)$ $h = -1$ trueb_best candidates. 72

Figure 8.12 ϕ vs. $\cos(\theta_\Phi)$ efficiency for $\Phi K^*(892)$ $h = -1$ bmatch_best candidates. 72

Figure 8.13 The truth $\Phi K^*(892)$ $h = +1$ $m_{K^0_S\pi}$. 73

Figure 8.14 The reco $\Phi K^*(892)$ $h = +1$ $m_{K^0_S\pi}$. 74

Figure 8.15 The reco $\Phi K^*(892)$ $h = +1$ $m_{K^0_S\pi}$ drawn with the bmatch_best candidate. 74

Figure 8.16 The reco $\Phi K^*(892)$ $h = +1$ $m_{K^0_S\pi}$ drawn without the bmatch_best candidate. 74

Figure 8.17 The $\Phi K^*(892)$ $h = +1$ $m_{K^0_S\pi}$ efficiency drawn with the reco bmatch_best histogram divided by the truth histogram. 74

Figure 8.18 The truth $\Phi K^*(892)$ $h = +1$ $\cos(\theta_{K^0_S\pi})$. 75

Figure 8.19 The reco $\Phi K^*(892)$ $h = +1$ $\cos(\theta_{K^0_S\pi})$. 75

Figure 8.20 The reco $\Phi K^*(892)$ $h = +1$ $\cos(\theta_{K^0_S\pi})$ drawn with the bmatch_best candidate. 75

Figure 8.21 The reco $\Phi K^*(892)$ $h = +1$ $\cos(\theta_{K^0_S\pi})$ drawn without the bmatch_best candidate. 75

Figure 8.22 The $\Phi K^*(892)$ $h = +1$ $\cos(\theta_{K^0_S\pi})$ efficiency drawn with the reco bmatch_best histogram divided by the truth histogram. 75

Figure 8.23 The truth $\Phi K^*(892)$ $h = +1$ $\cos(\theta_\Phi)$ 76

Figure 8.24 The reco$\Phi K^*(892)$ $h = +1$ $\cos(\theta_\Phi)$. 76

Figure 8.25 The reco $\Phi K^*(892)$ $h = +1$ $\cos(\theta_\Phi)$ drawn with the bmatch_best candidate. 76

Figure 8.26 The reco $\Phi K^*(892)$ $h = +1$ $\cos(\theta_\Phi)$ drawn without the bmatch_best candidate. 76

Figure 8.27 The $\Phi K^*(892)$ $h = +1$ $\cos(\theta_\Phi)$ efficiency drawn with the reco bmatch_best histogram divided by the truth histogram. 76

Figure 8.28 The truth $\Phi K^*(892)$ $h = +1$ ϕ angle. 77

Figure 8.29 The reco $\Phi K^*(892)$ $h = +1$ ϕ angle. 77

Figure 8.30 The reco $\Phi K^*(892)$ $h = +1$ ϕ angle drawn with the bmatch_best candidate. 77

Figure 8.31 The reco $\Phi K^*(892)$ $h = +1$ ϕ angle drawn without the bmatch_best candidate. 77

Figure 8.32 The $\Phi K^*(892)$ $h = +1$ ϕ efficiency drawn with the reco bmatch_best histogram divided by the truth histogram. . . 77

Figure 8.33 The truth $\Phi K^*(892)\ h = 0\ m_{K^0_S\pi}$. 78

Figure 8.34 The reco $\Phi K^*(892)\ h = 0\ m_{K^0_S\pi}$. 78

Figure 8.35 The reco $\Phi K^*(892)\ h = 0\ m_{K^0_S\pi}$ drawn with the bmatch_best candidate. 78

Figure 8.36 The reco $\Phi K^*(892)\ h = 0\ m_{K^0_S\pi}$ drawn without the bmatch_best candidate. 78

Figure 8.37 The $\Phi K^*(892)\ h = 0\ m_{K^0_S\pi}$ efficiency drawn with the reco bmatch_best histogram divided by the truth histogram. . . 78

Figure 8.38 The truth $\Phi K^*(892)\ h = 0\ \cos(\theta_{K^0_S\pi})$. 79

Figure 8.39 The reco $\Phi K^*(892)\ h = 0\ \cos(\theta_{K^0_S\pi})$. 79

Figure 8.40 The reco $\Phi K^*(892)\ h = 0\ \cos(\theta_{K^0_S\pi})$ drawn with the bmatch_best candidate. 79

Figure 8.41 The reco $\Phi K^*(892)\ h = 0\ \cos(\theta_{K^0_S\pi})$ drawn without the bmatch_best candidate. 79

Figure 8.42 The $\Phi K^*(892)\ h = 0\ \cos(\theta_{K^0_S\pi})$ efficiency drawn with the reco bmatch_best histogram divided by the truth histogram. 79

Figure 8.43 The truth $\Phi K^*(892)\ h = 0\ \cos(\theta_\Phi)$ 80

Figure 8.44 The reco$\Phi K^*(892)\ h = 0\ \cos(\theta_\Phi)$. 80

Figure 8.45 The reco $\Phi K^*(892)\ h = 0\ \cos(\theta_\Phi)$ drawn with the bmatch_best candidate. 80

Figure 8.46 The reco $\Phi K^*(892)\ h = 0\ \cos(\theta_\Phi)$ drawn without the bmatch_best candidate. 80

Figure 8.47 The $\Phi K^*(892)\ h = 0\ \cos(\theta_\Phi)$ efficiency drawn with the reco bmatch_best histogram divided by the truth histogram. 80

Figure 8.48 The truth $\Phi K^*(892)\ h = 0\ \phi$ angle. 81

Figure 8.49 The reco $\Phi K^*(892)\ h = 0\ \phi$ angle. 81

Figure 8.50 The reco $\Phi K^*(892)\ h = 0\ \phi$ angle drawn with the bmatch_best candidate. 81

Figure 8.51 The reco $\Phi K^*(892)$ $h = 0$ ϕ angle drawn without the bmatch_best candidate. 81

Figure 8.52 The $\Phi K^*(892)$ $h = 0$ ϕ efficiency drawn with the reco bmatch_best histogram divided by the truth histogram. . . 81

Figure 8.53 The truth $\Phi K^*(892)$ $h = -1$ $m_{K^0_S\pi}$. 82

Figure 8.54 The reco $\Phi K^*(892)$ $h = -1$ $m_{K^0_S\pi}$. 82

Figure 8.55 The reco $\Phi K^*(892)$ $h = -1$ $m_{K^0_S\pi}$ drawn without the bmatch_best candidate. 82

Figure 8.56 The reco $\Phi K^*(892)$ $h = -1$ $m_{K^0_S\pi}$ drawn without the bmatch_best candidate. 82

Figure 8.57 The $\Phi K^*(892)$ $h = -1$ $m_{K^0_S\pi}$ efficiency drawn with the reco bmatch_best histogram divided by the truth histogram. 82

Figure 8.58 The truth $\Phi K^*(892)$ $h = -1$ $\cos(\theta_{K^0_S\pi})$. 83

Figure 8.59 The reco $\Phi K^*(892)$ $h = -1$ $\cos(\theta_{K^0_S\pi})$. 83

Figure 8.60 The reco $\Phi K^*(892)$ $h = -1$ $\cos(\theta_{K^0_S\pi})$ drawn with the bmatch_best candidate. 83

Figure 8.61 The reco $\Phi K^*(892)$ $h = -1$ $\cos(\theta_{K^0_S\pi})$ drawn without the bmatch_best candidate. 83

Figure 8.62 The $\Phi K^*(892)$ $h = -1$ $\cos(\theta_{K^0_S\pi})$ efficiency drawn with the reco bmatch_best histogram divided by the truth histogram. 83

Figure 8.63 The truth $\Phi K^*(892)$ $h = -1$ $\cos(\theta_\Phi)$ 84

Figure 8.64 The reco $\Phi K^*(892)$ $h = -1$ $\cos(\theta_\Phi)$. 84

Figure 8.65 The reco $\Phi K^*(892)$ $h = -1$ $\cos(\theta_\Phi)$ drawn with the bmatch_best candidate. 84

Figure 8.66 The reco $\Phi K^*(892)$ $h = -1$ $\cos(\theta_\Phi)$ drawn without the bmatch_best candidate. 84

Figure 8.67 The $\Phi K^*(892)$ $h = -1$ $\cos(\theta_\Phi)$ efficiency drawn with the reco bmatch_best histogram divided by the truth histogram. 84

Figure 8.68 The truth $\Phi K^*(892)$ $h = -1$ ϕ angle. 85

Figure 8.69 The reco $\Phi K^*(892)$ $h = -1$ ϕ angle. 85

Figure 8.70 The reco $\Phi K^*(892)$ $h = -1$ ϕ angle drawn with the bmatch_best candidate. 85

Figure 8.71 The reco $\Phi K^*(892)$ $h = -1$ ϕ angle drawn without the bmatch_best candidate. 85

Figure 8.72 The $\Phi K^*(892)$ $h = -1$ ϕ efficiency drawn with the reco bmatch_best histogram divided by the truth histogram. . . 85

Figure 8.73 The truth $\Phi K^0_S\pi$ $h = 0$ $m_{K^0_S\pi}$. 86

Figure 8.74 The reco $\Phi K^0_S\pi$ $h = 0$ $m_{K^0_S\pi}$. 86

Figure 8.75 The reco $\Phi K^*(892)$ $h = 0$ $m_{K^0_S\pi}$ drawn without the bmatch_best candidate. 86

Figure 8.76 The reco $\Phi K^0_S\pi$ $h = 0$ $m_{K^0_S\pi}$ drawn without the bmatch_best candidate. 86

Figure 8.77 The $\Phi K^0_S\pi$ $h = 0$ $m_{K^0_S\pi}$ efficiency drawn with the reco bmatch_best histogram divided by the truth histogram. . . 86

Figure 8.78 The truth $\Phi K^0_S\pi$ $h = 0$ $\cos(\theta_{K^0_S\pi})$. 87

Figure 8.79 The reco $\Phi K^0_S\pi$ $h = 0$ $\cos(\theta_{K^0_S\pi})$. 87

Figure 8.80 The reco $\Phi K^0_S\pi$ $h = 0$ $\cos(\theta_{K^0_S\pi})$ drawn with the bmatch_best candidate. 87

Figure 8.81 The reco $\Phi K^0_S\pi$ $h = 0$ $\cos(\theta_{K^0_S\pi})$ drawn without the bmatch_best candidate. 87

Figure 8.82 The $\Phi K^0_S\pi$ $h = 0$ $\cos(\theta_{K^0_S\pi})$ efficiency drawn with the reco bmatch_best histogram divided by the truth histogram. 87

Figure 8.83 The truth $\Phi K^0_S\pi$ $h = 0$ $\cos(\theta_\Phi)$ 88

Figure 8.84 The reco$\Phi K^0_S\pi$ $h = 0$ $\cos(\theta_\Phi)$. 88

Figure 8.85 The reco $\Phi K^0_S\pi$ $h = 0$ $\cos(\theta_\Phi)$ drawn with the bmatch_best candidate. 88

Figure 8.86 The reco $\Phi K^0_S\pi$ $h = 0$ $\cos(\theta_\Phi)$ drawn without the bmatch_best candidate. 88

Figure 8.87 The $\Phi K^0_S\pi$ $h = 0$ $\cos(\theta_\Phi)$ efficiency drawn with the reco bmatch_best histogram divided by the truth histogram. . . 88

Figure 8.88 The truth $\Phi K^0_S\pi$ $h = 0$ ϕ angle. 89

Figure 8.89 The reco $\Phi K^0_S\pi$ $h = 0$ ϕ angle. 89

Figure 8.90 The reco $\Phi K^0_S\pi$ h=0 ϕ angle drawn with the bmatch_best candidate. 89

Figure 8.91 The reco $\Phi K^0_S\pi$ $h = 0$ ϕ angle drawn without the bmatch_best candidate. 89

Figure 8.92 The $\Phi K^0_S\pi$ $h = 0$ ϕ efficiency drawn with the reco bmatch_best histogram divided by the truth histogram. 89

Figure 8.93 Efficiency of $m_{K^0_S\pi}$ for different decay modes. 90

Figure 8.94 Efficiency of $\cos(\theta_{K^0_S\pi})$ for different decay modes. 91

Figure 8.95 Efficiency of $\cos(\theta_\Phi)$ for different decay modes. 91

Figure 8.96 Efficiency of ϕ for different decay modes. 92

Figure 8.97 Efficiency of $\cos(\theta_{K^0_S\pi})$ for the $K^*(892)$ $h = +1$ mode and a range of masses for the $K^0_S\pi$. 92

Figure 8.98 The truth $\Phi K^*(892)$ $h = 1$ $\cos(\theta_{K^0_S\pi})$ vs. $m_{K^0_S\pi}$ 95

Figure 8.99 The reco $\Phi K^*(892)$ $h = 1$ $\cos(\theta_{K^0_S\pi})$ vs. $m_{K^0_S\pi}$ 95

Figure 8.100 The reco $\Phi K^*(892)$ $h = 1$ $\cos(\theta_{K^0_S\pi})$ vs. $m_{K^0_S\pi}$ drawn with the bmatch_best candidate 95

Figure 8.101 The reco $\Phi K^*(892)$ $h = 1$ $\cos(\theta_{K^0_S\pi})$ vs. $m_{K^0_S\pi}$ drawn without the bmatch_best candidate. 95

Figure 8.102 The efficiency for the $\Phi K^*(892)$ $h = 1$ $\cos(\theta_{K^0_S\pi})$ vs. $m_{K^0_S\pi}$ obtained by dividing the reco bmatch_best histogram by the truth histogram 95

Figure 8.103 The truth $\Phi K^*(892)$ $h = 1$ ϕ angle vs. $\cos(\theta_\Phi)$. 96

Figure 8.104 The reco $\Phi K^*(892)$ $h = 1$ ϕ angle vs. $\cos(\theta_\Phi)$. 96

Figure 8.105 The reco $\Phi K^*(892)$ $h = 1$ ϕ angle vs. $\cos(\theta_\Phi)$ drawn without the bmatch_best candidate. 96

Figure 8.106 The reco $\Phi K^*(892)$ $h = 1$ ϕ angle vs. $\cos(\theta_\Phi)$ drawn without the bmatch_best candidate. 96

Figure 8.107 The $\Phi K^*(892)$ $h = 1$ ϕ angle vs. $\cos(\theta_\Phi)$ efficiency drawn by dividing the reco bmatch_best histogram by the truth histogram. 96

Figure 8.108 The truth $\Phi K^*(892)$ $h = 0$ $\cos(\theta_{K^0_S\pi})$ vs. $m_{K^0_S\pi}$ 97

Figure 8.109 The reco $\Phi K^*(892)$ $h = 0$ $\cos(\theta_{K^0_S\pi})$ vs. $m_{K^0_S\pi}$ 97

Figure 8.110 The reco $\Phi K^*(892)$ $h = 0$ $\cos(\theta_{K^0_S\pi})$ vs. $m_{K^0_S\pi}$ drawn with the bmatch_best candidate. 97

Figure 8.111 The reco $\Phi K^*(892)$ $h = 0$ $\cos(\theta_{K^0_S\pi})$ vs. $m_{K^0_S\pi}$ drawn without the bmatch_best candidate. 97

Figure 8.112 The $\Phi K^*(892)$ $h = 0$ $\cos(\theta_{K^0_S\pi})$ vs. $m_{K^0_S\pi}$ efficiency drawn by dividing the reco bmatch_best histogram by the truth histogram. 97

Figure 8.113 The truth $\Phi K^*(892)$ $h = 0$ ϕ angle vs. $\cos(\theta_\Phi)$. 98

Figure 8.114 The reco $\Phi K^*(892)$ $h = 0$ ϕ angle vs. $\cos(\theta_\Phi)$. 98

Figure 8.115 The reco $\Phi K^*(892)$ $h = 0$ ϕ angle vs. $\cos(\theta_\Phi)$ drawn without the bmatch_best candidate. 98

Figure 8.116 The reco $\Phi K^*(892)$ $h = 0$ ϕ angle vs. $\cos(\theta_\Phi)$ drawn without the bmatch_best candidate. 98

Figure 8.117 The $\Phi K^*(892)$ $h = 0$ ϕ angle vs. $\cos(\theta_\Phi)$ efficiency drawn by dividing the reco bmatch_best histogram by the truth histogram. 98

Figure 8.118 The truth $\Phi K^*(892)$ $h = -1$ $\cos(\theta_{K^0_S\pi})$ vs. $m_{K^0_S\pi}$ 99

Figure 8.119 The reco $\Phi K^*(892)$ $h = -1$ $\cos(\theta_{K^0_S\pi})$ vs. $m_{K^0_S\pi}$ 99

Figure 8.120 The reco $\Phi K^*(892)$ $h = -1$ $\cos(\theta_{K^0_S\pi})$ vs. $m_{K^0_S\pi}$ drawn with the bmatch_best candidate 99

Figure 8.121 The reco $\Phi K^*(892)$ $h = -1$ $\cos(\theta_{K^0_S\pi})$ vs. $m_{K^0_S\pi}$ drawn without the bmatch_best candidate. 99

Figure 8.122 The $\Phi K^*(892)$ $h = -1$ $\cos(\theta_{K^0_S\pi})$ vs. $m_{K^0_S\pi}$ efficiency drawn by dividing the reco bmatch_best histogram by the truth histogram. 99

Figure 8.123 The truth $\Phi K^*(892)$ $h = -1$ ϕ angle vs. $\cos(\theta_\Phi)$. 100

Figure 8.124 The reco $\Phi K^*(892)$ $h = -1$ ϕ angle vs. $\cos(\theta_\Phi)$. 100

Figure 8.125 The reco $\Phi K^*(892)$ $h = -1$ ϕ angle vs. $\cos(\theta_\Phi)$ drawn without the bmatch_best candidate. 100

Figure 8.126 The reco $\Phi K^*(892)$ $h = -1$ ϕ angle vs. $\cos(\theta_\Phi)$ drawn without the bmatch_best candidate. 100

Figure 8.127 The $\Phi K^*(892)$ $h = -1$ ϕ angle vs. $\cos(\theta_\Phi)$ efficiency drawn by dividing the reco bmatch_best histogram by the truth histogram. 100

Figure 8.128 The truth $\Phi K^0_S\pi$ $\cos(\theta_{K^0_S\pi})$ vs. $m_{K^0_S\pi}$ 101

Figure 8.129 The reco $\Phi K^0_S\pi$ $\cos(\theta_{K^0_S\pi})$ vs. $m_{K^0_S\pi}$ 101

Figure 8.130 The reco $\Phi K^0_S\pi$ $\cos(\theta_{K^0_S\pi})$ vs. $m_{K^0_S\pi}$ drawn with the bmatch_best candidate 101

Figure 8.131 The reco $\Phi K^0_S\pi$ $\cos(\theta_{K^0_S\pi})$ vs. $m_{K^0_S\pi}$ drawn without the bmatch_best candidate. 101

Figure 8.132 The $\Phi K^0_S\pi$ $\cos(\theta_{K^0_S\pi})$ vs. $m_{K^0_S\pi}$ efficiency drawn by dividing the reco bmatch_best histogram by the truth histogram. 101

Figure 8.133 The truth $\Phi K^0_S\pi$ ϕ angle vs. $\cos(\theta_\Phi)$. 102

Figure 8.134 The reco $\Phi K^0_S\pi$ ϕ angle vs. $\cos(\theta_\Phi)$. 102

Figure 8.135 The reco $\Phi K^0_S\pi$ ϕ angle vs. $\cos(\theta_\Phi)$ drawn without the bmatch_best candidate. 102

Figure 8.136 The reco $\Phi K^0_S\pi$ ϕ angle vs. $\cos(\theta_\Phi)$ drawn without the bmatch_best candidate. 102

Figure 8.137 The $\Phi K^0_S\pi$ ϕ angle vs. $\cos(\theta_\Phi)$ efficiency drawn by dividing the reco bmatch_best histogram by the truth histogram 102

Figure 8.138 Migration vectors for a few $B^\pm \to \phi(K^0_S\pi)^\pm_0$ not-matched candidates. Blue arrows represent events moving to a location $>$ 1.1 GeV and red arrows are for events moving to a location $<$ 1.1 GeV. 104

Figure 8.139 Migration vectors for a random number of $B^\pm \to \phi K^*(892)^\pm$ $h = +1$ not matched candidates. 105

Figure 8.140 Migration vectors for a random number of $B^\pm \to \phi K^*(892)^\pm$ $h = 0$ not matched candidates. 105

Figure 8.141 Migration vectors for a random number of $B^\pm \to \phi K^*(892)^\pm$ $h = -1$ not matched candidates. 105

Figure 8.142 Migration vectors for a random number of $B^\pm \to \phi K^*_2(1430)^\pm$ $h = +1$ not matched candidates. 106

Figure 8.143 Migration vectors for a random number of $B^\pm \to \phi K^*_2(1430)^\pm$ $h = 0$ not matched candidates. 106

Figure 8.144 Migration vectors for a random number of $B^\pm \to \phi K^*_2(1430)^\pm$ $h = -1$ not matched candidates. 106

Figure 9.1 ΔE distribution for the background. 108

Figure 9.2 ΔE distribution for the signal. 108

Figure 9.3 m_{bc} distribution for the background. 108

Figure 9.4 m_{bc} distribution for the signal. 108

Figure 9.5 ΔE vs m_{bc} distribution for background. 109

Figure 9.6 ΔE vs m_{bc} distribution for the signal. 109

Figure 9.7 ΔE vs m_{bc} profile distribution for the background. 109

Figure 9.8 ΔE vs m_{bc} profile distribution for the signal. 109

Figure 9.9 m_{bc} vs ΔE profile distribution for the background. 109

Figure 9.10 m_{bc} vs ΔE profile distribution for the signal. 109

Figure 9.11 Variation of the significance as a function of ANN1 and ANN2 cuts for no cut on the $K^0_S\pi^+$ mass. 112

Figure 9.12 Variation of the significance as a function of ANN1 and ANN2 cuts for $0.842 < m_{K^0_S\pi^+} < 0.942$ GeV. 112

Figure 9.13 Variation of the significance as a function of ANN1 and ANN2 cuts for no cut on the $K^0_S\pi^+$ mass. 112

Figure 9.14 Variation of the significance as a function of ANN1 and ANN2 cuts for $0.842 < m_{K^0_S\pi^+} < 0.942$ GeV. 112

Figure 9.15 2D fit example; the dots are fit results and the histogram shows simulated data. 113

Figure 10.1 Fit to ΔE for $B^+ \to \phi K^{*+}(892)$ h=+1 MC events. 117

Figure 10.2 Fit to a'_1 for $B^+ \to \phi K^{*+}(892)$ h=+1 MC events. 117

Figure 10.3 Fit to a'_2 for $B^+ \to \phi K^{*+}(892)$ h=+1 MC events. 117

Figure 10.4 Fit to a'_1 for light flavor MC background events. 118

Figure 10.5 Fit to a'_2 for light flavor MC background events. 118

Figure 10.6 Fit to a'_1 for heavy flavor MC background events. 118

Figure 10.7 Fit to a'_2 for light flavor MC background events. 118

Figure 10.8 Fit to a'_1 for $B^\pm$ signal simulation. 119

Figure 10.9 Fit to a'_2 for $B^\pm$ signal simulation. 119

Figure 10.10 Fit to m_{bc} for $B^\pm$ signal simulation. 119

Figure 10.11 Fit to ΔE for $B^\pm$ signal simulation. 119

Figure 10.12 Fitter input for light flavor and heavy flavor B^+ backgrounds. 120

Figure 10.13 Fitter input for light flavor and heavy flavor B^- backgrounds. 120

Figure 10.14 Fit to $m_{K^0_S\pi}$ for B^+ signal and background. 122

Figure 10.15 Fit to $m_{K^0_S\pi}$ for B^- signal and background. 122

Figure 10.16 Fit to $cos(\theta_{K^0_S\pi})$ for B^+ signal and background. 123

Figure 10.17 Fit to $cos(\theta_{K^0_S\pi})$ for B^- signal and background. 123

Figure 10.18 Fit to $cos(\theta_\Phi)$ for B^+ signal and background. 124

Figure 10.19 Fit to $cos(\theta_\Phi)$ for B^- signal and background. 124

Figure 10.20 Fit to Φ for B^+ signal and background. 125

Figure 10.21 Fit to Φ for B^- signal and background. 125

Figure 10.22 Fit to m_{bc} for B^+ signal and background. 126

Figure 10.23 Fit to m_{bc} for B^- signal and background. 126

Figure 10.24 Fit to a'_1 for B^+ signal and background. 127

Figure 10.25 Fit to a'_2 for B^- signal and background. 127

Figure 10.26 Fit to $m_{K^0_S\pi}$ for B^+ signal. 128

Figure 10.27 Fit to $m_{K^0_S\pi}$ for B^- signal. 128

Figure 10.28 Fit to $cos(\theta_{K^0_S\pi})$ for B^+ signal. 128

Figure 10.29 Fit to $cos(\theta_{K^0_S\pi})$ for B^- signal. 128

Figure 10.30 Fit to $cos(\theta_\Phi)$ for B^+ signal. 128

Figure 10.31 Fit to $cos(\theta_\Phi)$ for B^- signal. 128

Figure 10.32 Fit to Φ for B^+ signal. 129

Figure 10.33 Fit to Φ for B^- signal. 129

Figure 10.34 Fit to m_{bc} for B^+ signal. 129
Figure 10.35 Fit to m_{bc} for B^- signal. 129
Figure 10.36 Fit to ΔE for B^+ signal. 129
Figure 10.37 Fit to ΔE for B^- signal. 129
Figure 10.38 Fit to a_1' for B^+ signal and background. 130
Figure 10.39 Fit to a_2' for B^- signal and background. 130
Figure 10.40 Fit to $m_{K_S^0\pi}$ for B^+ background. 131
Figure 10.41 Fit to $m_{K_S^0\pi}$ for B^- background. 131
Figure 10.42 Fit to $cos(\theta_{K_S^0\pi})$ for B^+ background. 131
Figure 10.43 Fit to $cos(\theta_{K_S^0\pi})$ for B^- background. 131
Figure 10.44 Fit to $cos(\theta_\Phi)$ for B^+ background. 131
Figure 10.45 Fit to $cos(\theta_\Phi)$ for B^- background. 131
Figure 10.46 Fit to Φ for B^+ background. 132
Figure 10.47 Fit to Φ for B^- background. 132
Figure 10.48 Fit to m_{bc} for B^+ background. 132
Figure 10.49 Fit to m_{bc} for B^- background. 132
Figure 10.50 Fit to ΔE for B^+ background. 132
Figure 10.51 Fit to ΔE for B^- background. 132
Figure 10.52 Fit to a_1' for B^+ signal and background. 133
Figure 10.53 Fit to a_2' for B^- signal and background. 133
Figure 10.54 Branching fraction and f_L fitter input and output parameters. 134
Figure 10.55 A_{CP} and f_L fitter input and output parameters. 134

Figure 10.56 Angular fitter input and output parameters. 135

Figure 10.57 Difference in the angular parameters for fitter input and output. 135

Figure 10.58 Input and output number of B^+ and B^- heavy flavor and light flavor backgrounds. 136

Figure 10.59 Bias and pull distributions for branching fractions with 1x the signal. 137

Figure 10.60 Bias and pull distributions for amplitude fractions for B^- with 1x the signal. 137

Figure 10.61 Bias and pull distributions for phases with 1x the signal. . . 138

Figure 10.62 Bias and pull distributions for A_{CP} parameters with 1x the signal. 138

Figure 10.63 Bias and pull distributions for amplitude fractions for B^+ with 1x the signal. 139

Figure 10.64 Bias and pull distributions for Δ parameters with 1x the signal. 139

Figure 10.65 Bias and pull distributions for background parameters and 1x the signal. 140

Figure 10.66 Fit to $cos(\theta_{K^0_S\pi})$ for B^+ signal and background. 141

Figure 10.67 Fit to $cos(\theta_{K^0_S\pi})$ for B^- signal and background. 141

Figure 10.68 Fit to $cos(\theta_\Phi)$ for B^+ signal and background. 142

Figure 10.69 Fit to $cos(\theta_\Phi)$ for B^- signal and background. 142

Figure 10.70 Fit to ΔE for B^+ signal and background. 143

Figure 10.71 Fit to ΔE for B^- signal and background. 143

Figure 10.72 Fit to m_{bc} for B^+ signal and background. 144

Figure 10.73 Fit to m_{bc} for B^- signal and background. 144

Figure 10.74 Fit to $m_{K^0_S\pi}$ for B^+ signal and background. 145
Figure 10.75 Fit to $m_{K^0_S\pi}$ for B^- signal and background. 145
Figure 10.76 Fit to Φ for B^+ signal and background. 146
Figure 10.77 Fit to Φ for B^- signal and background. 146
Figure 10.78 Fit to $cos(\theta_{K^0_S\pi})$ for B^+ signal. 147
Figure 10.79 Fit to $cos(\theta_{K^0_S\pi})$ for B^- signal. 147
Figure 10.80 Fit to $cos(\theta_\Phi)$ for B^+ signal. 147
Figure 10.81 Fit to $cos(\theta_\Phi)$ for B^- signal. 147
Figure 10.82 Fit to ΔE for B^+ signal. 147
Figure 10.83 Fit to ΔE for B^- signal. 147
Figure 10.84 Fit to m_{bc} for B^+ signal. 148
Figure 10.85 Fit to m_{bc} for B^- signal. 148
Figure 10.86 Fit to $m_{K^0_S\pi}$ for B^+ signal. 148
Figure 10.87 Fit to $m_{K^0_S\pi}$ for B^- signal. 148
Figure 10.88 Fit to Φ for B^+ signal. 148
Figure 10.89 Fit to Φ for B^- signal. 148
Figure 10.90 Fit to $cos(\theta_{K^0_S\pi})$ for B^+ background. 149
Figure 10.91 Fit to $cos(\theta_{K^0_S\pi})$ for B^- background. 149
Figure 10.92 Fit to $cos(\theta_\Phi)$ for B^+ background. 149
Figure 10.93 Fit to $cos(\theta_\Phi)$ for B^- background. 149
Figure 10.94 Fit to ΔE for B^+ background. 149
Figure 10.95 Fit to ΔE for B^- background. 149

Figure 10.96 Fit to m_{bc} for B^+ background. 150

Figure 10.97 Fit to m_{bc} for B^- background. 150

Figure 10.98 Fit to $m_{K^0_S\pi}$ for B^+ background. 150

Figure 10.99 Fit to $m_{K^0_S\pi}$ for B^- background. 150

Figure 10.100 Fit to Φ for B^+ background. 150

Figure 10.101 Fit to Φ for B^- background. 150

Figure 10.102 Branching fraction and f_L fitter input and output parameters 151

Figure 10.103 A_{CP} and f_L fitter input and output parameters. 151

Figure 10.104 Angular fitter input and output parameters. 152

Figure 10.105 Difference in the angular parameters for fitter input and output. 152

Figure 10.106 Input and output number of B^+ and B^- heavy flavor and light flavor backgrounds. 153

Figure 10.107 Bias and pull distributions for branching fractions with 10x the signal. 155

Figure 10.108 Bias and pull distributions for amplitude fractions for B^- with 10x the signal. 155

Figure 10.109 Bias and pull distributions for phases with 10x the signal. . 156

Figure 10.110 Bias and pull distributions for A_{CP} parameters with 10x the signal. 156

Figure 10.111 Bias and pull distributions for amplitude fractions for B^+ with 10x the signal. 157

Figure 10.112 Bias and pull distributions for Δ parameters with 10x the signal. 157

Figure 10.113 Bias and pull distributions for background parameters and 10x the signal. 158

Figure 11.1 Fit to a_1' for $B^+ \to \overline{D}^0\pi^+$ MC events. 160

Figure 11.2 Fit to a_1' for $B^+ \to \overline{D}^0\pi^+$ data events. 160

Figure 11.3 Fit to $m(D^0)$ for $B^+ \to \overline{D}^0\pi^+$ MC events. 161

Figure 11.4 Fit to $m(D^0)$ for $B^+ \to \overline{D}^0\pi^+$ data events. 161

Figure 11.5 Fit to ΔE for $B^+ \to \overline{D}^0\pi^+$ MC events. 161

Figure 11.6 Fit to ΔE for $B^+ \to \overline{D}^0\pi^+$ data events. 161

Figure 12.1 Energy of photons radiated from kaon decays. 164

Figure 12.2 Energy of photons radiated from pion decays. 164

Figure A.1 Data Skim Out/In Ratio. 218

Figure A.2 Data Reco Out/In Ratio. 218

Figure A.3 Full stream 1 uds Skim Out/In Ratio. 218

Figure A.4 Full stream 1 uds Reco Out/In Ratio. 218

Figure A.5 Full stream 1 Charm Skim Out/In Ratio. 218

Figure A.6 Full stream 1 Charm Reco Out/In Ratio. 218

Figure A.7 Full stream 1 mixed Skim Out/In Ratio. 219

Figure A.8 Full stream 1 mixed Reco Out/In Ratio. 219

Figure A.9 Full stream 1 charged Skim Out/In Ratio. 219

Figure A.10 Full stream 1 charged Reco Out/In Ratio. 219

Figure A.11 Full stream 2 uds Skim Out/In Ratio. 219

Figure A.12 Full stream 2 uds Reco Out/In Ratio. 219

Figure A.13 Full stream 2 charm Skim Out/In Ratio. 220

Figure A.14 Full stream 2 charm Reco Out/In Ratio. 220

Figure A.15 Full stream 2 mixed Skim Out/In Ratio. 220
Figure A.16 Full stream 2 mixed Reco Out/In Ratio. 220
Figure A.17 Full stream 2 charged Skim Out/In Ratio. 220
Figure A.18 Full stream 2 charged Reco Out/In Ratio. 220
Figure A.19 Full stream 3 uds Skim Out/In Ratio. 221
Figure A.20 Full stream 3 uds Reco Out/In Ratio. 221
Figure A.21 Full stream 3 charm Skim Out/In Ratio. 221
Figure A.22 Full stream 3 charm Reco Out/In Ratio. 221
Figure A.23 Full stream 3 mixed Skim Out/In Ratio. 221
Figure A.24 Full stream 3 mixed Reco Out/In Ratio. 221
Figure A.25 Full stream 3 charged Skim Out/In Ratio. 222
Figure A.26 Full stream 3 charged Reco Out/In Ratio. 222
Figure A.27 Full stream 4 uds Skim Out/In Ratio. 222
Figure A.28 Full stream 4 uds Reco Out/In Ratio. 222
Figure A.29 Full stream 4 charm Skim Out/In Ratio. 222
Figure A.30 Full stream 4 charm Reco Out/In Ratio. 222
Figure A.31 Full stream 4 mixed Skim Out/In Ratio. 223
Figure A.32 Full stream 4 mixed Reco Out/In Ratio. 223
Figure A.33 Full stream 4 charged Skim Out/In Ratio. 223
Figure A.34 Full stream 4 charged Reco Out/In Ratio. 223
Figure A.35 Full stream 5 uds Skim Out/In Ratio. 223
Figure A.36 Full stream 5 uds Reco Out/In Ratio. 223
Figure A.37 Full stream 5 charm Skim Out/In Ratio. 224

Figure A.38 Full stream 5 charm Reco Out/In Ratio. 224

Figure A.39 Full stream 5 mixed Skim Out/In Ratio. 224

Figure A.40 Full stream 5 mixed Reco Out/In Ratio. 224

Figure A.41 Full stream 5 charged Skim Out/In Ratio. 224

Figure A.42 Full stream 5 charged Reco Out/In Ratio. 224

Figure B.1 Efficiency of $m_{K^0_S\pi}$ for different decay modes. 225

Figure B.2 Efficiency of $\cos(\theta_{K^0_S\pi})$ for different decay modes. 226

Figure B.3 Efficiency vs $\cos\theta_{K^0_S\pi}$ in the mass range [865, 915] MeV for K*(892) and $K^0_S\pi$ NR modes. The efficiencies are a lot closer when the mass range is restricted. 227

Figure B.4 Efficiency of $\cos(\theta_\Phi)$ for different decay modes. 228

Figure B.5 Efficiency of ϕ for different decay modes. 228

Chapter 1

Introduction

1.0.1 The Standard Model

The Standard Model (SM) is a theory of the fundamental particles and their interactions. It is comprised of two families of particles with different quantum spin characteristics: fermions and bosons. Fermions have half-integer spin and include all of the quarks and the leptons. Bosons have integer spin and consist of all the mediators of interactions: gluons, photons, $W^{\pm}$, Z^0, and the Higgs, which couples to massive fermions and weak bosons. Hadrons are composed of quarks and have two classifications of particles: mesons and baryons. Mesons are made up of a quark and an anti-quark. Baryons are composed of three quarks.

There are three generations of quarks. The first consisting of up (u) and down (d). The second, strange (s) and charm (c). And lastly, the third generation consists of the bottom (b) quark and the top (t) quark as seen in table 1.1.

Table 1.1 Properties of the Quarks

Generation	Flavor	Charge(e)	Mass
First	d (down)	-1/3	$4.7^{+0.5}_{-0.4}$ MeV
	u (up)	2/3	$2.2^{+0.6}_{-0.4}$ MeV
Second	s (strange)	-1/3	96^{+8}_{-4} MeV
	c (charm)	2/3	1.27 ± 0.03 GeV
Third	b (bottom)	-1/3	$4.18^{+0.04}_{-0.03}$ GeV
	t (top)	2/3	$173.21 \pm 0.51 \pm 0.71$ GeV

Charges and masses of the quarks [1].

The quarks also carry another type of charge: color. In chromodynamics, or the

study of strong interactions with quarks and gluons, it is color that plays the role of electric charge. Each gluon can come in three colors: red, green, and blue. All naturally occurring particles will either have all the colors or will be colorless. For baryons, there will be one unit of each color. For a meson, the quark will have one unit of a particular color, say red, for example, and then the anti-quark must have minus one unit of red.

The leptons are the electron, muon, and the tau particles each with charge $Q = -1$ (e) and a spin $S = 1/2$, and then the neutrinos: ν_e, ν_μ, and ν_τ with neutral charge $Q = 0$ and a spin $S = 1/2$.

According to the SM, there are four fundamental forces: the gravitational force, the electromagnetic force, the strong force, and the weak force. Gravity is the weakest of the four, but works over an infinite range. The electromagnetic force is mediated by the photon and has an infinite range as well. The electromagnetic force can be much stronger than the gravitational force. The strong force is responsible for keeping neutrons and protons bound in a nucleus. Though the strong force works only over a small range, it is the strongest force out of the four. Its mediator is the gluon. The $W^{\pm}$ and the Z^0 are responsible for the weak force. The weak force also has a short range.

The spin of a particle, J, and the parity, P, are often represented by the notation J^P. From this notation, we can characterize particles as follows

- 0^+: scalar
- 0^-: pseudoscalar
- 1^-: vector
- 1^+: axial vector
- 2^+: tensor

1.0.2 **CP Violation**

The Big Bang theory states when the universe was born equal amounts of matter and antimatter were created. When anti-matter and matter collide, they annihilate each other and release energy in the form of photons. Photons arising from the initial annihilation of matter and anti-matter are called the Cosmic Microwave Background. However, about one out of every billion quarks survived annihilation, creating the universe we know today. The mystery is where is the corresponding anti-matter?

In 1967 Andrei Sakharov proposed that CP violation could explain the observed matter-antimatter imbalance in the universe [2]. The C operator represents charge conjugation and when applied to a meson, it converts the quarks of the particle into their anti-quarks. Charge conjugation changes the sign of all the internal quantum numbers: charge, strangeness, charm, beauty, truth, baryon number, and lepton number. If the meson does not change under the interchange of the quark and the antiquark

$$C|q\bar{q}\rangle = |\bar{q}q\rangle \tag{1.1}$$

then the meson is called "C even" and the eigenvalue is $C = +1$. If

$$C|q\bar{q}\rangle = -|\bar{q}q\rangle \tag{1.2}$$

then the meson is called "C odd" and has an eigenvalue $C = -1$.

Parity (P) is the transformation of the sign(s) of spatial coordinates or a mirror reflection of the laws of nature. Only weak interactions have been found to violate parity and consequently violate CP symmetry.

In the standard model (SM), CP violation can be explained by an irreducible phase in the 3×3 Cabibbo-Kobayashi-Maskawa (CKM) quark mixing matrix. There are three types of CP violation: direct, indirect, and mixture of the two. Direct CP violation occurs only in decays. Indirect CP violation occurs only in oscillations such

as the oscillations of B^0 and $\bar{B}^0$. The third type of CP violation is in the interference between mixing and decay [3].

1.0.3 Introduction into Angular Analysis

Particles also have another property called the helicity, h, which is the projection of its spin, J, along its momentum. For particles with mass there are $2J+1$ possible helicity values: $-J$, $-J+1$, ..., $J-1$, J.

If for example, we have a spin 0 particle that decays into two particles, particle A and particle B, then the spin projection of the final state on the decay axis of the mother particle must be 0. Because of this particles A and B must have the same helicity. If the parent particle had two spin one daughters, then for one of the daughters, the helicity could be 1, 0, or -1. There is a corresponding complex amplitude a_λ for each of the helicities: a_{+1} and a_{-1} for the transverse helicities and a_0 for the longitudinal helicity. The helicity basis is made up of helicity eigenstates corresponding to each of these amplitudes.

1.0.4 Theoretical Understanding of $B \to VV$ Decays

Charmless B-meson decays such as $B^\pm \to \phi K^{*\pm}$ that are dominated by $b \to s$ penguin loop transitions could reveal non-SM physics. New particles have the potential of appearing in virtual loops, which in turn could create CP violation. Since we are studying charged B mesons, there are no oscillations so there is only direct CP violation [4]. By direct CP violation we mean the decay rates of the B^+ and B^- can be different.

Penguin diagrams in charmless B-decays may use the CKM matrix elements V_{tb} and V_{ts} and therefore can result in significant BF's. This is unlike D meson decays which involve the CKM elements V_{cb} and V_{ub} and could result in SM-dominated CP violation. Measurements of $B \to VV$ decays can be found in Fig. 1.1 from Ref. [4]. In

this analysis we are studying this mode and its BF in hopes of helping to illuminate the significance of penguin decay contributions and finding CP violation.

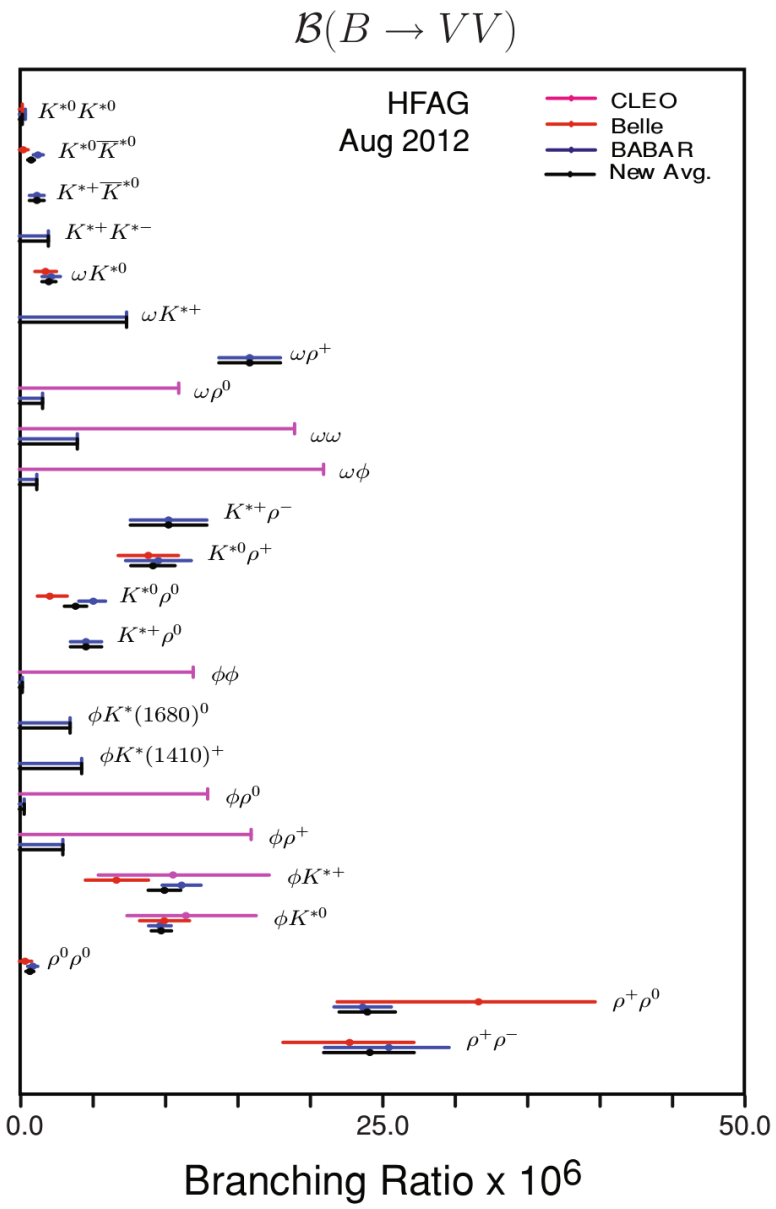

Figure 1.1: Measurements of branching fractions for B to VV decays from Ref. [4].

In the SM the simplest factorization does not yield CP violation, rather corrections to the factorization are needed for CPV. Factorization is an ansatz that continues to be tested in the high energy calculations. It is a method that factors parts of

a cross-section or decay into two parts: soft and perturbative or hard and non-perturbative. From 1999 to 2001, Beneke, Buchalla, Neubert, and Sachrajda [5] created a method that replaced the simple factorization with a factorization formula that includes spectator-scattering effects and radiative corrections both to account for CP violation effects. Other factorization methods include perturbative QCD (PQCD) and soft collinear theory.

Today, SM BF calculations for B meson decays are based on QCD factorization and flavor-SU(3) symmetry. The effects of direct CP violation in the SM are small in penguin diagrams, like our own, but still need to be measured precisely.

Transverse and longitudinal helicity amplitudes (or amplitudes with helicity 0 and helicity $+1$ and -1 respectively–explained in the "Physics Model" section) are not easily factorizable in decays to VV.

Polarization is expected to be mainly helicity 0 in $B \to VV$ decays due to vector minus axial vector coupling, $V - A$ [4]. However, experiments have shown that this is mainly seen in decays with a tree diagram, or decays that do not have a loop [4] (aka not a penguin loop in which a quark emits a virtual W only to reabsorb it and meanwhile interact with a gluon). More measurements are needed to confirm the behavior of $B \to VV$ decays.

Prof. Martin Beneke has provided us with updated theoretical predictions for values for the $B^{\pm} \to \phi K^{*\pm}$ decay mode which are shown in Table 1.2. These are an updated version from [6].

Table 1.2 Theorectical Predictions

Observable		Theory			Experiment
		default	constrained X_A	$\hat{\alpha}_4^c$ from data	
BrAv $/10^{-6}$	ϕK^{*-}	11^{+1+19}_{-1-10}	$10.1^{+0.5+7.2}_{-0.5-4.8}$	10^{+1+4+0}_{-1-3-0}	9.7 ± 1.5
	$\phi \bar{K}^{*0}$	10^{+1+19}_{-1-9}	$9.3^{+0.5+6.7}_{-0.5-4.5}$	9^{+1+4+0}_{-1-3-0}	9.5 ± 0.8
$A_{CP}/\%$	ϕK^{*-}	0^{+0+3}_{-0-1}	0^{+0+0}_{-0-0}	1^{+0+1+1}_{-0-1-2}	5 ± 11
	$\phi \bar{K}^{*0}$	1^{+0+1}_{-0-1}	1^{+0+0}_{-0-0}	2^{+1+1+1}_{-1-1-2}	-1 ± 6
$f_L/\%$	ϕK^{*-}	42^{+0+64}_{-0-38}	45^{+0+35}_{-0-31}	$50^{+0+22+0}_{-0-20-1}$	50 ± 7
	$\phi \bar{K}^{*0}$	42^{+0+63}_{-0-37}	44^{+0+35}_{-0-31}	$49^{+0+22+0}_{-0-20-0}$	49 ± 3
$A^0_{CP}/\%$	ϕK^{*-}	-1^{+0+4}_{-0-1}	-1^{+0+1}_{-0-1}	0^{+0+1+0}_{-0-3-0}	n/a
	$\phi \bar{K}^{*0}$	0^{+0+1}_{-0-3}	0^{+0+1}_{-0-0}	1^{+0+2+0}_{-0-4-0}	2 ± 7
$(f_\parallel - f_\perp)/\%$	ϕK^{*-}	0^{+0+3}_{-0-3}	0^{+0+2}_{-0-2}	0^{+0+3+}_{-0-3-}	12 ± 17
	$\phi \bar{K}^{*0}$	0^{+0+3}_{-0-3}	0^{+0+2}_{-0-2}	0^{+0+3+}_{-0-3-}	1 ± 7
$(A^\parallel_{CP} - A^\perp_{CP})/\%$	ϕK^{*-}	0^{+0+0}_{-0-0}	0^{+0+0}_{-0-0}	0^{+0+0+}_{-0-0-}	n/a
	$\phi \bar{K}^{*0}$	0^{+0+0}_{-0-0}	0^{+0+0}_{-0-0}	0^{+0+0+}_{-0-0-}	18 ± 28
$\phi_\parallel/^\circ$	ϕK^{*-}	-109^{+0+288}_{-0-56}	-41^{+0+35}_{-0-30}	$-43^{+0+18+1}_{-0-17-1}$	-60 ± 16
	$\phi \bar{K}^{*0}$	$-112^{+291+87}_{-55\ -54}$	-42^{+0+35}_{-0-30}	$-45^{+0+18+0}_{-0-17-0}$	-44 ± 8
$\Delta\phi_\parallel/^\circ$	ϕK^{*-}	0^{+0+0}_{-0-2}	0^{+0+0}_{-0-0}	0^{+0+2+0}_{-0-1-0}	n/a
	$\phi \bar{K}^{*0}$	0^{+0+0}_{-0-2}	0^{+0+0}_{-0-0}	0^{+0+2+0}_{-0-2-0}	6 ± 8
$(\phi_\parallel - \phi_\perp)/^\circ$	ϕK^{*-}	0^{+0+1}_{-0-1}	0^{+0+1}_{-0-1}	0^{+0+1+0}_{-0-1-0}	-12 ± 24
	$\phi \bar{K}^{*0}$	0^{+0+1}_{-0-1}	0^{+0+1}_{-0-1}	0^{+0+1+0}_{-0-1-0}	1 ± 11
$(\Delta\phi_\parallel - \Delta\phi_\perp)/^\circ$	ϕK^{*-}	0^{+0+1}_{-0-1}	0^{+0+0}_{-0-0}	0^{+0+1+0}_{-0-1-0}	n/a
	$\phi \bar{K}^{*0}$	0^{+0+1}_{-0-1}	0^{+0+0}_{-0-0}	0^{+0+1+0}_{-0-1-0}	3 ± 11

Theoretical predictions for observables for the $B^\pm \to \phi K^{*\pm}$ decay mode [6] .

1.0.5 Experimental Status of $B^\pm \to \phi K^{*\pm}$ decay measurements

A summary of prior experimental results are listed in Tables 1.3 and 1.4.

If we compare the charged mode tables with the neutral mode ones we can see that there are more empty boxes for the charged mode calculations and the errors in the charged modes tend to be larger than those in the neutral mode. This provides us further motivation for studying and measuring the charged modes. The f_L values are

Table 1.3 Results for $\mathcal{B}$ for B-meson Decays to $\phi K^0_S \pi$ Final States

	$\mathcal{B}$(in units of 10^{-6})	
	$B^+ \to \phi(K\pi)^{*+}_0$	$B^0 \to \phi(K\pi)^{*0}_0$
Belle [7, 8]	—	$4.3 \pm 0.4 \pm 0.4$
Babar [9, 10, 11]	$8.3 \pm 1.4 \pm 0.8$	$4.3 \pm 0.6 \pm 0.4$
PDG Average [12]	—	4.3 ± 0.4

	$\mathcal{B}$(in units of 10^{-6})	
	$B^+ \to \phi K^*(892)^+$	$B^0 \to \phi K^*(892)^0$
Belle [13, 7, 8]	$6.7^{+2.1+0.7}_{-1.9-1.0}$	$10.4 \pm 0.5 \pm 0.6$
Babar [10, 11]	$11.2 \pm 1.0 \pm 0.9$	$9.7 \pm 0.5 \pm 0.5$
LHCb [14]	—	—
CLEO [15]	$11.4^{+9.0+1.8}_{-6.3-1.8}$	$11.5^{+4.5+1.8}_{-3.7-1.7}$
PDG Average [12]	10.0 ± 2.0	10.0 ± 0.5

	$\mathcal{B}$(in units of 10^{-6})	
	$B^+ \to \phi K^*_0(1430)^+$	$B^0 \to \phi K^*_0(1430)^0$
Babar [9, 11]	$7.0 \pm 1.3 \pm 0.9$	$3.9 \pm 0.5 \pm 0.6$

	$\mathcal{B}$(in units of 10^{-6})	
	$B^+ \to \phi K^*_2(1430)^+$	$B^0 \to \phi K^*_2(1430)^0$
Belle [13]	—	$5.5^{+0.9}_{-0.7} \pm 1.0$
Babar [9, 11]	$8.4 \pm 1.8 \pm 1.0$	$7.5 \pm 0.9 \pm 0.5$
PDG Average [12]	—	6.8 ± 0.9

different for the vector and tensor channels. This needs to be further verified. More importantly, the BF values are different between the neutral and charged modes. If this is the case, then this would violate isospin symmetry. The charged decay mode needs to be studied further to see if these differences are real. We aim to have BF errors comparable or lower than the $\sim 20\%$ as indicated in the table for the charged mode.

Table 1.4 Measurements of the Longitudinal Polarization Fraction f_L for B-meson Decays to $\phi K^0_S \pi$ Final States

	f_L	
	$B^+ \to \phi(K\pi)^{*+}_0$	$B^0 \to \phi(K\pi)^{*0}_0$
Belle [7, 8]	$0.19 \pm 0.08 \pm 0.02$	—
Babar [9, 10, 11]	$0.21 \pm 0.05 \pm 0.02$	—
PDG Average [12]	0.20 ± 0.05	—

	f_L	
	$B^+ \to \phi K^*(892)^+$	$B^0 \to \phi K^*(892)^0$
Belle [13, 7, 8]	$0.52 \pm 0.08 \pm 0.03$	$0.499 \pm 0.030 \pm 0.018$
Babar [10, 11]	$0.49 \pm 0.05 \pm 0.03$	$0.494 \pm 0.034 \pm 0.013$
LHCb [14]	—	$0.497 \pm 0.019 \pm 0.015$
CLEO [15]	—	—
PDG Average [12]	0.50 ± 0.05	0.497 ± 0.017

	f_L	
	$B^+ \to \phi K^*_0(1430)^+$	$B^0 \to \phi K^*_0(1430)^0$
Babar [9, 11]	—	—

	f_L	
	$B^+ \to \phi K^*_2(1430)^+$	$B^0 \to \phi K^*_2(1430)^0$
Belle [13]	—	$0.918^{+0.029}_{-0.060} \pm 0.012$
Babar [9, 11]	$0.80^{+0.09}_{-0.10} \pm 0.03$	$0.901^{+0.046}_{-0.058} \pm 0.037$
PDG Average [12]	—	$0.913^{+0.028}_{-0.050}$

1.0.6 Introduction to the Modes Used in this Analysis

The following decay modes are used in this analysis:

- $B^{\pm} \to \phi K_S^0 \pi^{\pm}$ (non-resonant)
- $B^{\pm} \to \phi K^*(892)^{\pm} \to \phi K_S^0 \pi^{\pm}$
- $B^{\pm} \to \phi K_0^*(1430)^{\pm} \to \phi K_S^0 \pi^{\pm}$
- $B^{\pm} \to \phi K_2^*(1430)^{\pm} \to \phi K_S^0 \pi^{\pm}$

Note that in each decay there is an additional intermediate oscillation of $K^0 \to K_S^0$ with a probability of 50% (this is a kin to a branching fraction, $\mathcal{B}$). In this analysis, the $K^*(892)^{\pm}$ mode was the most easily reconstructed and most abundant. In addition, each ϕ decays to K^+K^-.

Each K^* is considered a "resonant" particle of the $K_S^0\pi^{\pm}$. This means the tightly bound $\bar{s}u$ quark pair (for K^{*+}) are short lived with a lifetime of $\sim 4 \times 10^{-23}s$. The "resonances" of the quark pair occur at energies such as 892 MeV and 1430 MeV. Note that the K_S^0 and the $\pi^{\pm}$ are two particles that have significantly longer lifetimes and travel distances than the resonances.

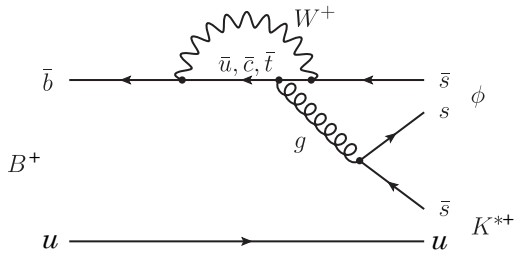

Figure 1.2: A penguin diagram of the $B^{\pm} \to \phi K^{*\pm}$ decay.

Figure 1.2 shows the penguin diagram of the $B^{\pm} \to \phi K^{*\pm}$ decay. The production of W^+ allows for virtual quarks of $\bar{u}, \bar{c}$, or $\bar{t}$. A hard gluon, that is a gluon with a lot of energy, is emitted along with a soft gluon (not pictured) in order to conserve color.

The hard gluon decays to a $s\bar{s}$ pair. The gluon couplings are a strong interaction whereas the rest of the decay is considered weak.

Basic Properties of Particles in Decay Chain

The table below contains some useful properties of the particles used in this decay. Note the "..." is used when there is either no studied full width is available. The K and the π are long-lived enough to have narrow widths that cannot be directly measured. B mesons have a half width but is not worth reporting since we cannot measure it. The width's for the B's are so small that if we were to attempt to measure it, we would end up measuring experimental resolution instead.

Table 1.5 Properties of Particles in this Decay Analysis

Particle	$I(J^P)$	Mass (MeV)	Full Width, Γ (MeV)
$B^{\pm}$	$\frac{1}{2}(0^-)$	5279.31 ± 0.15	...
$\phi(1020)$	$\frac{1}{2}^-(0^{--})$	1019.461 ± 0.019	4.266 ± 0.031
$K^*(892)^{\pm}$	$\frac{1}{2}(1^-)$	891.66 ± 0.26	50.8 ± 0.9
$K_0^*(1430)^{\pm}$	$\frac{1}{2}(0^+)$	1425 ± 50	270 ± 80
$K_2^*(1430)^{\pm}$	$\frac{1}{2}(2^+)$	1425.6 ± 1.5	98.5 ± 2.7
K_S^0	$\frac{1}{2}(0^-)$	497.61 ± 0.01	...
$K^{\pm}$	$\frac{1}{2}(0^-)$	493.677 ± 0.016	...
$\pi^{\pm}$	$\frac{1}{2}^-(0^-)$	139.57018 ± 0.00035	...

Basic properties on the particles in this decay analysis as reported by the Particle Data Group. Note for the ϕ and π the second column represents $I^G(J^{PC})$.

Chapter 2

The KEKB Accelerator

The Belle detector sits at the collision point of the asymmetric energy e^+e^- collider the KEK B-Factory, KEKB. Running started December 1998 and KEKB finished its high energy career June 2010 after it achieved the world record luminosity of 2.11×10^{34} cm^{-2}s^{-1} [16].

The 8 GeV electron beam and the 3.5 GeV positron beam created collisions at a center-of-mass energy, $\sqrt{s}$, of 10.58 GeV, which is equal to the mass of the $\Upsilon(4S)$. These two beams are accelerated in two rings, the high-energy ring (HER) and the low-energy ring (LER) respectively with a circumference of 3 km [17]. Both are installed side-by-side in a tunnel 11m below ground level as seen in Fig. 2.1.

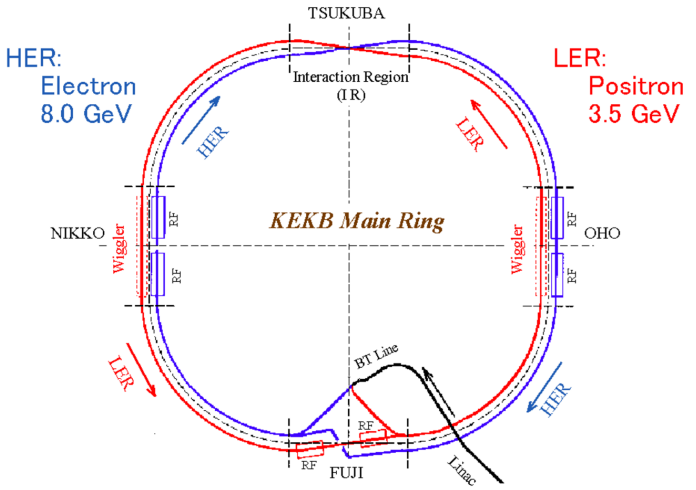

Figure 2.1: Shows the configuration of the two KEKB rings and the collision site at Tsukuba experimental hall where the Belle detector is located [18].

After 2007, KEKB implemented crab cavities which rotated the bunches of particles in each of the beams. This allowed the bunches to collide head on in attempts of improving luminosity. Fig. 2.2 shows the bunches of the beams before and after crab cavities.

While there was improvement in the luminosity, it didn't help much in accumulating more data due to the time spent in accelerator studies.

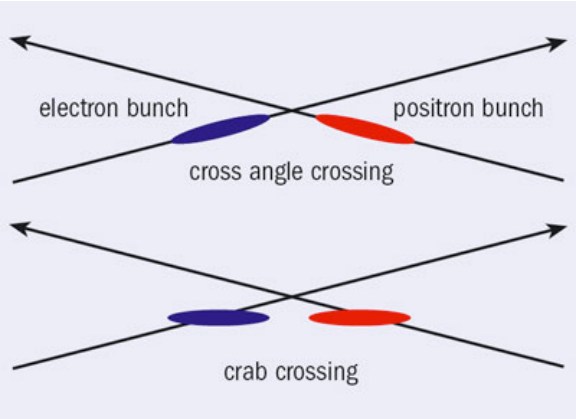

Figure 2.2: Shows the bunches of the beams rotated so that the bunches collide head-on [19].

Table 2.1 shows the machine parameters of KEKB during the last stage of operation.

Table 2.1 KEKB Machine Parameters

Parameters		KEKB
Beam energy	(GeV)	$8.0(e^-)$, $3.5(e^+)$
Beam current	(A)	$1.2(e^-)$, $1.6(e^+)$
Beam size at IP x	(μm)	80
y	(μm)	1
z	(mm)	5
Luminosity	($\mathrm{cm^{-2}s^{-1}}$)	2.1×10^{34}
Number of beam bunches		1584
Bunch spacing	(m)	1.84
Beam crossing angle	(mrad)	$\pm$11 (crab-crossing)

Machine parameters of KEKB during the last stage of its operation [4].

Chapter 3

The Belle Detector

This analysis is based on the data collected by the Belle detector, which sits at the interaction point of the asymmetric-energy e^+e^- collider, KEKB. The Belle detector is located at KEK, the High Energy Accelerator Research Organization in Tsukuba Ibaraki Prefecture, Japan.

The primary goal of the Belle detector is measuring properties in rare B meson decays to verify the Kobayashi-Maskawa mechanism that describes CP violation in the standard model. Other important aims were to precisely measure the decays of τ leptons, and bottom and charm mesons, and to search for rare or forbidden processes in the SM.

Most of the data was accumulated at the $\Upsilon(4S)$ resonance in order to obtain plenty of B mesons for studying CP violation. Data was also obtained at the $\Upsilon(1S)$, $\Upsilon(2S)$, $\Upsilon(3S)$, and $\Upsilon(5S)$ for hadron spectroscopy and the studying of B_S^0 meson properties. In addition, Belle has also obtained data at various $\Upsilon(nS)$ for studying charm physics with D mesons [20]. As seen in Fig. 3.1, the Belle detector is made out of the following subdetectors which surround a 1.5 T superconducting solenoid

- Extreme Forward Calorimeter
- Silicon Vertex Detector (SVD)
- Central Drift Chamber (CDC)
- Aerogel Cherenkov Counters (ACC)

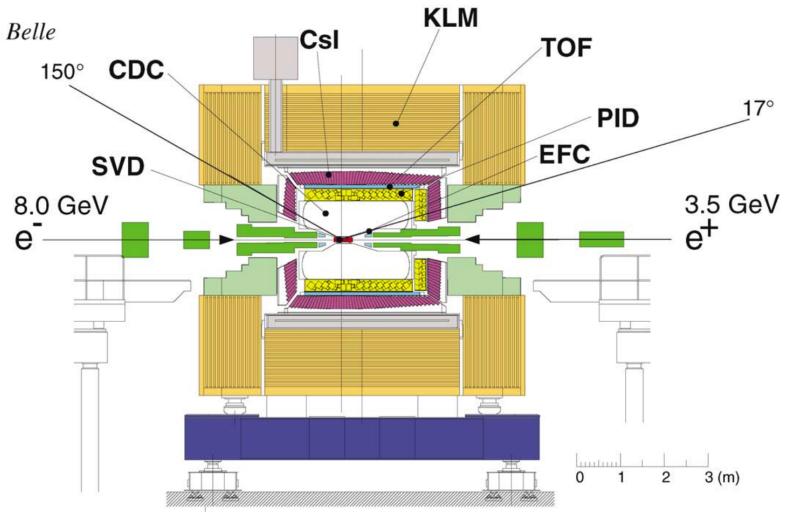

Figure 3.1: A side view of the Belle Detector and all its subcomponents [20]

- Time-Of-Flight Counter (TOF)
- Electromagnetic Calorimeter (ECL)
- K_L and Muon Detector (KLM)

3.0.1 Beam Pipe and Interaction Point

Though not a subdetector, the beam pipe around the interaction point (IP) is crucial to the design of the detector. The e^+ and e^- beams are collided with a crossing angle of ± 11 mrad as seen in Fig. 3.2. The beams are collided at an angle in order to eliminate the need for separation-bend magnets. This significantly reduces beam-related backgrounds in the detector. The e^+ beam was configured horizontally with the axis of the detector solenoid so that the lower-energy energy beam would not suffer bending in the 1.5 T solenoid field as if it was off-axis. There is a 22mr angle between the e^- (high-energy) beam and the axis of the solenoid.

The beam pipe thickness is designed to be thin in order to reduce coulomb scattering in the beam-pipe wall and the first layer of the silicon vertex detector, and to improve the z-vertex position resolution. The vertex detector also needed to be

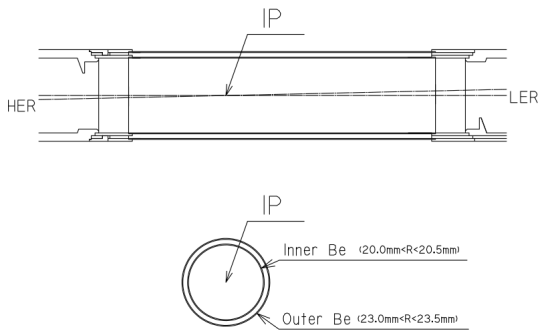

Figure 3.2: The cross-section of the beam pipe at the interaction point. The crossing angle between beams is ±11 mrad.

placed as close to the IP as possible since the vertex resolution improves inversely with the distance to the first detector layer. The beam pipe at the IP has an inner and outer wall, which allows the beam the pipe to be cooled and shields the silicon vertex detector from the heat produced from the beam at about a few hundred watts. The 2.5 mm gap between the walls of the cylinder is filled with helium gas for cooling. From $-4.6\text{cm} \leq z \leq 10.1\text{cm}$ the inner and outer beam pipe cylinder is constructed out of beryllium, with the inner wall having a diameter of 30mm before 2003 and 40mm after [21]. In this central region, both pipes have a 0.5mm thickness. In order to reduce X-ray background, the outer cylinder is covered with a 20μm gold sheet.

3.0.2 **Extreme Forward Calorimeter**

The extreme forward calorimeter (EFC) lies close to the IP in the ranges from 6.4° to 11.5° in the forward direction and 163.3° to 171.2° in the backward direction. The EFC is composed of radiation-hard bismuth germanate (BGO) crystals as shown in Fig. 3.3. This subdetector is used to improve the experimental sensitivity for some physics processes (such as $B \to \tau\nu$). It also serves to reduce backgrounds for the central drift chamber, and used as a monitor for the beam for KEKB control and a luminosity monitor for the detector (by measuring the rate of Bhabha events) [20].

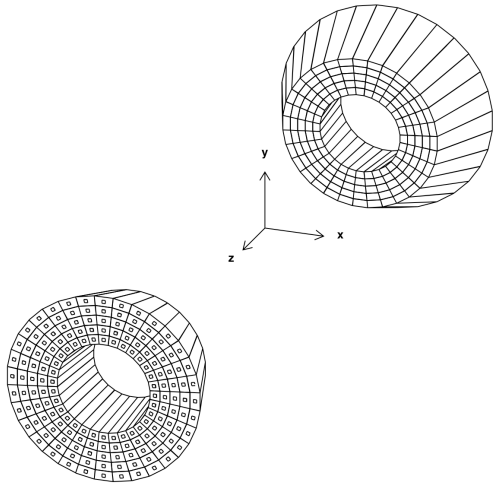

Figure 3.3: Configuration of the BGO crystals of the extreme forward calorimeter [20].

3.0.3 **Silicon Vertex Detector**

The Silicon Vertex Detector (SVD) was the most precise of the two subdetectors tracking charged particles. The SVD is composed of double-sided silicon strip detectors (DSSD) that measure the tracks of charged particles that come out of the beam-pipe. This information is used to reconstruct both primary and secondary vertices for particles with low momentum (which do not travel further into the detector because of the strong magnetic field). The silicon strip detectors are an arrangement of metallic strip-shaped implants on a low doped fully depleted SI wafer implants. Once the strips are connected to a charge sensitive amplifier the system acts as many charge collecting electrodes. The SVD has strips in alternating directions to track the charged particles.

The SVD is an important tool for studying time-dependent CP asymmetries, because of its ability to measure the separation decay between the B and $\bar{B}$. Separation between B and $\bar{B}$ at the KEKB is on the order of 200 μm. The detector has resolution of about 100μm in the z-direction.

The first version of the SVD used in Belle, SVD I, is comprised of three "ladders"

or layers as seen in two orientations in Fig. 3.4.

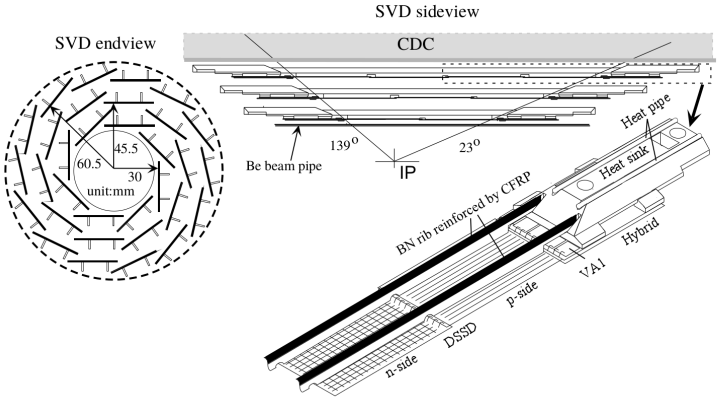

Figure 3.4: Shows the three ladders or layers of the SVD along the endview and side. A close-up of one of the ends of the SVDI with the double-sided silicon strip detectors (DSSD) is also shown.

A new SVD (SVD II) was installed in 2003 and provided improvements. The solid angle coverage increased as well as another DSSD layer was added.

3.0.4 **Central Drift Chamber**

The central drift chamber (CDC) is the second subdetector that tracks charged particles. The CDC is a wire drift chamber consisting of a gas, conducting wires, and electronics attached to the ends of the electronics. A picture of the wires within the CDC is shown in Fig. 3.5. It is able to measure the momentum and energy loss, dE/dx, of charged particles from the radius of curvature and $\beta = v/c$, respectively. This subdetector is less precise than the SVD, but covers a larger area for less cost than the silicon vertex detectors.

The CDC is asymmetric in the z direction allowing an angular coverage of $17° \leq \theta \leq 150°$ as seen in Fig. 3.6.

Figure 3.5: Shows the wires of CDC [22].

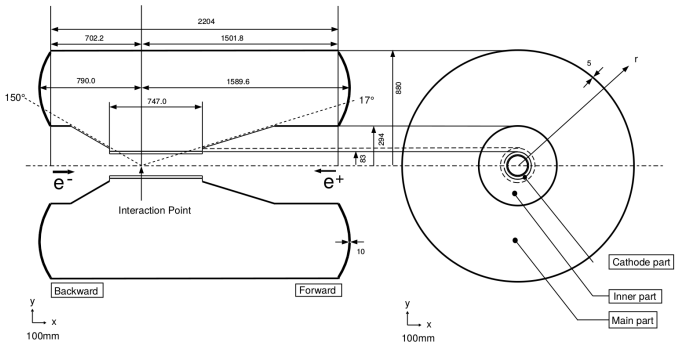

Figure 3.6: The layout of the CDC [20].

3.0.5 **Aerogel Cherenkov Counters**

The aerogel Cherenkov counters (ACC) are one of two PID subdetectors in Belle. In Belle PID we are mainly concerned in discerning between $\pi^{\pm}$ and $K^{\pm}$. The separation is important for the study of CP violation in B meson decays. The ACC covers the barrel region and one of the endcap regions in the forward direction (that is the side that the lower-energy positron beam enters from) as seen in Fig. 3.7

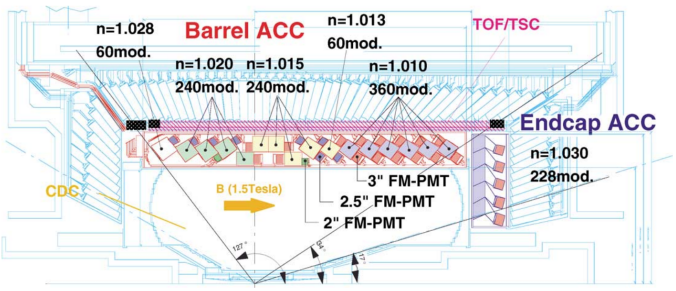

Figure 3.7: Shows the layout of the ACC.

This subdetector is made up of 1188 modules and 1788 fine-mesh PMTs to readout the produced Cherenkov photons. Charged kaons and pions can be distinguished by using the amount of photons and the Cherenkov angle produced in the medium. A diagram of an ACC module is shown in Fig. 3.8.

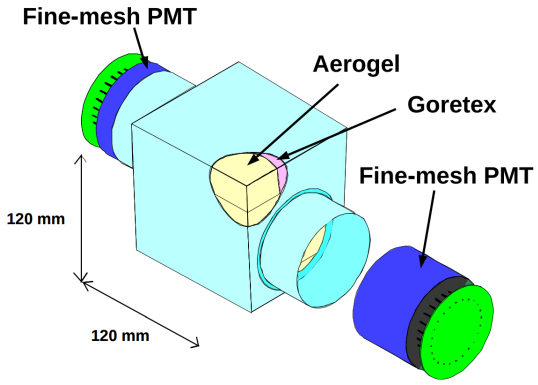

Figure 3.8: Shows a figure of the typical ACC module.

The silica aerogels are a nanostructured material with high surface area, low density, and high porosity. Once charged particles go through this substance, Cherenkov

photons are produced which are then detected by the fine-mesh PMTs.

3.0.6 **Time-Of-Flight Counter**

The time-of-flight (TOF) counter is the second PID detector in the barrel region. Using plastic scintillation counters, it achieves a resolution of $\sim$ 100ps for particles below 1.2 GeV/c, which is applicable to about 90% of the particles produced in $\Upsilon(4S)$ decays. This allows for efficient b-flavor tagging. The K/π separation is utilized to tag the charm particle from the B meson, and in turn the B meson flavor itself at decay time.

The TOF detector is also able to provide quick timing signals for the trigger system. The trigger system is then able to generate gate signals for ADCs and stop signals for TDCs.

3.0.7 **Electromagnetic Calorimeter**

The electromagnetic calorimeter (ECL) detects photons efficiently and measures their energy and position with good resolution. It is comprised of 8736 pieces of CsI(Tl) crystals that are spread on both endcaps and on the barrel. A figure of the electromagnetic calorimeter can be seen in Fig. 3.9.

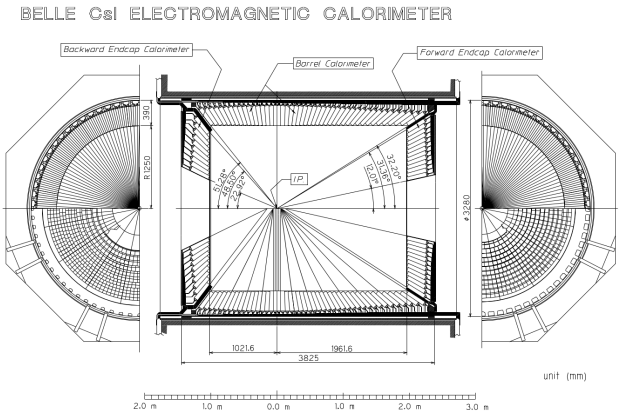

Figure 3.9: Shows the overall configuration of the ECL.

3.0.8 K_L and Muon Detector (KLM)

The KLM is designed to identify K_L's and muons over a broad range of momentum. This subdetector consists of 14 iron layers sandwiched between 15 layers of resistive plate counters covering the barrel and the endcaps of the Belle detector. The barrel section covers a range of 45 to 125° in the polar angle. The endcaps extend this range to 20° to 155°. Some panels are shown in 3.10.

Figure 3.10: Shows the combined iron and tracking components for the endcap portion of the KLM.

Chapter 4

Particle Identification

The most common charged and stable particles within Belle's energy constraints are e, μ, π, K and p. For physics analyses, we are mainly concerned in discerning between $\pi^{\pm}$ and $K^{\pm}$. The $\mu^{\pm}$, $p/\bar{p}$, and $e^{\pm}$ are less common, and at least the leptons are easier to identify using their behavior in calorimeters.

In high energy experiments, particle tracks are assigned a probability of being a certain particle. This particle identification (PID) rate and the mis-identification, or mis-ID, rate can be used to characterize the performance of a detector as a function of momentum, $\cos(\theta)$, and ϕ. The θ angle is measured with respect to the electron beam direction, or z-axis, as seen in the Belle upgraded detector, Belle II, in Fig. 4.1.

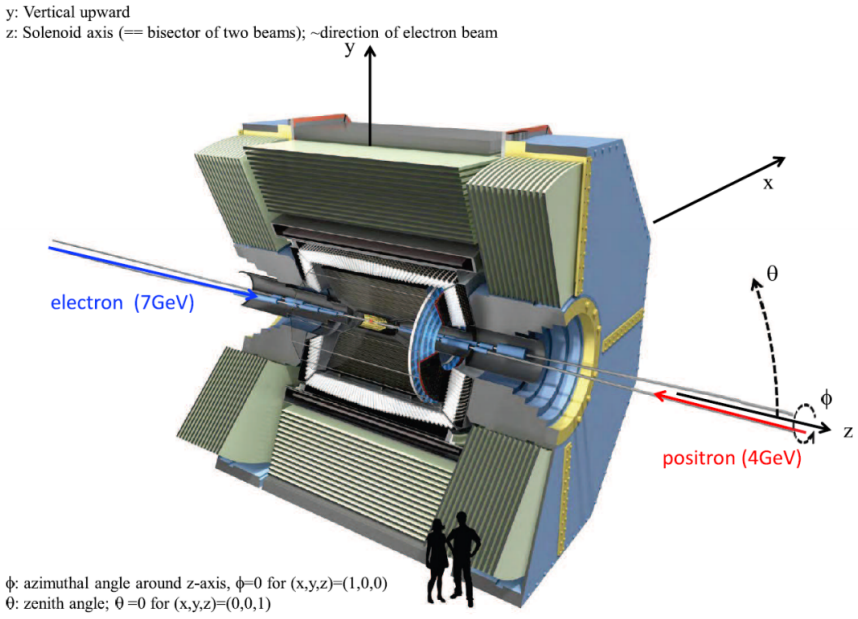

Figure 4.1: Coordinates of the Belle detector as shown on the Belle II detector [23]

4.0.1 Preliminary Belle PID Study

As a side project, using Belle MC simulated data for the non-resonant mode $B^{\pm} \to \phi K_S^0 \pi^{\pm}$, where the $\phi \to K^+K^-$ and the $K_S^0 \to \pi^{\pm}\pi^{\mp}$, we created a series of kaon/pion efficiency plots for different particle identification (PID) rates.

The momentum, $\cos(\theta)$, and ϕ spectra for the K^+, K^-, and π can be seen in Figs. 4.2 through 4.4.

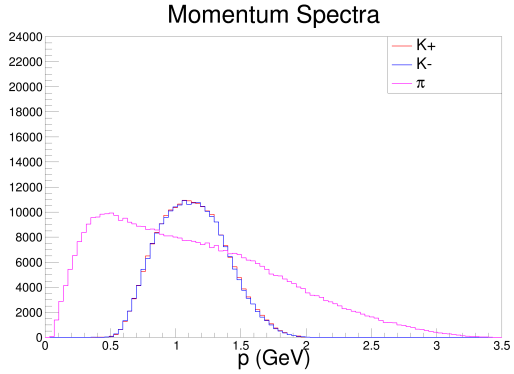

Figure 4.2: The spectrum of the momenta for K^+, K^-, and the π.

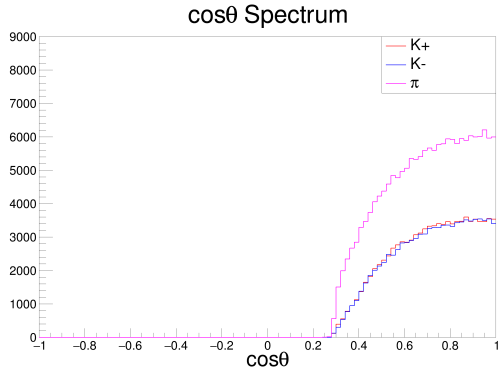

Figure 4.3: The $\cos(\theta)$ spectrum for the K^+, K^-, and the π.

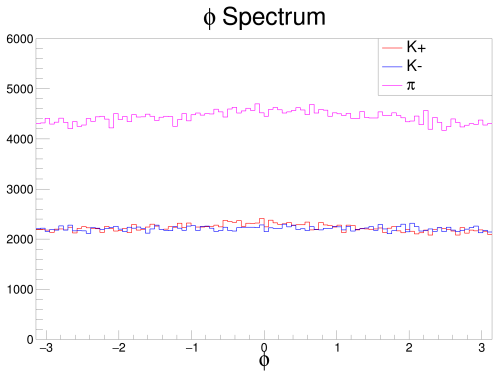

Figure 4.4: The ϕ spectrum for the K^+, K^-, and the π.

Figs. 4.5 through 4.9 show the kaon efficiency and the π mis-ID rate versus momentum for a range of cuts on the kaon id. Each figure shows the efficiency for the K^+, K^-, and the π being misidentified as a kaon rate. This mis-ID was obtained by

taking one minus the kaon ID rate. It is an upper limit for the π, since other less common particles, $\mu^{\pm}$, $p/\bar{p}$, and $e^{\pm}$, were ignored in this calculation.

Note that the Belle particle ID works by using either the time taken for particles to travel to the high time precision TOP detector using the time-of-flight (TOF) technique, or by using Cherenkov light emitted by tracks as they go through the Aerogel Cherenkov counters. The TOF detector works best as a PID detector at low momenta since these particles will have radically different velocities. Since these have low momenta, they can be described by: $p = mv$. Therefore by knowing the momentum, p, and the velocity, v, we can immediately infer the mass and particle type. At higher momenta, the velocity saturates to c and the formula for momentum becomes $p \approx mc\gamma$. Since we do not know γ, it is no longer easy to infer m from p.

Thus at higher momenta, we need PID information from a different detector. Cherenkov detectors work well at higher momenta because the particles are well above threshold to produce Cherenkov light. Until extremely high momenta are reached, kaons and pions of the same momentum produce different amounts of Cherenkov light at different Cherenkov angles θ_C. For the higher momenta of pions and kaons in our decay mode the Cherenkov detector is therefore more useful.

Figs. 4.10 through 4.14 show the K/π efficiency versus cos θ for various kaon ID cuts and Figs. 4.15 through 4.19 show the K/π efficiency versus the ϕ angle.

The K/π efficiency plots were created by looking at the ratio of number of events from a m_{bc} plot with a cut on the kaon ID to the same quantity from a m_{bc} plot without a cut on ID.

As seen in the plots, kaon efficiency falls off with increasing momentum. The mis-ID rate for π's to be found as K's is seen to be typically less than 5%. As expected, in the K/π efficiency versus cos θ plots, all points lie in the forward direction. The efficiency plots for the ϕ angle are roughly flat, which reflects the symmetry of the detector.

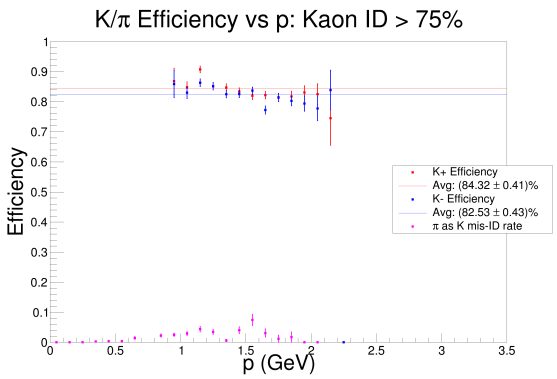

Figure 4.5: The K/π efficiency versus momentum for ID rates greater than 0.75.

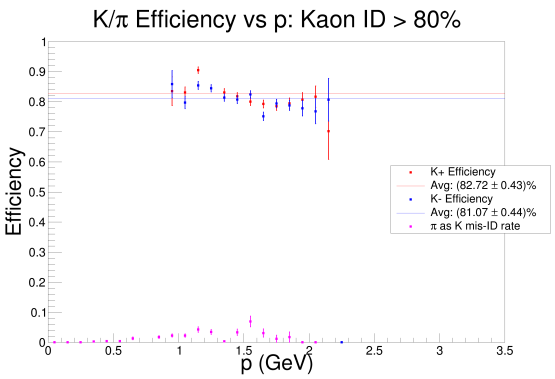

Figure 4.6: The K/π efficiency versus momentum for ID rates greater than 0.8.

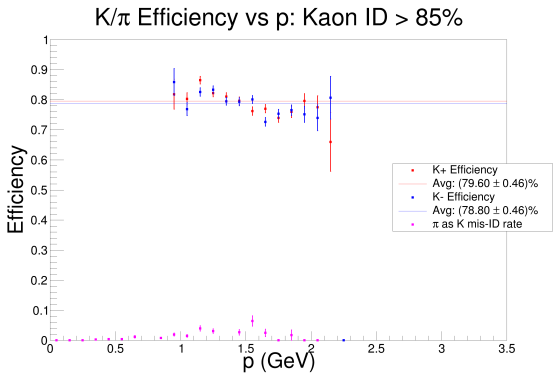

Figure 4.7: The K/π efficiency versus momentum for ID rates greater than 0.85.

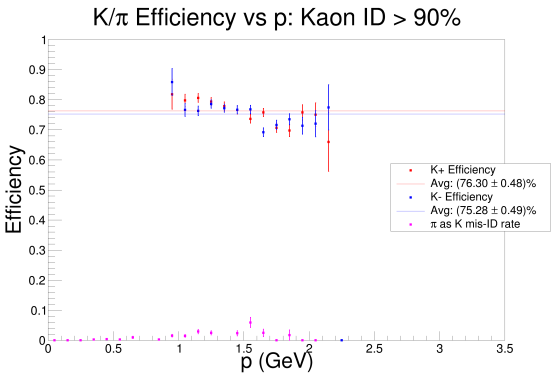

Figure 4.8: The K/π efficiency versus momentum for ID rates greater than 0.9.

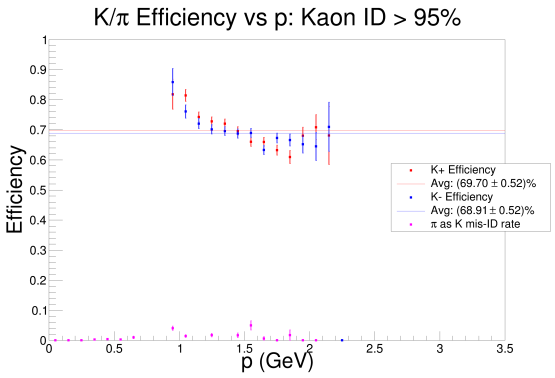

Figure 4.9: The K/π efficiency versus momentum for ID rates greater than 0.95.

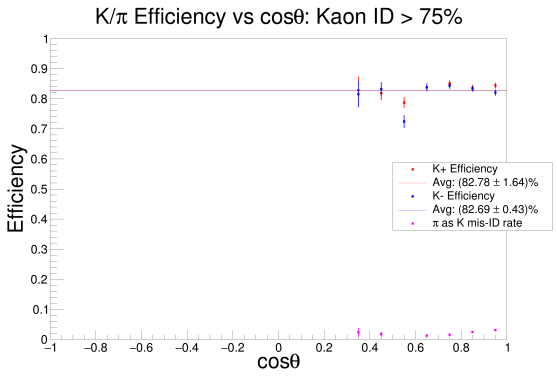

Figure 4.10: The K/π efficiency versus cos(θ) for ID rates greater than 0.75.

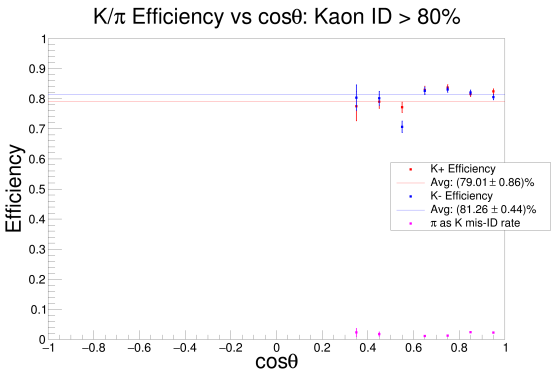

Figure 4.11: The K/π efficiency versus cos(θ) for ID rates greater than 0.8.

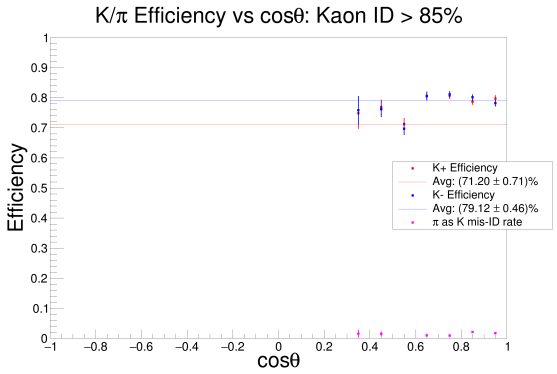

Figure 4.12: The K/π efficiency versus cos(θ) for ID rates greater than 0.85.

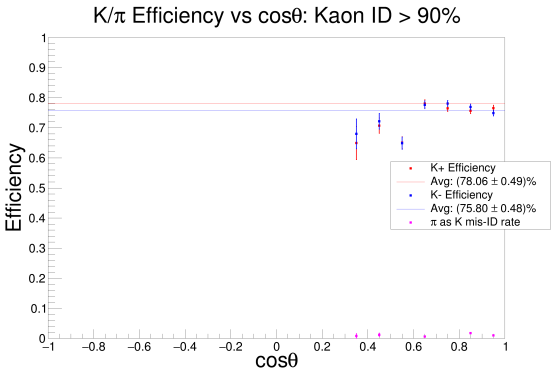

Figure 4.13: The K/π efficiency versus cos(θ) for ID rates greater than 0.90.

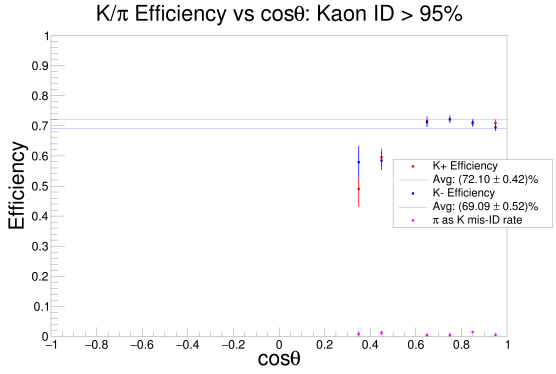

Figure 4.14: The K/π efficiency versus cos(θ) for ID rates greater than 0.95.

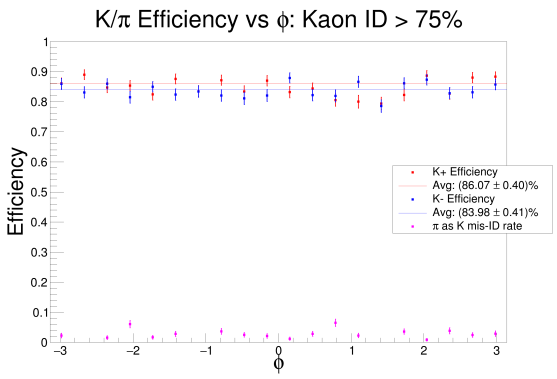

Figure 4.15: The K/π efficiency versus ϕ for ID rates greater than 0.75.

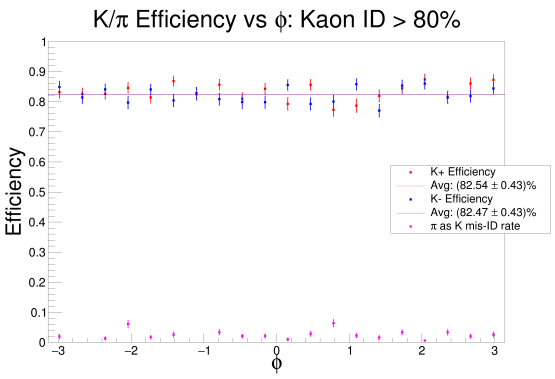

Figure 4.16: The K/π efficiency versus ϕ for ID rates greater than 0.8.

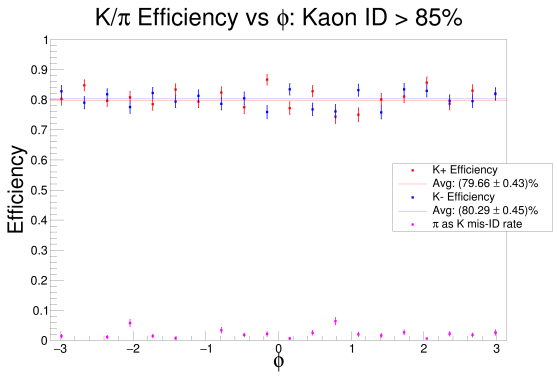

Figure 4.17: The K/π efficiency versus ϕ for ID rates greater than 0.85.

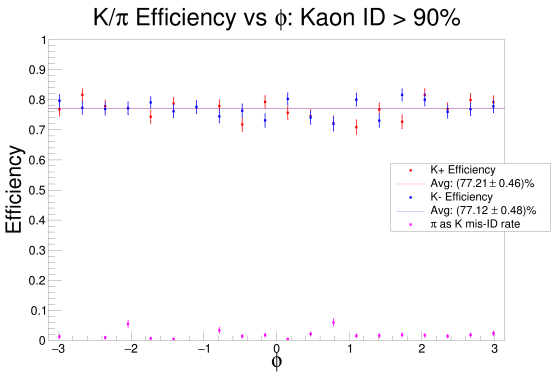

Figure 4.18: The K/π efficiency versus ϕ for ID rates greater than 0.9.

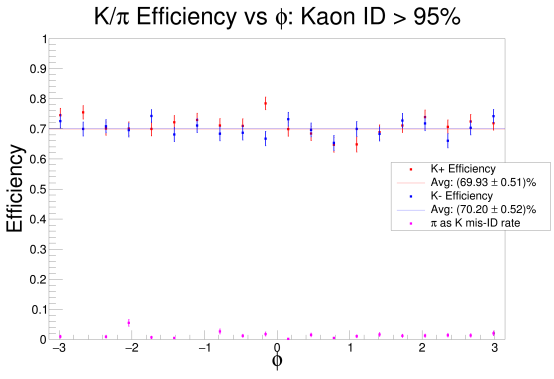

Figure 4.19: The K/π efficiency versus ϕ for ID rates greater than 0.95.

Chapter 5

Data Overview

In this chapter we provide an overview of how data was processed and used. Some Belle jargon will be used for the benefit of Belle readers.

5.0.1 **Event Reconstruction**

In order to produce B mesons, two finely calibrated beams, a 3.5 GeV e^+ beam and a 8 GeV e^- beam are collided inside the barrel of the Belle detector. Belle only detects the charged particles $e^{\pm}$, $\mu^{\pm}$, $\pi^{\pm}$, $K^{\pm}$, and $p\bar{p}$ and neutral particles: γ, K_L and $n\bar{n}$. Everything else is too short-lived to be detected. If the result is a $b\bar{b}$ pair, it will have an energy of 10.58 GeV then the $b\bar{b}$ quarks create the resonance meson $\Upsilon(4S)$. Because of the asymmetric nature of the collider, the $\Upsilon(4S)$ is moving in the lab frame and decays into either a B^+B^- or $B^0\bar{B}^0$. Note that each B has an energy of 5.29 GeV and the B^+ is composed of $\bar{b}u$ quarks and the B^0 meson is composed of $\bar{b}d$ quarks. The motion of the $\Upsilon(4S)$ results in Lorentz-boosted decay products. This boosting allows us to make time-dependent measurements, which are relevant neutral mode B decays. Belle accumulated 100 inverse fb, and collected$\sim 10^7$ B meson pair events along with a large number of background events at the $\Upsilon(4S)$ [20]. The final state particles were identified using the TOF system and the aerogel Cherenkov systems described in the detector chapter.

We are able to reconstruct unstable particles from their stable decay products and reproduce an e^+e^- decay in a process called event reconstruction. This is achieved through use of reconstruction algorithms and code. An example of this is where

$\phi \to K^+K^-$ where $K^+ \to \pi^+\pi^-$ and $K^- \to \pi^+\pi^-$. This decay chain is reconstructed from the four charged pions. The C++ reconstruction code acts like a module in the Belle framework, takes the detector collected data as its input, where there are all types of events, and reconstructs only the events selected.

5.0.2 Signal and Background

The reconstruction process does not always get the decay right. Though the reconstruction may be designed for one type of decay chain, there could be a number of other processes that pass through our reconstruction code. The correctly reconstructed events are called "signal" and the mis-reconstructed events are known as "background".

A combinatoric background in reconstructing events is normal and refers to when we mix tracks in the same event. For example we could combine a good ϕ and a good K_S^0 with track one as the π^+ or with track two as a π^+. This could give us two different B^+ candidates.

5.0.3 Skimming

Our signal MC is generated and then simulated through our detector. Event reconstruction was done by EVTGEN [24]. MC simulation of the detector was conducted by GEANT3 [25]. We run the reconstruction code on the MC simulated data and the Belle collected data to select the events under investigation. We do this because there is a variety of events in the data and it is large in size. Belle performs the first round of skimming to reduce time spent and the size of the data. To skim, we set some basic selection criteria and then reject many of the background events without much damage to the signal strength.

Skimming Criteria

For data and generic MC, the final states were not explicitly reconstructed as the K^{*+} resonances. The resonances were studied when fitting, and appear as peaks in the $K\pi$ invariant mass plot.

Our skim selected two charged kaons, and a charged π and a K_s^0 for the reconstruction of ϕ and a charged K^*, respectively. Belle detects K_s^0 after it decays into two oppositely charged pions. The charged kaons and pions were required to have a PID value greater than 0.6 where the pion identification likihood (pion ID) is given by

$$\text{pion ID} = \frac{\mathcal{L}_\pi}{\mathcal{L}_K + \mathcal{L}_\pi} \tag{5.1}$$

$\mathcal{L}_\pi$ and $\mathcal{L}_K$ are the likelihoods of charged tracks being due to a pion and kaon respectively. The pion ID is the probability for a given charged particle to be a pion, as a opposed to a kaon.

The ϕ was composed of two oppositely charged kaons and was restricted to 0.950 GeV $< m_\phi <$ 1.69 GeV. The loose initial selection criteria for the charged π were $|m_{\pi^\pm} - m_{\pi^\pm}^{PDG}| < 0.6$ GeV. Selection for the K_s^0 candidates were made using the Belle Mdst vee2 table and requiring an invariant mass $|m_{K_s^0} - m_{K_s^0}^{PDG}| < 0.035$ GeV.
The charged pion, K_s^0 and ϕ were combined to give a charged B. The energy of the candidate B minus the energy of the beam in the CM frame, was required to be $|\Delta E| = E_B^* - E_{beam}^* < 0.3$ GeV. [This is better because the beam energy is very precisely known from the accelerator design.] The beam constrained mass, or $m_{bc} = \sqrt{(E_{beam}^*)^2 - p_B^{*2}}$ (where p_B^* is the momentum of the B-meson candidate in the CM frame) was selected to have $m_{bc} > 5.2$ GeV. These selection requirements conclude the skimming part of the analysis.

The number of data events coming in, "Skim In," and out, "Skim Out," in the event number tables in the appendix.

5.0.4 MC Simulated Data

The quality of data depends on the detector's ability to identify assorted processes with very little misidentification. We use MC simulated data containing information on both with and without the detector effects. Generic MC samples are produced in generation and simulation. Generation uses physics predictions to randomly generate events. Simulation of the detectors was conducted by GEANT3 [25]. After going through the above steps, final generic MC samples are then added to a larger sample according to their world accepted branching fraction. Generic MC simulated data is used to determine various background processes and for optimization of selection criteria. We also use signal MC data which contains only a specific decay mode. We use the signal MC data to determine the efficiency for the simulation and reconstruction.

5.0.5 MC Truth Matching

With Belle MC data we have the ability to trace back the physics process back before detector effect. The data before the detector effects is called the generator level information. We often use this generator information to classify events into signal and background in a process called MC truth matching.

In this analysis call the generator-level data "Truth" data. This represents our signal data before detector effects. The "Reco" data describe MC signal after detector simulation.

Combining tracks in an event in different ways can lead to more than one candidate B-meson even within a single event. The candidate is not always the "true" best candidate.

5.0.6 Reconstruction

The reconstruction part of this process focuses on reconstructing the B vertex and radiative final state energy. Cuts made on the reconstructed data includes $|\Delta E| < 0.2$

GeV and the charged kaons and pions must have a particle-ID probability greater than 0.6 where the kaon identification likelihood, KID, is defined as

$$\text{KID} = \frac{\mathcal{L}_K}{\mathcal{L}_K + \mathcal{L}_\pi} \tag{5.2}$$

The KID is the probability for a given charged particle to be a kaon, as a opposed to a pion.

The number of events going into the reconstruction, "Reco In," can be found in event processing tables in the appendix. To find the number of events that were lost between the skimming and reconstruction processes, the reconstruction tables include a final check column. This takes the difference between the skim output and the reco input. Out of the 24515324 events that should be there, 7404 events were lost due to processing complications. These complications arose when small parts of the data failed to run through our reconstruction. This was not an error with the reconstruction code, but rather with the data itself. This is approximately 0.03% of the total events coming out of the skim.

5.0.7 **Data**

This analysis uses skimmed data. We used:

- The complete case b, on-resonance data, HadronB(j) skimmed data
- Five complete streams of generic, case b, on-resonance MC, where a complete stream is given by 11 experiments worth of MC from SVD1 and 15 experiments from SVD2
- A generated signal MC for $B^\pm \to \phi K^{*\pm}(892)$, $B^\pm \to \phi K_0^{*\pm}(1430)$, and $B^\pm \to \phi K_2^{*\pm}(1430)$
- Rare data sets, which corresponds to 50 times the amount of rare decays in real data

Scripts extracted the number of incoming and outgoing events in our two-stage skim and reconstruction. These numbers were then compared with Belle's event documentation. Tables with event numbers can be found in the "Appendix" subsection.

Chapter 6

Physics Model

6.0.1 Basic Theory

As a precursor to more rigorous theory in the decay, first we start with a quick review of some particle physics basics.

The decay rate, Γ, is the probability per unit time that any given particle will decay. This can be expressed as

$$\Gamma = \frac{1}{\tau} \tag{6.1}$$

where τ is the mean lifetime of a particle. The total decay rate, which is the sum of the rates of decay for individual particle decay modes, is

$$\Gamma_{tot} = \sum_{i=1}^{q} \Gamma_i \tag{6.2}$$

where Γ_i is the individual decay mode and q is the number of modes the parent particle decays into.

The branching fraction is the ratio of particles that decay via a specific decay with respect to the total number of particles that decay by all modes.

$$\mathcal{B} = \frac{\Gamma_i}{\Gamma_{tot}} \tag{6.3}$$

To calculate the transition rate we use Enrico Fermi's Golden rule. This states that a decay rate is given by the product of the square of the absolute matrix element and the phase space factor.

Suppose we have the decay

$$1 \rightarrow 2 + 3 + 4 + \cdots + n \tag{6.4}$$

where particle 1 is at rest and decays into $n-1$ other particles then the decay rate according to the Golden rule is

$$\Gamma = \frac{S}{2\hbar m_1}\int |\mathcal{M}|^2(2\pi)^4\delta^4(P_1-P_2-P_3\cdots-P_n)\times\prod_{j=2}^{n}2\pi\delta(P_j^2-m_j^2c^2)\theta(P_j^0)\frac{d^4P_j}{(2\pi)^4} \quad (6.5)$$

where S is a statistical factor that accounts for multiple identical particles in the final state (for s multiple identical particles in the final state S gets a factor of $1/s!$), $\mathcal{M}$ is the matrix element, m_j is the mass of the of the jth particle and P_j denotes the four-momentum. The matrix element contains information about the dynamics of a decay and is a function of the four-momentum. In Eqn.(6.5) everything after the $\times$ is considered the phase space factor. This describes how much momentum space a final state has to decay.

6.0.2 **Angular Distribution**

For the $B^{\pm} \to \phi K^{*\pm}$ system where $\phi \to K^+K^-$ and $K^{*\pm} \to K_S^0\pi^{\pm}$ the angular distribution is described by the helicity angles θ_1, θ_2, and Φ in the rest frames of the parent K^{*+}, Φ, and B, respectively, as shown in Fig. 6.1. Note that this figure incorporates 3 different rest frames!

Here θ_1 is the angle between the K_S^0 projection and the $K^{*\pm}$ decay line and θ_2 is the difference in the $K^{\pm}$ and ϕ projections. [Since we use the cosines of the θ angles, sign ambiguities do not matter.] Φ is the angle between the two decay frames. The variable θ_1 is also called $\theta_{K_S^0\pi}$ and the variable θ_2 is also called θ_{Φ}.

To obtain a branching fraction we take the partial decay width for a particular decay and divide it by the total decay width of the parent particle. For a pseudoscalar B meson to decay into two particles with spins J_1 and J_2 the partial decay width is given by

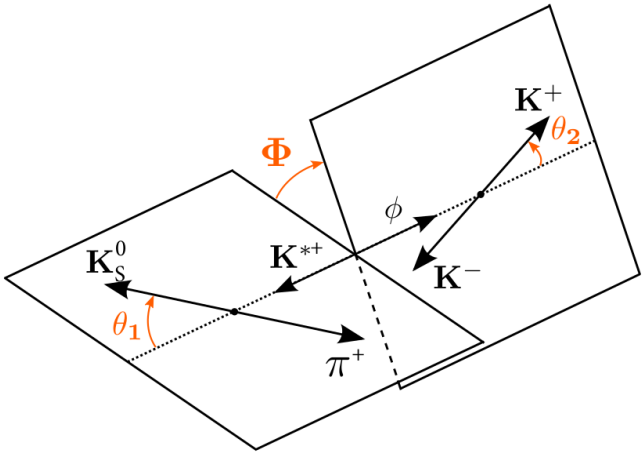

Figure 6.1: Illustration of the three helicity angles given in the rest frame of the parent particles for the $B^+ \to \phi K^{*+}$ decay. Angles are defined similarly for the charge-conjugate decay mode.

$$\frac{d^3\Gamma}{d\cos\theta_1 d\cos\theta_2 d\Phi} \propto \left| \sum_\lambda A_\lambda Y^\lambda_{J_1}(\theta_1, \Phi)\, Y^{-\lambda}_{J_2}(-\theta_2, 0) \right|^2 \tag{6.6}$$

This equation sums over the helicity states λ, each with a A_λ as a complex helicity amplitude, and with the spherical harmonic, Y^m_l, represented as $Y^\lambda_{J_1}$ or $Y^{-\lambda}_{J_2}$. The helicity could be any discrete value between $-j$ and $+j$, with j being the smaller of the daughter spins J_1 and J_2 (to conserve angular momentum).

For example, in the $B^\pm \to \phi K^*_2(1430)^\pm$ mode the tensor $K^*_2(1430)^\pm$ has a spin of 2. The vector particle ϕ has a spin of 1, limiting this decay to three helicity states: $+1$, 0, and -1. If J_2 represents the spin of the ϕ then the J_1 would represent either the spin of the $K^0_S\pi^\pm$ ($J_1 = 0$), $K^*_0(1430)^\pm$ ($J_1 = 0$), $K^*(892)^\pm$ ($J_1 = 1$), or the $K^*_2(1430)^\pm$ ($J_1 = 2$). Taking this into account, along with the concept that different helicities could provide different complex amplitudes we get

$$\frac{d^3\Gamma}{d\cos\theta_1 d\cos\theta_2 d\Phi} \propto \left| \sum_\lambda A_{J\lambda} Y^\lambda_J(\theta_1, \Phi)\, Y^{-\lambda}_1(\theta_2, 0) \right|^2, \tag{6.7}$$

where spin $J \equiv J_1$ and $A_{J\lambda}$ is the corresponding complex helicity amplitude of the partial wave with spin J. The sign of the θ_2 is absorbed into the amplitude.

6.0.3 **Mass distribution**

For this analysis we study the mass distributions for the P- and D-wave components (those waves with angular orbital momentum quantum numbers $\ell = 1$ and 2 respectively) separately from the S-wave ($\ell = 0$). Specifically, we study the shape of the $K^0_S\pi^\pm$ invariant-mass spectrum $M_{K^0_S\pi}$ because it is one of four variables that will help us understand the parameters of the decay.

To parameterize the lineshape of the P- and D-wave components as a function of the invariant mass m, we use a relativistic spin-dependent Breit-Wigner (BW) amplitude R_J [26]

$$R_J(m) = \frac{m_J\Gamma_J(m)}{(m_J^2 - m^2) - im_J\Gamma_J(m)} = \sin\delta_J e^{i\delta_J}, \tag{6.8}$$

where we use scattering theory notation convention

$$\cot\delta_J = \frac{m_J^2 - m^2}{m_J\Gamma_J(m)}. \tag{6.9}$$

The phase shift δ_J describes how much the J^{th} partial width is being shifted as mass increases. By convention, we call the phase shift zero at threshold and increase it from there.

The mass-dependent widths for spins $J = 1$ and $J = 2$ are

$$\Gamma_1(m) = \Gamma_1\frac{m_1}{m}\frac{1 + r^2q_1^2}{1 + r^2q^2}\left(\frac{q}{q_1}\right)^3, \tag{6.10}$$

$$\Gamma_2(m) = \Gamma_2\frac{m_2}{m}\frac{9 + 3r^2q_2^2 + r^4q_2^4}{9 + 3r^2q^2 + r^4q^4}\left(\frac{q}{q_2}\right)^5, \tag{6.11}$$

where Γ_J is the resonance width of the P- or D-wave components, m_J the resonance mass, and q the magnitude of the momentum of a daughter particle in the rest frame of the resonance (note: $|q_{K^0_S}| = |q_\pi|$ in the rest frame of the resonance). The variable q_J is this same momentum at $m = m_J$, and r the interaction radius, which is the range of the potential of the resonance.

The above equations for the mass-dependent width use the Blatt–Weisskopf penetration factors. The BW penetration factors are just the parts of Eqs. 6.10 and 6.11, which depend on r. They grow more complicated with increasing J value. And all they do is describe the greater difficulty of penetrating the centrifugal barrier for higher J. It's not known if they are exact, but it's "carried over" from nuclear physics under the assumption that mesons obey Blatt and Weisskopf's theory for nuclei from the 50's So it is to be viewed as an approximation

To evaluate the invariant-mass spectrum of the S-wave components, we will use results for $K\pi$ scattering obtained from the LASS experiment [27]. The lineshape of spinless components can be described by

$$R_0(m) = \sin\delta_0 e^{i\delta_0}, \tag{6.12}$$

where

$$\delta_0 = \Delta R + \Delta B, \tag{6.13}$$

ΔR is a contribution from the resonant $K_0^{*+}(1430)$ and ΔB represents the contribution from the non-resonant $K_S^0\pi^+$ mode. ΔR is parameterized by the function

$$\cot\Delta R = \frac{m_0^2 - m^2}{m_0\Gamma_0(m)}, \tag{6.14}$$

where m_0 and Γ_0 are the resonance mass and width respectively, and $\Gamma_0(m)$ is defined by

$$\Gamma_0(m) = \Gamma_0\frac{m_0}{m}\left(\frac{q}{q_0}\right). \tag{6.15}$$

The contribution from the $K_S^0\pi^+$ mode is parameterized by

$$\cot\Delta B = \frac{1}{aq} + \frac{bq}{2}, \tag{6.16}$$

where b is effective range and a is the scattering length.

To compute the amplitude $M_J(m)$ we multiply the lineshape, R_J, with the two body phase factor

$$M_J(m) = \frac{m}{q} R_J(m). \tag{6.17}$$

Parameters used in this analysis can be found in Table 6.1.

Table 6.1 Resonance Parameters for S-, P-, and D-Wave Components

Parameter	$(K\pi)_0^{*\pm}$ $J=0$	$K^*(892)^\pm$ $J=1$	$K_2^*(1430)^\pm$ $J=2$
m_J (MeV)	$1435 \pm 5 \pm 5$	895.94 ± 0.22	1432.4 ± 1.3
Γ_J (MeV)	$279 \pm 6 \pm 21$	48.7 ± 0.8	109 ± 5
r (GeV^{-1})	$\cdots$	3.4 ± 0.7	2.7 ± 1.3
a (GeV^{-1})	$1.95 \pm 0.09 \pm 0.06$	$\cdots$	$\cdots$
b (GeV^{-1})	$1.76 \pm 0.36 \pm 0.67$	$\cdots$	$\cdots$

The S-wave parameters, as well as interaction radii were obtained from Ref. [28], which has updated values with respect to Ref. [27]. The for the P- and D-waves the parameters m_J and Γ_J are taken from Ref. [26].

6.0.4 **Mass-angular Distribution**

To calculate the partial decay width we combine the mass distribution with the angular distribution

$$\frac{d^4\Gamma}{d\cos\theta_1 d\cos\theta_2 d\Phi dM_{K\pi}} \propto |\mathcal{M}|^2 \times F_{M_{\phi K}}(M_{K\pi}), \tag{6.18}$$

where $F_{M_{\phi K}}(M_{K\pi})$ is a phase space factor that describes the three-body kinematics in $B^\pm \to \phi K_S^0 \pi^\pm$.

The phase factor is assumed to be a constant amplitude, since there are no resonances in the $\phi K_S^0 \pi^\pm$ invariant mass spectrum. This can be computed for each value of $M_{K_S^0\pi} = m$ given by the kinematics in Ref. [26]

$$F(m) = 2m\left[m^2_{\rm max}(m) - m^2_{\rm min}(m)\right], \tag{6.19}$$

where m^2_{max} and m^2_{min} are the maximum and minimum values squared of the Dalitz plot range of the $\phi K_S^0 \pi$ invariant mass $M_{\phi K}$ for a given $M_{K\pi}$ value. The $F(m)$ is

the same as the $F_{M_{\phi K}}$ above, but we keep this notation to be consistent with the convention already established by the neutral mode paper [13].

The matrix element squared for the S- P- and D-wave is given by

$$\begin{aligned} |\mathcal{M}|^2 = |&\mathcal{A}_0\left(M_{K\pi}, \cos\theta_1, \cos\theta_2, \Phi\right) \\ &+\mathcal{A}_1\left(M_{K\pi}, \cos\theta_1, \cos\theta_2, \Phi\right) \\ &+\mathcal{A}_2\left(M_{K\pi}, \cos\theta_1, \cos\theta_2, \Phi\right)|^2, \end{aligned} \tag{6.20}$$

where the function-amplitudes, $\mathcal{A}_0$, $\mathcal{A}_1$, and $\mathcal{A}_2$ are composed of a product of the angular distribution from Eq.(6.7) and the mass distribution from Eq.(6.17). This yields

$$\mathcal{A}_0\left(M_{K\pi}, \cos\theta_1, \cos\theta_2, \Phi\right) = A_{00} Y_0^0(\theta_1, \Phi) Y_1^0(-\theta_2, 0) \times M_0(M_{K\pi}), \tag{6.21}$$

$$\mathcal{A}_1\left(M_{K\pi}, \cos\theta_1, \cos\theta_2, \Phi\right) = \sum_{\lambda=0,\pm1} A_{1\lambda} Y_1^{\lambda}(\theta_1, \Phi) Y_1^{-\lambda}(-\theta_2, 0) \times M_1(M_{K\pi}), \tag{6.22}$$

and

$$\mathcal{A}_2\left(M_{K\pi}, \cos\theta_1, \cos\theta_2, \Phi\right) = \sum_{\lambda=0,\pm1} A_{2\lambda} Y_2^{\lambda}(\theta_1, \Phi) Y_1^{-\lambda}(-\theta_2, 0) \times M_2(M_{K\pi}), \tag{6.23}$$

The seven complex helicity amplitudes described in the equations above can be characterized by 14 real parameters (or 28 if we measure B^+ and B^- separately).

The partial decay width is defined by

$$\frac{d^4\Gamma^{\pm}}{d\cos\theta_1 d\cos\theta_2 d\Phi dM_{K\pi}} \propto F_{M_{\phi K}}\left(M_{K\pi}\right) \times |\mathcal{M}^{\pm}|^2, \tag{6.24}$$

where $\mathcal{M}^+$ is the matrix element for $B^+ \to \phi K_S^0 \pi^+$, $\mathcal{M}^-$ is the matrix element for $B^- \to \phi K_S^0 \pi^-$.

As keeping with the theory presented in other analyses, for parameters we use averages and asymmetries in amplitude fractions and the averages and differences of the phases instead of amplitudes. Our parameters are defined similarly with the Belle neutral mode paper [13].

The CP basis has different eigenstates than that of the helicity basis. Though the helicity basis is easier for the experimentalists to use, the theorists report their work in the CP basis. The CP eigenstates are

$$CP-\text{even longitudinal: } A_L = a_0 \tag{6.25}$$

$$CP-\text{even transverse: } A^{\perp}_{J\lambda} = \frac{A_{+1J} + A_{-1J}}{\sqrt{2}} \tag{6.26}$$

$$CP-\text{odd transverse: } A^{\parallel}_{J\lambda} = \frac{A_{+1J} - A_{-1J}}{\sqrt{2}} \tag{6.27}$$

where $A_{J\lambda} = a_{J\lambda}\exp(i\varphi_{J\lambda})$. Note that "0" and "$L$" are commonly interchangeably used for the longitudinal amplitude.

The fractions of each polarization are then

$$f_{LJ} = \frac{|A_{LJ}|^2}{|A_{LJ}|^2 + |A_{\parallel J}|^2 + |A_{\perp J}|^2} \tag{6.28}$$

$$f_{\perp J} = \frac{|A_{\perp J}|^2}{|A_{LJ}|^2 + |A_{\parallel J}|^2 + |A_{\perp J}|^2} \tag{6.29}$$

where they satisfy the relation

$$1 = f_{LJ} + f_{\perp J} + f_{\parallel J} \tag{6.30}$$

The branching fraction for each partial-wave J is

$$\mathcal{B}_J = \frac{1}{2}(\bar{\Gamma}_J + \Gamma_J)/\Gamma_{\text{total}} \tag{6.31}$$

where $\bar{\Gamma}_J$ refers to the Γ associated with the B^- candidate and Γ_J refers to the Γ associated with the B^+ candidate. This notation will be used for Eqns.(6.31) through (6.41) where if no CPV was considered, Eq.(6.41) would collapse to $\mathcal{B}_J = \Gamma_J/\Gamma_{\text{total}}$. The branching fraction can also be written as

$$\mathcal{B}_J = \frac{1}{2}(\mathcal{B}_{JB-} + \mathcal{B}_{JB+}) \tag{6.32}$$

The relative phase between the the parallel and perpendicular amplitudes,$\phi_{\parallel J}$ and $\phi_{\perp J}$, respectively are

$$\phi_{\parallel J} = \frac{1}{2}(\arg(\bar{A}_{J\parallel}/\bar{A}_{J0}) + \arg(A_{J\parallel}/A_{J0})) \tag{6.33}$$

and

$$\phi_{\perp J} = \frac{1}{2}(\arg(\bar{A}_{J\perp}/\bar{A}_{J0}) + \arg(A_{J\perp}/A_{J0}) - \pi) \tag{6.34}$$

The phase for the longitudinal component is

$$\delta_{0J} = \frac{1}{2}(\arg(\bar{A}_{00}/\bar{A}_{J0}) + \arg(A_{00}/A_{J0})) \tag{6.35}$$

where arg is the phase of its complex argument. These phases are defined as to increase with increasing mass to avoid a two-fold phase ambiguity [29]. The parameter to measure the amount of CP-violation in each partial wave is given by $\mathcal{A}_{CPJ}$ where

$$\mathcal{A}_{CPJ} = (\bar{\Gamma}_J - \Gamma_J)/(\bar{\Gamma}_J + \Gamma_J) \tag{6.36}$$

The transverse and perpendicular components of $\mathcal{A}_{CPJ}$ are

$$\mathcal{A}^0_{CPJ} = \frac{|\bar{A}_{J0}|^2/\sum|\bar{A}_{J\lambda}|^2 - |A_{J0}|^2/\sum|A_{J\lambda}|^2}{|\bar{A}_{J0}|^2/\sum|\bar{A}_{J\lambda}|^2 + |A_{J0}|^2/\sum|A_{J\lambda}|^2} \tag{6.37}$$

and

$$\mathcal{A}^\perp_{CPJ} = \frac{|\bar{A}_{J\perp}|^2/\sum|\bar{A}_{J\lambda}|^2 - |A_{J\perp}|^2/\sum|A_{J\lambda}|^2}{|\bar{A}_{J\perp}|^2/\sum|\bar{A}_{J\lambda}|^2 + |A_{J\perp}|^2/\sum|A_{J\lambda}|^2} \tag{6.38}$$

The difference in the phases is given by

$$\Delta\phi_{\parallel J} = \frac{1}{2}(\arg(\bar{A}_{J\parallel}/\bar{A}_{J0}) - \arg(A_{J\parallel}/A_{J0})) \tag{6.39}$$

and

$$\Delta\phi_{\perp J} = \frac{1}{2}(\arg(\bar{A}_{J\perp}/\bar{A}_{J0}) - \arg(A_{J\perp}/A_{J0}) - \pi) \tag{6.40}$$

where the extra π accounts for the sign flip of $\bar{A}_{J\perp} = A_{J\perp}$ (both of which are defined relative to the J=0 amplitude) and

$$\Delta\delta_{0J} = \frac{1}{2}(\arg(\bar{A}_{00}/\bar{A}_{J0}) - \arg(A_{00}/A_{J0})) \tag{6.41}$$

To fit using the above equations, some modifications had to be made. First, because the fitter could make the asymmetries $\mathcal{A}^0_{CPJ}$ close to ± 1 and the values of f_{LJ} close to unity, the values of f_{LJ} for the B^- and B^+ lie outside the physical region of [0, 1]. To solve this, we directly used parameters f^-_{LJ} and f^+_{LJ} for the B^- and B^+ respectively. We have the 26 parameters listed clearly immediately after Eqn. 6.42. These are for signal. Additionally we have four parameters that tell us the numbers of background events (B+ and B-, and heavy flavor, "hf" and light flavor "lf"). Thus, our data consist of 8 quantities per selected B candidate: four physics variables (mkspi, costh1, costh2, phi) and four signal / background discrimination variables (m_{bc}, Δ E, ANN1, ANN2). The data format was described earlier in the "Data Overview" chapter and the signal model has just been described. There are 26 signal parameters described below. No constraints are applied in our fits.

The last problem is when the fitter varied f_{LJ} and $f_{\perp J}$ so that they were both close to unity, this caused the value of $f_{\parallel J}$ to lie outside the physical region [0, 1]. Thus a new modified version of $f_{\perp J}$ was used called $f'_{\perp J}$ where

$$f_{\perp J} \equiv f'_{\perp J}(1 - f_{LJ}) \tag{6.42}$$

Thus, the final list of fit parameters used by the MINUIT fitter is as follows:

(0-2) $\mathcal{B}_0$, $\mathcal{B}_1$, and $\mathcal{B}_2$: the average branching fraction for each spin state.

(3-4) f_{L1}^{-}, and f_{L2}^{-}, the longitudinal fractions for B^- meson decays with J = 1, 2, respectively for the $K_S^0\pi^-$ system.

(5-6) $f_{\perp 1}^{-\prime}$, and $f_{\perp 2}^{-\prime}$, the "perp" fractions for B^- meson decays with $J = 1, 2$, respectively for the $K_S^0\pi^-$ system.

(7-8) $\phi_{\|J}$ for spins 1 and 2.

(9-10) $\phi_{\perp J}$ for spins 1 and 2.

(11-12) δ_{0J} for spins 1 and 2.

(13-15) $\mathcal{A}_{CPJ}$ for spins 0, 1, 2.

(16-17) f_{L1}^{+}, and f_{L2}^{+}, the longitudinal fractions for B^+ meson decays with J = 1, 2, respectively for the $K_S^0\pi^+$ system.

(18-19) $f_{\perp 1}^{+\prime}$, and $f_{\perp 2}^{+\prime}$, the "perp" fractions for B^+ meson decays with $J = 1, 2$, respectively for the $K_S^0\pi^+$ system.

(20-21) $\Delta\phi_{\|J}$ for spins 1, 2.

(22-23) $\Delta\phi_{\perp J}$ for spins 1, 2.

(24-25) $\Delta\delta_{0J}$ for spins 1, 2.

6.0.5 **Comparing the EVTGEN and Physics Models**

Because we did not know the parameters used by EVTGEN, we tried different Breit Wigner (BW) functions to model the "truth"-matched signal data and varied parameters (M_0, Γ_0, and R) until we obtained the closest match. Through using ROOT CERN's MINUIT package we found that a relativistic BW with resonant mass $M_0 = 890$ MeV, resonant spin-dependent width $\Gamma_0 = 50$ MeV, and interaction radius $R = 18$ GeV^{-1} achieved the closest fit to EVTGEN MC. Fig. 6.2 and Fig. 6.3

show relativistic spin-dependent Breit-Wigners with different R's and different $2j+1$ powers for the mass-dependent widths. The best fit was obtained using the parameter values described above and by using the χ^2 values for each fit.

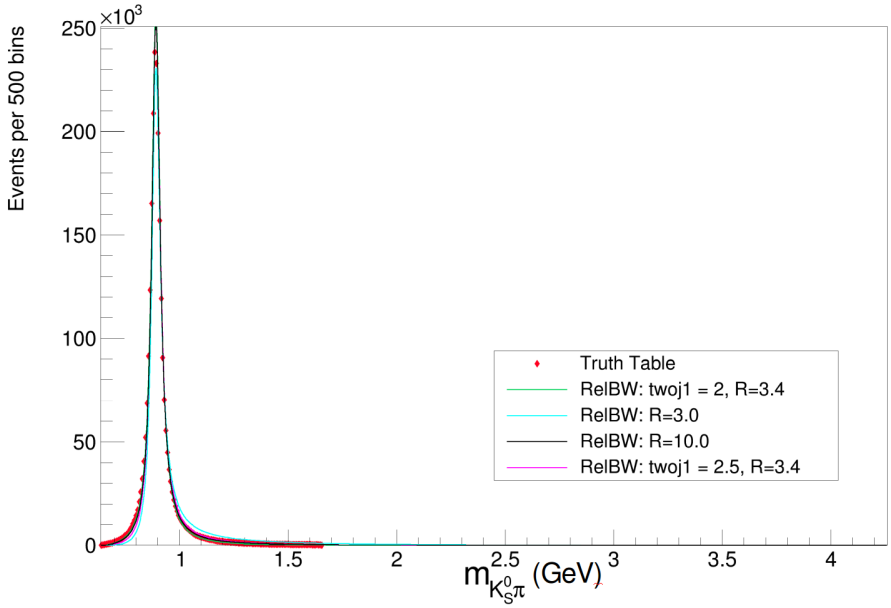

Figure 6.2: Shows different $m_{K^0_S\pi}$ curves using data from all $K^*(892)$ helicity modes. All physics models are relativistic spin-dependent Breit-Wigners with different interaction radius, denoted here as "R" and different $2j+1$ powers for the mass-dependent widths

Figs. 6.4 through 6.15 show the distributions for $m_{K^0_S\pi}$, $\cos(\theta_{K^0_S\pi})$, $\cos(\theta_\Phi)$, and ϕ for each helicity of the $K^*(892)$ signal MC. MINUIT was used to find values of the resonant mass and width, and the interaction radius for the Relativistic spin-dependent Breit-Wigner physics model.

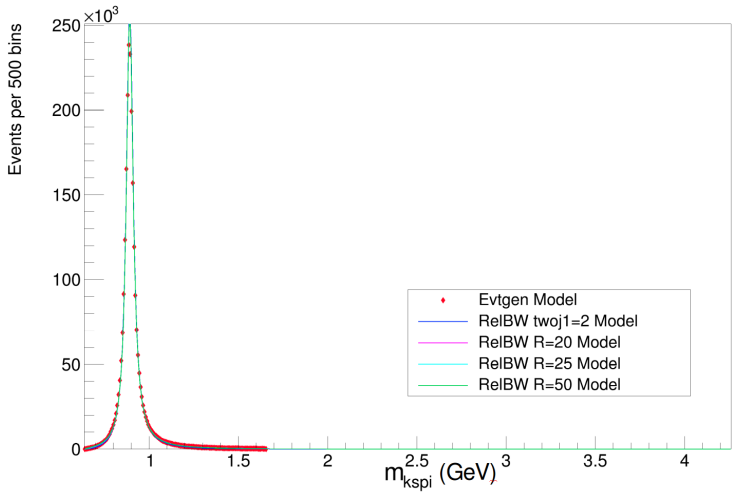

Figure 6.3: Shows different $m_{K^0_S\pi}$ curves using data from all $K^*(892)$ helicity modes. All physics models are relativistic spin-dependent Breit-Wigners with different interaction radius, denoted here as "R."

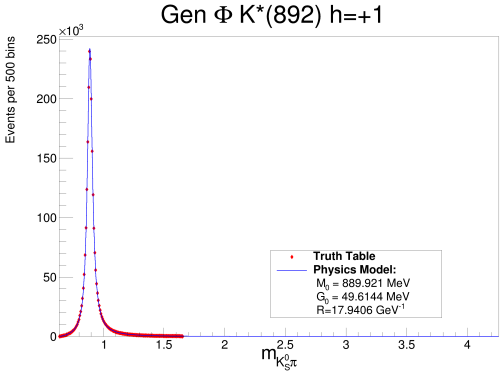

Figure 6.4: The EvtGen and physics models for $\Phi K^*(892)$ helicity=+1 $m_{K^0_S\pi}$ range.

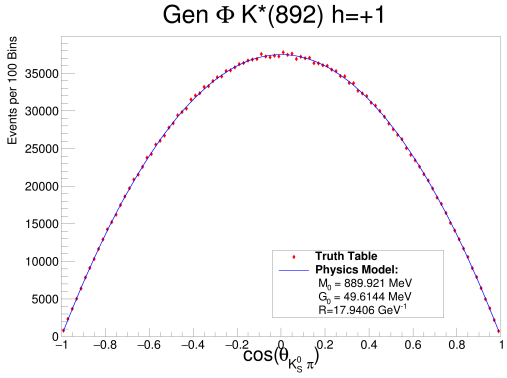

Figure 6.5: The EvtGen and physics models for $\Phi K^*(892)$ helicity=+1 $cos(\theta_{K^0_S\pi})$.

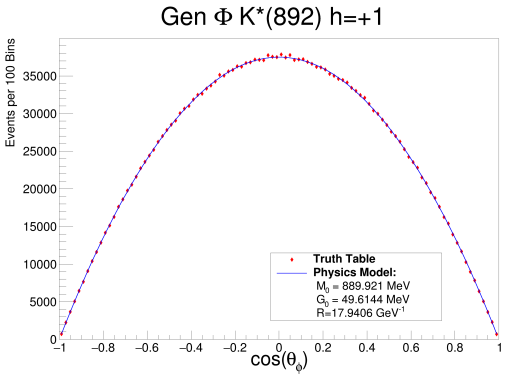

Figure 6.6: The EvtGen and physics models for $\Phi K^*(892)$ helicity=+1 $cos(\theta_\Phi)$.

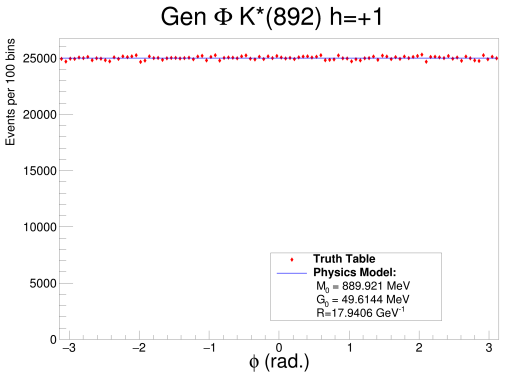

Figure 6.7: The EvtGen and physics models for $\Phi K^*(892)$ helicity=+1 ϕ angle.

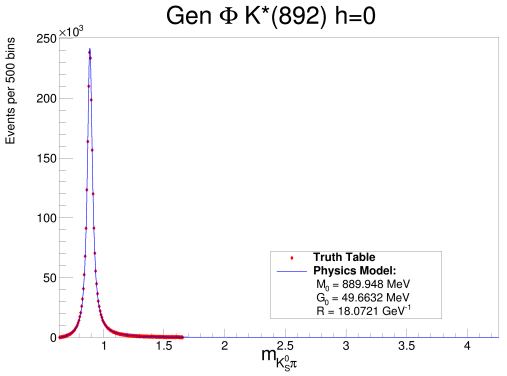

Figure 6.8: The EvtGen and physics models for $\Phi K^*(892)$ helicity=0 $m_{K^0_S\pi}$.

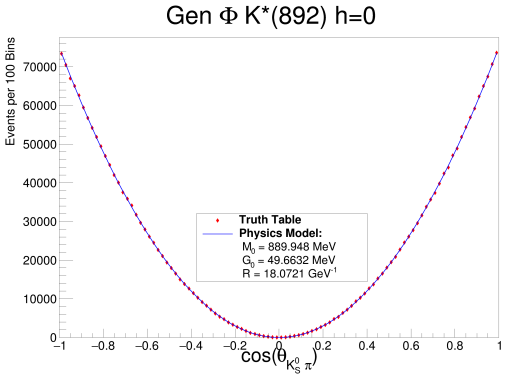

Figure 6.9: The EvtGen and physics models for $\Phi K^*(892)$ helicity=0 $cos(\theta_{K^0_S\pi})$.

Notice how Figs. 6.9 and 6.10 have a different distribution of events in comparison to those from helicity ± 1. The $m_{K^0_S\pi}$ distributions for all three helicities of the $\phi K^{*\pm}(892)$ mode. Likewise, for each mode the ϕ angle is the same: flat.

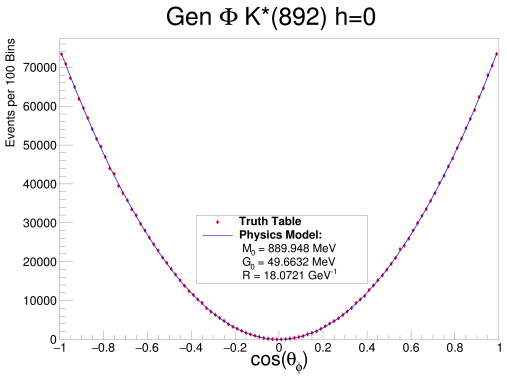

Figure 6.10: The EvtGen and physics models for $\Phi K^*(892)$ helicity=0 $cos(\theta_\Phi)$.

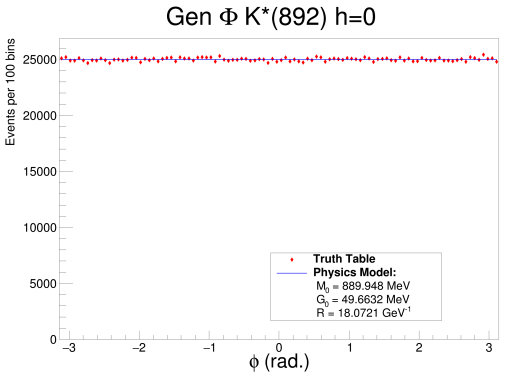

Figure 6.11: The EvtGen and physics models for $\Phi K^*(892)$ helicity=0 ϕ angle.

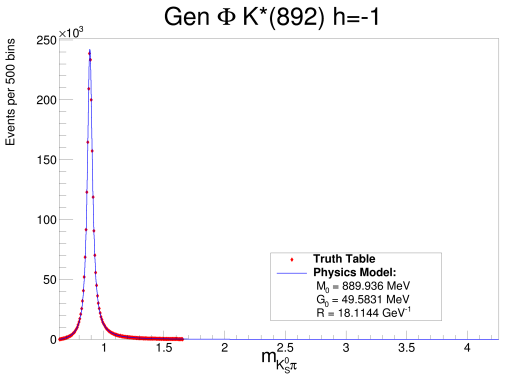

Figure 6.12: The EvtGen and physics models for $\Phi K^*(892)$ helicity=-1 $m_{K^0_S\pi}$.

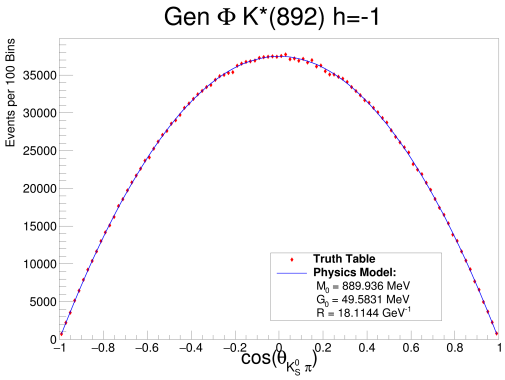

Figure 6.13: The EvtGen and physics models for $\Phi K^*(892)$ helicity=-1 $cos(\theta_{K^0_S\pi})$.

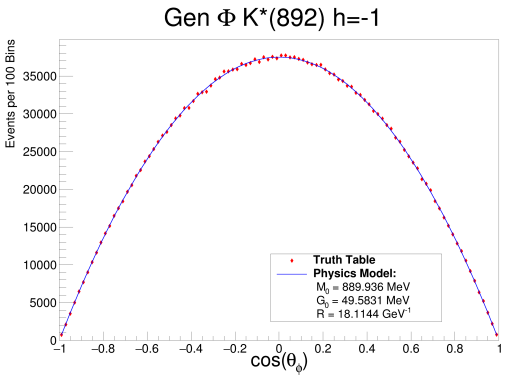

Figure 6.14: The EvtGen and physics models for $\Phi K^*(892)$ helicity=-1 $cos(\theta_\Phi)$.

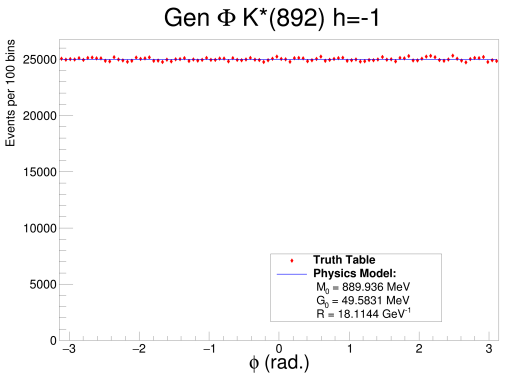

Figure 6.15: The EvtGen and physics models for $\Phi K^*(892)$ helicity=-1 ϕ angle.

Chapter 7

Sources of Background

The MC background we use in this analysis is continuum (i.e. $e^+e^- \to$ hadrons) as opposed to $e^+e^- \to \Upsilon(4S) \to$ hadrons. Backgrounds are separated into six categories:

- uds : Events from $e^+e^- \to u\bar{u}$ (or $d\bar{d}$ or $s\bar{s}$)
- charm : Events from $e^+e^- \to c\bar{c}$
- charged: Events from $e^+e^- \to B^+B^-$
- mixed: Events from $e^+e^- \to B^0\bar{B}^0$
- rare charged: Rare events with luminosity 50x normal data
- rare mixed: Rare events luminosity 50x normal data

Rare decays originate from charged or neutral B-mesons and come from decays modes where the signal mode has one or more particles swapped with those from another event.

7.0.1 **Background Reduction**

In order to deal with background reduction we conduct a multivariate analysis (MVA) after the skimming and reconstruction processes. This MVA approach allows us to determine the effect of each variable and to study the performance of the variables as signal background discriminates. We use two MVA's: one to study the shape of the events in the CM frame for B events and non-B events and the second as a candidate

selector (and uses further variables for background reduction). B events always result in decay products that disperse in space isotropically in the $\Upsilon(4S)$ CM frame. Non-B events are more jet-like in this frame.

Choice of Multi-Variate Analyzer and Input Distributions

Both MVA's were chosen as artificial neural networks (ANN) because of the continuous nature of some of the variables and broad regions that rule out MVA's like a binary decision tree (BDT). To verify that ANN's were the best choice, we took our second ANN and used ROOT's TMVA package [30] created a plot of background rejection vs signal efficiency for different MVA's as shown in Fig. 7.1.

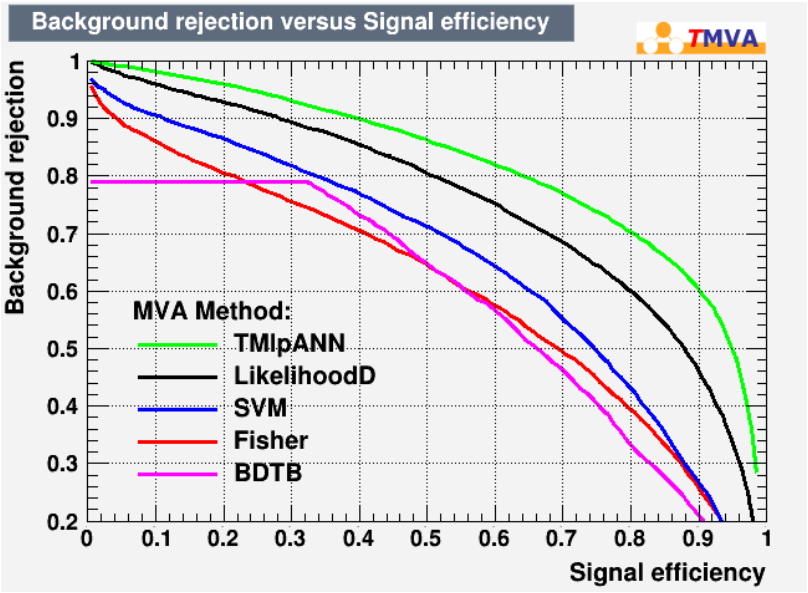

Figure 7.1: A background rejection vs signal efficiency plot for various MVA's.

In this figure, a curve that is higher in background rejection and signal efficiency represents a better MVA. From Fig. 7.1 we see that the ANN does better than the other MVA's.

We train our ANN's using signal MC events to be "signal" and generic background events to be "background". We check for overtraining by comparing the output for

the test and training sample. Figure 7.17 below shows that there is no overtraining. See below for more details.

Artificial Neural Network based on event shape: ANN1

Our first artificial Neural Network uses our event shape variables to discriminate between backgrounds and *uds* events, and between $c\bar{c}$ and B-meson events.

Variables used in this neural network include: R_2, qr, cosb, cosbt, costhr, k0et, k0hoo0, k0hoo1, k0hoo2, k0hoo3, k0hoo4, k0hso00, k0hso01, k0hso02, k0hso03, k0hso04, k0hso10, k0hso12, k0hso14, k0hso20, k0hso22, k0hso24.

These variables are all event shape variables. For instance, R_2 is a measure of the sphericity of the event. For the other variables, early work was done by Fox and Wolfram [31] and subsequently refined by some Belle authors.

The performance of the ANN separating the signal and background can be seen in Fig. 7.2, where the signal distribution is in red and the the blue represents the background distribution. Note that the signal curve is $\sim$1000$\times$ lower in height in real data. To maximize the signal to background ratio we make a cut on the ANN output at 0.2.

Note the mean and standard deviation reflect that most events are right above our cut. This means we are still reducing background without losing a lot of our signal.

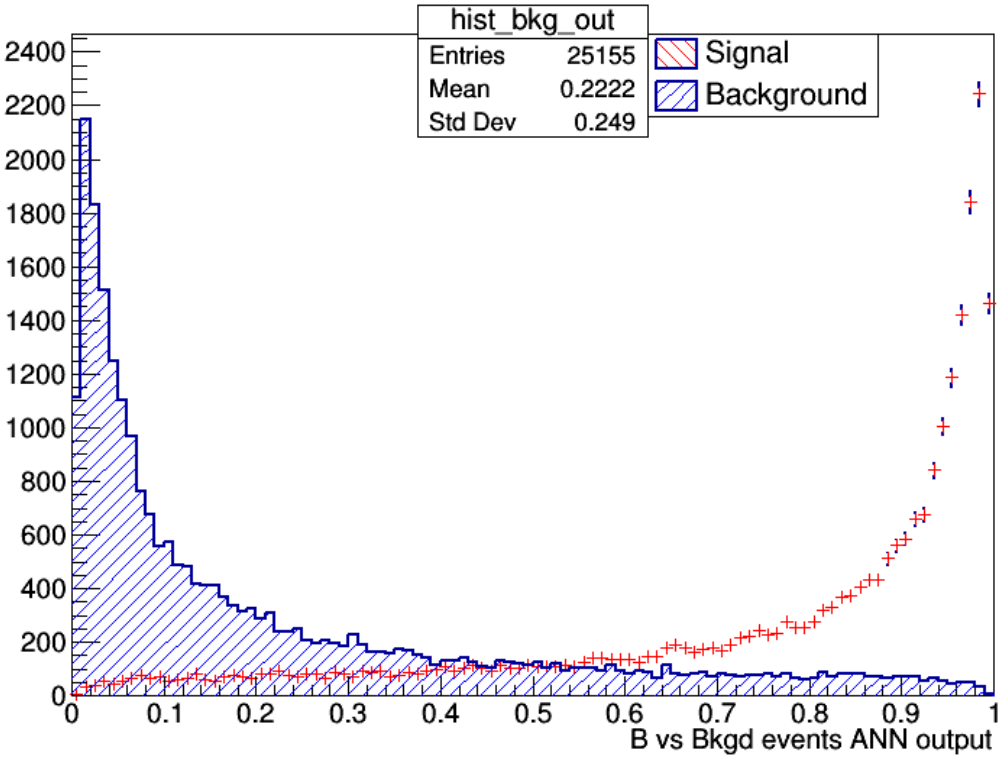

Figure 7.2: Output of the first ANN (event shape) for signal and background.

Artificial Neural Network based on kinematics: ANN2

We can further reduce our backgrounds using an ANN for the best candidate B's based on kinematics. The variables our ANN2 used includes:

- The B-meson vertex $\log_{10}(\chi^2)$ (log10_bverchi), which is the χ^2 for the hypothesis that two or more tracks originate from the same point (called the vertex)
- the differences in the x, y, and z locations of the B vertex and the IP (b_ip_x_diff, b_ip_y_diff, b_ip_z_diff)
- the difference in the z of the two B vertices (deltaz)
- the K^0_S mass-squared (k0mm2),

- the magnitude of the K_S^0 momentum (k0s_momentum),
- the magnitude of the ϕ momentum (phi_momentum),
- the magnitude of the π momentum (pi_momentum),
- the particle identification probabilities (k1_id, k2_id, p_id),
- and the $\log_{10}(\chi^2)$ and z of the K_S^0 vertex (log10_kschisq, log10_kszdist).

Figures 7.3-7.5 compare the signal and background distributions of the variables above.

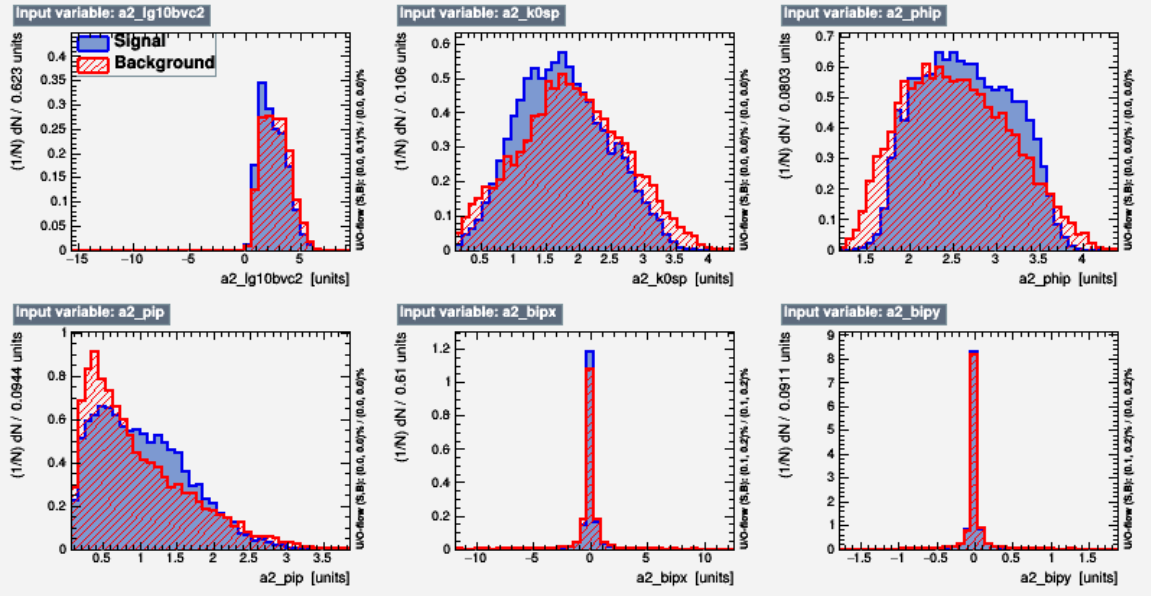

Figure 7.3: Comparison of signal and background distributions for the first set of variables that are input to ANN2.

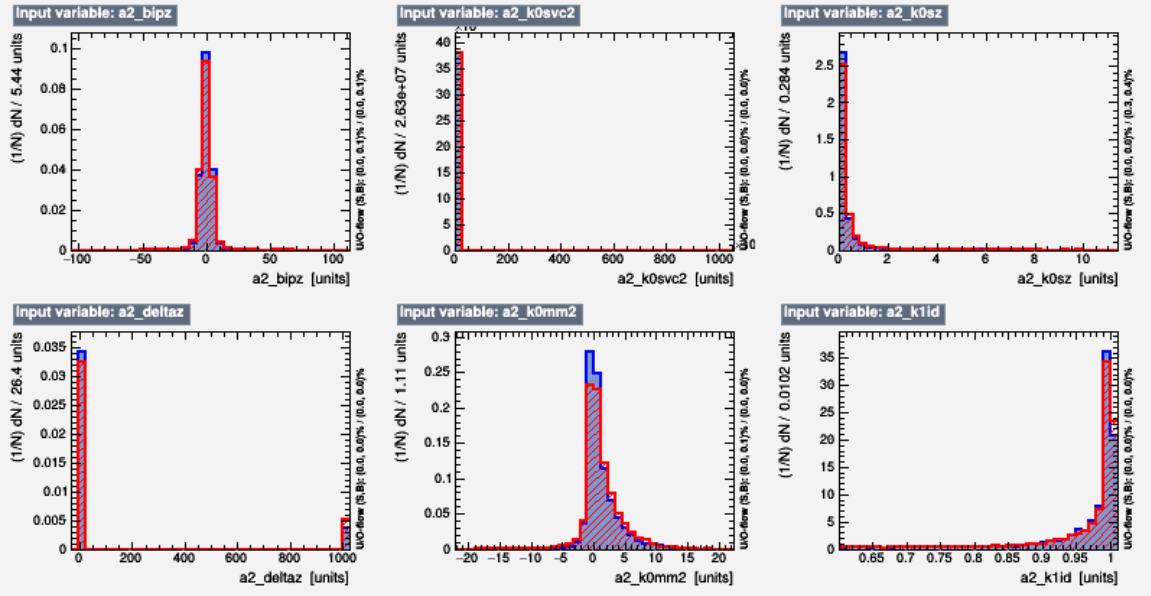

Figure 7.4: Comparison of signal and background distributions for the second set of variables that are input to ANN2.

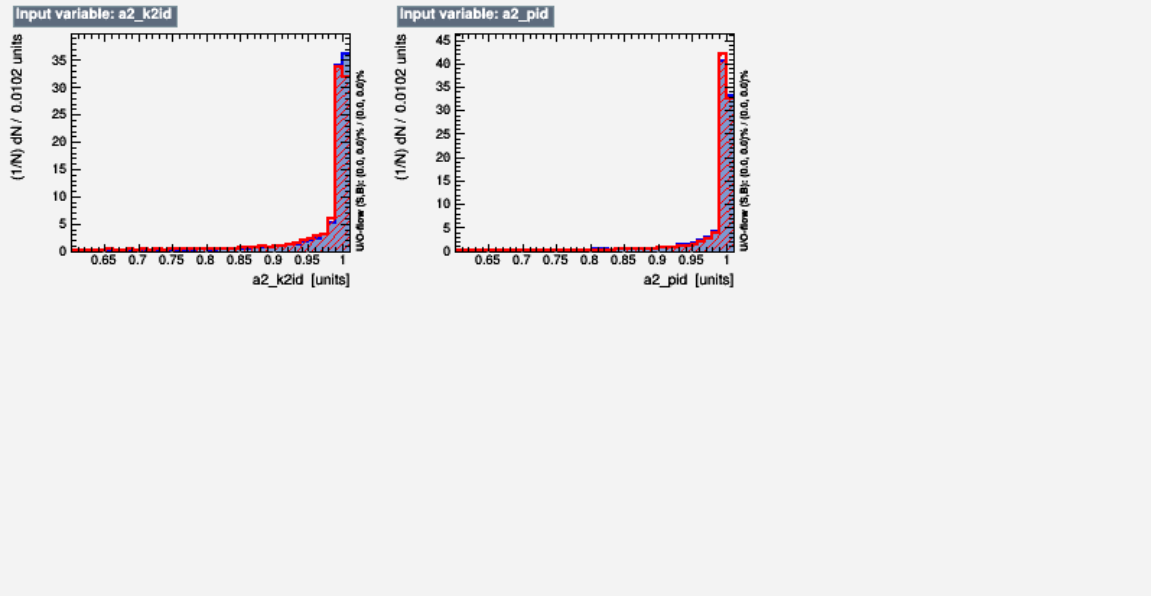

Figure 7.5: Comparison of signal and background distributions for the third set of variables that are input to ANN2.

Figures 7.6 and 7.7 show correlation matrices for the background or signal variables respectively. The bright green found in these plots show that there is zero correlation between the variables. The red along the horizontal marks correlation

and is expected since this is the testing of the variables with itself. We find that there is some correlation between the momenta of the K^0_S, ϕ, and π momenta (which is to be expected).

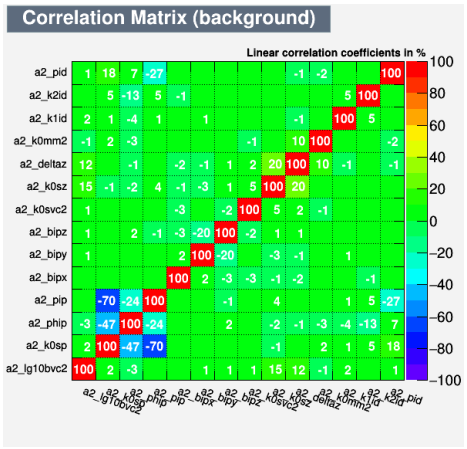

Figure 7.6: The correlation matrix for background variables.

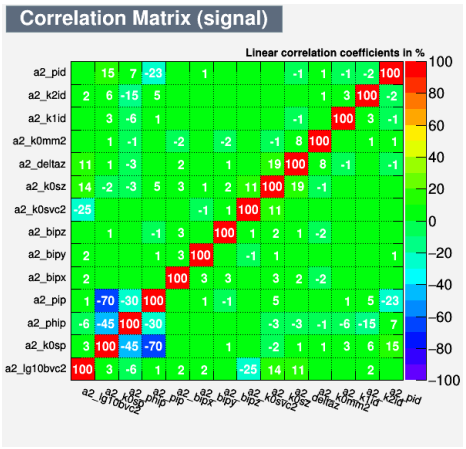

Figure 7.7: The correlation matrix for signal variables.

The following Figs. 7.8 through 7.12 show the signal and background output for each MVA. In Fig. 7.12 the signal shape is well-defined from the background: a good characteristic of a good MVA training.

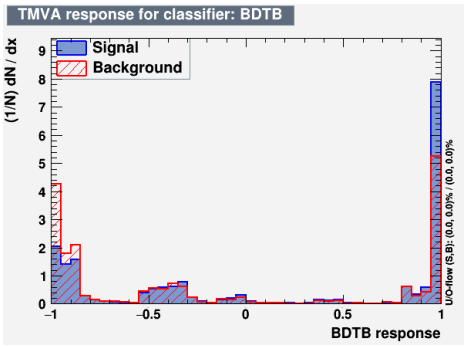

Figure 7.8: Signal and background output for the binary decision tree (BDTB) classifier.

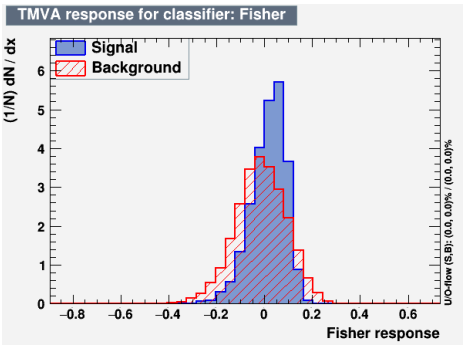

Figure 7.9: Signal and background output for the Fisher classifier.

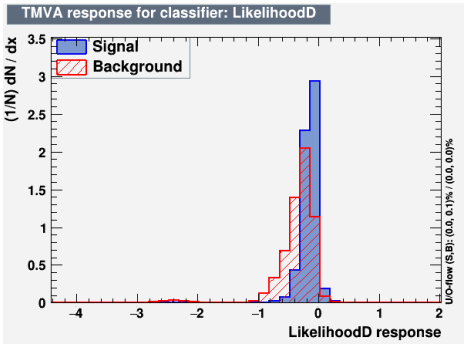

Figure 7.10: Signal and background output for the LikelihoodD classifier.

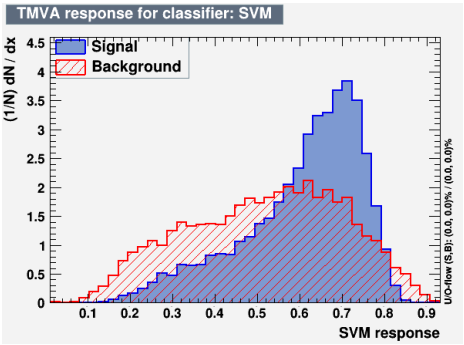

Figure 7.11: Signal and background output for the SVM classifier.

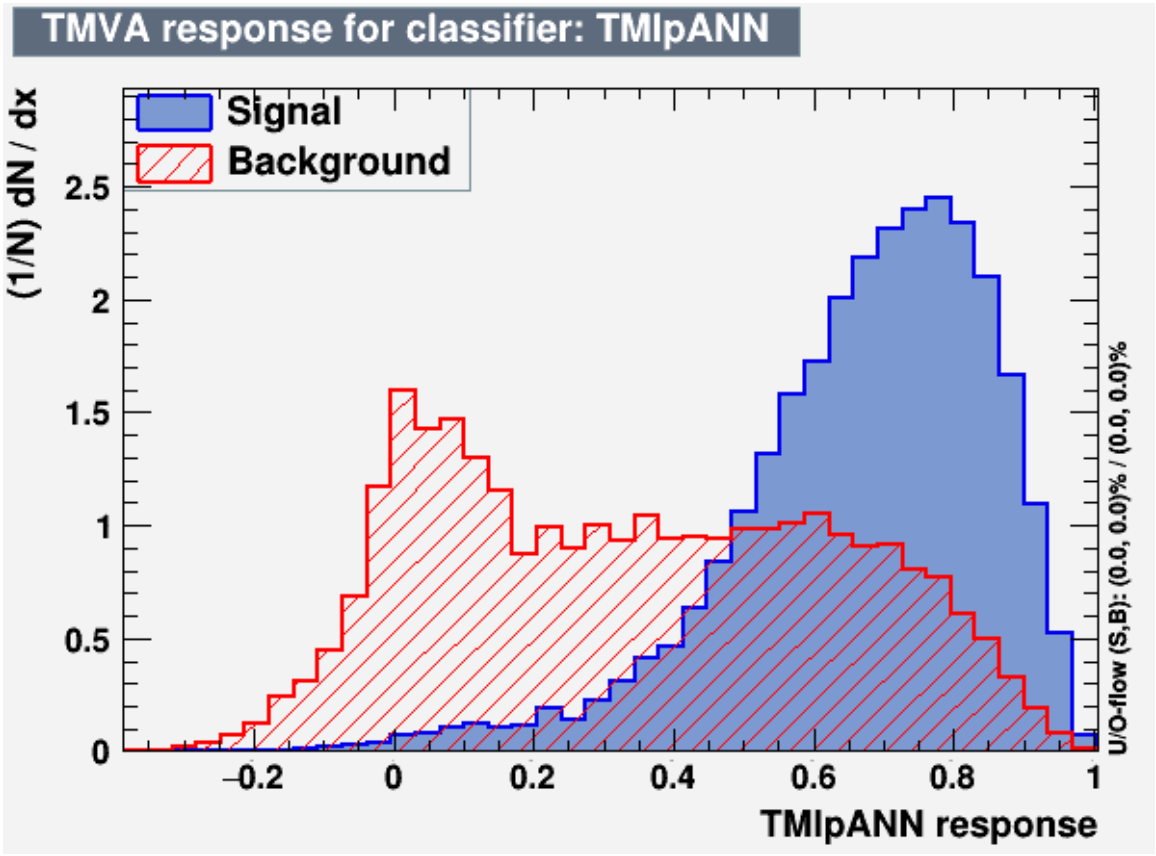

Figure 7.12: Signal and background output for the TMlpANN classifier.

Figures 7.13 through 7.17 show the overtraining checks for the different MVA's. If signal and background have the same shape, then the sample is overtrained. The ANN classifier, which we used in this analysis, did well.

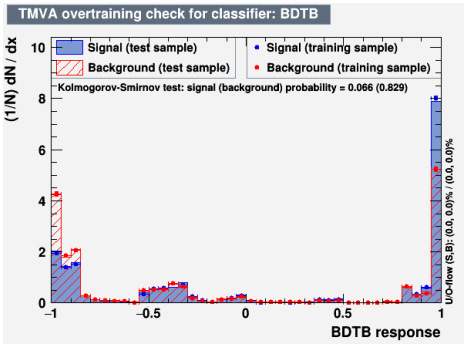

Figure 7.13: Overtraining check for the BDTB classifier.

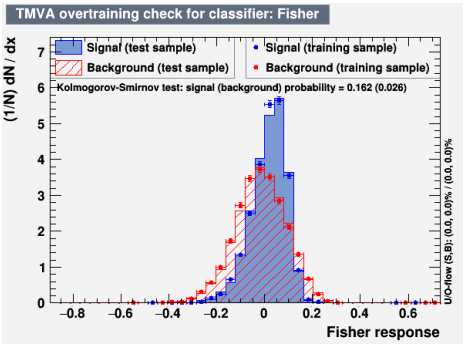

Figure 7.14: Overtraining check for the Fisher classifier.

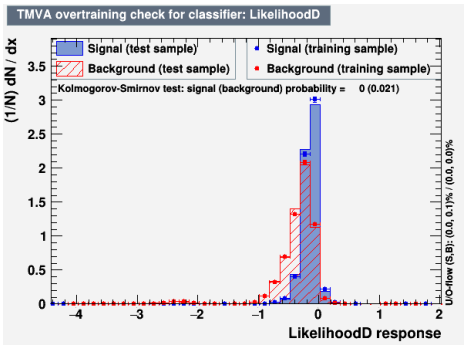

Figure 7.15: Overtraining check for the LikelihoodD classifier.

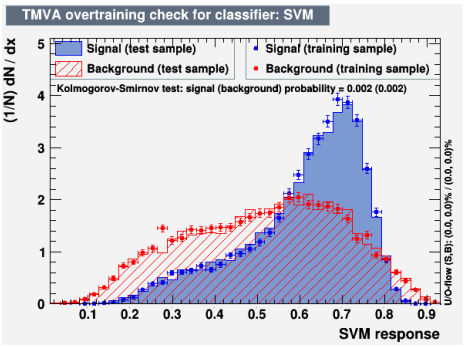

Figure 7.16: Overtraining check for the SVM classifier.

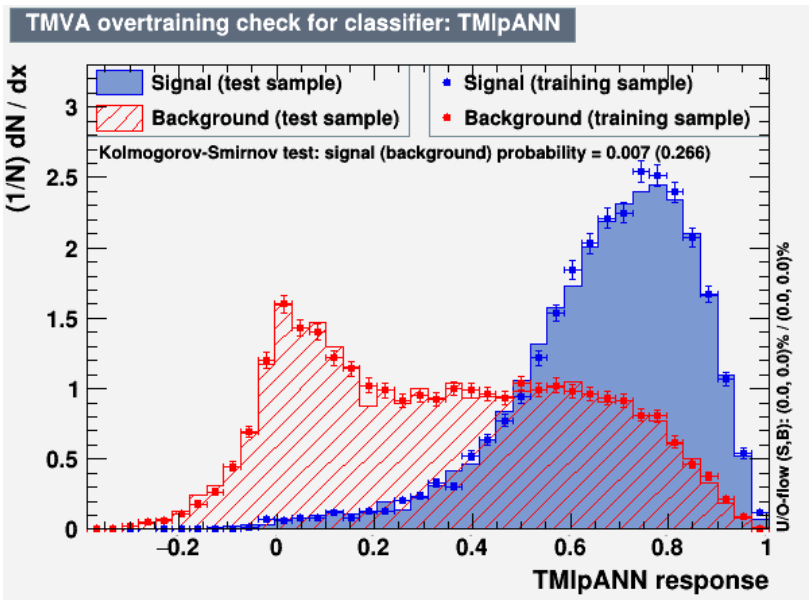

Figure 7.17: Overtraining check for the TMlpANN classifier.

7.0.2 **Background Reduction**

Background was attempted to be eliminated with our first artificial neural network (ANN) which is based on event shape in the CM frame. Those events with more spherical (isotropic) shapes were kept while jet-like backgrounds were removed.

Background events were tabulated for each of the backgrounds mentioned above using the same cuts as applied to data except that the m_{bc} variable is restricted to the 6 MeV range [5.276, 5.282] GeV.

Another cut, $m(K_S^0 K^+ K^-) \ni [1.855,\ 1.875]$ GeV, was used to remove a large background from $D^0 \to \phi K_S^0$.

The following background tables were created while running our first ANN with tight cuts. Each background mode was separated into types where the K_S^0 or the charged pion arise from the same B-meson as the ϕ as follows, where we denote the (grand)parent B of the ϕ by B_ϕ:

(0) Neither the K_S^0 nor the π^+ match.

(1) Only the π^+ has the B_ϕ as a (grand)parent.

(2) Only the K_S^0 has the B_ϕ as a (grand)parent.

(3) Both the K_S^0 and the π^+ have the B_ϕ as a (grand)parent.

All entries are produced by the EVTGen [24] output. Sometimes decay products are unrecognizable and look like nonsense. Thankfully, those decays are negligible backgrounds (denoted by $xxxx$ in the tables).

Table 7.1 Mixed Background With Tight ANN Cuts

Decay Mode	No match	π match	K_S^0 match	π, K_S^0 match	Sum of Types
$B^0 \to D^- \pi^+$; $D^- \to \phi\pi^-$	0	1	0	0	1
$B^0 \to D^{*+} \pi^-$; $D^+ \to \phi\pi^+$	0	1	0	0	1
Total:	0	2	0	0	2

Table 7.2 Charged Background With Tight ANN Cuts

Decay Mode	No match	π match	K_S^0 match	π, K_S^0 match	Sum of Types
$B^- \to D^0 \pi^-$; $D^0 \to \phi\bar{K}^0$	0	1	0	0	1
$B^- \to \chi_{c1}(1P) K^-$	0	0	0	1	1
$B^- \to D_s^+ \pi^- K^-$	0	0	0	1	1
Total:	0	1	0	2	3

Table 7.3 Charm Background With Tight ANN Cuts

Decay Mode	No match	π match	K_S^0 match	π, K_S^0 match	Sum of Types
$D_s^{*+} \to D_s^+\gamma$; $D_s^+ \to \phi e^+\nu_e$	4	0	0	0	4
$D_s^{*+} \to D_s^+\gamma$; $D_s^+ \to \phi\pi^+$	4	0	0	0	4
$c \to 0$; $xxxxx \to \gamma\gamma\gamma\gamma\gamma\bar{c}gggcD^{*-}\pi^+ K^{*-}K^+D^{*0}$	1	0	0	0	1
$D^{*-} \to D^0\pi^-$; $\bar{D^0} \to \phi\pi^0$	1	0	0	0	1
$\bar{D^{*0}} \to \bar{D^0}\pi^0$	1	0	0	0	1
$D^- \to \phi\pi^-\pi^0$	1	0	0	0	1
$D_s^+ \to \phi\pi^+$	1	0	0	0	1
$\Lambda_c^+ \to \Lambda\pi^+\pi^0\rho^0$; $xxxxx \to \gamma\gamma\gamma cg\bar{c}\Lambda_c^+\bar{n}\rho^-\bar{D^0}$	1	0	0	0	1
$D_s^+ \to \phi e^+\nu_e$	1	0	0	0	1
$D_s^+ \to \phi\rho^+$	1	0	0	0	1
$\bar{D^0} \to \phi K^0$	1	0	0	0	1
$D_s^- \to \phi\pi^-\pi^-\pi^+$	0	1	0	0	1
$u \to$; $xxxxx \to \gamma\gamma\gamma\gamma\gamma\gamma c\bar{u}\bar{c}ggu D^{*+}\pi^- K^{*+}K^-D^{*-}\pi^0\pi^+$	1	0	0	0	1
$D^{**+} \to D^+\pi^0$	1	0	0	0	1
Total:	19	1	0	0	20

Table 7.4 uds Background With Tight ANN Cuts

Decay Mode	No match	π match	K_S^0 match	π, K_S^0 match	Sum of Types
$\phi \to K^+K^-$; $xxxxx \to$ $\gamma\gamma\gamma\gamma\gamma\gamma sgg\bar{s}\phi K^{*-}\omega$ $\rho^0\pi^0K^{*+}$	1	0	0	0	1
$\phi \to K^+K^-$; $xxxxx \to$ $\gamma\gamma\gamma\gamma\gamma\bar{s}ggggs\phi K^{*+}$ $a_1(1260)^-$ $\rho^0\rho^+\pi^0$ $K_0^*(1430)^-$	1	0	0	0	1
$\Lambda \to \gamma\gamma$; $xxxxx \to$ $\gamma\gamma\gamma\gamma\bar{s}gggggsK^0$ $\pi^+\rho^0\pi^-\pi^0$ $-2214\rho^+\Lambda K^+K^-$	1	0	0	0	1
$\phi \to K^+K^-$; $xxxxx \to$ $\gamma\gamma\gamma\gamma sgggggg\bar{s}\phi 3224$ $\rho^-\bar{p}\pi^0\omega K^{*+}$	1	0	0	0	1
$\phi \to K^+K^-$; $xxxxx \to$ $\gamma\gamma\gamma\gamma\gamma sggg\bar{s}\phi\bar{K^0}\pi^0$ $f_0(1370)\pi^0\rho^0K^{*0}$	1	0	0	0	1
$\phi \to K^+K^-$; $xxxxx \to$ $\gamma\gamma\gamma\gamma sggggg\bar{s}\phi\bar{K^0}\omega K^{*0}$ $K^{*-}\rho^+\rho^0K^0$	1	0	0	0	1
$\phi \to K^+K^-$; $xxxxx \to$ $\gamma\gamma\gamma sgggg\bar{s}\phi\bar{K^0}\rho^-\pi^+$ $\pi^-\rho^+\pi^-\pi^+K^0$	1	0	0	0	1
$\bar{K^{*0}} \to K^-\pi^+$; $xxxxx \to$ $\gamma\gamma\gamma sggg\bar{d}\bar{s}gd\bar{K^{*0}}\rho^0\rho^0$ $\pi^-\rho^+K^0\pi^+\pi^-$	1	0	0	0	1
$\phi \to K^+K^-$; $xxxxx \to$ $\gamma\gamma sgggggg\bar{s}\phi\bar{K^{*0}}\rho^-$ $f_0(1370)\omega\pi^+\pi^0K^0$	1	0	0	0	1
$\phi \to K^+K^-$; $xxxxx \to$ $\gamma\gamma\gamma\bar{u}s\bar{s}ggu K^-\phi K^+$ $\bar{\Delta^{++}}p\bar{K^0}K^+$	1	0	0	0	1

Decay Mode	No match	π match	K^0_S match	π, K^0_S match	Sum of Types
$\phi \to K^+K^-$; $xxxxx \to \gamma\gamma\gamma\bar{s}gggsK^{*+}\rho^-\pi^+ \pi^-\pi^+\rho^-\bar{K^{*0}}\phi$	1	0	0	0	1
$d \to$; $xxxxx \to \gamma\gamma\gamma dgggggg\bar{d}K^{*0}K^- \pi^+n-2214K^{*+}K^{*-}\pi^+$	1	0	0	0	1
$\phi \to K^+K^-$; $xxxxx \to \gamma\gamma\gamma\gamma\bar{s}d\bar{d}ggggs\phi K^0\bar{n} p\rho^-\pi^0\pi^+\pi^-\bar{K^0}$	1	0	0	0	1
$\phi \to K^+K^-$; $xxxxx \to \gamma\gamma\gamma s\bar{d}dgg\bar{s}\bar{K^0}dggg\bar{s} \Delta^- f_2(1270)\bar{\Delta^0}\rho^+K^0\phi$	1	0	0	0	1
$\phi \to K^+K^-$; $xxxxx \to \gamma\gamma\gamma\bar{s}ggggsK^0\pi^+\omega\pi^0 \rho^0K_2^*(1430)^-\phi$	1	0	0	0	1
$\phi \to K^+K^-$; $xxxxx \to \gamma\gamma\gamma\bar{s}gggs\phi K^{*+}K^{*-} K^+\pi^-\omega\rho^0\bar{K^0}$	1	0	0	0	1
$\phi \to K^+K^-$; $xxxxx \to \gamma\gamma sg\bar{s}\bar{s}ggs\bar{K^0}\rho^0K^{*0}\phi K^+\rho^-\rho^+K^-$	1	0	0	0	1
$\phi \to K^+K^-$; $xxxxx \to \gamma\gamma sgggg\bar{s}\phi K^-\pi^+\pi^- \pi^0\pi^0a_2(1320)^+\pi^- K_0^*(1430)^+$	1	0	0	0	1
$\phi \to K^+K^-$; $xxxxx \to \gamma\gamma\gamma\bar{s}ggggsK^0\rho^0\rho^0\pi^0 \bar{K^{*0}}\phi$	1	0	0	0	1
$\phi \to K^+K^-$; $xxxxx \to \gamma\gamma sgggggg\bar{s}\phi\bar{K^0}\pi^-\pi^0 a_1(1260)^+\rho^0K^{*0}$	1	0	0	0	1

Decay Mode	No match	π match	K_S^0 match	π, K_S^0 match	Sum of Types
$\phi \to K^+K^-$; $xxxxx \to \gamma\gamma\gamma sggggg\bar{s}\phi\bar{K^0}\eta'\rho^-\Delta^{++}\bar{p}K^{*0}$	1	0	0	0	1
$\phi \to K^+K^-$; $xxxxx \to \gamma\gamma\bar{s}gggggggs\phi K^{*+}\rho^-\pi^+\pi^0 b_1(1235)^0\pi^0\pi^-\bar{K^0}$	1	0	0	0	1
$\phi \to K^+K^-$; $xxxxx \to \gamma\gamma\gamma\gamma\bar{u}gggggguK^{*-}K^{*0}\pi^+\rho^0 K^{*-}\phi K^{*+}$	1	0	0	0	1
$\phi \to K^+K^-$; $xxxxx \to \gamma\gamma\gamma sgggggg\bar{s}K^{*-}\rho^0 p\bar{n}\eta K^{*0}\phi$	1	0	0	0	1
Total:	24	0	0	0	24

Table 7.5 Mixed RareMC Background With Tight ANN Cuts

Decay Mode	No match	π match	K_S^0 match	π, K_S^0 match	Sum of Types
$B^0 \to K^{*0}\phi$	0	0	56	10	66
$B^0 \to \phi K_0^*(1430)^0$	0	7	29	0	36
$B^0 \to K_2^*(1430)^0\phi$	0	7	24	2	33
$B^0 \to \phi K^0$	0	0	20	0	20
$B^0 \to \rho^0\phi$	0	9	0	0	9
$\bar{B^0} \to \bar{K^{*0}}\phi$; $\Upsilon(4S) \to B^0\bar{B^0}$	4	0	0	0	4
$\bar{B^0} \to \bar{K^0} f_0(1500)$	0	0	2	2	4
$B^0 \to K^{*+}K^{*-}$	0	0	2	2	4
$\bar{B^0} \to f_1(1285)\bar{K^0}$	0	0	2	2	4
$\bar{B^0} \to \phi\bar{K^0}\pi^0$	0	0	3	0	3
$B^0 \to K_2^*(1430)^0\phi$; $\phi \to K^+K^-$	0	2	0	0	2
$B^0 \to D^-D_s^+$	0	0	0	2	2
$B^0 \to D^{*-}\pi^+\rho^-\pi^+\eta'$; $D^- \to K^0\eta\pi^-$	0	2	0	0	2
$B^0 \to D_s^+\pi^-$	0	0	0	2	2
$B^0 \to D^{*-}\pi^+\pi^0\omega$; $\phi \to K^+K^-$	0	0	2	0	2
$B^0 \to 30343\gamma$	0	0	2	0	2
$\bar{B^0} \to \phi\eta(1295)$; $\Upsilon(4S) \to \bar{B^0}B^0$	0	2	0	0	2
$\bar{B^0} \to \phi\phi$; $\Upsilon(4S) \to B^0B^0$	2	0	0	0	2
$\bar{B^0} \to D_1(2420)^+D_s^-$; $D_1(2420)^+ \to D^{*0}\pi^+$	0	2	0	0	2
$B^0 \to D^-\pi^+K^0\bar{K^{*0}}$	0	0	0	2	2
$B^0 \to \phi K^*(1680)^0$	0	0	2	0	2
$B^0 \to \phi f_0(1370)$	0	2	0	0	2
$B^0 \to K^{*0} f_0(1370)$	0	0	2	0	2
$\bar{B^0} \to D_1(H)^+\mu^-\bar{\nu_\mu}$	0	0	0	2	2
$B^0 \to D_s^{*-}K^{*+}$; $D_s^- \to \phi\pi^-$	0	0	2	0	2
$\bar{B^0} \to D^{*+}D^{*-}\bar{K^0}$	0	2	0	0	2
$B^0 \to D^{*-}a_1(1260)^+\pi^-\pi^+\gamma$; $a_1(1260)^+ \to \rho^+\pi^0$	0	0	0	2	2

Decay Mode	No match	π match	K^0_S match	π, K^0_S match	Sum of Types
$\bar{B^0} \to D^+\mu^-\bar{\nu_\mu}$; $\Upsilon(4S) \to \bar{B^0}B^0$	0	2	0	0	2
$\bar{B^0} \to D_s^+\pi^-\gamma$; $D_s^+ \to \phi\pi^+$	0	2	0	0	2
$\bar{B^0} \to D^-\mu^+\nu_\mu$; $D^- \to \rho^- K^0$	0	0	2	0	2
$B^0 \to D^{*0}\bar{D^{*0}}$; $\Upsilon(4S) \to \bar{B^0}B^0$	0	2	0	0	2
$B^0 \to D_1(2420)^- e^+\nu_e$; $D_1(2420)^- \to D^{*-}\pi^0$	0	0	0	2	2
$\bar{B^0} \to \bar{K^0}K^0\bar{K^{*0}}$	0	0	0	2	2
$\bar{B^0} \to \bar{K^{*0}}\phi$; $\phi \to K^+K^-$	0	0	2	0	2
$\bar{B^0} \to D^+\omega\pi^-$	0	0	0	2	2
$B^0 \to \phi\phi$	0	0	0	2	2
$\bar{B^0} \to D_s^{*+}K^-$; $\phi \to K^+K^-$	2	0	0	0	2
$\bar{B^0} \to D_s^-K^+$; $D_s^- \to \phi\pi^-$	0	2	0	0	2
$\bar{B^0} \to \phi b_1(1235)^0$	0	2	0	0	2
$B^0 \to K_2^*(1430)^0\phi$; $K_2^*(1430)^0 \to K^0\pi^0$	0	0	0	1	1
$\bar{B^0} \to K^{*+}D_s^-$; $f_0(1370) \to \pi^+\pi^-$	0	0	1	0	1
$\bar{B^0} \to D^-\pi^+\eta\omega$; $\eta \to \pi^0\pi^0\pi^0$	0	0	0	1	1
$\bar{B^0} \to D^{*-}\pi^+\eta$; $\bar{D^0} \to f_0(1370)K^0$	0	1	0	0	1
$B^0 \to \bar{\Sigma_c^0}\rho^- p$; $\bar{\Sigma_c^0} \to \bar{\Lambda_c^-}\pi^+$	0	0	1	0	1
$\bar{B^0} \to D_s^{*+}\rho^-$; $D_s^+ \to \phi e^+\nu_e$	0	1	0	0	1
Total:	8	47	154	38	247

Table 7.6 Charged Rare MC Background With Tight ANN Cuts

Decay Mode	No match	π match	K_S^0 match	π, K_S^0 match	Sum of Types
$B^- \to K^{*-} f_0(1370)$	0	0	3	53	56
$B^+ \to a_1(1260)^+ K^0$	0	0	2	41	43
$B^+ \to K^+ K^- K^{*+}$	0	0	0	25	25
$B^- \to \phi\rho^-$	0	9	1	4	14
$B^- \to K^{*-} f_0(1370)$	0	0	0	8	8
$B^+ \to \phi K^0 \pi^+$	1	2	0	2	5
$B^- \to K^{*-} K^{*0}$	0	0	0	5	5
$B^- \to \phi K^-$	0	2	2	0	4
$B^- \to K^{*-} f_0(1370)$; $K^{*-} \to \bar{K^0}\pi^-$	1	2	0	0	3
$B^- \to \phi \bar{K^0} \pi^- \gamma$	1	0	0	2	3
$B^- \to \phi a_1(1260)^-$	0	2	0	1	3
$B^+ \to K^0 \bar{K^{*0}} K^+$; $\bar{K^{*0}} \to K^- \pi^+$	0	0	2	0	2
$B^+ \to K^{*+} \pi^+ \pi^-$	0	0	0	2	2
$B^- \to \eta(1440) f_0(1370)$	0	0	0	2	2
$B^+ \to a_1(1260)^+ K^0$; $a_1(1260)^+ \to f_0(600)\pi^+$	0	0	2	0	2
$B^- \to K^{*-} K^{*0}$; $K^{*0} \to K^+ \pi^-$	2	0	0	0	2
$B^+ \to K^0 \bar{K^{*0}} K^+$	0	0	2	0	2
$B^+ \to \bar{D^0} \mu^+ \nu_\mu$	0	0	0	2	2
$B^+ \to \pi^+ \bar{\Sigma_c^{*--}} \Delta^{++}$	0	1	0	0	1
$B^+ \to K^{*+} \bar{K^{*0}}$; $\Upsilon(4S) \to B^- B^+$	0	0	1	0	1
$B^- \to K_S^0 K_L^0 \pi^-$; $\Upsilon(4S) \to B^+ B^-$	1	0	0	0	1
$B^- \to J/\psi(1S) \bar{K^0} \pi^- \pi^0$; $K_1(1270)^0 \to \rho^0 K^0$	0	0	0	1	1
$B^- \to a_1(1260)^- \Sigma_c^{*+} \bar{p}$	0	0	0	1	1
$B^+ \to \rho^+ \bar{D^0}$; $\bar{D^0} \to K^0 \pi^0 \pi^0 \pi^0$	0	1	0	0	1
$B^- \to K^{*0} K^0 K^-$; $K^{*0} \to K^+ \pi^-$	0	0	0	1	1
$B^+ \to \bar{D^0} \pi^- \pi^+ \pi^+$	0	0	0	1	1
$B^- \to D^{*0} D_s^-$; $D^0 \to K^{*-} e^+ \nu_e$	1	0	0	0	1

Decay Mode	No match	π match	K^0_S match	π, K^0_S match	Sum of Types
$B^- \to D^{*0} D^- \bar{K^0}$	0	0	0	1	1
$B^- \to D^{*0} \rho^0 \pi^- \rho^0$	0	1	0	0	1
$B^+ \to K^{*+} f_0(1370)$; $f_0(1370) \to K^+ K^-$	0	1	0	0	1
$B^+ \to \bar{D^{*0}} \pi^+ \rho^0 \pi^0 K^0$; $\Upsilon(4S) \to B^+ B^-$	0	0	0	1	1
$B^+ \to a_1(1260)^+ K^0$; $\bar{K^{*0}} \to K^- \pi^+$	1	0	0	0	1
$B^- \to a_1(1260)^- K^0$; $\Upsilon(4S) \to B^+ B^-$	1	0	0	0	1
$B^+ \to K^+ \bar{K^0} \pi^0 \gamma$; $\pi^0 \to \gamma\gamma$	1	0	0	0	1
$B^+ \to \bar{D^{*0}} \pi^- \pi^+ \pi^+ \pi^0$	0	0	0	1	1
$B^+ \to D_s^- \pi^+ K^+ \pi^0 \pi^0$; $D_s^- \to \phi \pi^-$	0	0	1	0	1
$B^+ \to \bar{D^0} D^0 K^+$	0	0	0	1	1
$B^- \to D^{*0} \rho^-$	0	0	0	1	1
$B^- \to K^{*-} f_0(1370)$; $\Upsilon(4S) \to B^+ B^-$	1	0	0	0	1
$B^- \to D^0 e^- \bar{\nu_e}$	0	0	0	1	1
$B^+ \to \bar{D^{*0}} \rho^+$; $\bar{D^0} \to K^0 \pi^+ e^- \bar{\nu_e}$	1	0	0	0	1
$B^+ \to D_s^+ \pi^0$; $\Upsilon(4S) \to B^- B^+$	0	1	0	0	1
$B^- \to \phi \pi^0 \pi^-$; $\phi \to K^+ K^-$	1	0	0	0	1
$B^+ \to \bar{D^{*0}} a_1(1260)^+$; $\bar{D^0} \to K^+ \mu^- \bar{\nu_\mu}$	0	1	0	0	1
$B^- \to D^{*0} p \Delta^{++}$; $D^0 \to K^- e^+ \nu_e$	0	0	0	1	1
$B^+ \to \bar{D^{*0}} \pi^+ \pi^0 \omega$	0	0	0	1	1
$B^- \to D^{*0} \pi^- \pi^0 \bar{K^0}$	0	1	0	0	1
$B^- \to D^0 \pi^-; D^0 \to \phi \bar{K^0}$	0	0	1	0	1
$B^- \to D^{*0} \pi^-$	0	0	1	0	1
Total:	13	24	18	159	214

Table 7.7 Summary Table Background With Tight ANN Cuts

Decay Mode	No match	π match	K_S^0 match	π, K_S^0 match	Sum of Types
K*(892) signal	0	0	0	7	7
Mixed background	0	2	0	0	2
Charged background	0	1	0	2	3
charm background	19	1	0	0	20
uds background	24	0	0	0	24
Mixed Rare MC	8 / 50	47 / 50	154 / 50	38 / 50	247 / 50
Charged Rare MC	13 / 50	24 / 50	18 / 50	159 / 50	214 / 50

Summary of backgrounds for each type (types are explained in the text). The background from signal modes, also known as self cross-feed, is shown at the top. The background modes are the next section. The rare MC backgrounds shown in the last subsection are to be divided by 50, as indicated, and should *not* be added to the backgrounds above.

Chapter 8

Efficiency of Selection

The efficiency is the fraction of events that make it through the selection and reconstruction process. We use the efficiency to recover the true physics variable distributions. In this chapter we describe the efficiency as obtained from the MC.

8.0.1 Comparing trueb_best and bmatch_best Efficiencies

A truth table B-meson variable, "trueb" was only available for all the helicities of the the $\Phi K^*(892)$ mode, due to a processing error. The "trueb" variable tells us if the reco candidate is truly the signal candidate based on matching the truth table list. Thus we created another variable called "bmatch" by using the momenta of the tracks to figure out which candidate is the true candidate in the MC list. In the following plots we compare these two variables in the $\Phi K^*(892)$ modes (where both are available) and confirm that both give identical results. So in the other modes where "trueb" is unavailable we use "bmatch".

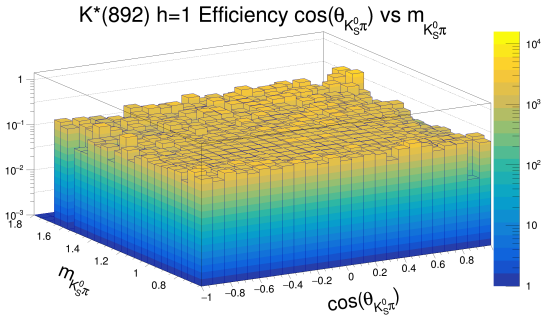

Figure 8.1: $\cos(\theta_{K^0_S\pi})$ vs. $m_{K^0_S\pi}$ efficiency for $\Phi K^*(892)$ $h = +1$ trueb_best candidates.

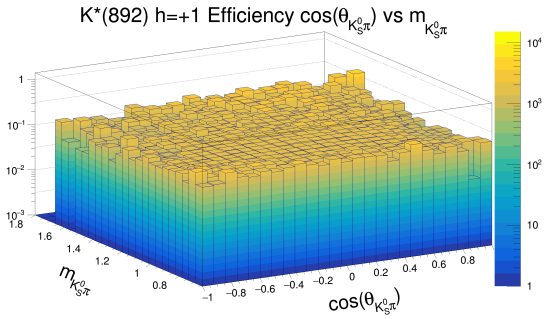

Figure 8.2: $\cos(\theta_{K^0_S\pi})$ vs. $m_{K^0_S\pi}$ efficiency for $\Phi K^*(892)$ $h = +1$ bmatch_best candidates

Note how Figs. 8.1 and 8.2 look nearly identical. This test on a known mode, such as $\Phi K^*(892)$ $h = +1$, allows us to confirm that "bmatch_best" can be used in place of "trueb".

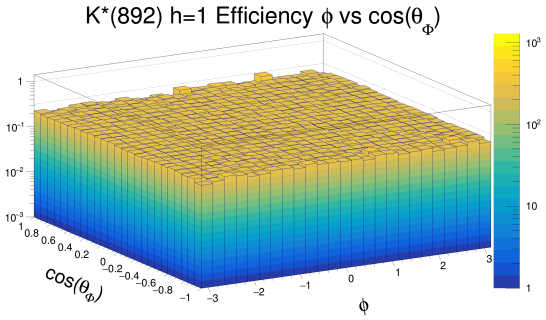

Figure 8.3: ϕ vs. $\cos(\theta_\Phi)$ efficiency for Φ $K^*(892)$ $h = +1$ trueb_best candidates.

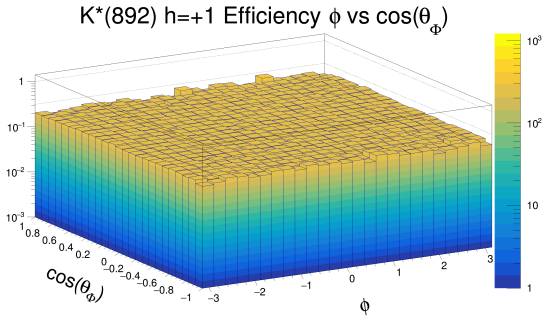

Figure 8.4: ϕ vs. $\cos(\theta_\Phi)$ efficiency for $\Phi K^*(892)$ $h = +1$ bmatch_best candidates.

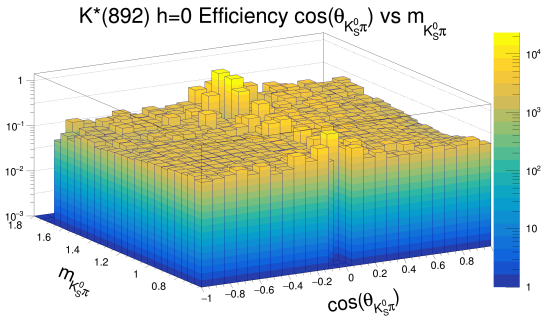

Figure 8.5: $\cos(\theta_{K^0_S\pi})$ vs. $m_{K^0_S\pi}$ efficiency for $\Phi K^*(892)$ $h = 0$ trueb_best candidates.

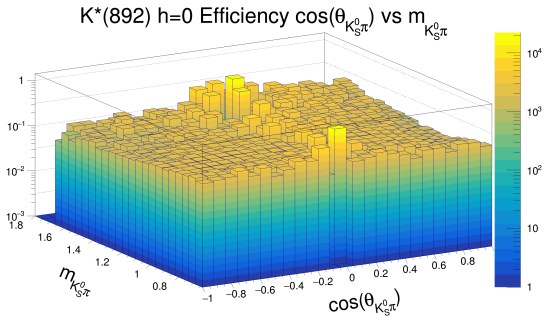

Figure 8.6: $\cos(\theta_{K^0_S\pi})$ vs. $m_{K^0_S\pi}$ efficiency for $\Phi K^*(892)$ $h = 0$ bmatch_best candidates.

In most of Figs. 8.5 through 8.117 there is a ridge at $\cos(\theta_{K^0_S\pi}) = 0$ and $\cos(\theta_\Phi) = 0$. This is an artifact of low numbers of events as seen in Figs. 6.9 and 6.10.

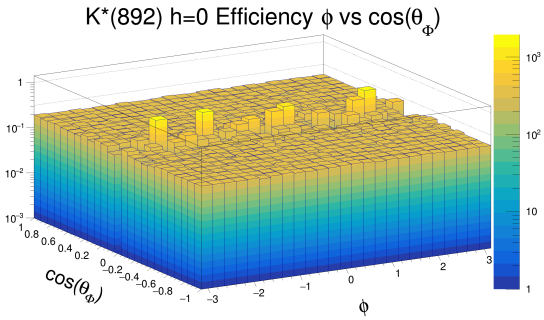

Figure 8.7: ϕ vs. $\cos(\theta_\Phi)$ efficiency for $\Phi K^*(892)$ $h = 0$ trueb_best candidates.

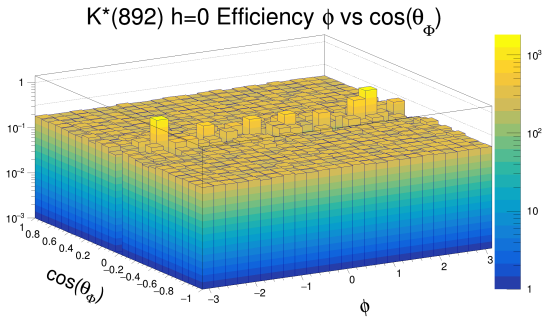

Figure 8.8: ϕ vs. $\cos(\theta_\Phi)$ efficiency for $\Phi K^*(892)$ $h = 0$ bmatch_best candidates.

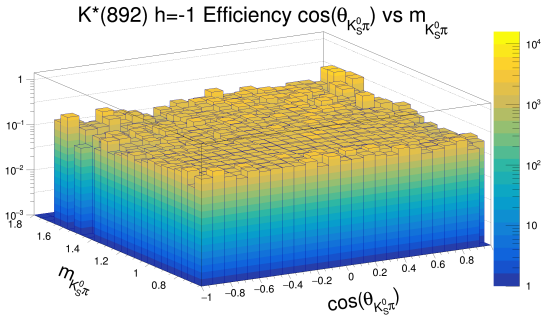

Figure 8.9: $\cos(\theta_{K^0_S\pi})$ vs. $m_{K^0_S\pi}$ efficiency for $\Phi K^*(892)$ $h = -1$ trueb_best candidates.

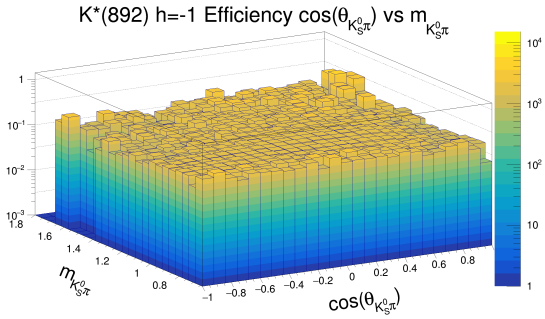

Figure 8.10: $\cos(\theta_{K^0_S\pi})$ vs. $m_{K^0_S\pi}$ efficiency for $\Phi K^*(892)$ $h = -1$ bmatch_best candidates.

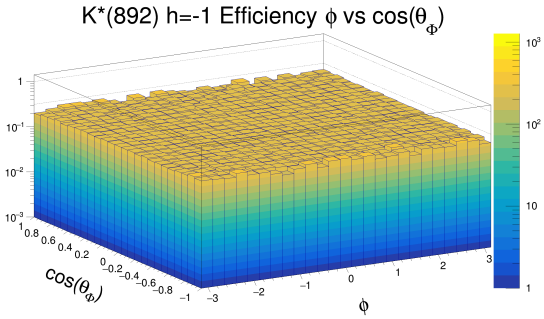

Figure 8.11: ϕ vs. $\cos(\theta_\Phi)$ efficiency for $\Phi K^*(892)$ $h = -1$ trueb_best candidates.

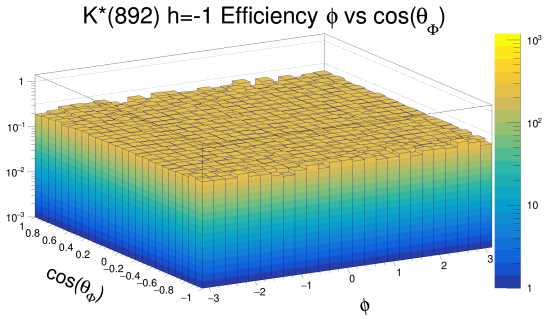

Figure 8.12: ϕ vs. $\cos(\theta_\Phi)$ efficiency for $\Phi K^*(892)$ $h = -1$ bmatch_best candidates.

8.0.2 **1D Physics Variables Plots**

In this subsection the following pages contain 1D histograms of the reconstructed ("reco") and truth ("true") variables. The reconstructed figures are comprised of sets of 3 plots each where the first plot displays the MC "as is" with all events (real and not real candidates), the second displays the best B candidate (using "bmatch_best") and the last one displays candidates that are not the true candidate B. The "truth" plots are generated from the truth table variables from the signal MC files. The 1D plots generated for the physics variables $\cos(\theta_{K^0_S\pi})$, $\cos(\theta_\Phi)$, $m_{K^0_S\pi}$, and the ϕ angle. The last plot of each variable is an efficiency drawn with the reco "bmatch_best" histogram divided by the truth histogram. All the following plots in this subsection have been created with error bars.

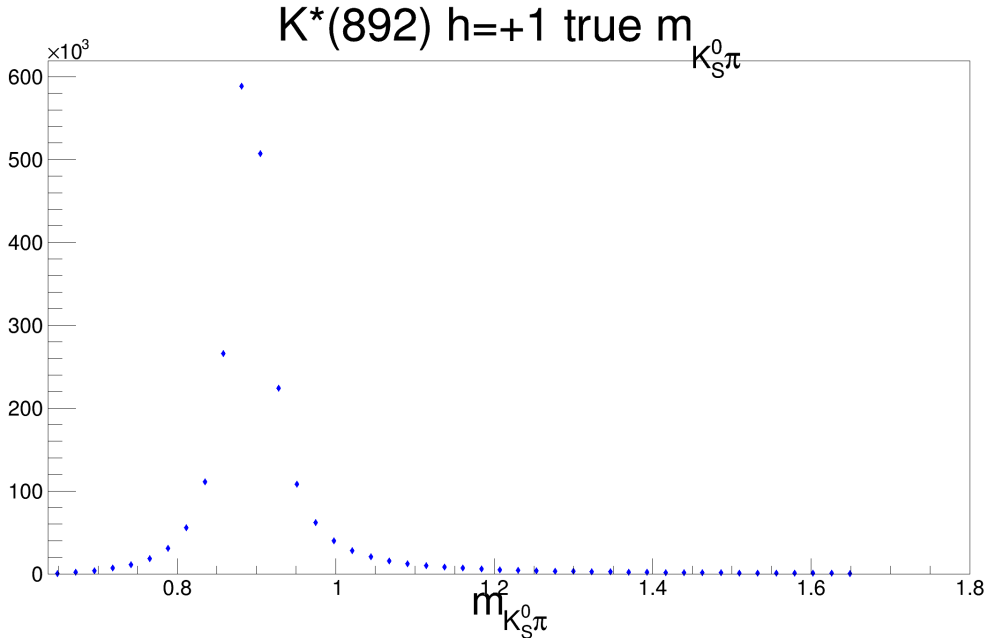

Figure 8.13: The truth $\Phi K^*(892)$ $h = +1$ $m_{K^0_S\pi}$.

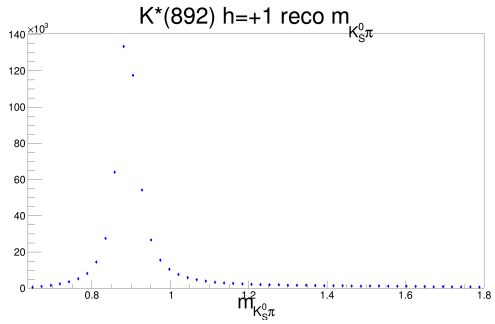

Figure 8.14: The reco $\Phi K^*(892)$ $h = +1$ $m_{K^0_S\pi}$.

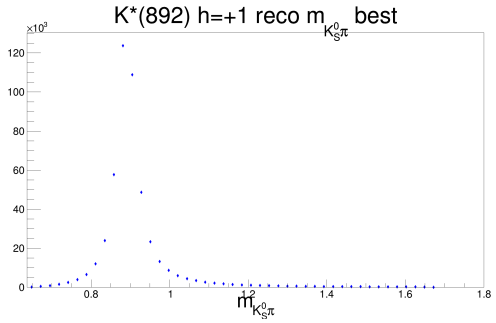

Figure 8.15: The reco $\Phi K^*(892)$ $h = +1$ $m_{K^0_S\pi}$ drawn with the bmatch_best candidate.

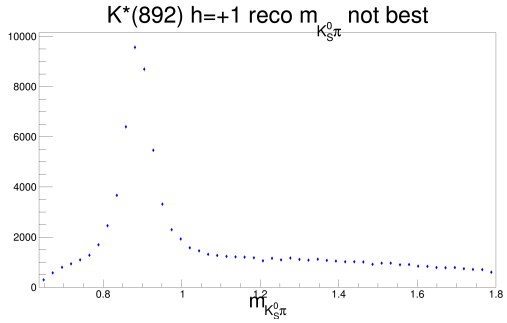

Figure 8.16: The reco $\Phi K^*(892)$ $h = +1$ $m_{K^0_S\pi}$ drawn without the bmatch_best candidate.

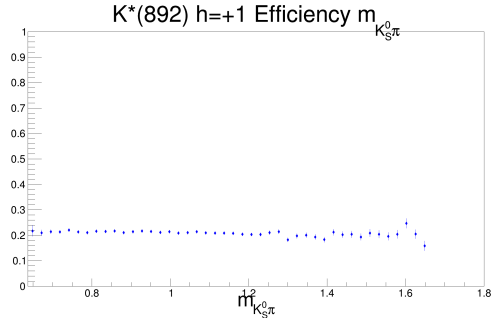

Figure 8.17: The $\Phi K^*(892)$ $h = +1$ $m_{K^0_S\pi}$ efficiency drawn with the reco bmatch_best histogram divided by the truth histogram.

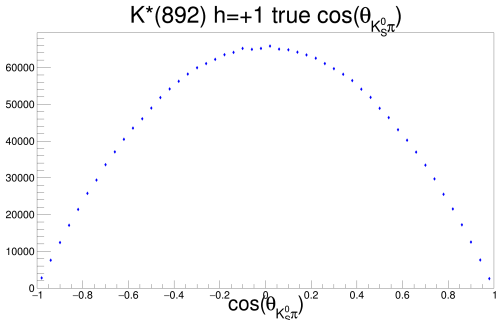

Figure 8.18: The truth $\Phi K^*(892)$ $h = +1$ $\cos(\theta_{K^0_S\pi})$.

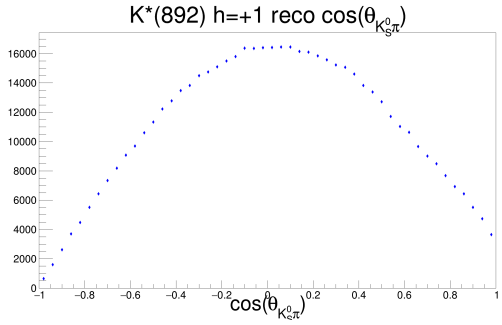

Figure 8.19: The reco $\Phi K^*(892)$ $h = +1$ $\cos(\theta_{K^0_S\pi})$.

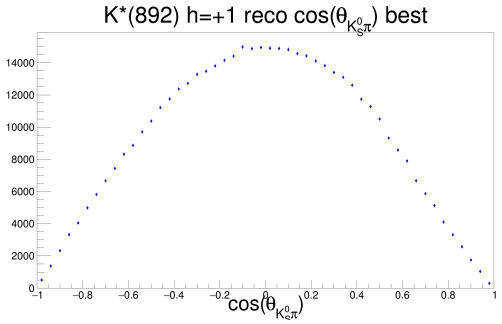

Figure 8.20: The reco $\Phi K^*(892)$ $h = +1$ $\cos(\theta_{K^0_S\pi})$ drawn with the bmatch_best candidate.

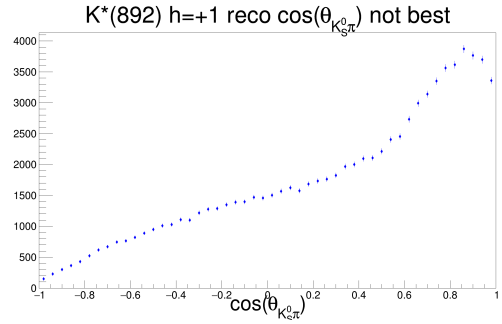

Figure 8.21: The reco $\Phi K^*(892)$ $h = +1$ $\cos(\theta_{K^0_S\pi})$ drawn without the bmatch_best candidate.

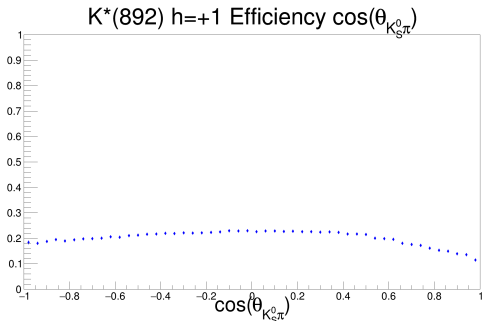

Figure 8.22: The $\Phi K^*(892)$ $h = +1$ $\cos(\theta_{K^0_S\pi})$ efficiency drawn with the reco bmatch_best histogram divided by the truth histogram.

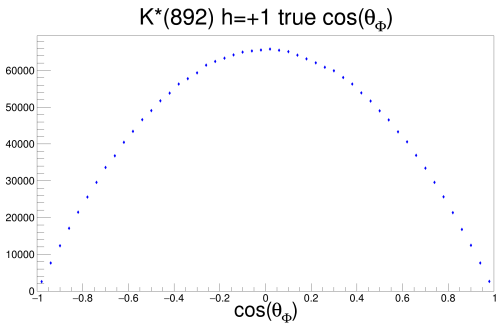

Figure 8.23: The truth $\Phi K^*(892)$ $h = +1$ $\cos(\theta_\Phi)$

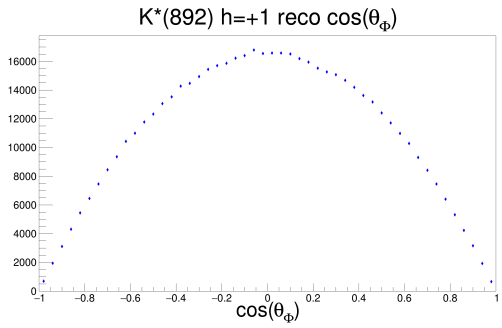

Figure 8.24: The reco$\Phi K^*(892)$ $h = +1$ $\cos(\theta_\Phi)$.

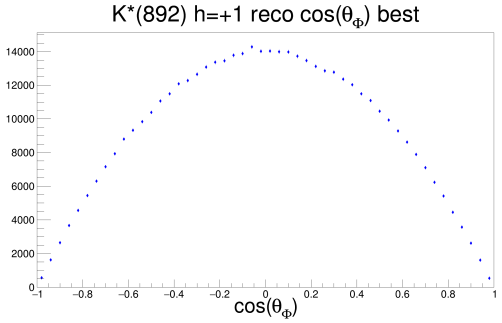

Figure 8.25: The reco $\Phi K^*(892)$ $h = +1$ $\cos(\theta_\Phi)$ drawn with the bmatch_best candidate.

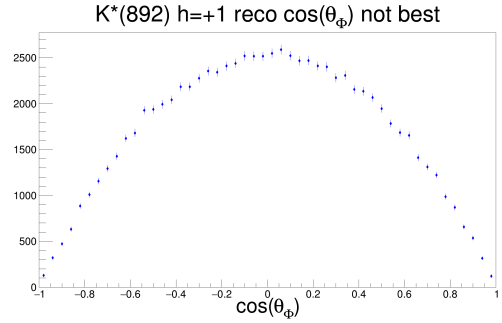

Figure 8.26: The reco $\Phi K^*(892)$ $h = +1$ $\cos(\theta_\Phi)$ drawn without the bmatch_best candidate.

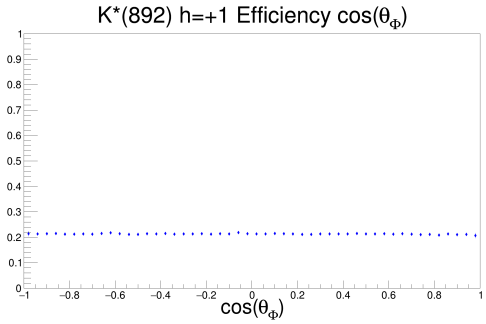

Figure 8.27: The $\Phi K^*(892)$ $h = +1$ $\cos(\theta_\Phi)$ efficiency drawn with the reco bmatch_best histogram divided by the truth histogram.

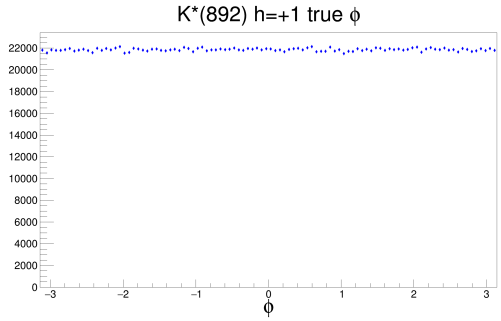

Figure 8.28: The truth $\Phi K^*(892)$ $h = +1$ ϕ angle.

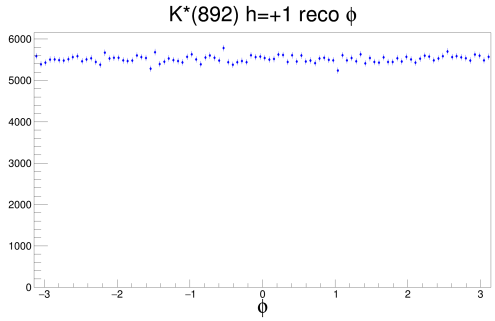

Figure 8.29: The reco $\Phi K^*(892)$ $h = +1$ ϕ angle.

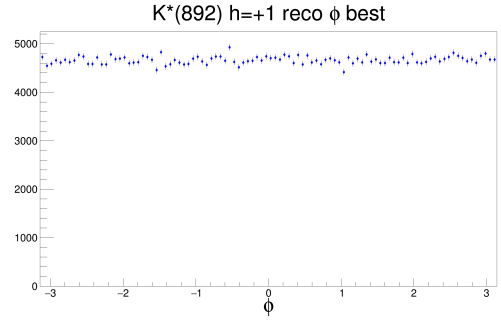

Figure 8.30: The reco $\Phi K^*(892)$ $h = +1$ ϕ angle drawn with the bmatch_best candidate.

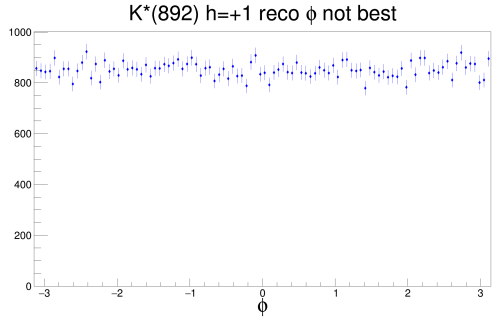

Figure 8.31: The reco $\Phi K^*(892)$ $h = +1$ ϕ angle drawn without the bmatch_best candidate.

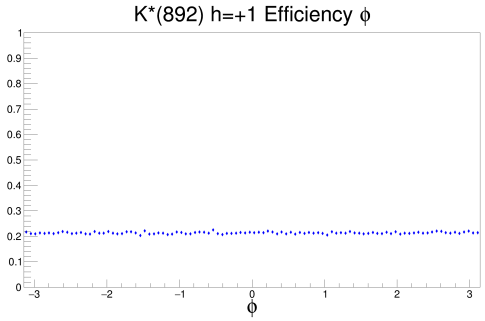

Figure 8.32: The $\Phi K^*(892)$ $h = +1$ ϕ efficiency drawn with the reco bmatch_best histogram divided by the truth histogram.

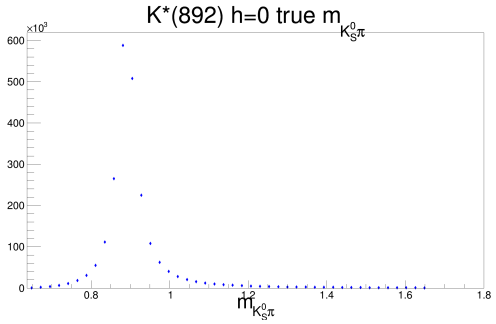

Figure 8.33: The truth $\Phi K^*(892)$ $h = 0$ $m_{K^0_S\pi}$.

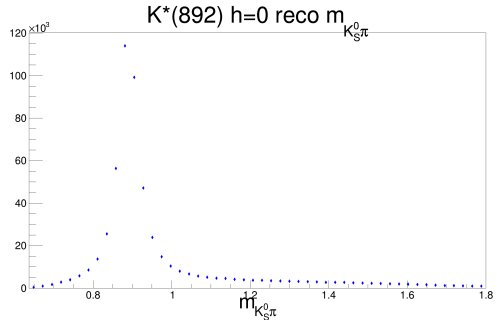

Figure 8.34: The reco $\Phi K^*(892)$ $h = 0$ $m_{K^0_S\pi}$.

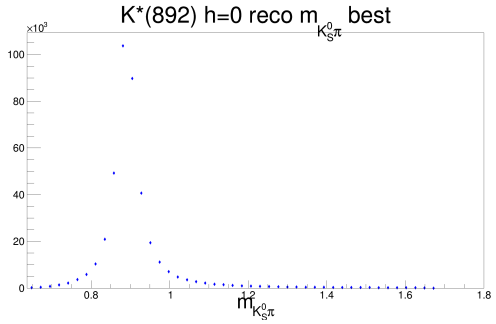

Figure 8.35: The reco $\Phi K^*(892)$ $h = 0$ $m_{K^0_S\pi}$ drawn with the bmatch_best candidate.

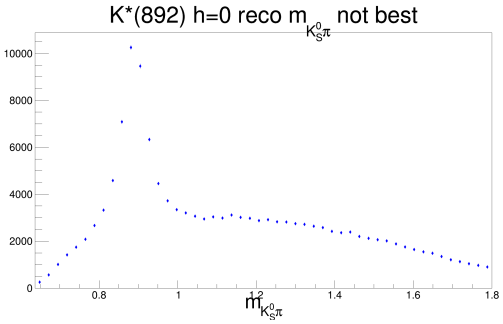

Figure 8.36: The reco $\Phi K^*(892)$ $h = 0$ $m_{K^0_S\pi}$ drawn without the bmatch_best candidate.

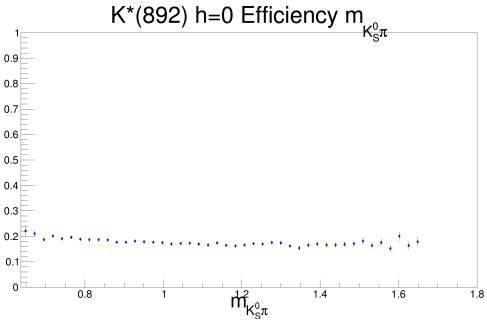

Figure 8.37: The $\Phi K^*(892)$ $h = 0$ $m_{K^0_S\pi}$ efficiency drawn with the reco bmatch_best histogram divided by the truth histogram.

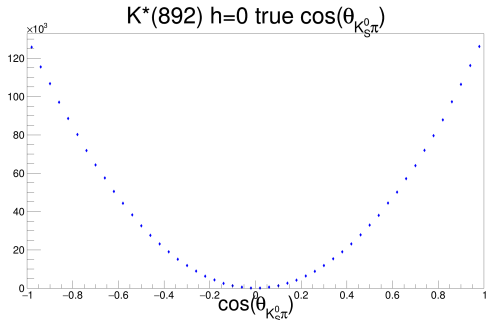

Figure 8.38: The truth $\Phi K^*(892)$ $h = 0$ $\cos(\theta_{K^0_S\pi})$.

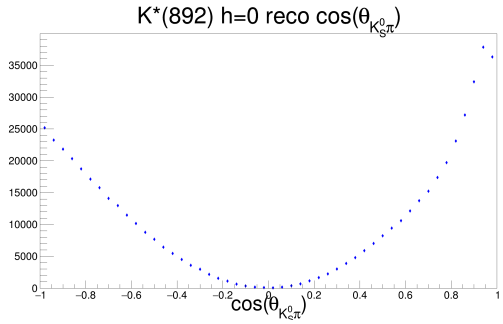

Figure 8.39: The reco $\Phi K^*(892)$ $h = 0$ $\cos(\theta_{K^0_S\pi})$.

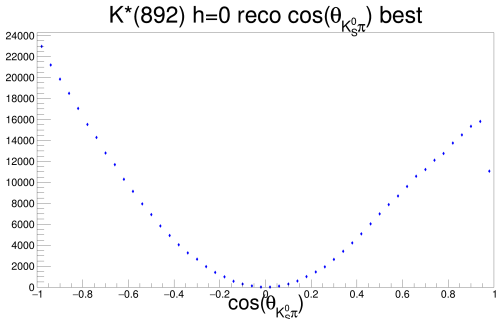

Figure 8.40: The reco $\Phi K^*(892)$ $h = 0$ $\cos(\theta_{K^0_S\pi})$ drawn with the bmatch_best candidate.

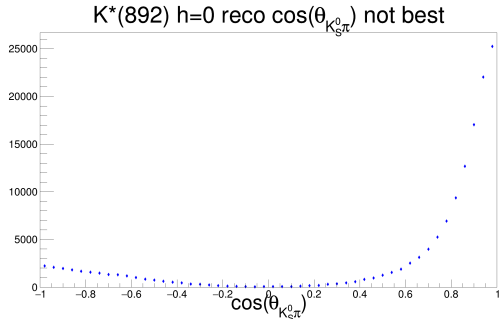

Figure 8.41: The reco $\Phi K^*(892)$ $h = 0$ $\cos(\theta_{K^0_S\pi})$ drawn without the bmatch_best candidate.

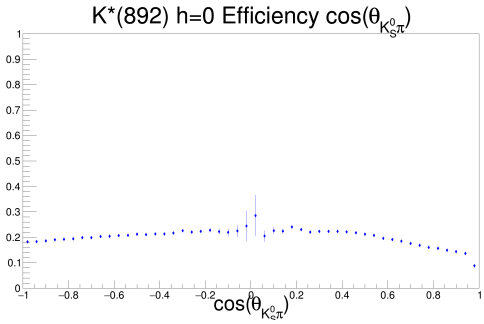

Figure 8.42: The $\Phi K^*(892)$ $h = 0$ $\cos(\theta_{K^0_S\pi})$ efficiency drawn with the reco bmatch_best histogram divided by the truth histogram.

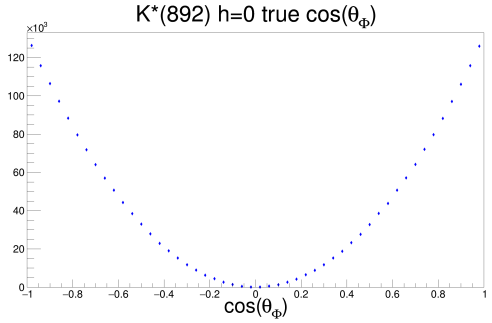

Figure 8.43: The truth $\Phi K^*(892)$ $h = 0$ $\cos(\theta_\Phi)$

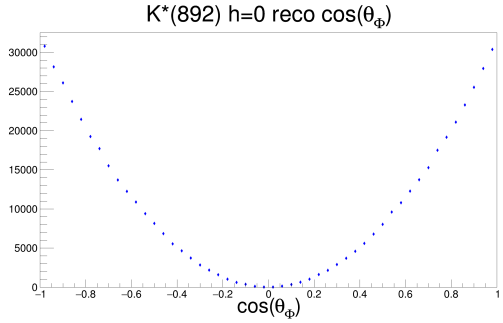

Figure 8.44: The reco$\Phi K^*(892)$ $h = 0$ $\cos(\theta_\Phi)$.

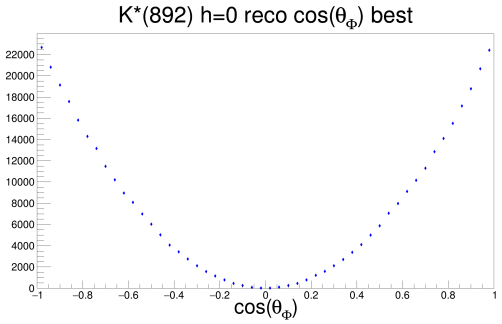

Figure 8.45: The reco $\Phi K^*(892)$ $h = 0$ $\cos(\theta_\Phi)$ drawn with the bmatch_best candidate.

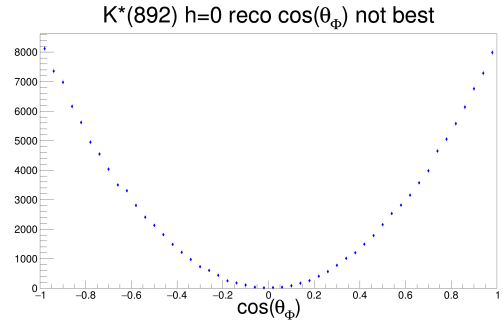

Figure 8.46: The reco $\Phi K^*(892)$ $h = 0$ $\cos(\theta_\Phi)$ drawn without the bmatch_best candidate.

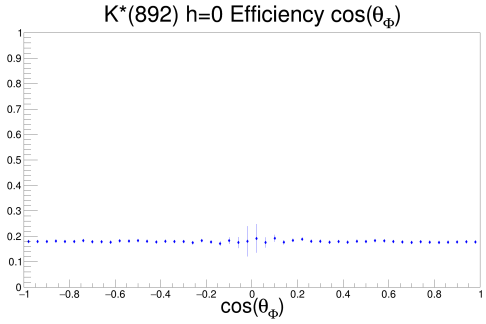

Figure 8.47: The $\Phi K^*(892)$ $h = 0$ $\cos(\theta_\Phi)$ efficiency drawn with the reco bmatch_best histogram divided by the truth histogram.

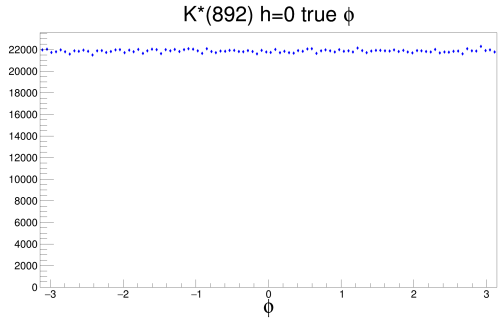

Figure 8.48: The truth $\Phi K^*(892)$ $h = 0$ ϕ angle.

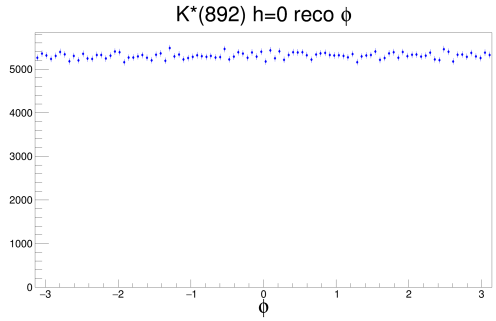

Figure 8.49: The reco $\Phi K^*(892)$ $h = 0$ ϕ angle.

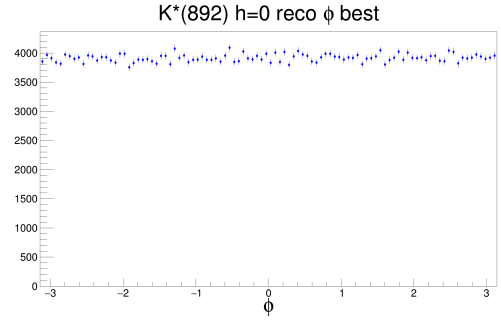

Figure 8.50: The reco $\Phi K^*(892)$ $h = 0$ ϕ angle drawn with the bmatch_best candidate.

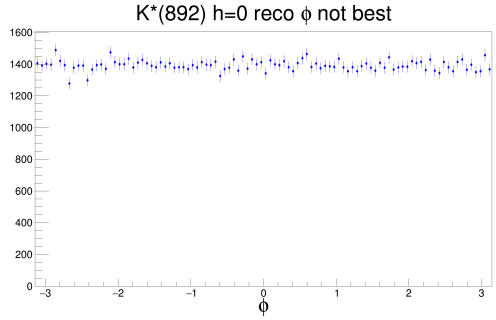

Figure 8.51: The reco $\Phi K^*(892)$ $h = 0$ ϕ angle drawn without the bmatch_best candidate.

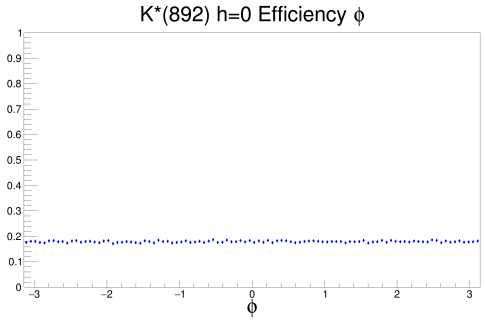

Figure 8.52: The $\Phi K^*(892)$ $h = 0$ ϕ efficiency drawn with the reco bmatch_best histogram divided by the truth histogram.

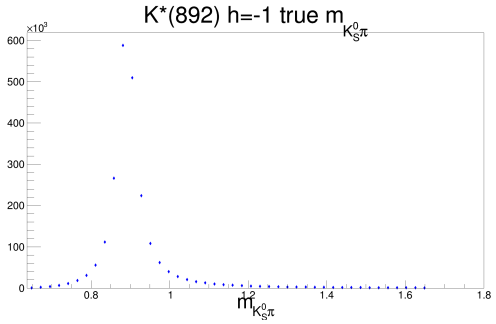

Figure 8.53: The truth $\Phi K^*(892)$ $h = -1$ $m_{K^0_S\pi}$.

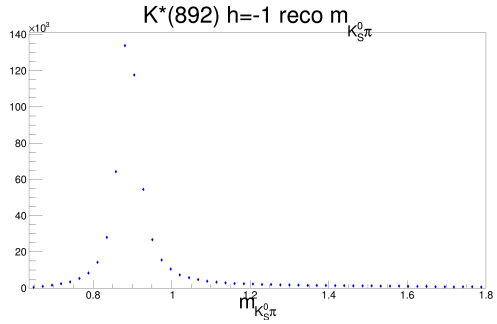

Figure 8.54: The reco $\Phi K^*(892)$ $h = -1$ $m_{K^0_S\pi}$.

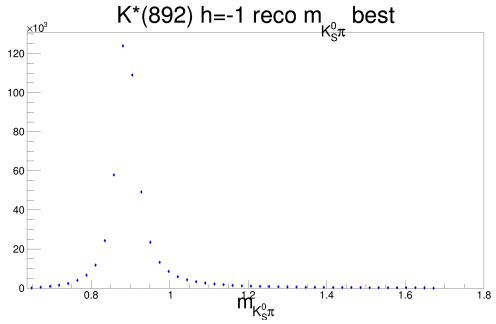

Figure 8.55: The reco $\Phi K^*(892)$ $h = -1$ $m_{K^0_S\pi}$ drawn without the bmatch_best candidate.

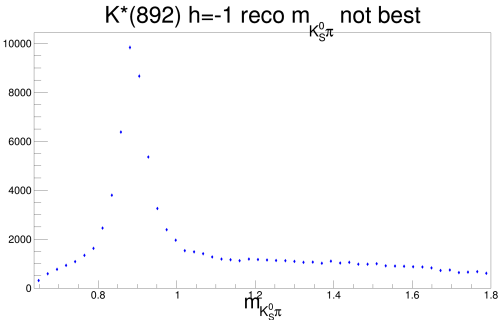

Figure 8.56: The reco $\Phi K^*(892)$ $h = -1$ $m_{K^0_S\pi}$ drawn without the bmatch_best candidate.

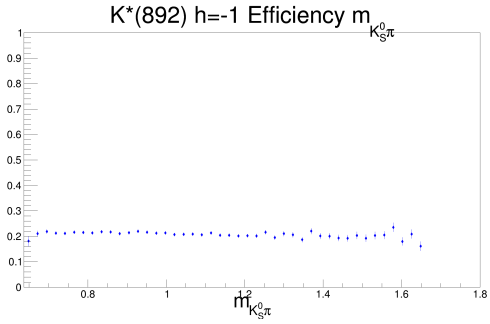

Figure 8.57: The $\Phi K^*(892)$ $h = -1$ $m_{K^0_S\pi}$ efficiency drawn with the reco bmatch_best histogram divided by the truth histogram.

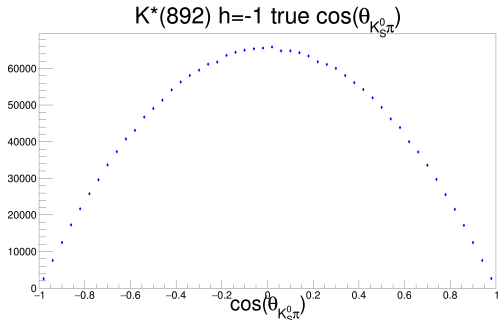

Figure 8.58: The truth $\Phi K^*(892)$ $h = -1$ $\cos(\theta_{K^0_S\pi})$.

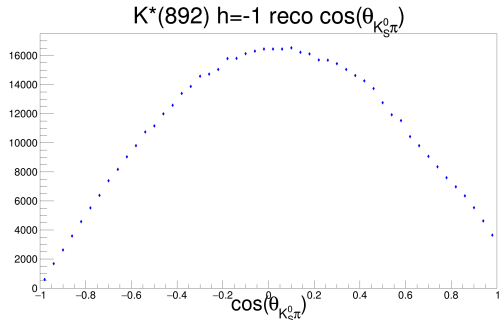

Figure 8.59: The reco $\Phi K^*(892)$ $h = -1$ $\cos(\theta_{K^0_S\pi})$.

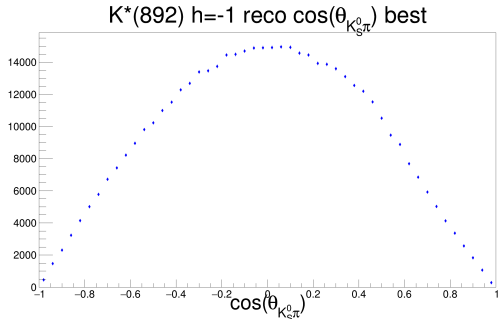

Figure 8.60: The reco $\Phi K^*(892)$ $h = -1$ $\cos(\theta_{K^0_S\pi})$ drawn with the bmatch_best candidate.

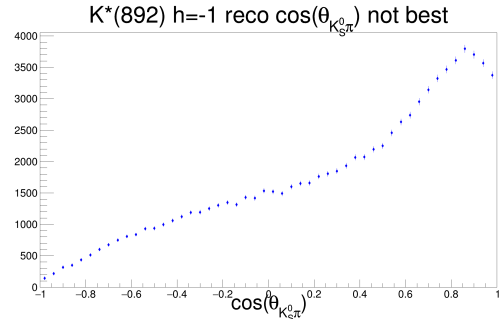

Figure 8.61: The reco $\Phi K^*(892)$ $h = -1$ $\cos(\theta_{K^0_S\pi})$ drawn without the bmatch_best candidate.

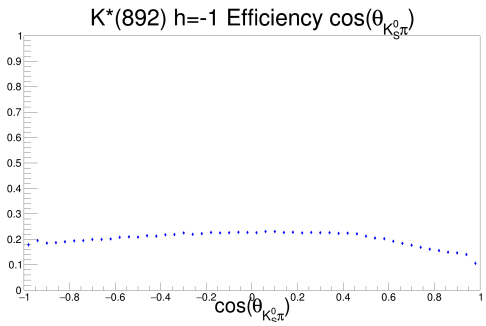

Figure 8.62: The $\Phi K^*(892)$ $h = -1$ $\cos(\theta_{K^0_S\pi})$ efficiency drawn with the reco bmatch_best histogram divided by the truth histogram.

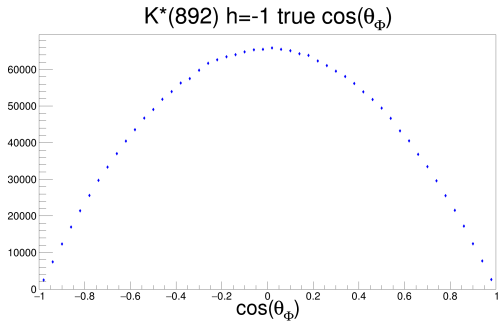

Figure 8.63: The truth $\Phi K^*(892)$ $h = -1$ $\cos(\theta_\Phi)$

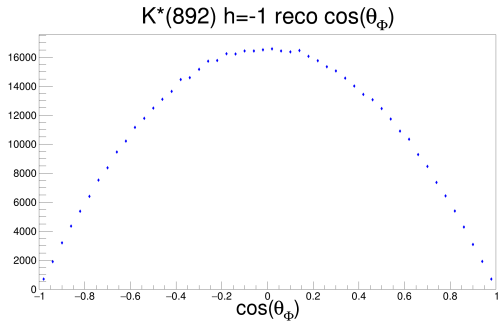

Figure 8.64: The reco $\Phi K^*(892)$ $h = -1$ $\cos(\theta_\Phi)$.

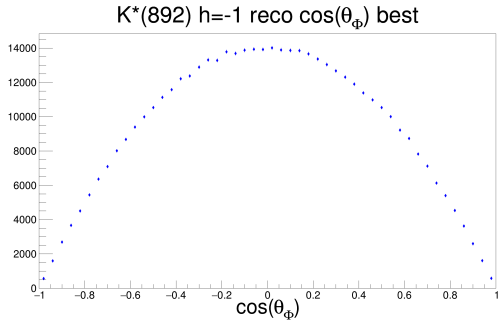

Figure 8.65: The reco $\Phi K^*(892)$ $h = -1$ $\cos(\theta_\Phi)$ drawn with the bmatch_best candidate.

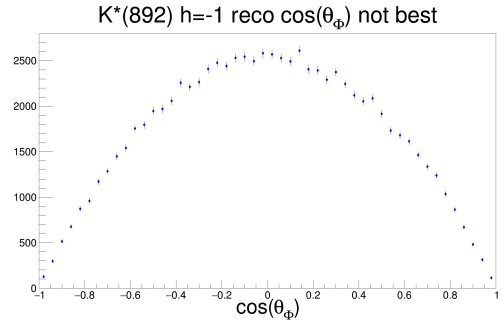

Figure 8.66: The reco $\Phi K^*(892)$ $h = -1$ $\cos(\theta_\Phi)$ drawn without the bmatch_best candidate.

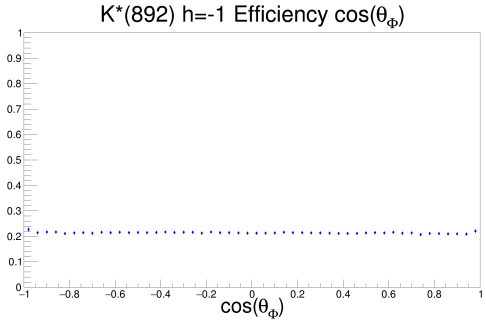

Figure 8.67: The $\Phi K^*(892)$ $h = -1$ $\cos(\theta_\Phi)$ efficiency drawn with the reco bmatch_best histogram divided by the truth histogram.

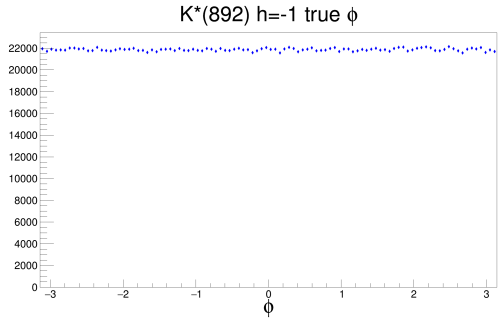

Figure 8.68: The truth $\Phi K^*(892)$ $h = -1$ ϕ angle.

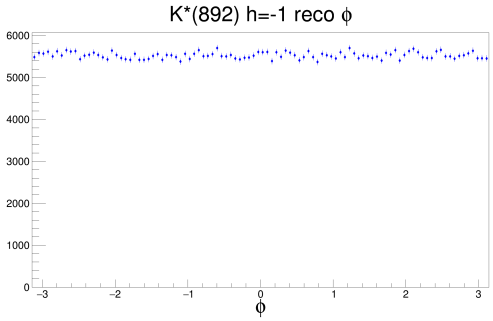

Figure 8.69: The reco $\Phi K^*(892)$ $h = -1$ ϕ angle.

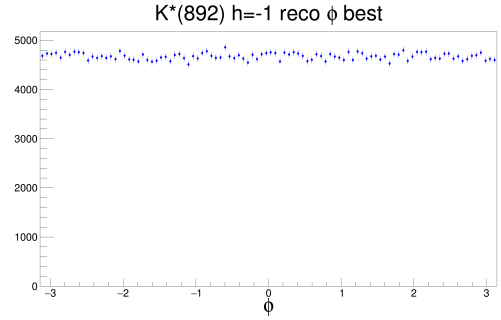

Figure 8.70: The reco $\Phi K^*(892)$ $h = -1$ ϕ angle drawn with the bmatch_best candidate.

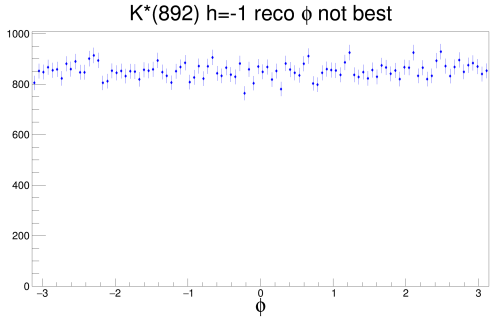

Figure 8.71: The reco $\Phi K^*(892)$ $h = -1$ ϕ angle drawn without the bmatch_best candidate.

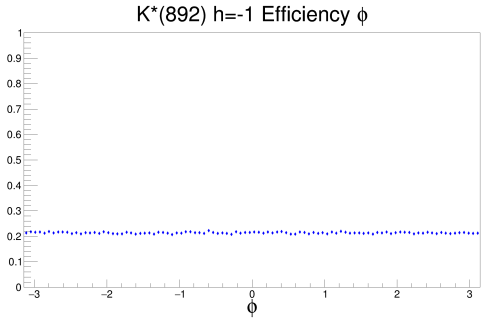

Figure 8.72: The $\Phi K^*(892)$ $h = -1$ ϕ efficiency drawn with the reco bmatch_best histogram divided by the truth histogram.

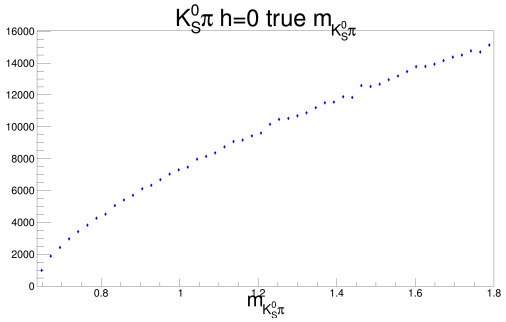

Figure 8.73: The truth $\Phi K^0_S\pi$ $h = 0$ $m_{K^0_S\pi}$.

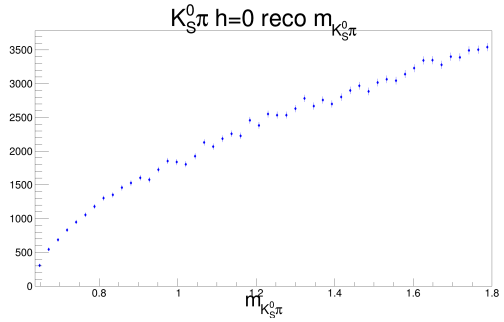

Figure 8.74: The reco $\Phi K^0_S\pi$ $h = 0$ $m_{K^0_S\pi}$.

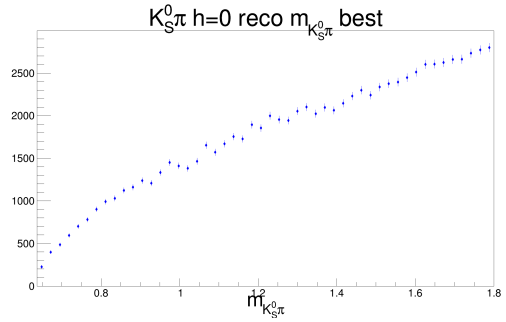

Figure 8.75: The reco $\Phi K^*(892)$ $h = 0$ $m_{K^0_S\pi}$ drawn without the bmatch_best candidate.

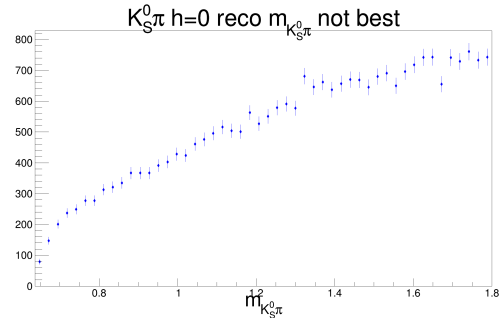

Figure 8.76: The reco $\Phi K^0_S\pi$ $h = 0$ $m_{K^0_S\pi}$ drawn without the bmatch_best candidate.

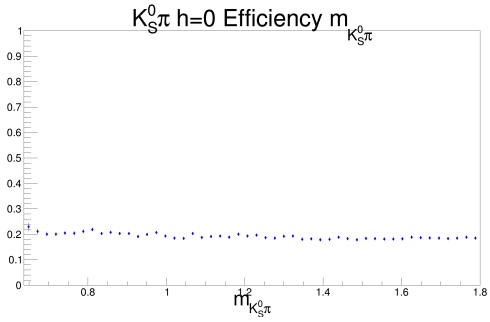

Figure 8.77: The $\Phi K^0_S\pi$ $h = 0$ $m_{K^0_S\pi}$ efficiency drawn with the reco bmatch_best histogram divided by the truth histogram.

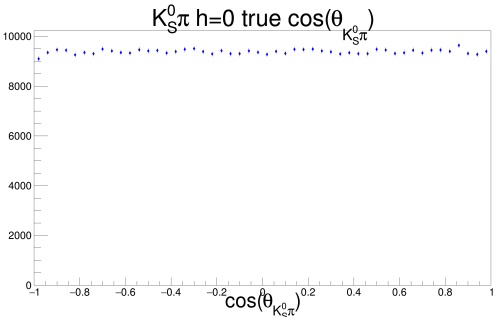

Figure 8.78: The truth $\Phi K^0_S\pi$ $h = 0$ $\cos(\theta_{K^0_S\pi})$.

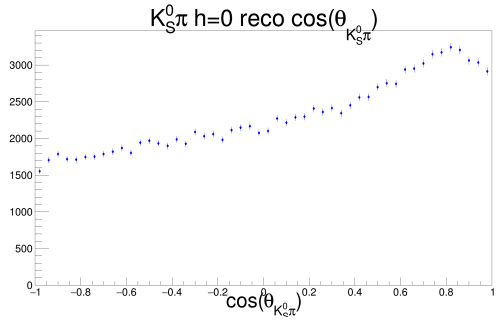

Figure 8.79: The reco $\Phi K^0_S\pi$ $h = 0$ $\cos(\theta_{K^0_S\pi})$.

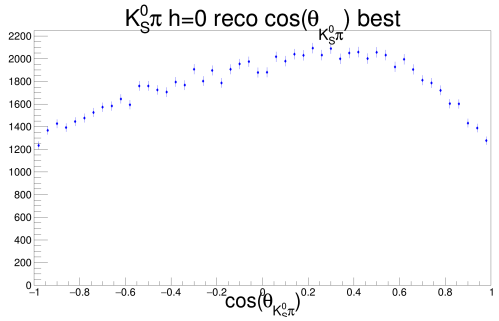

Figure 8.80: The reco $\Phi K^0_S\pi$ $h = 0$ $\cos(\theta_{K^0_S\pi})$ drawn with the bmatch_best candidate.

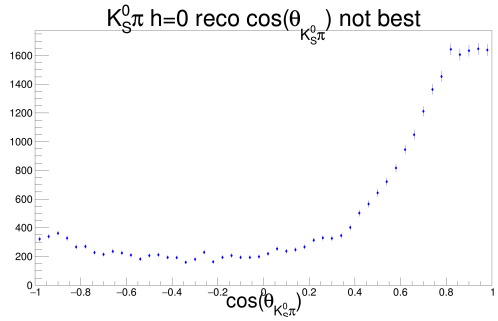

Figure 8.81: The reco $\Phi K^0_S\pi$ $h = 0$ $\cos(\theta_{K^0_S\pi})$ drawn without the bmatch_best candidate.

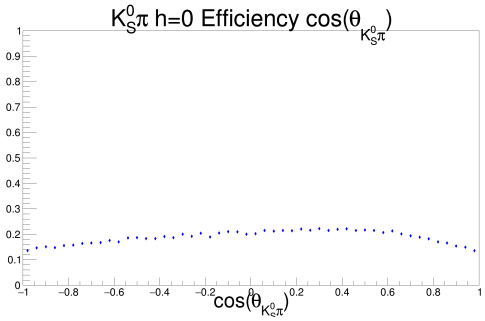

Figure 8.82: The $\Phi K^0_S\pi$ $h = 0$ $\cos(\theta_{K^0_S\pi})$ efficiency drawn with the reco bmatch_best histogram divided by the truth histogram.

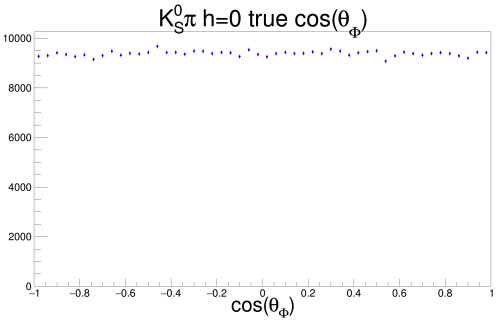

Figure 8.83: The truth $\Phi K^0_S\pi$ $h = 0$ $\cos(\theta_\Phi)$

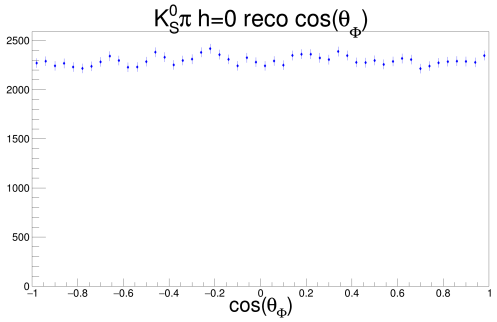

Figure 8.84: The reco$\Phi K^0_S\pi$ $h = 0$ $\cos(\theta_\Phi)$.

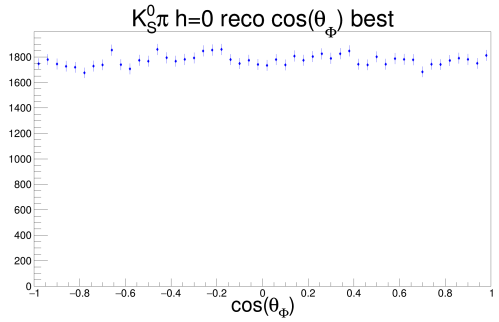

Figure 8.85: The reco $\Phi K^0_S\pi$ $h = 0$ $\cos(\theta_\Phi)$ drawn with the bmatch_best candidate.

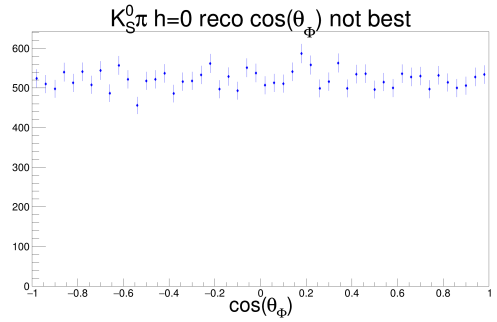

Figure 8.86: The reco $\Phi K^0_S\pi$ $h = 0$ $\cos(\theta_\Phi)$ drawn without the bmatch_best candidate.

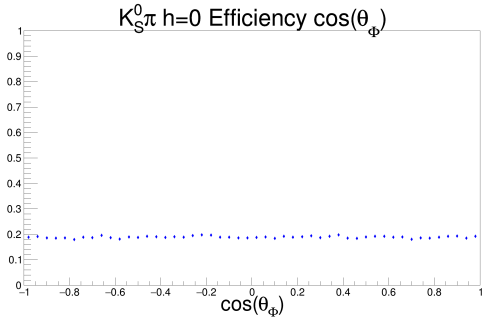

Figure 8.87: The $\Phi K^0_S\pi$ $h = 0$ $\cos(\theta_\Phi)$ efficiency drawn with the reco bmatch_best histogram divided by the truth histogram.

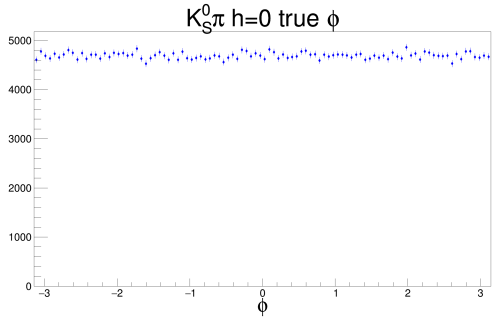

Figure 8.88: The truth $\Phi K^0_S\pi$ $h = 0$ ϕ angle.

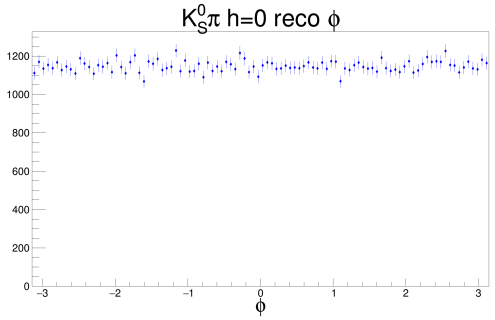

Figure 8.89: The reco $\Phi K^0_S\pi$ $h = 0$ ϕ angle.

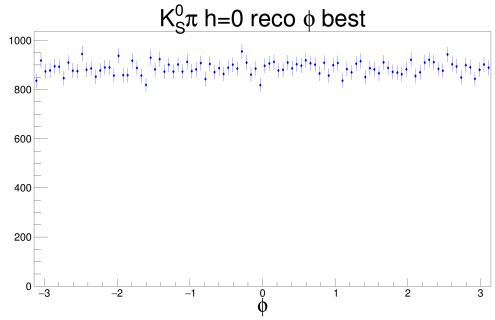

Figure 8.90: The reco $\Phi K^0_S\pi$ h=0 ϕ angle drawn with the bmatch_best candidate.

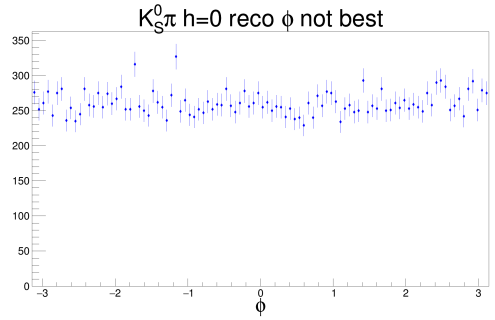

Figure 8.91: The reco $\Phi K^0_S\pi$ $h = 0$ ϕ angle drawn without the bmatch_best candidate.

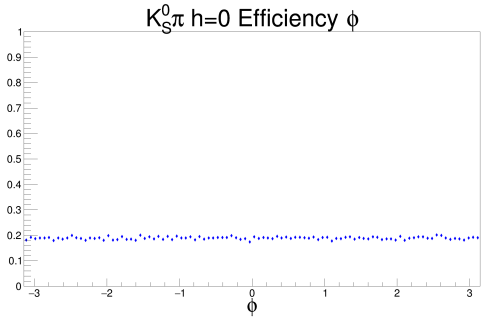

Figure 8.92: The $\Phi K^0_S\pi$ $h = 0$ ϕ efficiency drawn with the reco bmatch_best histogram divided by the truth histogram.

8.0.3 **1D Efficiency Plots**

In this subsection we show the efficiency vs. the four physics variables with the four modes (3 helicities of the $K^{*\pm}(892)$ and the $K^0_S\pi$ mode) superimposed. A close-up of these distributions can be seen in Appendix B.

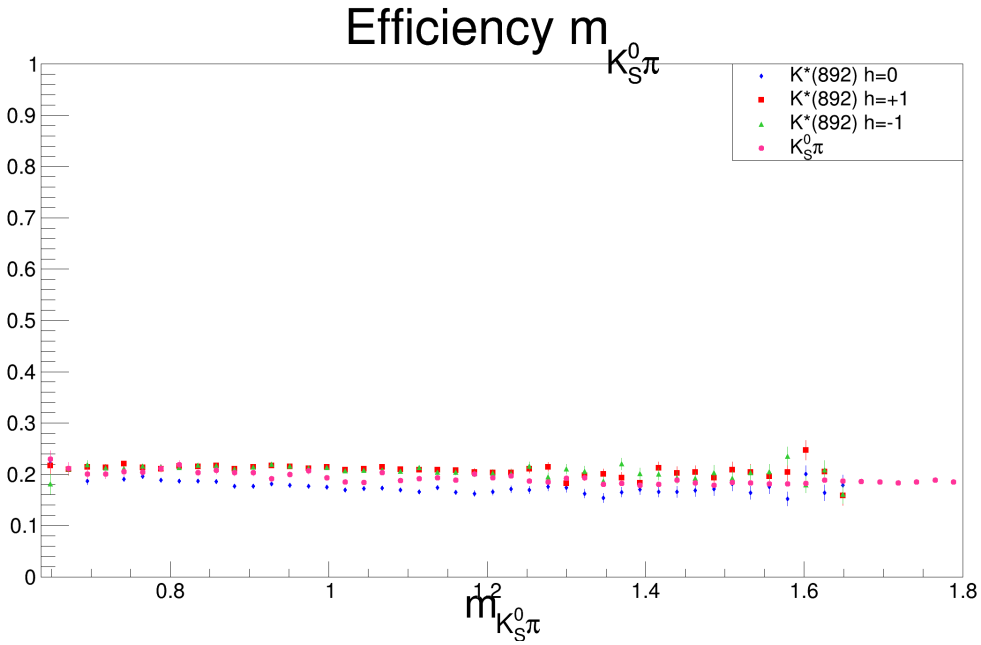

Figure 8.93: Efficiency of $m_{K^0_S\pi}$ for different decay modes.

Looking at Figs. 8.93 through 8.96 one can see for a narrow slice of variable that the efficiency does not depend much on the helicity or on the mode. Differences in Fig. 8.94 show the efficiency drops from around 5% at low $\cos\theta$ and 2% at high $\cos\theta$ to well under a percent. The spike in efficiencies and large error bars for $K^*(892)$ h = 0 at $\cos(\theta_{K^0_S\pi}) = 0$ is due to low statistics.

Since all the modes appear to have similar efficiencies, we studied the mass range of the $K^0_S\pi$ and compared it with the efficiency of the $K^*(892)$ h=+1 for the $\cos(\theta_{K^0_S\pi})$ distribution.

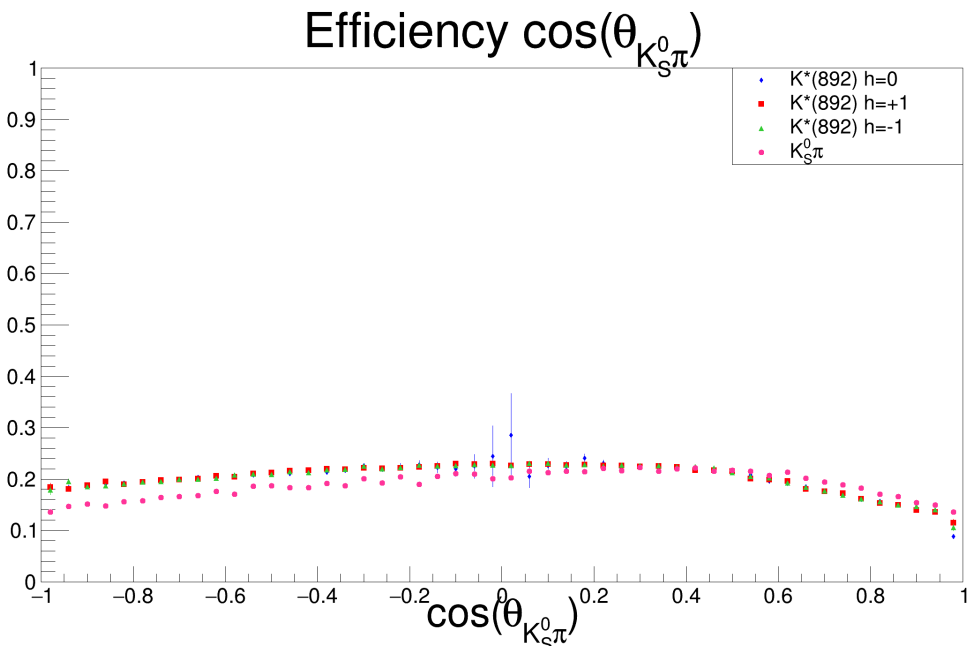

Figure 8.94: Efficiency of $\cos(\theta_{K^0_S\pi})$ for different decay modes.

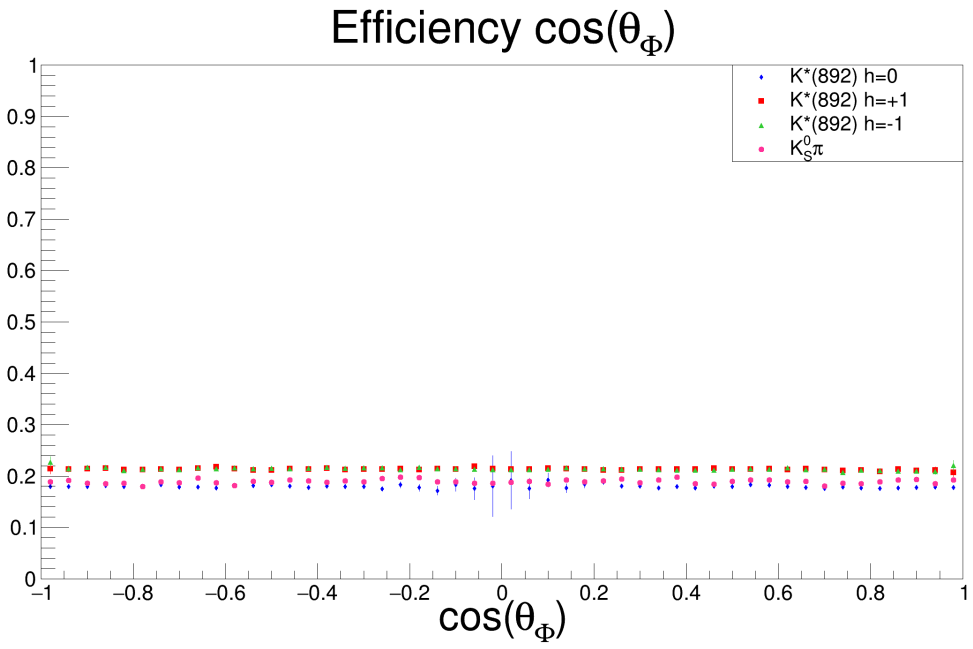

Figure 8.95: Efficiency of $\cos(\theta_\Phi)$ for different decay modes.

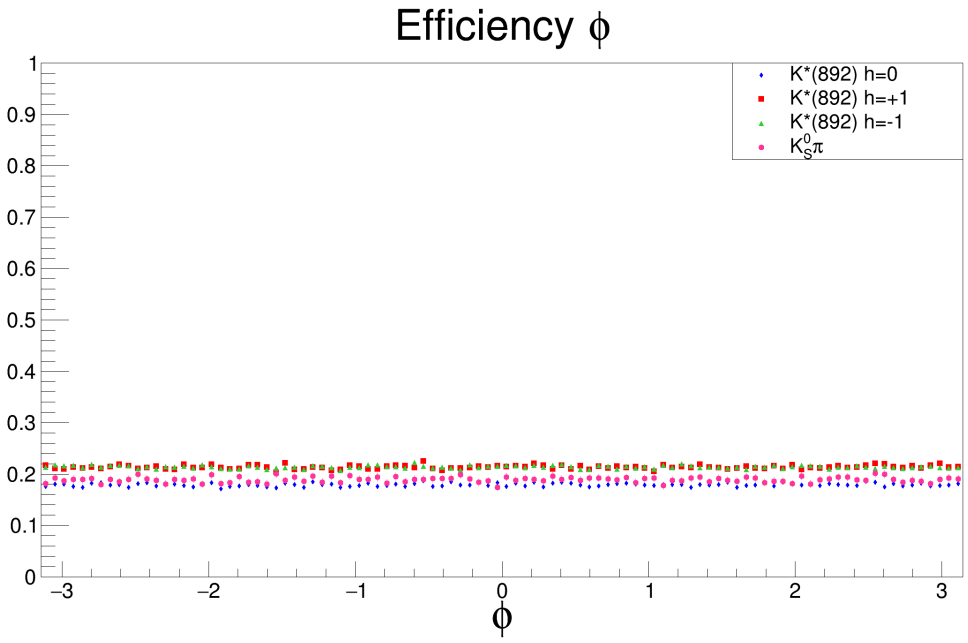

Figure 8.96: Efficiency of ϕ for different decay modes.

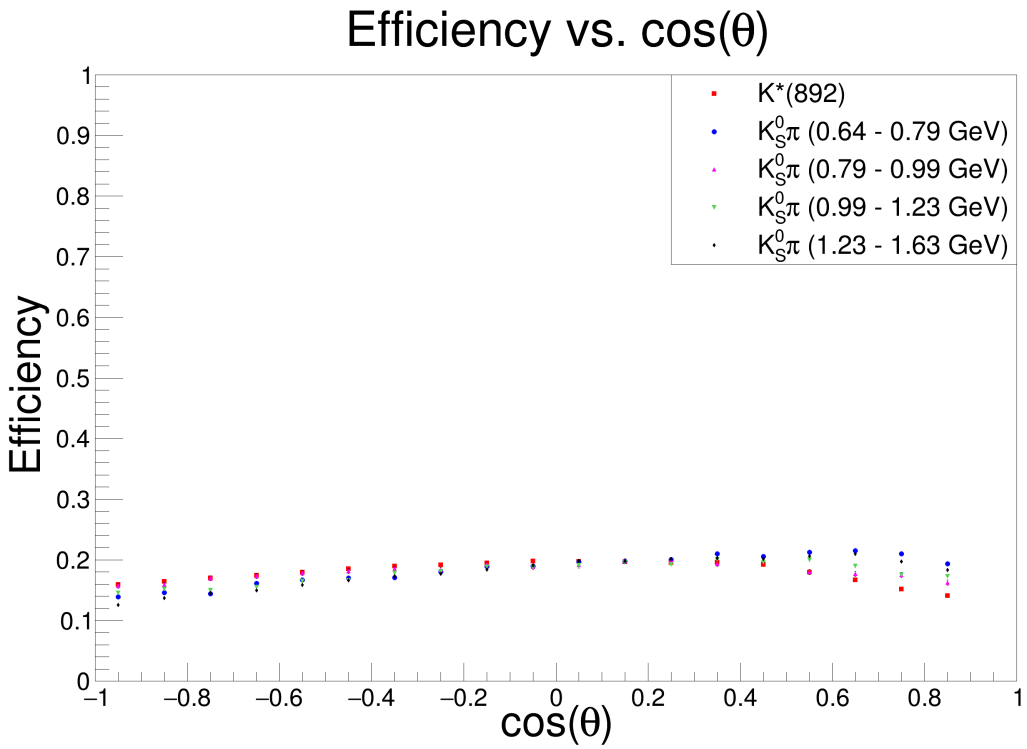

Figure 8.97: Efficiency of $\cos(\theta_{K^0_S\pi})$ for the $K^*(892)$ $h = +1$ mode and a range of masses for the $K^0_S\pi$.

In Fig. 8.97 we can see that the $K^0_S\pi$ 892 MeV mass slice efficiency is almost the same as the $K^*(892)$ MeV mass efficiency (the variance at high $\cos(\theta_{K^0_S\pi})$ will be covered using a systematic uncertainty). Thus we proceed to use the $K^0_S\pi$ mode to model the efficiency. Since the $\cos(\theta_\Phi)$ and the ϕ efficiency distributions are essentially flat, we focus on modeling the $m_{K^0_S\pi}$ and $\cos(\theta_{K^0_S\pi})$.

To model this 2-dimensional space we fit the efficiency vs. $\cos(\theta_{K^0_S\pi})$ in slices of mass. In each slice of mass we obtain 4 coefficients from fitting cubics to the distribution. Each of these coefficients is then plotted vs. the average mass of each mass slice. We then fit another set of cubics to the average of each mass slice. Thus we get the efficiency coefficient for a given mass, and those we get an efficiency for a given $cos(\theta_{K^0_S\pi})$.

The 2-dimensional efficiency function is:

$$\begin{array}{rl} \epsilon(m',c') = & (a_{00}+a_{01}m'+a_{02}m'^2+a_{03}m'^3) \\ + & (a_{10}+a_{11}m'+a_{12}m'^2+a_{13}m'^3)c' \\ + & (a_{20}+a_{21}m'+a_{22}m'^2+a_{23}m'^3)c'^2 \\ + & (a_{30}+a_{31}m'+a_{32}m'^2+a_{33}m'^3)c'^3 \end{array} \tag{8.1}$$

where $m' \equiv (m - m_0)$ and $c' \equiv (c - c_0)$ and m_0 and c_0 are chosen to be points where the efficiency curves are closest to each other (aka we picked the "origin" of the data so that our fit works for the efficiency). This is for convention and other values could have been chosen for m_0 and c_0, which would result in different coefficients.

8.0.4 **2D Plots**

This subsection contains a fraction of the 2D plots generated for the physics variables $\cos(\theta_{K^0_S\pi})$, $\cos(\theta_\Phi)$, $m_{K^0_S\pi}$, and the ϕ angle.

These plots are very critical to our understanding. Plots 8.98 and 8.99 show that the reco plot looks similar to the truth plot, except for a ridge at high $\cos(\theta_1)$. This implies that there is some self-cross-feed background (that is particles like pions in the event are being mis-labeled which leads to fake candidates). To investigate

further we divide the reco MC data into two categories (as seen in Figs. 8.100 and 8.101): the first set of events are where the "best" candidate is the one that is selected in an event (using bmatch_best) and the second figure is the distribution for events in which the "best" candidate is not picked. Notice the large ridge in Figs. 8.101 compared to 8.100. This ridge at large $\cos(\theta_1)$ arises from combinatorics. The most likely situation is pions in the event are combining with "good" ϕ and K^0_S particles from the real B. We will deal with our combinatoric background in a coming chapter which, briefly, is negligible.

Figure 8.102 shows the efficiency for the $\phi K^*(892)$ h=+1 $\cos(\theta_{K^0_S\pi})$ vs. $m_{K^0_S\pi}$ obtained by dividing the reco bmatch_best histogram by the truth histogram.

Figures 8.103 through 8.107 show the truth and reco equivalent for $\Phi K^*(892)$ helicity=1 ϕ angle vs. $\cos(\theta_\Phi)$.

The helicity=0 (in Figs. 8.108 through 8.117) version of the $cos(\theta_{K^0_S\pi})$ vs. $m_{K^0_S\pi}$ and the ϕ angle vs. $\cos(\theta_\Phi)$ shows features that are different from the helicity ±1. Most strikingly is the large dip at $\cos(\theta_{K^0_S\pi}) = 0$ and $\cos(\theta_\Phi) = 0$. This means that there are few events at $\theta_{K^0_S\pi} = 90°$ and $\theta_\Phi) = 90°$. Looking back at Fig. 6.1, we can see this means that there are very few events when K^+ moves along the path of the ϕ and when K^0_S moves along the path of its parent $K^{*\pm}$. This result is consistent with our knowledge of B-decays that they are isotropic in shape, rather than jet-like.

These plots show that the 2D space is not flat and therefore cannot be modeled by a product of 1D functions.

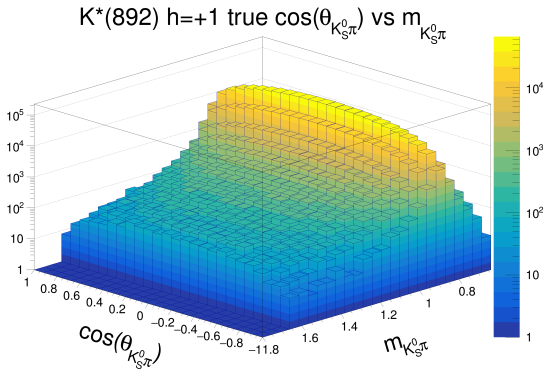

Figure 8.98: The truth $\Phi K^*(892)$ $h = 1$ $\cos(\theta_{K^0_S\pi})$ vs. $m_{K^0_S\pi}$

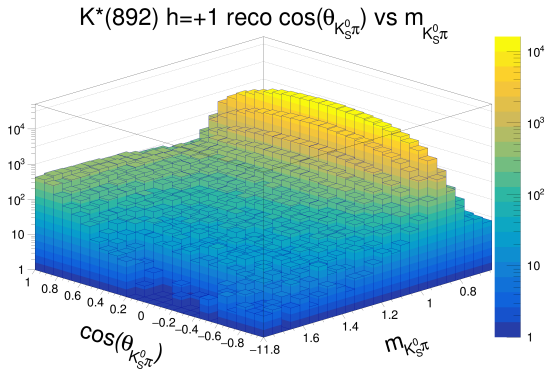

Figure 8.99: The reco $\Phi K^*(892)$ $h = 1$ $\cos(\theta_{K^0_S\pi})$ vs. $m_{K^0_S\pi}$

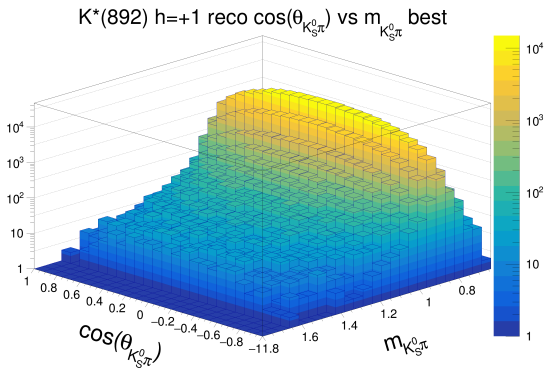

Figure 8.100: The reco $\Phi K^*(892)$ $h = 1$ $\cos(\theta_{K^0_S\pi})$ vs. $m_{K^0_S\pi}$ drawn with the bmatch_best candidate

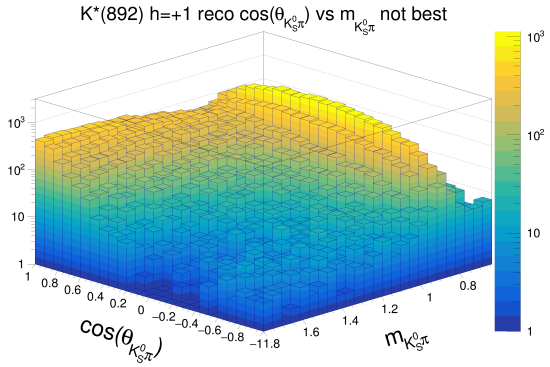

Figure 8.101: The reco $\Phi K^*(892)$ $h = 1$ $\cos(\theta_{K^0_S\pi})$ vs. $m_{K^0_S\pi}$ drawn without the bmatch_best candidate.

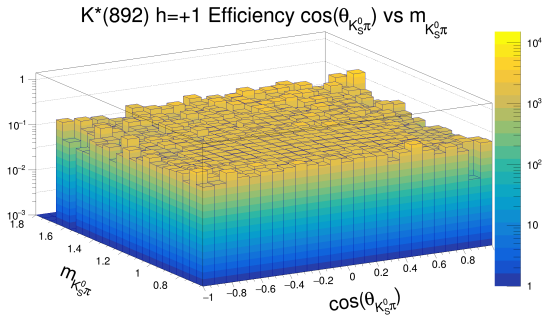

Figure 8.102: The efficiency for the $\Phi K^*(892)$ $h = 1$ $\cos(\theta_{K^0_S\pi})$ vs. $m_{K^0_S\pi}$ obtained by dividing the reco bmatch_best histogram by the truth histogram

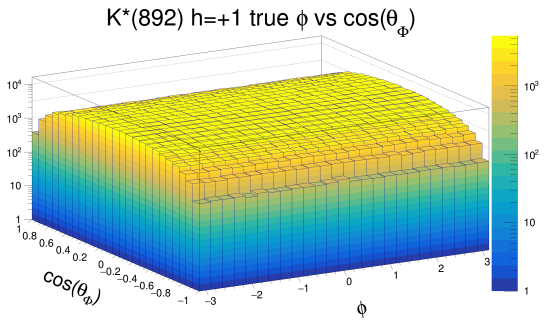

Figure 8.103: The truth $\Phi K^*(892)$ $h = 1$ ϕ angle vs. $\cos(\theta_\Phi)$.

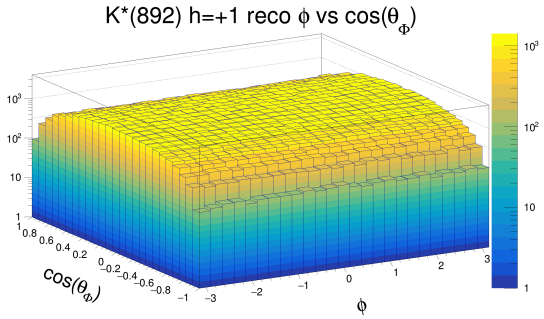

Figure 8.104: The reco $\Phi K^*(892)$ $h = 1$ ϕ angle vs. $\cos(\theta_\Phi)$.

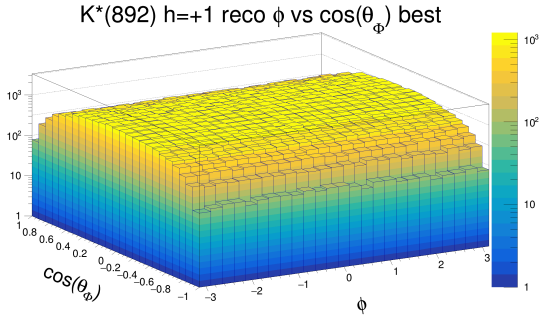

Figure 8.105: The reco $\Phi K^*(892)$ $h = 1$ ϕ angle vs. $\cos(\theta_\Phi)$ drawn without the bmatch_best candidate.

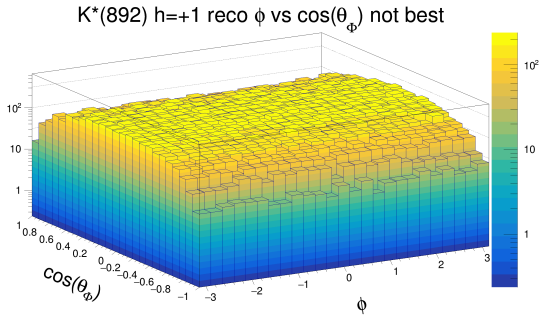

Figure 8.106: The reco $\Phi K^*(892)$ $h = 1$ ϕ angle vs. $\cos(\theta_\Phi)$ drawn without the bmatch_best candidate.

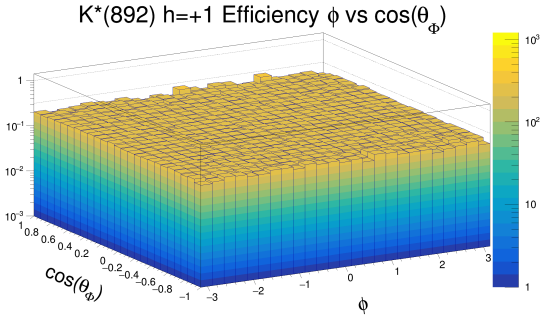

Figure 8.107: The $\Phi K^*(892)$ $h = 1$ ϕ angle vs. $\cos(\theta_\Phi)$ efficiency drawn by dividing the reco bmatch_best histogram by the truth histogram.

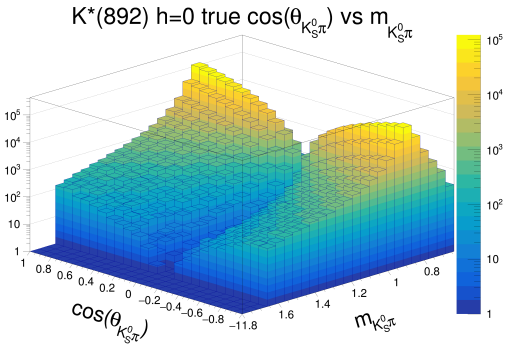

Figure 8.108: The truth $\Phi K^*(892)$ $h = 0$ $\cos(\theta_{K^0_S\pi})$ vs. $m_{K^0_S\pi}$

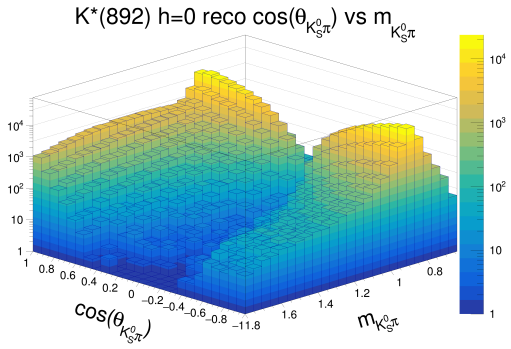

Figure 8.109: The reco $\Phi K^*(892)$ $h = 0$ $\cos(\theta_{K^0_S\pi})$ vs. $m_{K^0_S\pi}$

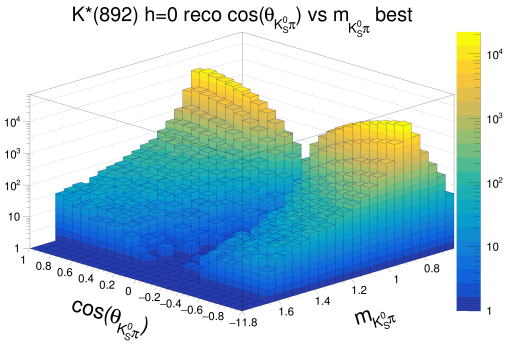

Figure 8.110: The reco $\Phi K^*(892)$ $h = 0$ $\cos(\theta_{K^0_S\pi})$ vs. $m_{K^0_S\pi}$ drawn with the bmatch_best candidate.

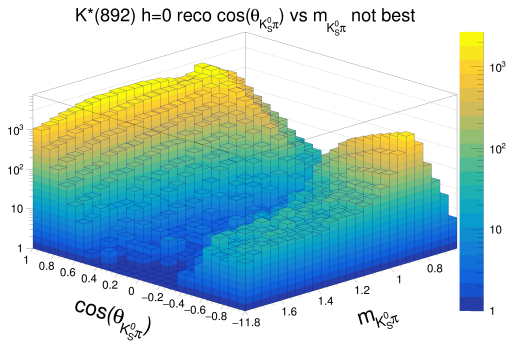

Figure 8.111: The reco $\Phi K^*(892)$ $h = 0$ $\cos(\theta_{K^0_S\pi})$ vs. $m_{K^0_S\pi}$ drawn without the bmatch_best candidate.

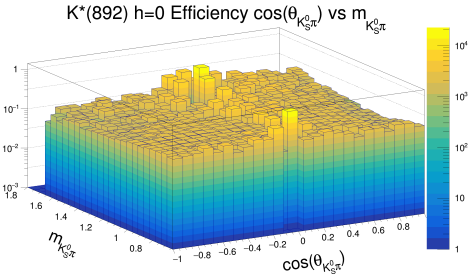

Figure 8.112: The $\Phi K^*(892)$ $h = 0$ $\cos(\theta_{K^0_S\pi})$ vs. $m_{K^0_S\pi}$ efficiency drawn by dividing the reco bmatch_best histogram by the truth histogram.

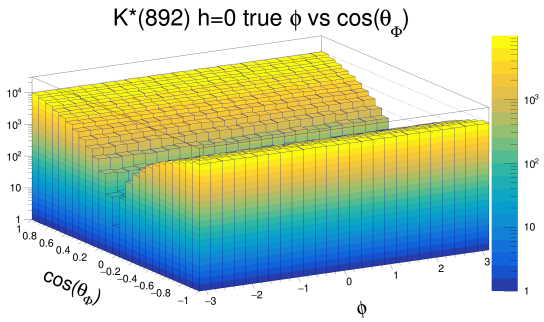

Figure 8.113: The truth $\Phi K^*(892)$ $h = 0$ ϕ angle vs. $\cos(\theta_\Phi)$.

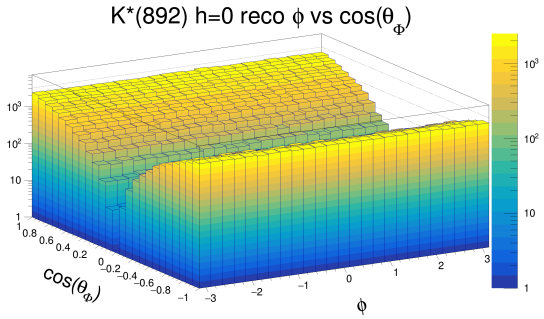

Figure 8.114: The reco $\Phi K^*(892)$ $h = 0$ ϕ angle vs. $\cos(\theta_\Phi)$.

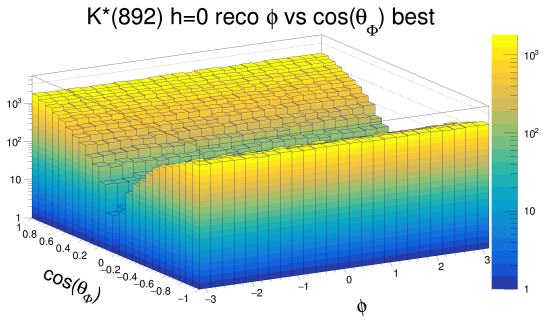

Figure 8.115: The reco $\Phi K^*(892)$ $h = 0$ ϕ angle vs. $\cos(\theta_\Phi)$ drawn without the bmatch_best candidate.

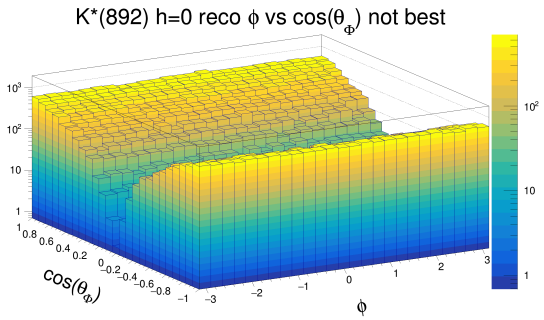

Figure 8.116: The reco $\Phi K^*(892)$ $h = 0$ ϕ angle vs. $\cos(\theta_\Phi)$ drawn without the bmatch_best candidate.

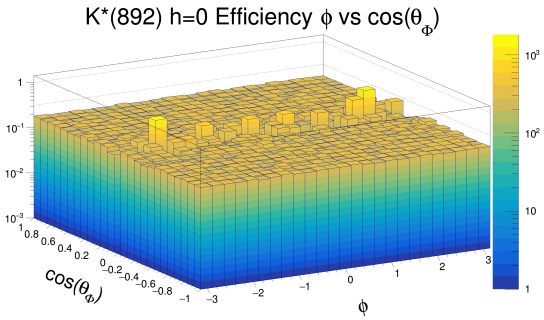

Figure 8.117: The $\Phi K^*(892)$ $h = 0$ ϕ angle vs. $\cos(\theta_\Phi)$ efficiency drawn by dividing the reco bmatch_best histogram by the truth histogram.

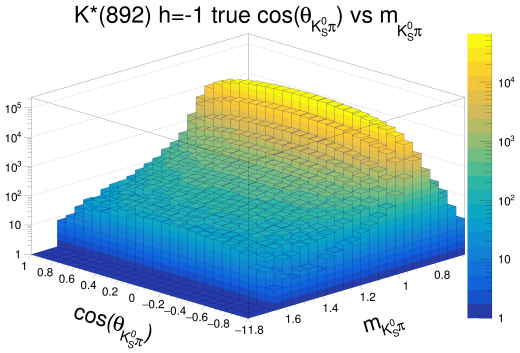

Figure 8.118: The truth $\Phi K^*(892)$ $h = -1$ $\cos(\theta_{K^0_S\pi})$ vs. $m_{K^0_S\pi}$

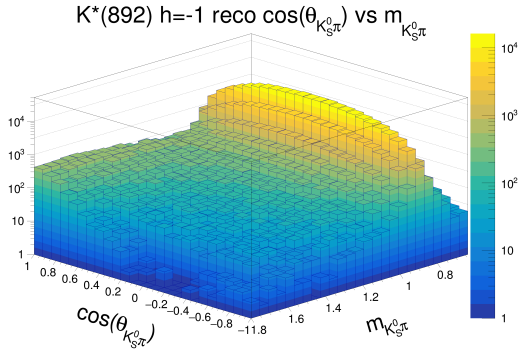

Figure 8.119: The reco $\Phi K^*(892)$ $h = -1$ $\cos(\theta_{K^0_S\pi})$ vs. $m_{K^0_S\pi}$

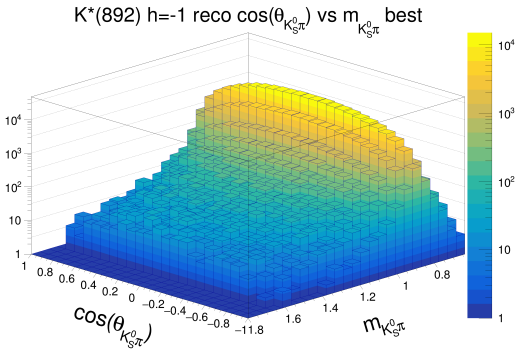

Figure 8.120: The reco $\Phi K^*(892)$ $h = -1$ $\cos(\theta_{K^0_S\pi})$ vs. $m_{K^0_S\pi}$ drawn with the bmatch_best candidate

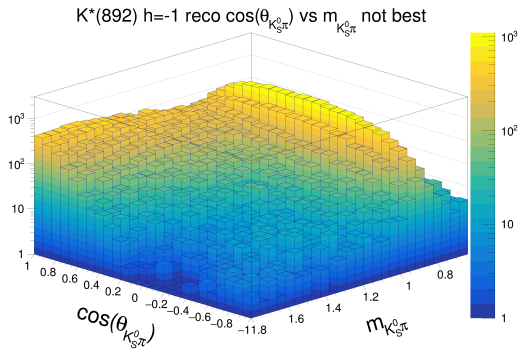

Figure 8.121: The reco $\Phi K^*(892)$ $h = -1$ $\cos(\theta_{K^0_S\pi})$ vs. $m_{K^0_S\pi}$ drawn without the bmatch_best candidate.

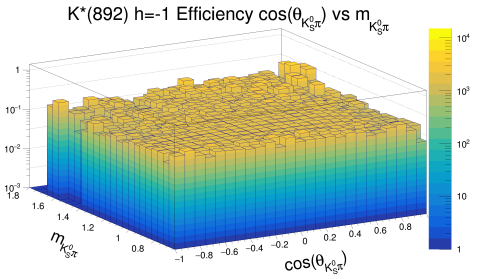

Figure 8.122: The $\Phi K^*(892)$ $h = -1$ $\cos(\theta_{K^0_S\pi})$ vs. $m_{K^0_S\pi}$ efficiency drawn by dividing the reco bmatch_best histogram by the truth histogram.

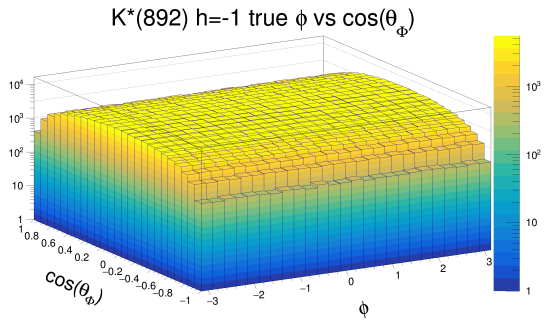

Figure 8.123: The truth $\Phi K^*(892)$ $h = -1$ ϕ angle vs. $\cos(\theta_\Phi)$.

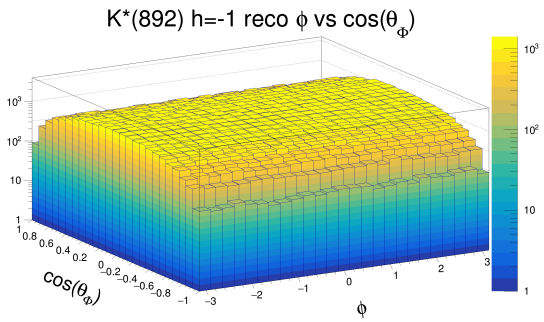

Figure 8.124: The reco $\Phi K^*(892)$ $h = -1$ ϕ angle vs. $\cos(\theta_\Phi)$.

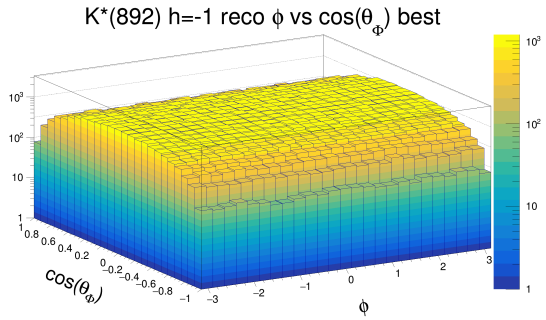

Figure 8.125: The reco $\Phi K^*(892)$ $h = -1$ ϕ angle vs. $\cos(\theta_\Phi)$ drawn without the bmatch_best candidate.

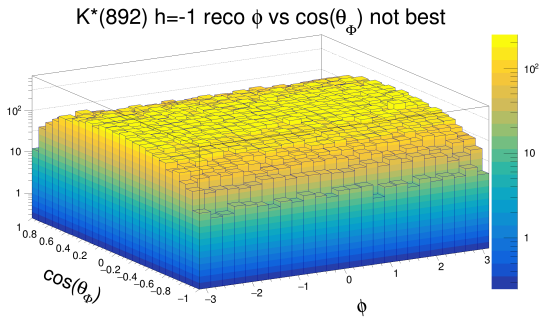

Figure 8.126: The reco $\Phi K^*(892)$ $h = -1$ ϕ angle vs. $\cos(\theta_\Phi)$ drawn without the bmatch_best candidate.

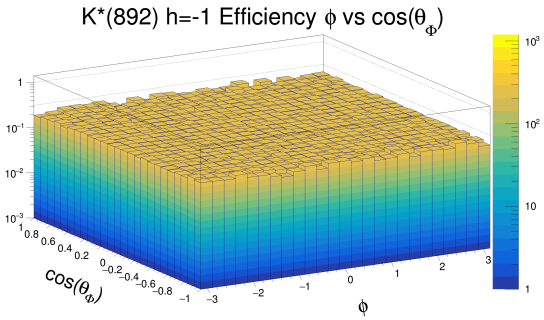

Figure 8.127: The $\Phi K^*(892)$ $h = -1$ ϕ angle vs. $\cos(\theta_\Phi)$ efficiency drawn by dividing the reco bmatch_best histogram by the truth histogram.

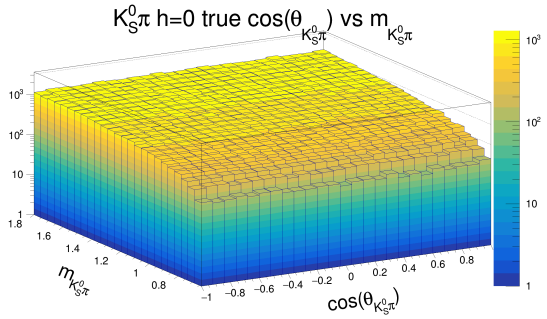

Figure 8.128: The truth $\Phi K^0_S\pi$ $\cos(\theta_{K^0_S\pi})$ vs. $m_{K^0_S\pi}$

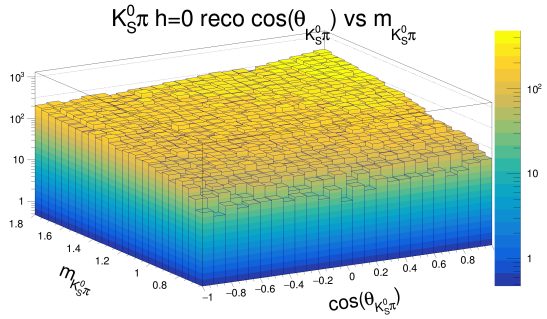

Figure 8.129: The reco $\Phi K^0_S\pi$ $\cos(\theta_{K^0_S\pi})$ vs. $m_{K^0_S\pi}$

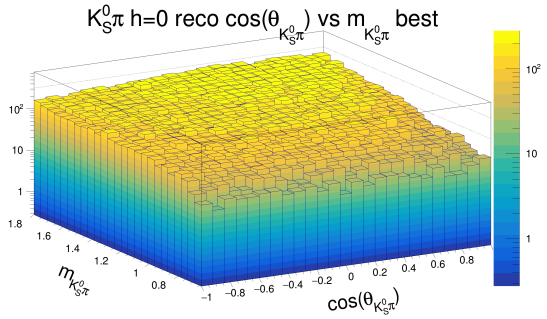

Figure 8.130: The reco $\Phi K^0_S\pi$ $\cos(\theta_{K^0_S\pi})$ vs. $m_{K^0_S\pi}$ drawn with the bmatch_best candidate

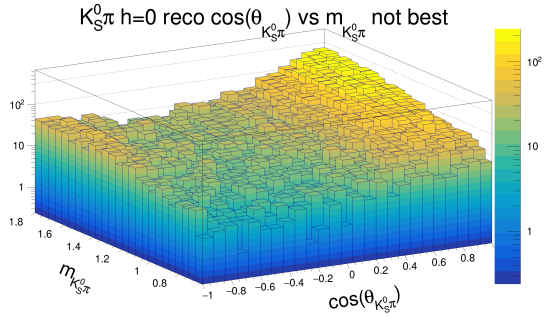

Figure 8.131: The reco $\Phi K^0_S\pi$ $\cos(\theta_{K^0_S\pi})$ vs. $m_{K^0_S\pi}$ drawn without the bmatch_best candidate.

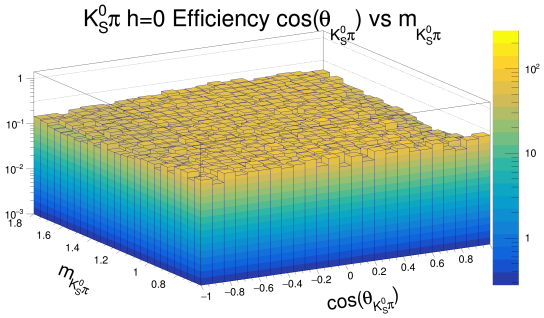

Figure 8.132: The $\Phi K^0_S\pi$ $\cos(\theta_{K^0_S\pi})$ vs. $m_{K^0_S\pi}$ efficiency drawn by dividing the reco bmatch_best histogram by the truth histogram.

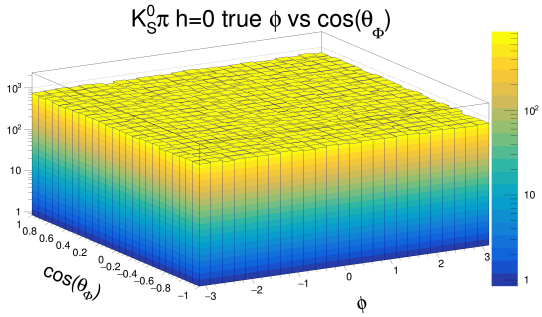

Figure 8.133: The truth $\Phi K^0_S\pi$ ϕ angle vs. cos(θ_Φ).

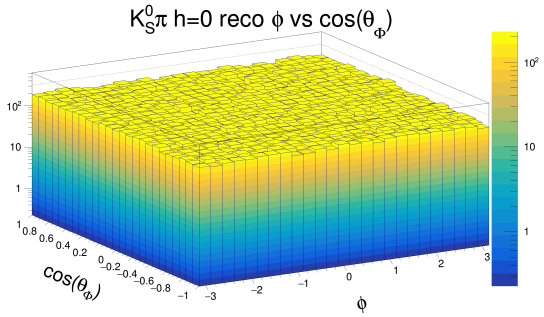

Figure 8.134: The reco $\Phi K^0_S\pi$ ϕ angle vs. cos(θ_Φ).

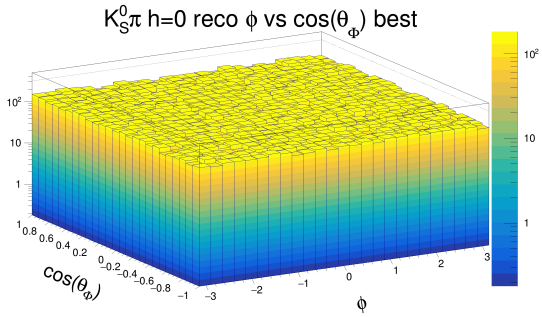

Figure 8.135: The reco $\Phi K^0_S\pi$ ϕ angle vs. cos(θ_Φ) drawn without the bmatch_best candidate.

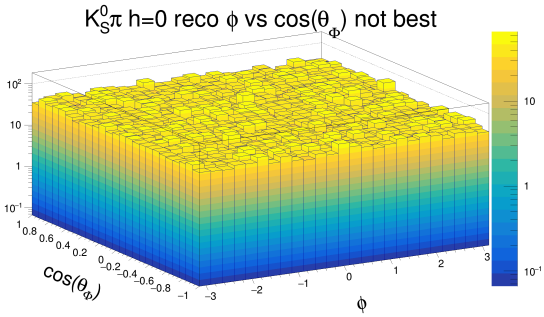

Figure 8.136: The reco $\Phi K^0_S\pi$ ϕ angle vs. cos(θ_Φ) drawn without the bmatch_best candidate.

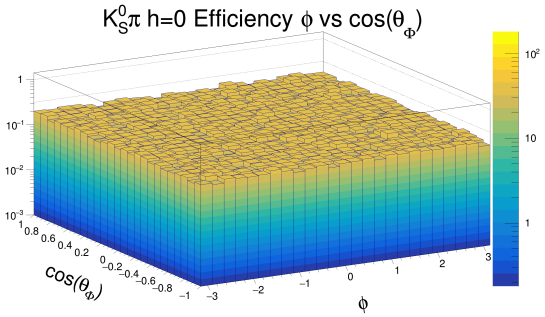

Figure 8.137: The $\Phi K^0_S\pi$ ϕ angle vs. cos(θ_Φ) efficiency drawn by dividing the reco bmatch_best histogram by the truth histogram

8.0.5 **Migration of Events**

This next subsection attempts to explain the ridges at high $\cos(\theta_{K^0_S\pi})$ in the 2D plots of the preceding subsection. To do this we create a "migration" plot in which we plot the path of the variables from the Evtgen stage to the reconstruction stage. We took a random sample of candidates for each mode that were not matched by the true B candidate and created a vector symbol that started at the Evtgen stage and pointed to the reco position. Fig. 8.138 for example maps the vectors for a random number of $B^{\pm} \to \phi(K^0_S\pi)^{\pm}_0$ not matched candidates, where blue arrows represent events moving to a location $>$ 1.1 GeV and red arrows are for events moving to a location $<$ 1.1 GeV.

The Belle neutral mode analysis cut out this background by making the cut $\cos(\theta_{K^0_S\pi}) < 0.75$. The authors called this as a self cross-feed background created by the swapping of a signal pion with some other pion in the event. The cut was made in order to cut out the peaking background at $\cos(\theta_{K^0_S\pi}) = 0.80$.

To avoid this background we use the same cut. The efficiencies finally used (and parameterized as described earlier) were after all cuts, including this cut.

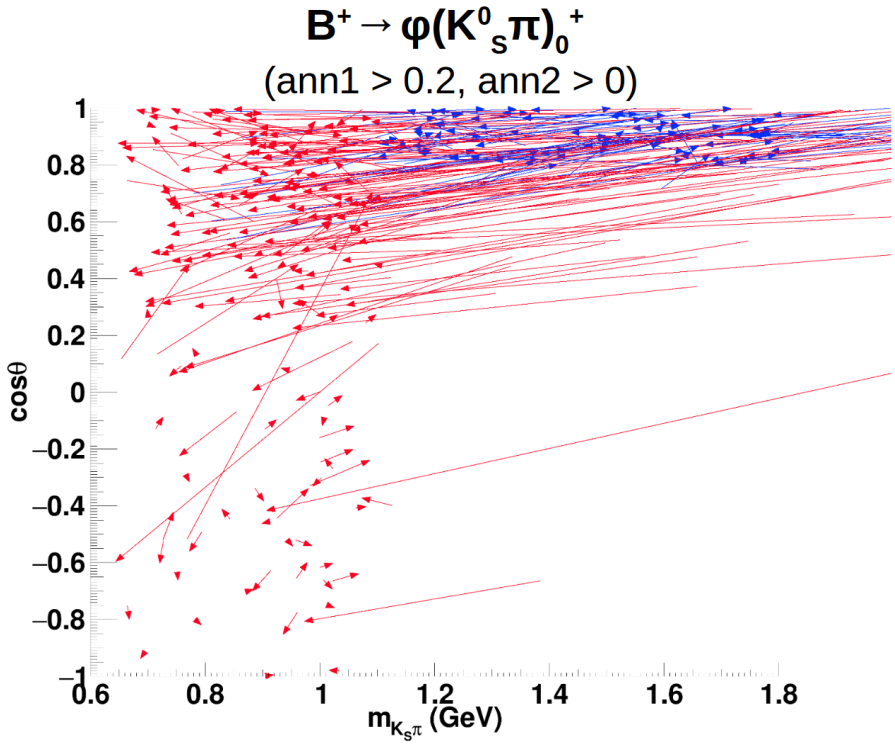

Figure 8.138: Migration vectors for a few $B^{\pm} \to \phi(K^0_S\pi)^{\pm}_0$ not-matched candidates. Blue arrows represent events moving to a location > 1.1 GeV and red arrows are for events moving to a location < 1.1 GeV.

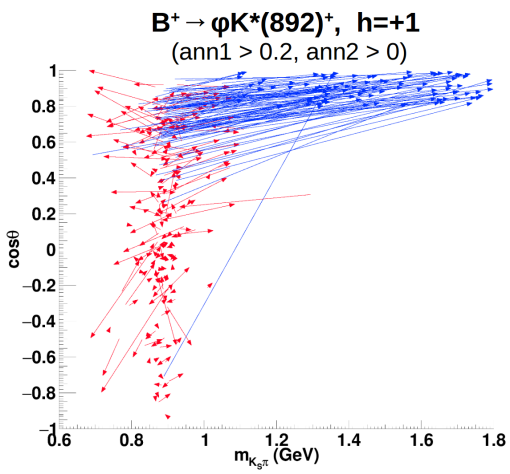

Figure 8.139: Migration vectors for a random number of $B^{\pm} \rightarrow \phi K^{*}(892)^{\pm}$ $h = +1$ not matched candidates.

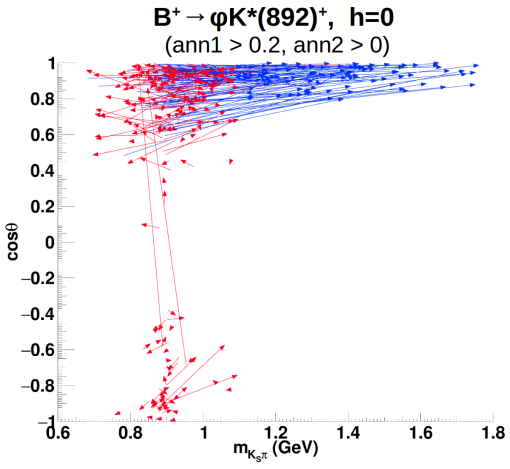

Figure 8.140: Migration vectors for a random number of $B^{\pm} \rightarrow \phi K^{*}(892)^{\pm}$ $h = 0$ not matched candidates.

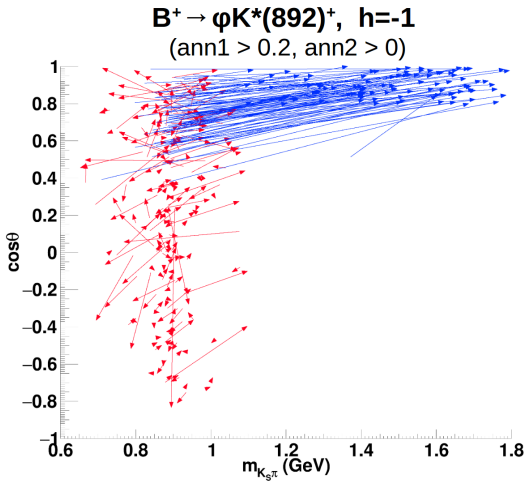

Figure 8.141: Migration vectors for a random number of $B^{\pm} \rightarrow \phi K^{*}(892)^{\pm}$ $h = -1$ not matched candidates.

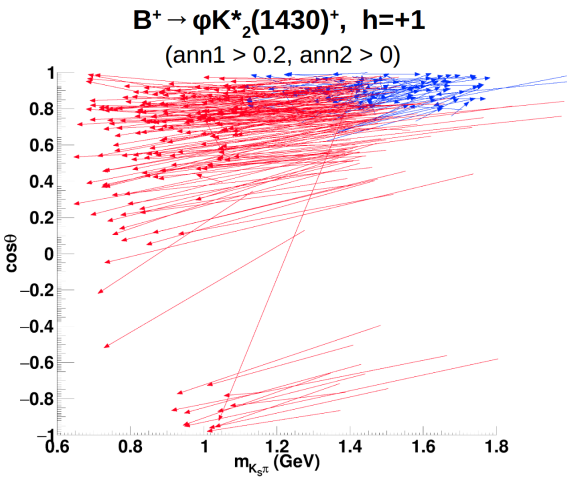

Figure 8.142: Migration vectors for a random number of $B^{\pm} \to \phi K_2^*(1430)^{\pm}$ $h = +1$ not matched candidates.

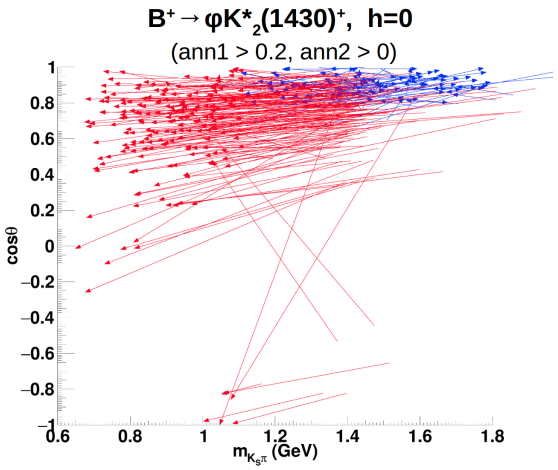

Figure 8.143: Migration vectors for a random number of $B^{\pm} \to \phi K_2^*(1430)^{\pm}$ $h = 0$ not matched candidates.

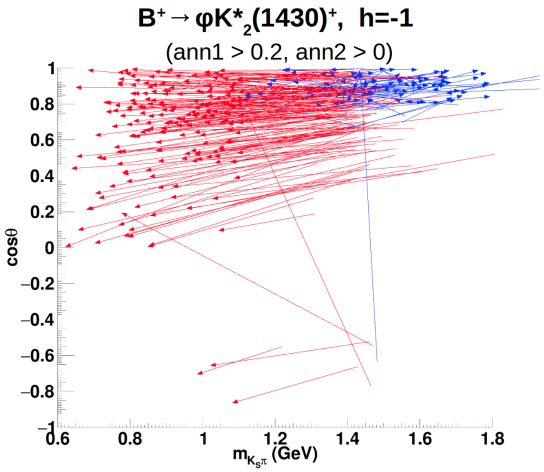

Figure 8.144: Migration vectors for a random number of $B^{\pm} \to \phi K_2^*(1430)^{\pm}$ $h = -1$ not matched candidates.

Chapter 9

Early Fits for Yields and BFs

In this chapter we perform two simple fits for yields and BFs using the mode $B^{\pm} \to \phi K^{*+}(892)$ for all three helicities. First we created "fake data". To do this we generated $2.75{\times}10^6$ events using Belle MC where the $\Upsilon(4S) \to B^+B^-$, $K^{*+}(892) \to K^0_S\pi^+$, and $\phi \to K^+K^-$ are all forced with 100% probability. The Upsilon decay does not matter if we compare to Belle data since only either the B^+ or B^- produced is considered signal (the other side of the decay is called the "tag" side). The Belle experiment recorded an integrated luminosity of 775 fb^{-1}, that equates to $8.52{\times}10^8$ events were recorded, and this in turn implies that $8.78{\times}10^8$ charged B-mesons were produced.

To calculate the number of signal events for fake data we used a fraction f_D of the fake data, where

$$f_D = \frac{8780}{6 \times 2.75 \times 10^6} = 0.000532 \tag{9.1}$$

where the 8780 is the number of events we would expect on Belle for BF($B^{\pm} \to \phi K^{*\pm}(892)$) = $10.0\times\ 10^{-6}$. The $\frac{1}{6}$ is a result of B($\phi \to K^+K^-$), B($K^0 \to K^0_S$), B($K^0_S \to \pi^+\pi^-$), which are respectively 1/2, 1/2, 69% (note that the BF for $K^0 \to K^0_S$ is really more an oscillation fraction). The $2.75{\times}10^6$ is the amount of generated signal MC.

Using this calculation, we generate "fake data" samples by randomly selecting 0.05321212% of the signal events. We then used these signal events with a full MC stream (that is streams 0 and 10 or 1 and 11, etc.) We presume that we have a ∼5% efficiency for this mode and we would get a ∼10% statistical error when we account

for background.

We begin by plotting the distribution for our two most important variables: ΔE and m_{bc}. These can be seen in Figures 9.1- 9.6. Note that these figures use $\Phi K^*(892)$ signal MC for all 3 helicities. The corresponding profile plots can be seen in Figs. 9.7 through 9.10. Profile plots are not a projection or a slice, but rather they show the mean (or rms) of one variable in slices of the other variable.

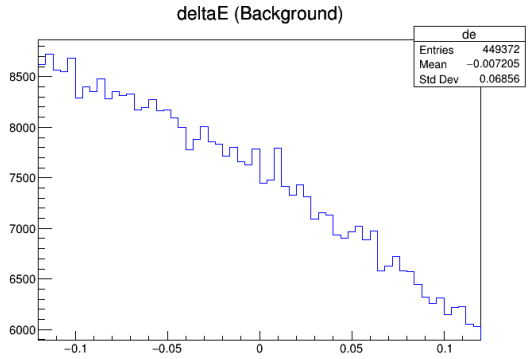

Figure 9.1: ΔE distribution for the background.

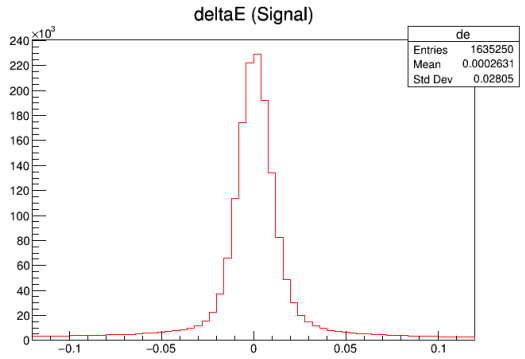

Figure 9.2: ΔE distribution for the signal.

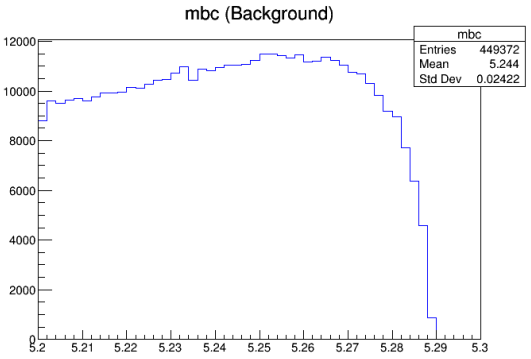

Figure 9.3: m_{bc} distribution for the background.

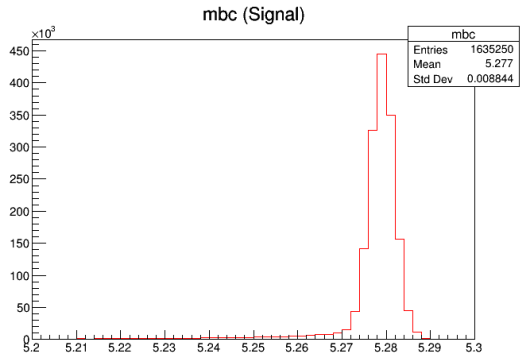

Figure 9.4: m_{bc} distribution for the signal.

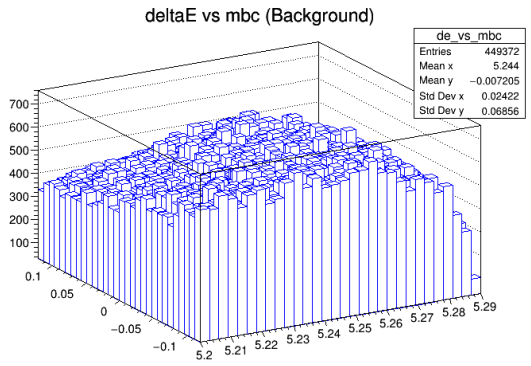

Figure 9.5: ΔE vs m_{bc} distribution for background.

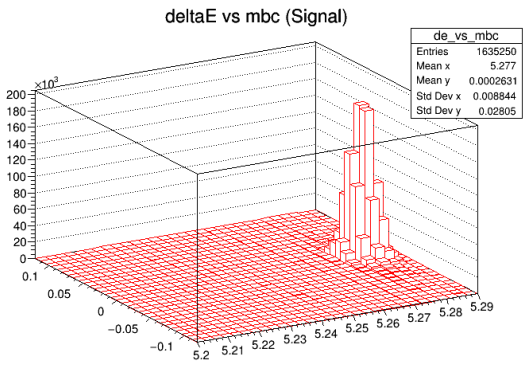

Figure 9.6: ΔE vs m_{bc} distribution for the signal.

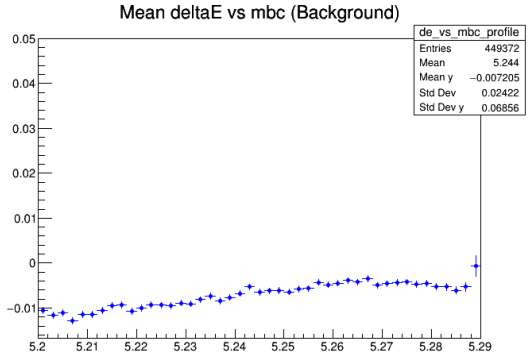

Figure 9.7: ΔE vs m_{bc} profile distribution for the background.

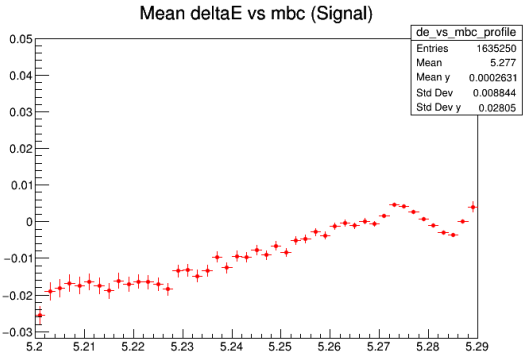

Figure 9.8: ΔE vs m_{bc} profile distribution for the signal.

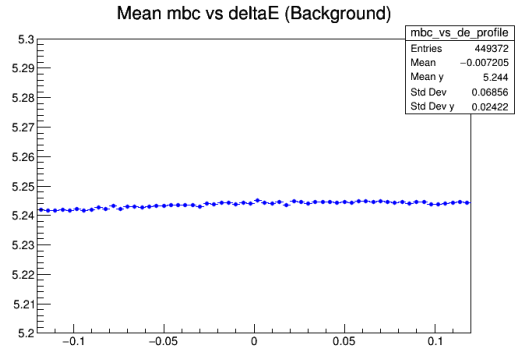

Figure 9.9: m_{bc} vs ΔE profile distribution for the background.

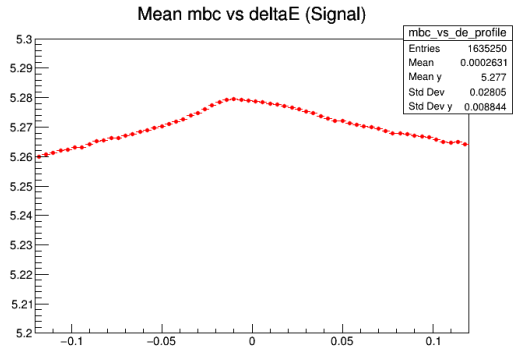

Figure 9.10: m_{bc} vs ΔE profile distribution for the signal.

From the 2-D histogram and the profile plots, we see that there is little correlation between background m_{bc} and ΔE (that is the profile plots are relatively straight and

the 2-D histogram is relatively uniform in distribution). In contrast the signal shows some correlation in the profile plots where there is a mix of $B^+ \to \phi K^{*+}(892)$ and $B^+ \to \phi K_0^{*+}(1430)$.

Note that we have many so many events because we are using the full signal MC to make the plots. We do not use fake data to get MC distribution. We use the full MC when we can; fake data is only used for the final fit to see what a Belle-sized data set gives us as a result.

9.0.1 Cut and Count Method

Our first method of calculating the significance of our signal was using a "cut and count" method on the distributions. This is potentially the most unbiased way to find the yield.

First, we define two regions: the "inner" region for events in the $m_{bc} \in [5.27, 5.29]$ (GeV) and $\Delta E \in [-0.03, 0.06]$ (GeV) space and the "outer" region as the space where $m_{bc} \ni [5.25, 5.29]$ (GeV) or $\Delta E \ni [-0.03, 0.06]$. The inner region contains mostly signal whereas the outer region is dominated by background. Let number of signal events in the inner and outer region be N_{si} and N_{so} and the numbers of background events in the inner and outer boxes be N_{bi} and N_{bo}, respectively.

To obtain the number of signal events, N_S, we take te total number of events and subtract by the predicted background. We obtain the following fractions from MC

$$f_{si} \equiv N_{si}/(N_{si} + N_{so}) \tag{9.2}$$

$$f_{so} \equiv N_{so}/(N_{si} + N_{so}) \tag{9.3}$$

$$f_{bi} \equiv N_{bi}/(N_{bi} + N_{bo}) \tag{9.4}$$

$$f_{bo} \equiv N_{bo}/(N_{bi} + N_{bo}) \tag{9.5}$$

These fractions vary with different cuts. In this chapter we try varying the cuts

on the ANN outputs to improve the significance. Using the following expressions, we can find the total number of signal (N_S) and background events (N_B)

$$N_S = \frac{(f_{bo}N_i - f_{bi}N_o)}{(f_{bo}f_{si} - f_{bi}f_{so})} \tag{9.6}$$

$$N_B = \frac{(f_{si}N_o - f_{so}N_i)}{(f_{bo}f_{si} - f_{bi}f_{so})} \tag{9.7}$$

where the numbers of events in the inner and outer boxes, N_i and N_o, are given by

$$N_i = f_{bi}N_B + f_{si}N_S \tag{9.8}$$

$$N_o = f_{bo}N_B + f_{so}N_S \tag{9.9}$$

We can calculate the errors on the N_S and N_B using the equations above and the usual error propagation. Uncertainties in the different backgrounds cause systematics errors to arise in this procedure resulting in changes in the background shape and uncertainties in the signal shape. The signal box is wide enough to cover the effects of data-MC smearing differences, and there are no peaks or sharp behavior from the background in the signal box. Thus we expect an insignificant systematic error. The statistical significance, or $N_S/\Delta N_S$, of the signal yield can be studied as a function of cuts on the ANN parameters. We can use the ANN parameters, called a_1 and a_2 to optimize the significance, and therefore use that to get the result.

This cut-and-count method is validated by using the "fake data" sets that we have created, where we know the number of signal events in the outer and inner region. We can then find the fit results from the generated values.

Figs. 9.11 and 9.12 show the the variation in the signal significance vs. the cuts on the ANN1 and ANN2 outputs, with and without, respectively a mass cut on $K^0_S\pi$. We conclude that a mass cut on $K^0_S\pi$ yields a better significance than without and ann2 should remain low or at zero for a higher significance.

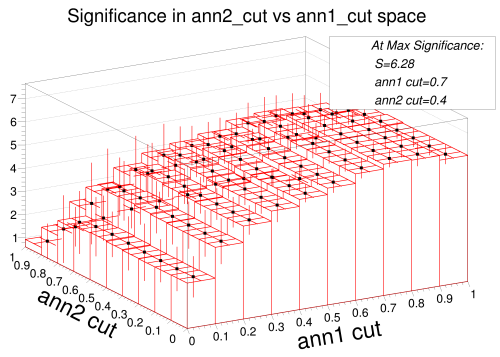

Figure 9.11: Variation of the significance as a function of ANN1 and ANN2 cuts for no cut on the $K^0_S\pi^+$ mass.

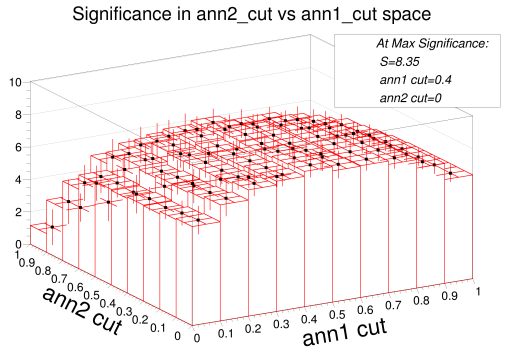

Figure 9.12: Variation of the significance as a function of ANN1 and ANN2 cuts for $0.842 < m_{K^0_S\pi^+} < 0.942$ GeV.

9.0.2 **2D Fit Method**

We perform a simple fit with MC signal and background. Figs. 9.13 and 9.14 show the the variation in the signal significance vs. the cuts on the ANN1 and ANN2 outputs, with and without, respectively a mass cut on $K^0_S\pi$.

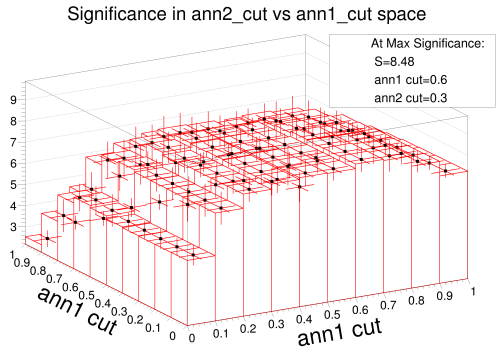

Figure 9.13: Variation of the significance as a function of ANN1 and ANN2 cuts for no cut on the $K^0_S\pi^+$ mass.

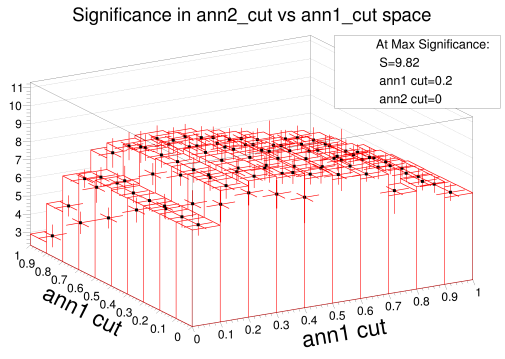

Figure 9.14: Variation of the significance as a function of ANN1 and ANN2 cuts for $0.842 < m_{K^0_S\pi^+} < 0.942$ GeV.

Below is an example of a 2D fit.

Comparing the significance plots (Figs. 9.11, 9.12, 9.13, 9.14) we come to a few conclusions. First, the significance is a little higher with a $m_{K^0_S\pi}$ mass cut. Second, the significance is higher with the 2D method, rather than the cut-and-count method. This indicates that a multi-dimensional unbinned fit should yield even better results.

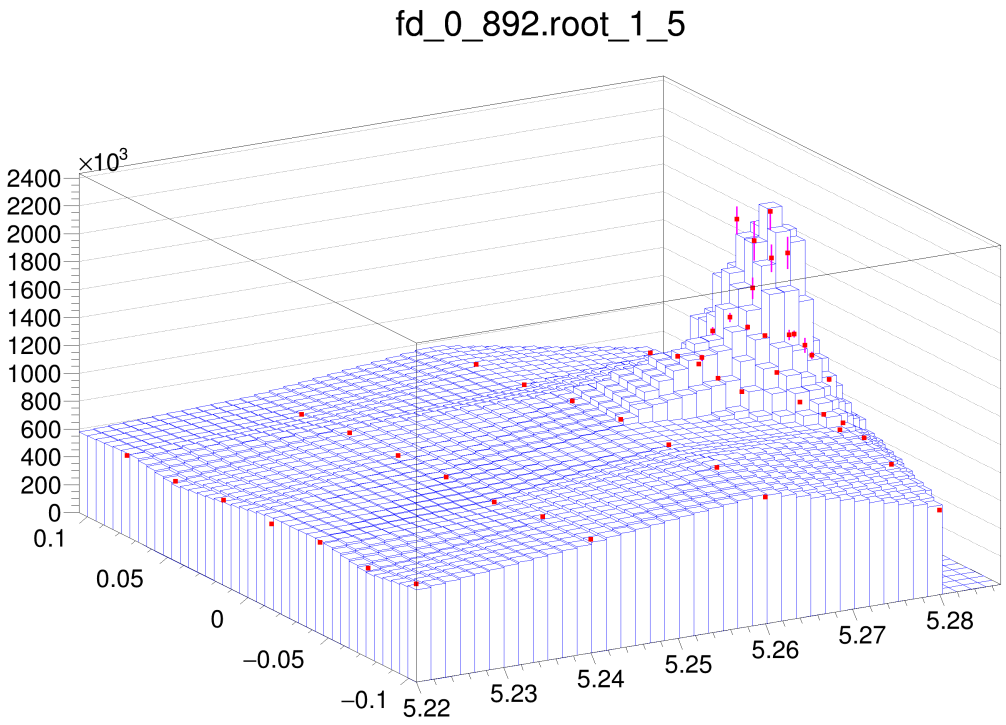

Figure 9.15: 2D fit example; the dots are fit results and the histogram shows simulated data.

The best significance from our fake data sets is almost 10σ. This is reasonable since the neutral mode paper observed a 17σ signal [We expect, due to BF's ratios of the K^0 oscillating to K^0_S and the K^0_S decaying to $\pi^+\pi^-$, roughly a factor of 3 less data than in the neutral mode]. Since we have less statistics than the neutral mode (that is a factor 3 less), we expect a reduction by a factor of 1.732 in significance.

Chapter 10

Full Unbinned Fits for BFs and Amplitudes

We explain the maximum likelihood (ML) unbinned fits in this chapter.

In order to create fits, we needed "fake data" sets of MC data that varied statistically from set to set and that mimic what we would expect to obtain from Belle data. To do this we first categorize our background in two different categories for every B^+ and B^-: event: light flavor ("lf"), and heavy flavor ("hf"). Light flavor refers to $u\bar{u}$, $d\bar{d}$, and $s\bar{s}$ ("uds") events and heavy flavor refers to $c\bar{c}$ and $b\bar{b}$ (charged and mixed) events. The heavy flavor background is mostly dominated by $c\bar{c}$.

Studies were conducted on "1x" and "10x" fake data, where the factor refers to the amount of signal generated. In both cases, the background is the same. For each of B^+ and B^- we generate 3800 "lf" background events and 3500 "hf"background events using Poisson statistics. These numbers come from the 37,793 "lf" and 35,262 "hf" events for the five streams of generic MC that satisfy ANN1 > 0.2 and $\cos\theta_{K^0_S\pi} < 0.75$. The background for a data set is created by a program we wrote named "toymc", which uses the generic background pdf's and the rejection method. This program also generates signal candidates for the data set using a signal pdf that is 4D ($m_{K^0_S\pi}$, $cos\theta_{K^0_S\pi}$, $cos\theta_\phi$, ϕ) $\times$ 2D (m_{bc}, ΔE) $\times$ 2D (ANN$_1$, ANN$_2$).

We obtain the number of signal events for each charge using the Belle neutral mode measurement and multiplying by $0.5 \times 878. \times 0.5 \times 0.489 \times 0.6667 \times \epsilon_{avg}$. This gives us the BF's in parts per million (ppm). The first factor of $\frac{1}{2}$ comes from the fact we are calculating the BF's for the charges separately. The number 878 comes from the number of events gathered by Belle (852 million) times the BF of Upsilon into

charged B-mesons (2.0×0.514).The last factor of $\frac{2}{3}$ is dropped for the $J = 0$ mode. The rest of the equation comes from the fact that only 1/2 the produced neutral kaons turn into K^0_S, 0.489 of the ϕ-mesons decay into K^+K^-, and lastly we also multiply by $(1-(2q-1)A_{CP})$, where q is the B-meson charge and the CP asymmetry parameter is A_{CP}. For the "10x" data the BF's are multiplied by a factor of 10.

These toymc data sets are then fit in an 8-dimensional space consisting of the 4 physics variables $\{m_{K^0_S\pi}$, $\cos(\theta_{K^0_S\pi})$, $\cos(\theta_\phi)$, $\Phi\}$ and 4 signal/background discrimination variables $\{m_{bc}$, ΔE, a'_1, $a'_2\}$. The last two primed variables are transformed ANN parameter outputs as the following

$$a'_1 = \ln\left(\frac{a_1}{(1-a_1)}\right), \qquad a'_2 = \ln\left(\frac{a_2}{(1-a_2)}\right) \tag{10.1}$$

For our fits, two of our discrimination variables, a'_1 and a'_2, are used either in an ANN-based universal pdf fitter or we use them to fit individual distributions in a'_1 and a'_2 and then use those fits in our 8D model. Tables 10.2 and 10.1 list the parameters for used in the individual pdfs. The fits of the distributions can be seen in Figs. 10.1 through 10.7.

Table 10.1 Parameters for Fits to a'_2

	a'_2	
	Peak Position	FWHM
$\phi K^*(892)^\pm$ h=+1	0.982	1.80
$\phi K^*(892)^\pm$ h=0	0.957	1.74
$\phi K^*(892)^\pm$ h=-1	0.987	1.82
$\phi K^0_S\pi^\pm$	0.914	1.79
$\phi K^*_2(1430)^\pm$ h=+1	0.851	1.75
$\phi K^*_2(1430)^\pm$ h=0	0.859	1.75
$\phi K^*_2(1430)^\pm$ h=-1	0.862	1.75
uds Background	0.23	1.44
cb Background	0.22	1.43

Table 10.2 Parameters for Fits to a_1' and ΔE

	a_1'			ΔE (MeV)
	Peak Position	Width	Tail	FWHM
Control Mode Signal	1.67 ± 0.006	1.86 ± 0.002	0.116 ± 0.001	27.5
Control Mode Data	1.91 ± 0.060	1.85 ± 0.028	0.182 ± 0.013	32.8
$\phi K^*(892)^\pm$ h=+1	1.14 ± 0.007	2.56 ± 0.014	0.338 ± 0.0040	20.1
$\phi K^*(892)^\pm$ h=0	1.13 ± 0.0090	2.49 ± 0.016	0.311 ± 0.005	20.9
$\phi K^*(892)^\pm$ h=-1	1.13 ± 0.007	2.53 ± 0.0135	0.321 ± 0.004	20.0
$\phi K_S^0 \pi^\pm$	1.70 ± 0.014	2.36 ± 0.022	0.326 ± 0.0090	20.6
$\phi K_2^*(1430)^\pm$ h=+1	1.70 ± 0.006	2.34 ± 0.009	0.323 ± 0.004	21.4
$\phi K_2^*(1430)^\pm$ h=0	1.70 ± 0.006	2.33 ± 0.009	0.319 ± 0.003	21.4
$\phi K_2^*(1430)^\pm$ h=-1	1.70 ± 0.006	2.32 ± 0.009	0.319 ± 0.004	21.4
uds Background	-3.94 ± 0.763	2.63 ± 0.456	0.0871 ± 0.055	
cb Background	-4.00 ± 1.31	2.39 ± 0.682	0.014 ± 0.140	

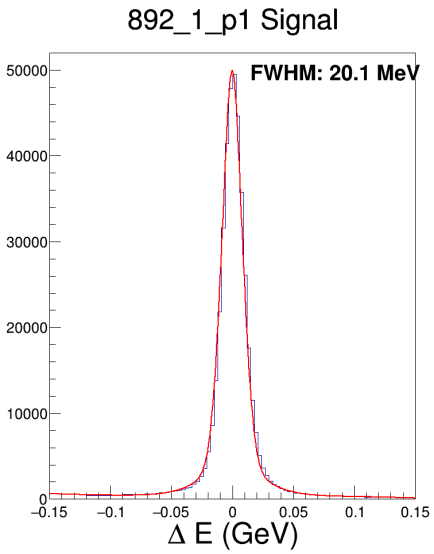

Figure 10.1: Fit to ΔE for $B^+ \to \phi K^{*+}(892)$ h=+1 MC events.

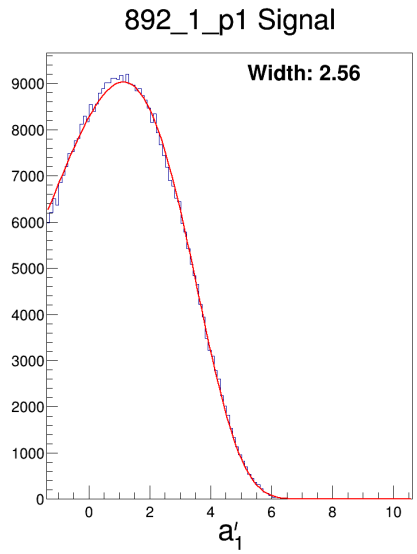

Figure 10.2: Fit to a_1' for $B^+ \to \phi K^{*+}(892)$ h=+1 MC events.

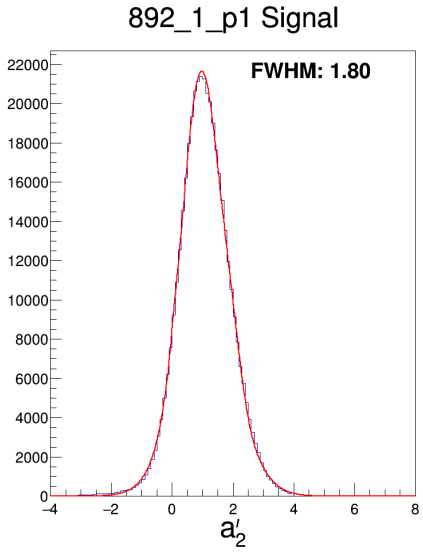

Figure 10.3: Fit to a_2' for $B^+ \to \phi K^{*+}(892)$ h=+1 MC events.

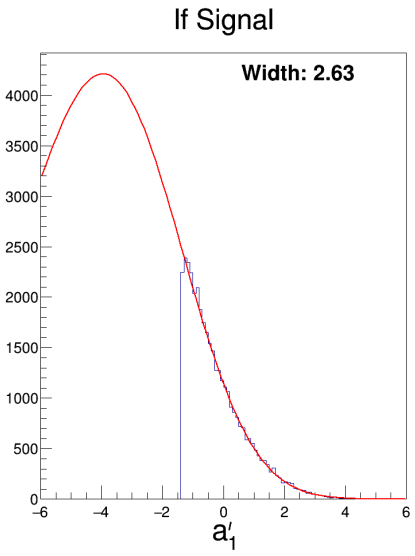

Figure 10.4: Fit to a'_1 for light flavor MC background events.

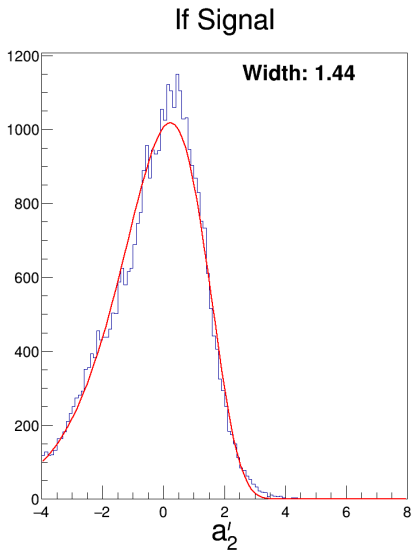

Figure 10.5: Fit to a'_2 for light flavor MC background events.

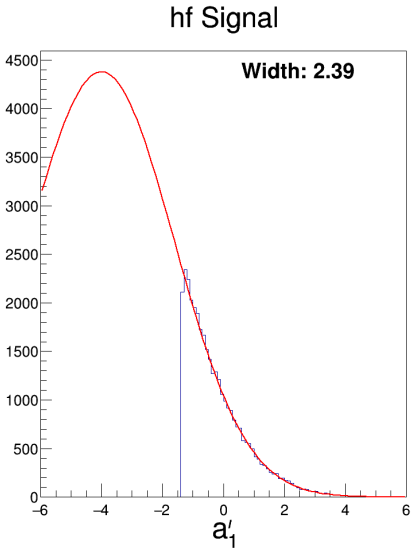

Figure 10.6: Fit to a'_1 for heavy flavor MC background events.

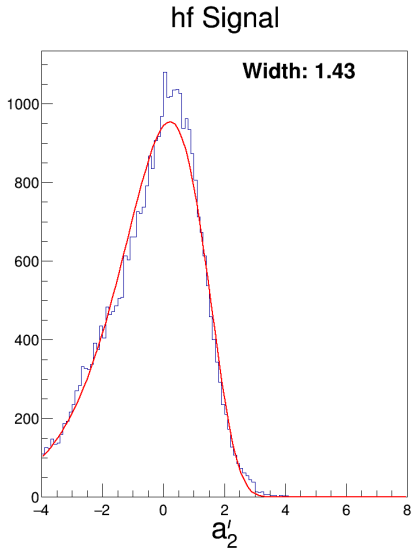

Figure 10.7: Fit to a'_2 for light flavor MC background events.

The fitter described above is an unbinned ML fit where the efficiency comes from MC simulation. The signal pdf is a 4-dimensional pdf described by Eqn. 6.24 times an efficiency function. The efficiency function is a two-dimensional function described by cubics in $\cos(\theta_{K^0_S\pi})$ whose coefficients are themselves cubics in $m_{K^0_S\pi}$ that are extracted

from MC data as explained in subsection 8.0.3. The two-dimensional m_{bc}-ΔE pdf is a distribution also derived from MC.

We use cubics plus Breit-Wigners for the mass peaks for the background, as displayed in Figs. 10.12 and 10.13; the background pdf is composed of a product of six of these 1D-distributions.

We can also use the signal pdfs in the S/B discrimination variables to fit using a product of 1-dimensional pdf's. Fits to 1D's can be seen in figures 10.8 through 10.11.

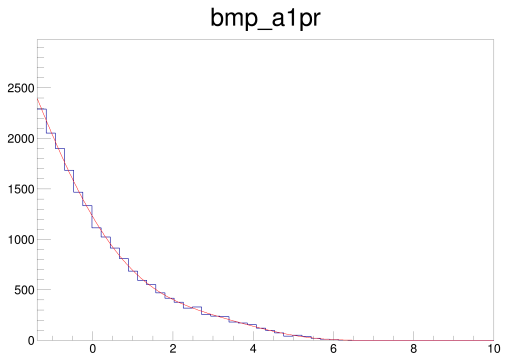

Figure 10.8: Fit to a_1' for $B^{\pm}$ signal simulation.

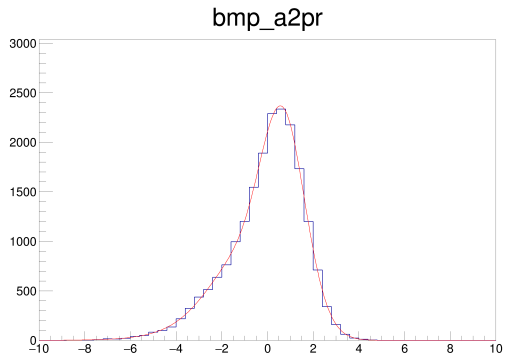

Figure 10.9: Fit to a_2' for $B^{\pm}$ signal simulation.

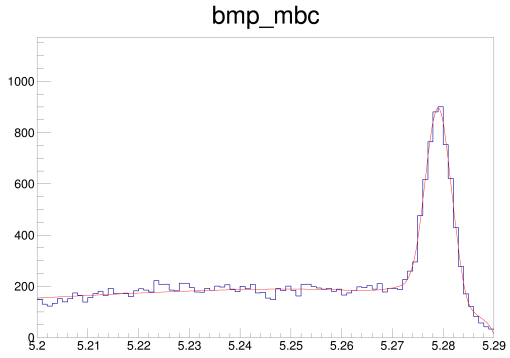

Figure 10.10: Fit to m_{bc} for $B^{\pm}$ signal simulation.

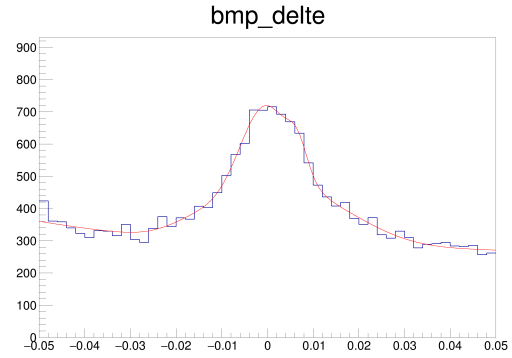

Figure 10.11: Fit to ΔE for $B^{\pm}$ signal simulation.

10.0.1 **Full Unbinned Fits for 1x Signal Data**

We used Belle neutral mode parameters to create full unbinned fits for 1x signal as shown in Figs. 10.16 through 10.47. The fits are very good. To monitor the quality of the fit, we plotted the input and output values for each parameter in Figs. 10.54 through 10.58.

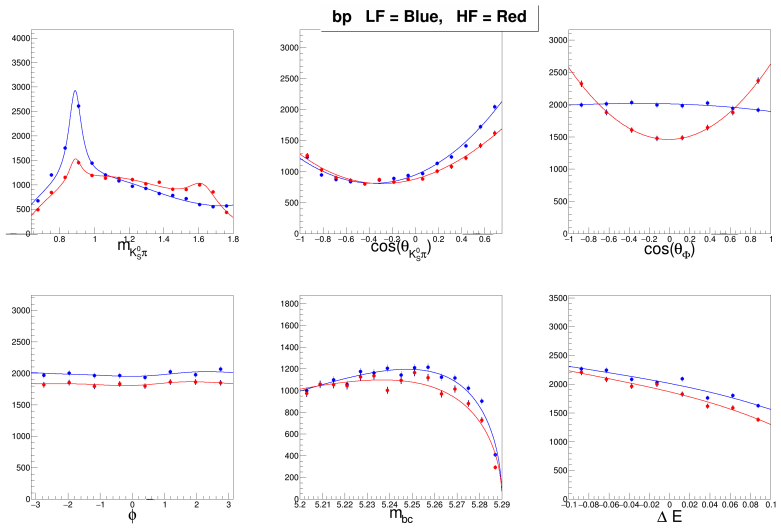

Figure 10.12: Fitter input for light flavor and heavy flavor B^+ backgrounds.

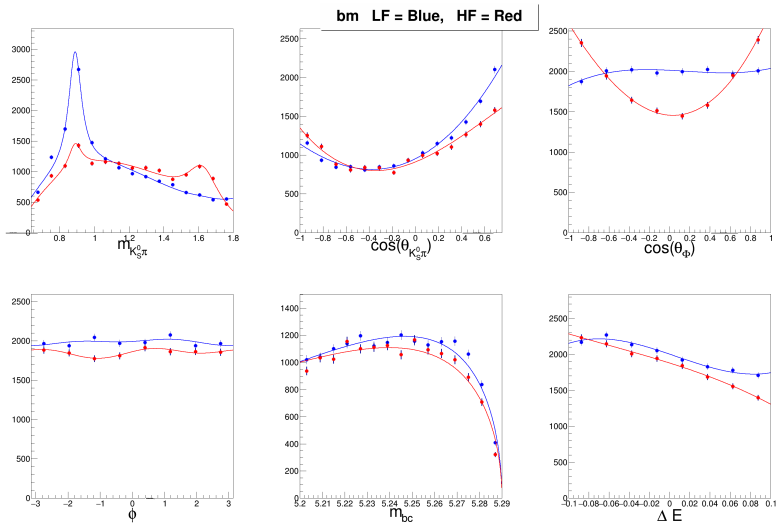

Figure 10.13: Fitter input for light flavor and heavy flavor B^- backgrounds.

Table 10.3 Input Values, Bias Means, and Pull RMS for 1x Signal Fits to 320 Toy MC Data Sets

	Parameter	Input	Bias Mean	Par Err	Pull RMS
1	B_0 (ppm)	4.3000	-0.2790 ± 0.0381	0.6816	1.1257 ± 0.0445
2	B_1 (ppm)	10.4000	-0.3567 ± 0.0436	0.7802	0.9709 ± 0.0384
3	B_2 (ppm)	5.5000	-0.0948 ± 0.0373	0.6676	1.0415 ± 0.0412
4	$f^-_{L1} \times 10$	0.4840	-0.0114 ± 0.0038	0.0675	1.0354 ± 0.0409
5	$f^-_{L2} \times 10$	0.9030	-0.0125 ± 0.0026	0.0460	0.9947 ± 0.0393
6	$f^{-\prime}_{\perp 1} \times 10$	0.5250	0.0019 ± 0.0056	0.1002	1.0613 ± 0.0420
7	$f^{-\prime}_{\perp 2} \times 10$	0.5770	-0.0377 ± 0.0135	0.2422	1.3695 ± 0.0541
8	$\phi_{\parallel 1}$	2.2300	-0.0102 ± 0.0087	0.1560	1.0190 ± 0.0403
9	ϕ_{par2}	-2.5232	-0.0044 ± 0.0302	0.5398	1.2753 ± 0.0504
10	$\phi_{\perp 1}$	2.3700	-0.0126 ± 0.0089	0.1598	1.0076 ± 0.0398
11	$\phi_{\perp 2}$	-1.8332	0.0768 ± 0.0260	0.4655	1.0985 ± 0.0434
12	δ_{01}	2.9100	-0.0397 ± 0.0092	0.1643	1.0750 ± 0.0425
13	δ_{02}	-2.7532	-0.0180 ± 0.0096	0.1721	1.0432 ± 0.0412
14	A_{CP0}	0.0930	-0.0051 ± 0.0094	0.1681	1.0571 ± 0.0418
15	A_{CP1}	-0.0070	0.0094 ± 0.0049	0.0869	1.0907 ± 0.0431
16	A_{CP2}	0.1550	0.0073 ± 0.0063	0.1136	0.9709 ± 0.0384
17	$f^+_{L1} \times 10$	0.5140	-0.0137 ± 0.0037	0.0659	1.0384 ± 0.0410
18	$f^+_{L2} \times 10$	0.9330	-0.0339 ± 0.0029	0.0518	0.9566 ± 0.0378
19	$f^{+\prime}_{\perp 1} \times 10$	0.4220	0.0037 ± 0.0055	0.0982	1.0180 ± 0.0402
20	$f^{+\prime}_{\perp 2} \times 10$	0.8360	-0.1401 ± 0.0135	0.2415	0.9490 ± 0.0375
21	$\Delta\phi_{\parallel 1}$	0.0200	-0.0059 ± 0.0094	0.1680	1.0649 ± 0.0421
22	$\Delta\phi_{\parallel 2}$	-0.0200	-0.0615 ± 0.0337	0.6035	1.2358 ± 0.0488
23	$\Delta\phi_{\perp 1}$	0.0500	-0.0154 ± 0.0102	0.1830	1.1128 ± 0.0440
24	$\Delta\phi_{\perp 2}$	-0.1900	0.0419 ± 0.0264	0.4724	1.1055 ± 0.0437
25	$\Delta\delta_{01}$	0.0800	-0.0294 ± 0.0107	0.1912	1.1020 ± 0.0436
26	$\Delta\delta_{02}$	0.0600	0.0237 ± 0.0095	0.1706	1.0297 ± 0.0407
27	B^-_{LF}	3800	-97.82 ± 11.28	201.85	1.1272 ± 0.0446
28	B^-_{HF}	3500	105.88 ± 11.17	199.82	1.1047 ± 0.0437
29	B^+_{LF}	3800	248.40 ± 12.69	226.99	1.0741 ± 0.0425
30	B^+_{HF}	3500	-244.51 ± 12.67	226.64	1.0851 ± 0.0429

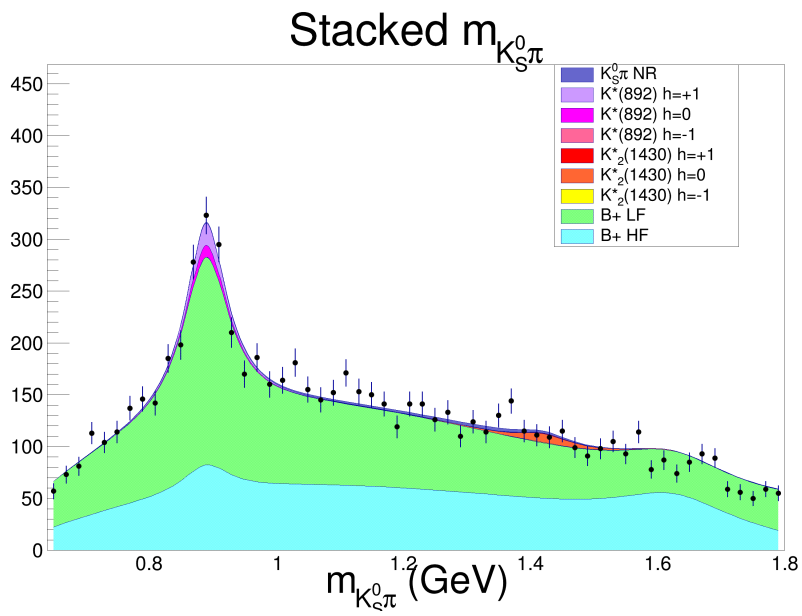

Figure 10.14: Fit to $m_{K^0_S\pi}$ for B^+ signal and background.

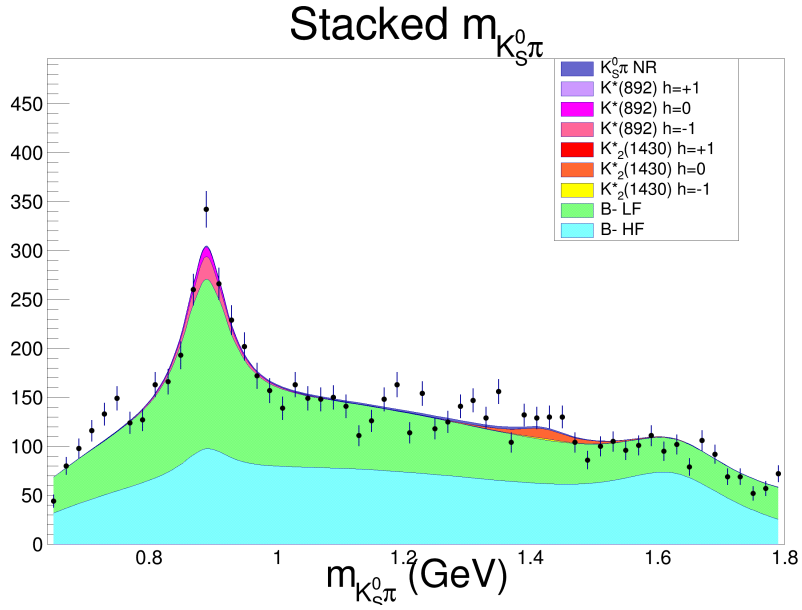

Figure 10.15: Fit to $m_{K^0_S\pi}$ for B^- signal and background.

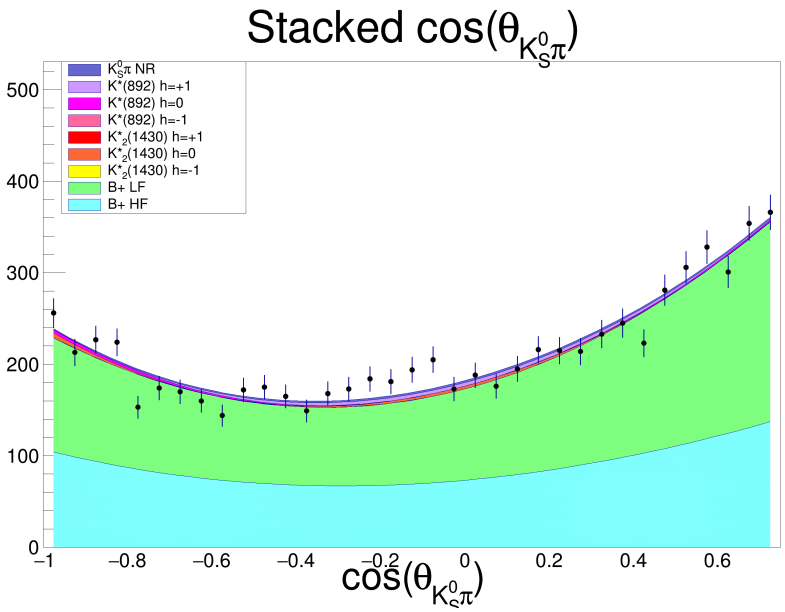

Figure 10.16: Fit to $cos(\theta_{K^0_S\pi})$ for B^+ signal and background.

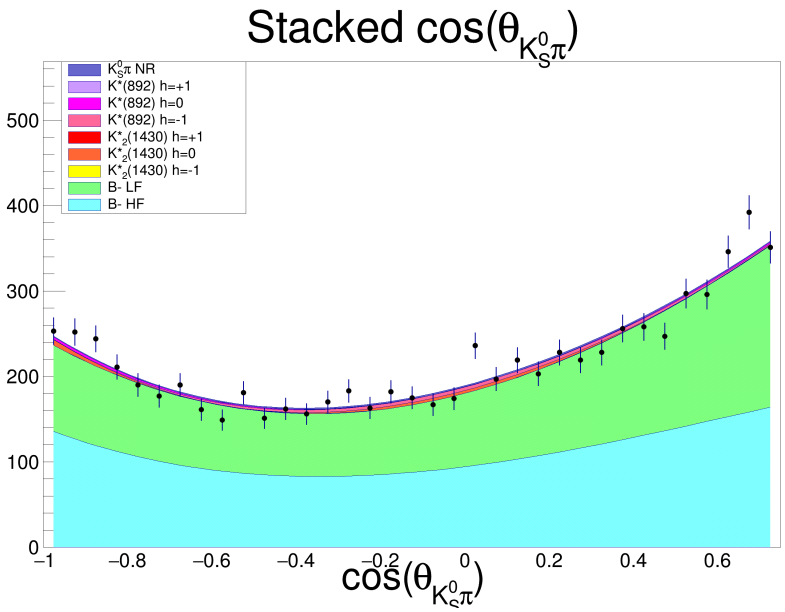

Figure 10.17: Fit to $cos(\theta_{K^0_S\pi})$ for B^- signal and background.

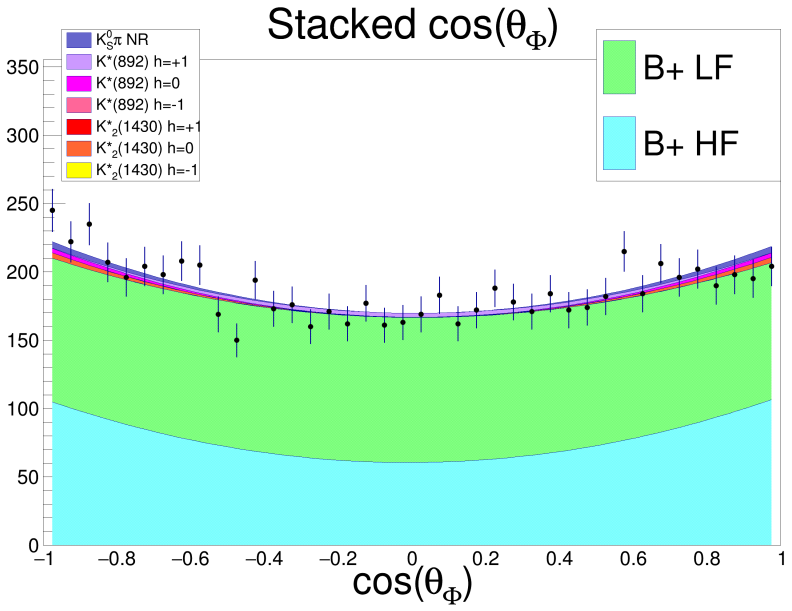

Figure 10.18: Fit to $cos(\theta_\Phi)$ for B^+ signal and background.

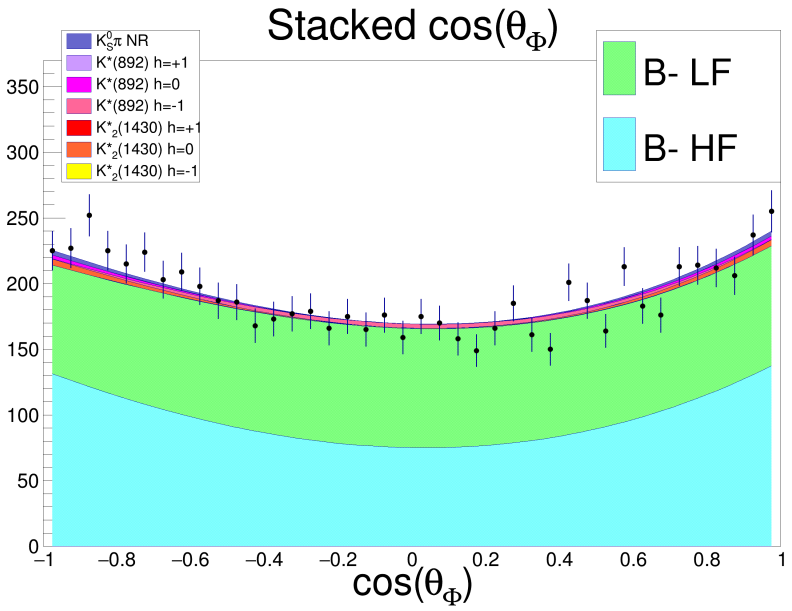

Figure 10.19: Fit to $cos(\theta_\Phi)$ for B^- signal and background.

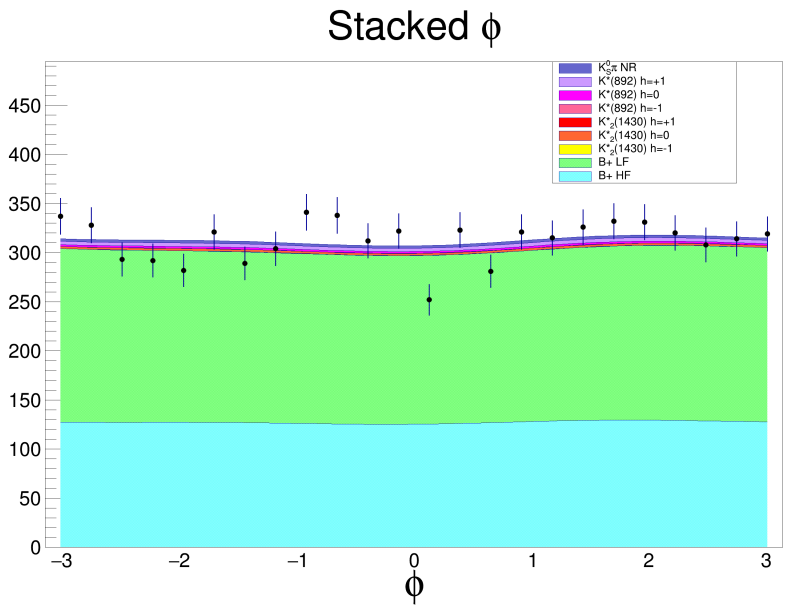

Figure 10.20: Fit to Φ for B^+ signal and background.

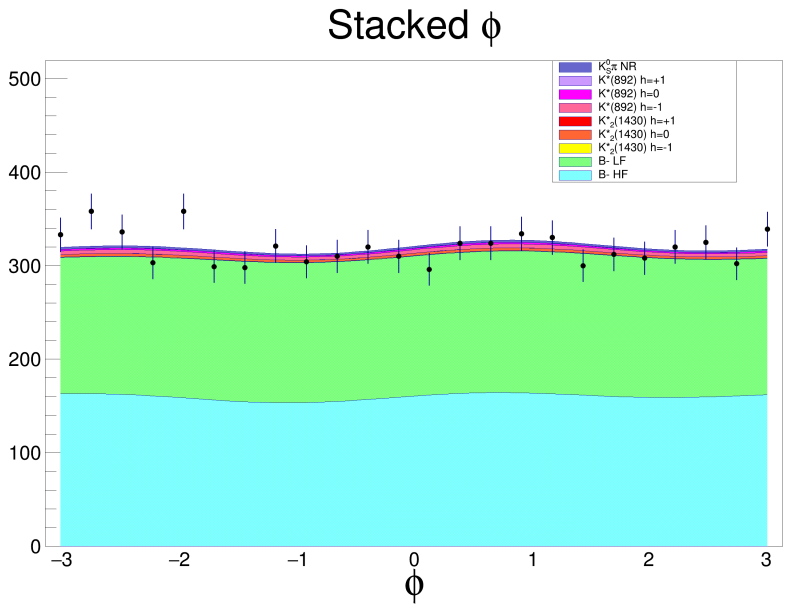

Figure 10.21: Fit to Φ for B^- signal and background.

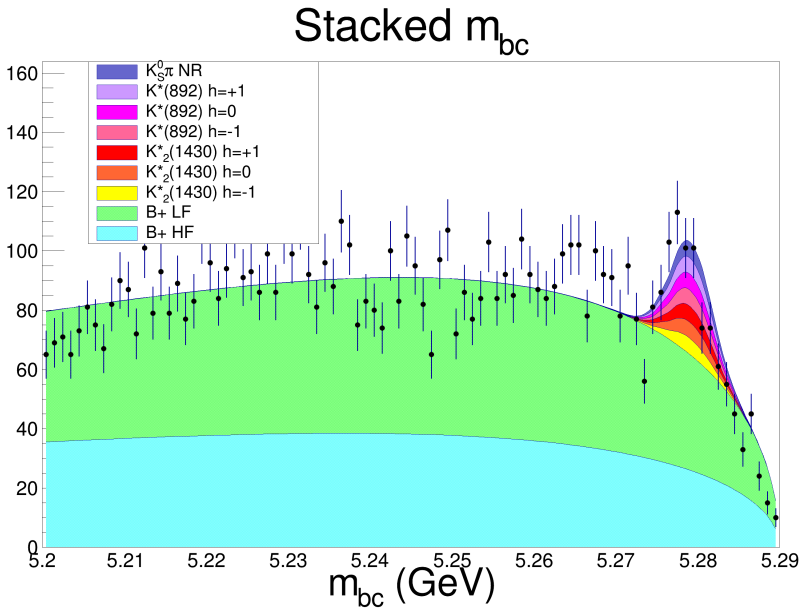

Figure 10.22: Fit to m_{bc} for B^+ signal and background.

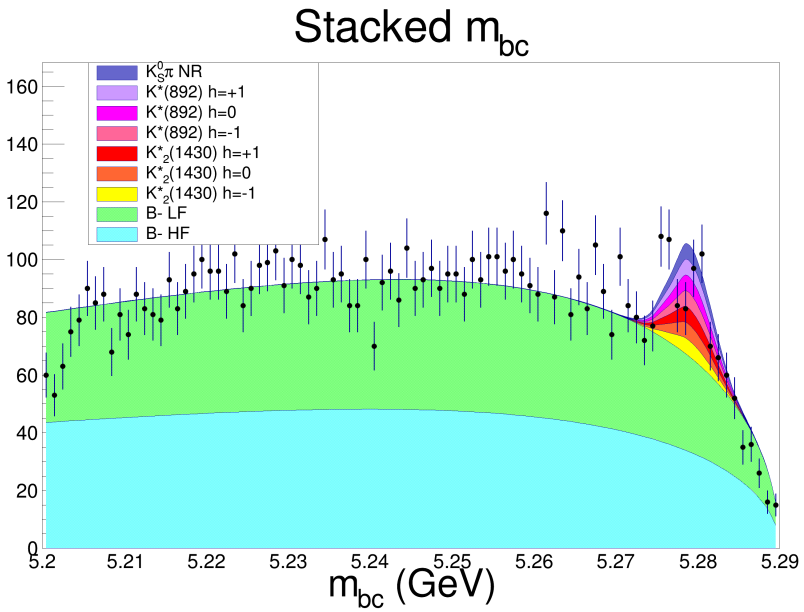

Figure 10.23: Fit to m_{bc} for B^- signal and background.

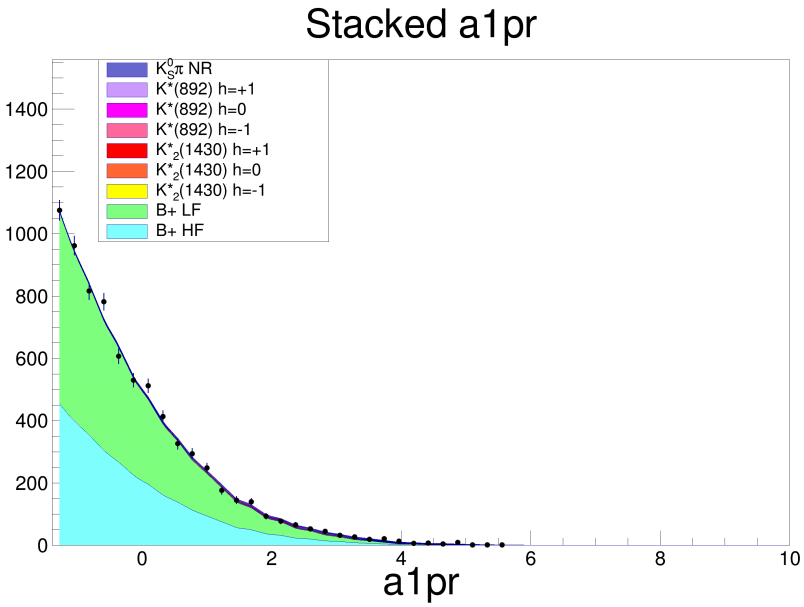

Figure 10.24: Fit to a_1' for B^+ signal and background.

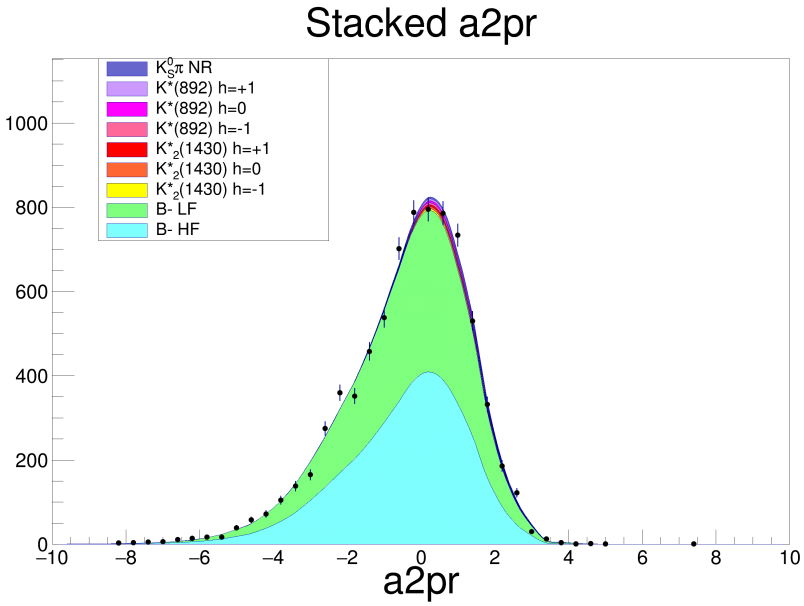

Figure 10.25: Fit to a_2' for B^- signal and background.

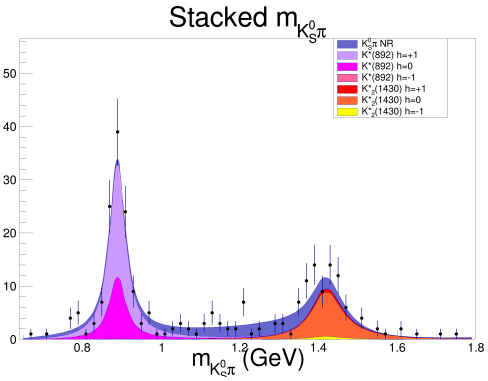

Figure 10.26: Fit to $m_{K^0_S\pi}$ for B^+ signal.

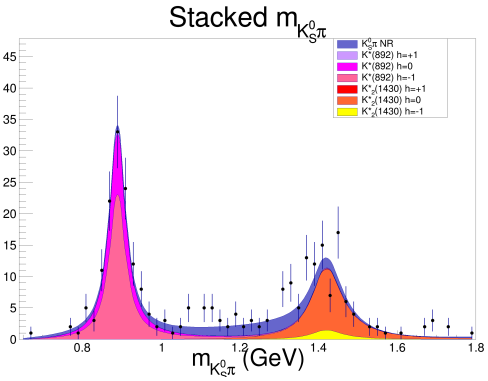

Figure 10.27: Fit to $m_{K^0_S\pi}$ for B^- signal.

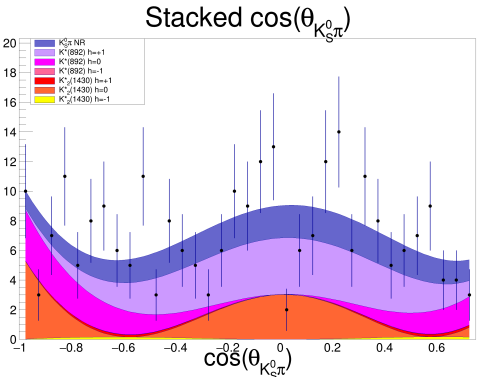

Figure 10.28: Fit to $cos(\theta_{K^0_S\pi})$ for B^+ signal.

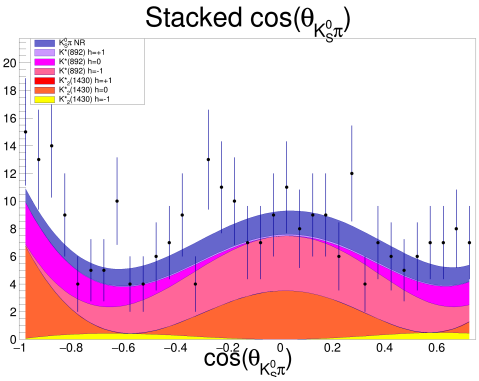

Figure 10.29: Fit to $cos(\theta_{K^0_S\pi})$ for B^- signal.

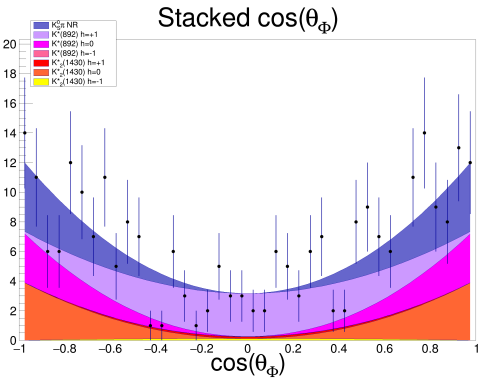

Figure 10.30: Fit to $cos(\theta_\Phi)$ for B^+ signal.

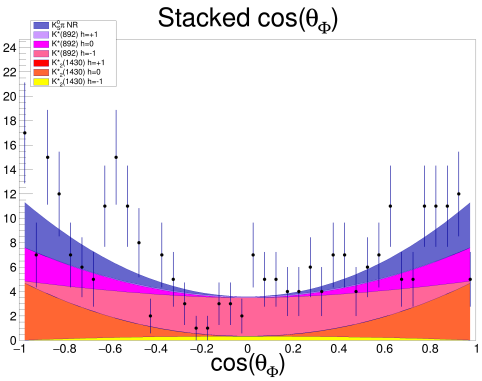

Figure 10.31: Fit to $cos(\theta_\Phi)$ for B^- signal.

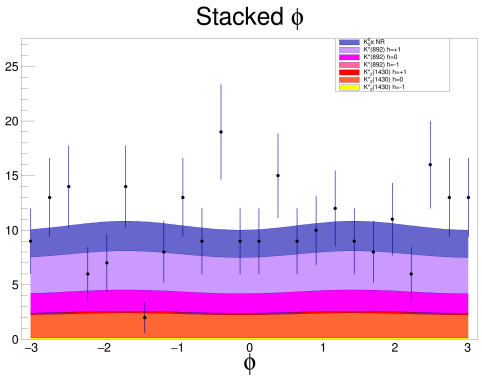

Figure 10.32: Fit to Φ for B^+ signal.

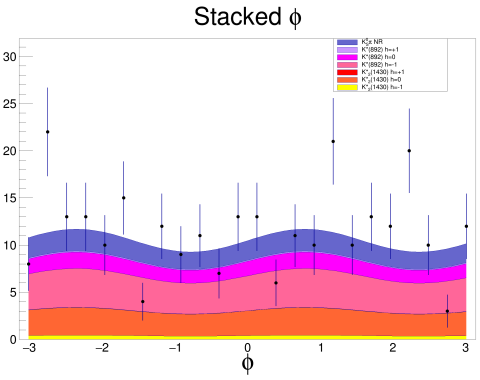

Figure 10.33: Fit to Φ for B^- signal.

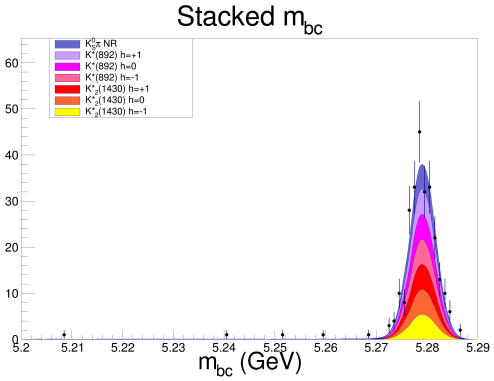

Figure 10.34: Fit to m_{bc} for B^+ signal.

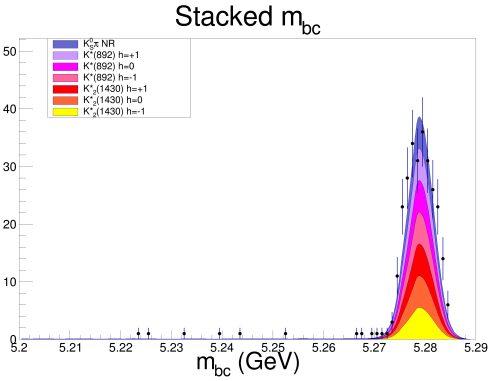

Figure 10.35: Fit to m_{bc} for B^- signal.

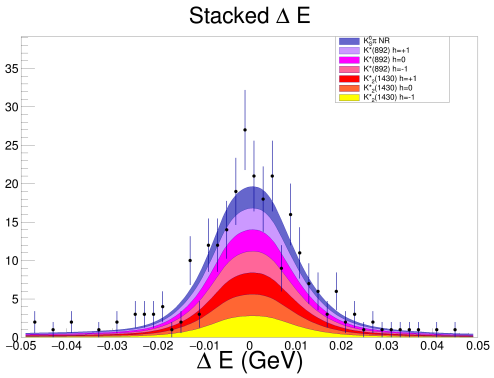

Figure 10.36: Fit to ΔE for B^+ signal.

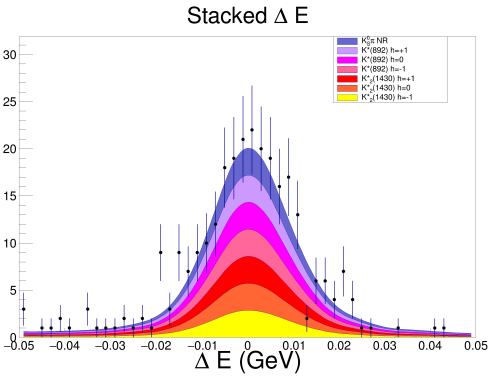

Figure 10.37: Fit to ΔE for B^- signal.

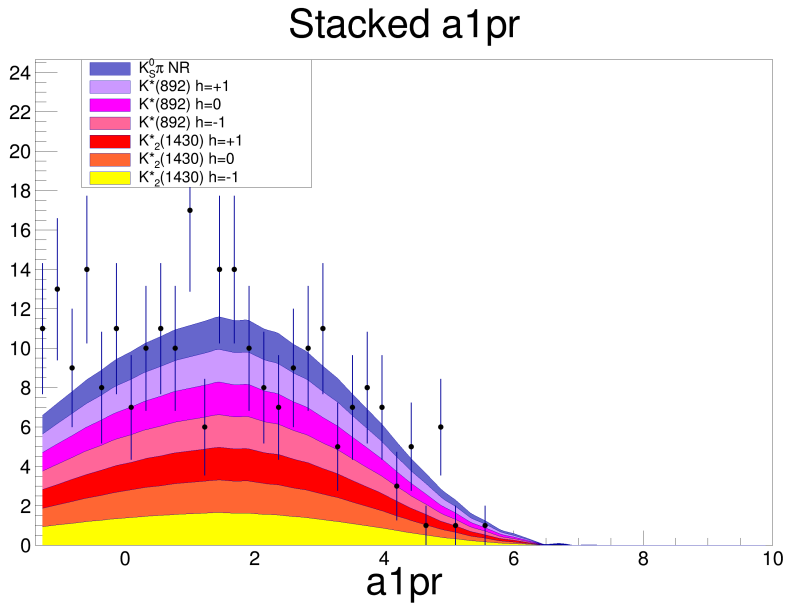

Figure 10.38: Fit to a_1' for B^+ signal and background.

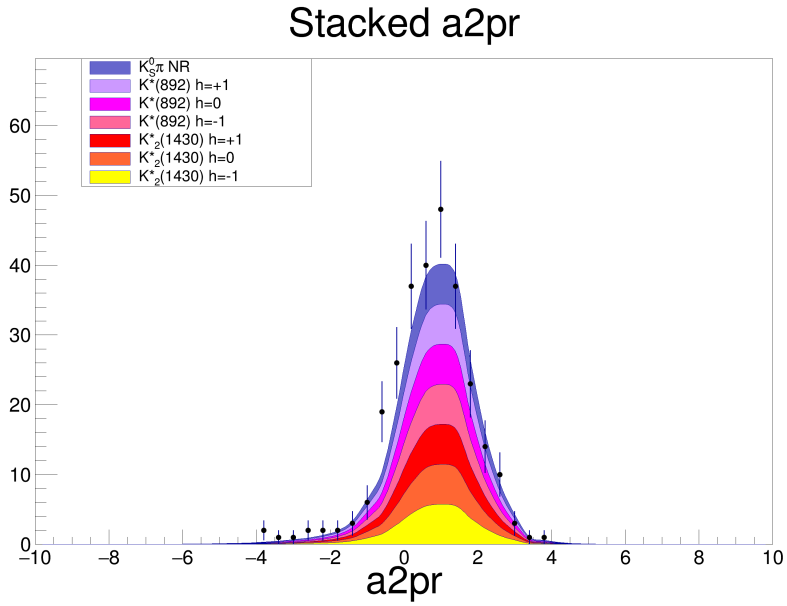

Figure 10.39: Fit to a_2' for B^- signal and background.

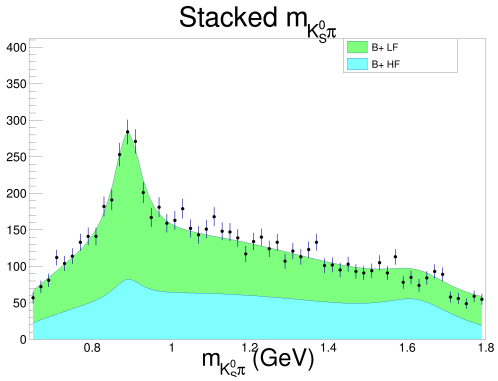

Figure 10.40: Fit to $m_{K^0_S\pi}$ for B^+ background.

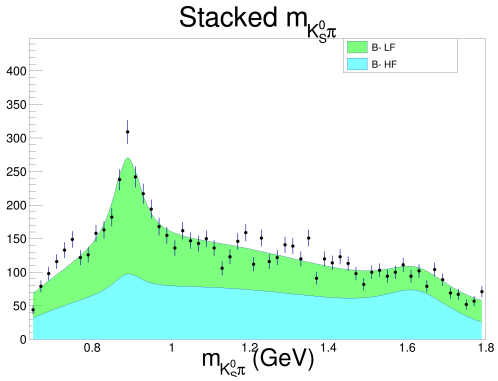

Figure 10.41: Fit to $m_{K^0_S\pi}$ for B^- background.

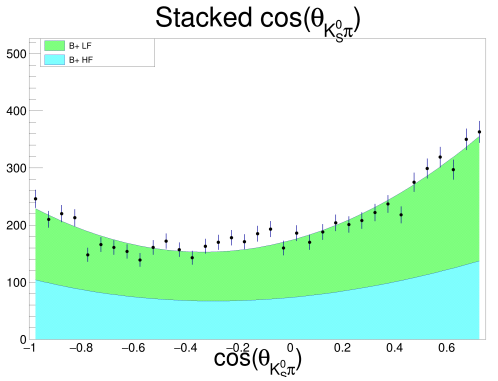

Figure 10.42: Fit to $cos(\theta_{K^0_S\pi})$ for B^+ background.

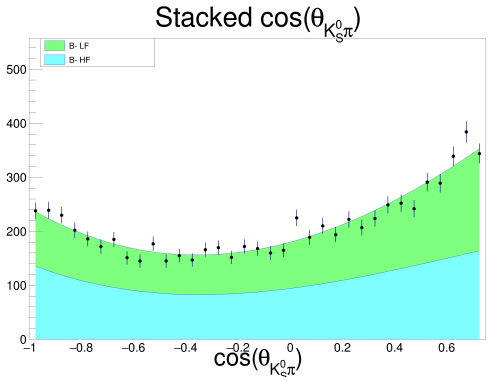

Figure 10.43: Fit to $cos(\theta_{K^0_S\pi})$ for B^- background.

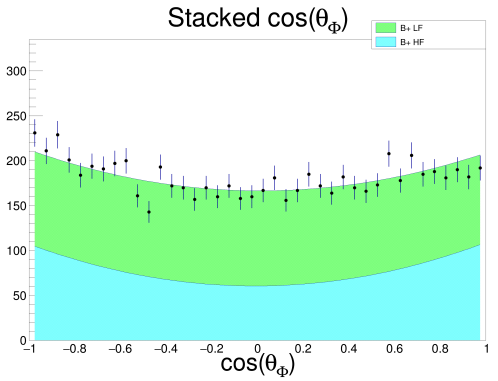

Figure 10.44: Fit to $cos(\theta_\Phi)$ for B^+ background.

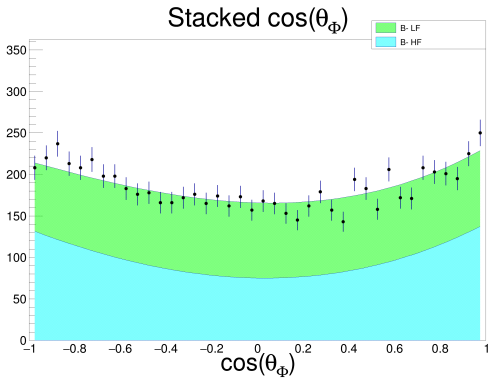

Figure 10.45: Fit to $cos(\theta_\Phi)$ for B^- background.

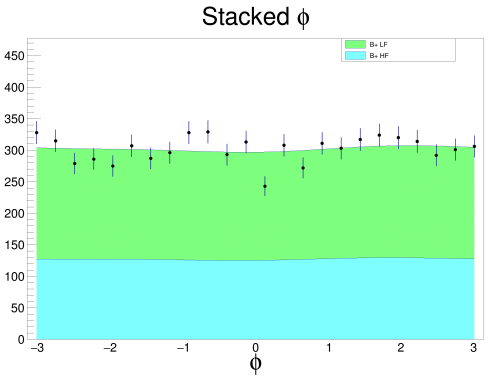

Figure 10.46: Fit to Φ for B^+ background.

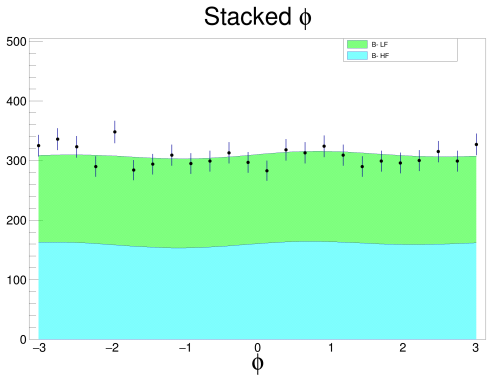

Figure 10.47: Fit to Φ for B^- background.

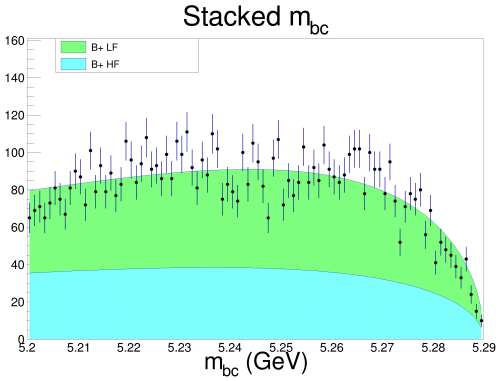

Figure 10.48: Fit to m_{bc} for B^+ background.

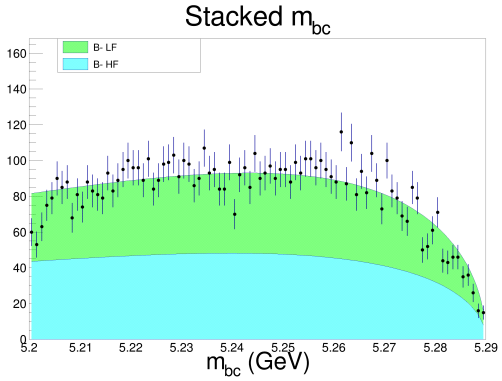

Figure 10.49: Fit to m_{bc} for B^- background.

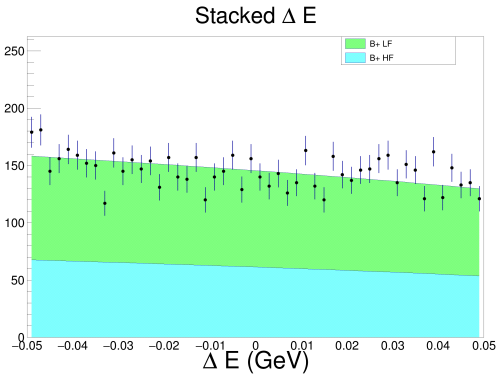

Figure 10.50: Fit to ΔE for B^+ background.

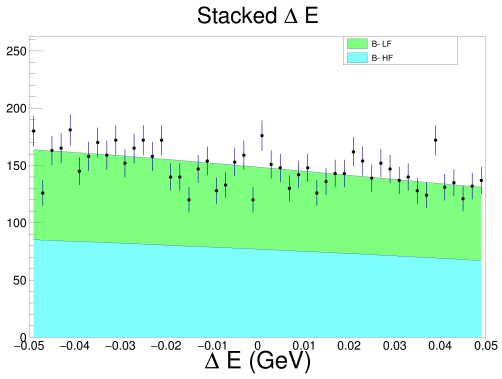

Figure 10.51: Fit to ΔE for B^- background.

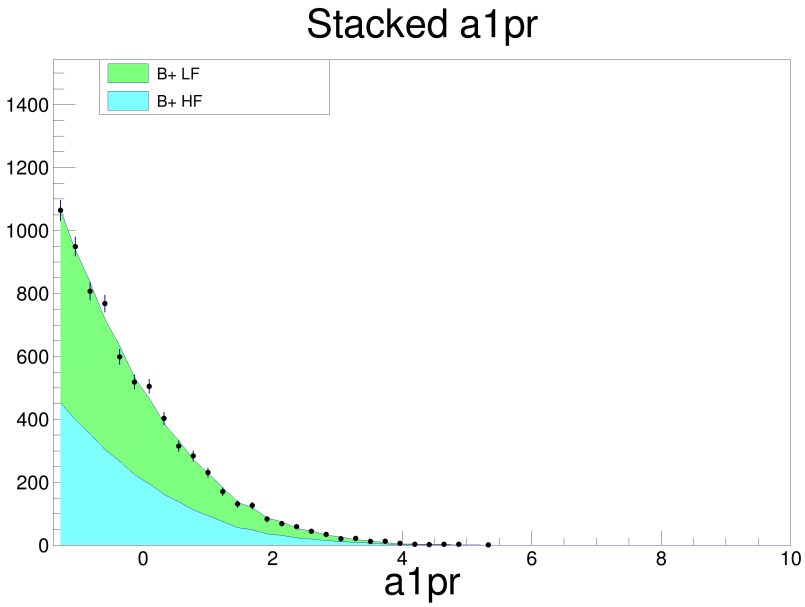

Figure 10.52: Fit to a_1' for B^+ signal and background.

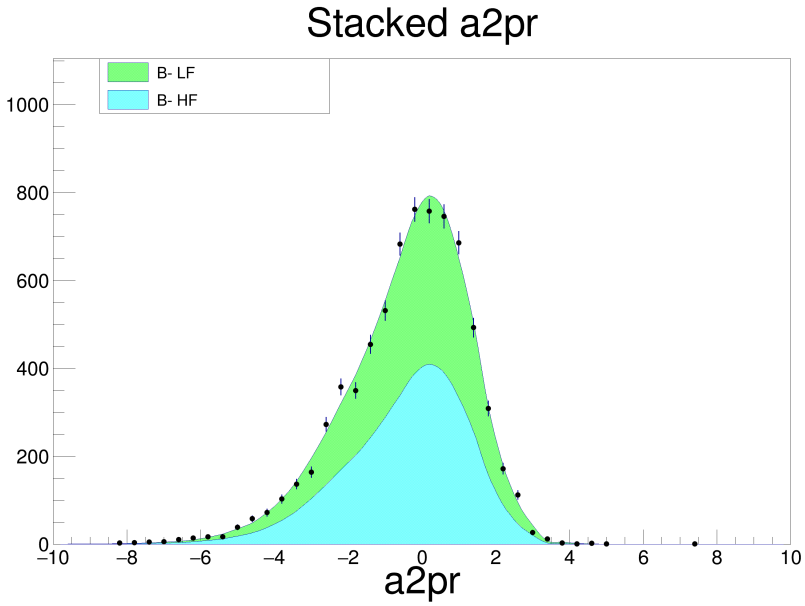

Figure 10.53: Fit to a_2' for B^- signal and background.

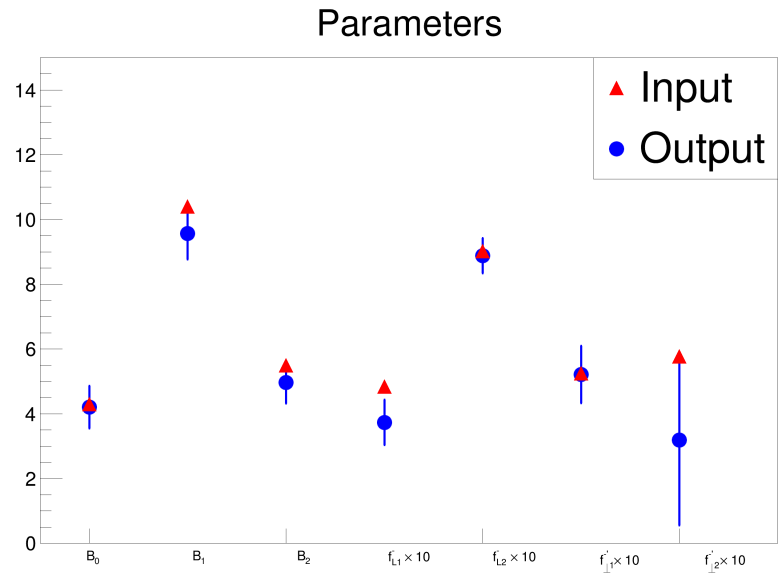

Figure 10.54: Branching fraction and f_L fitter input and output parameters.

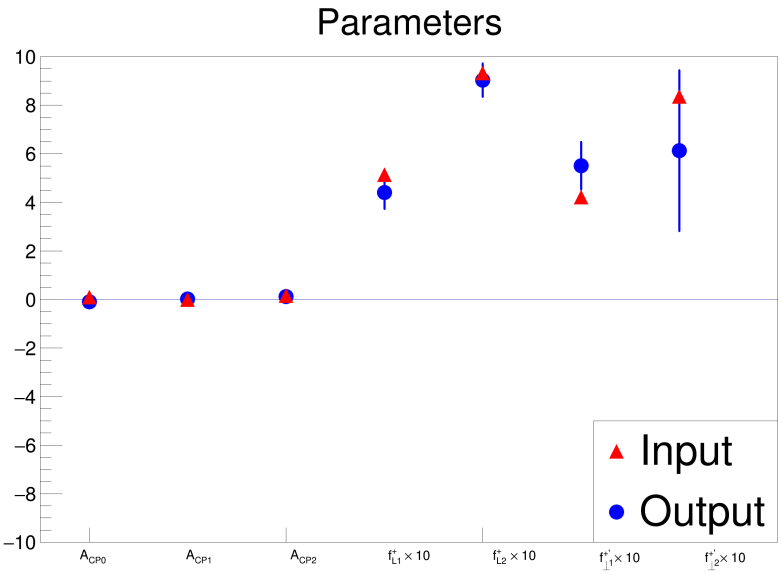

Figure 10.55: A_{CP} and f_L fitter input and output parameters.

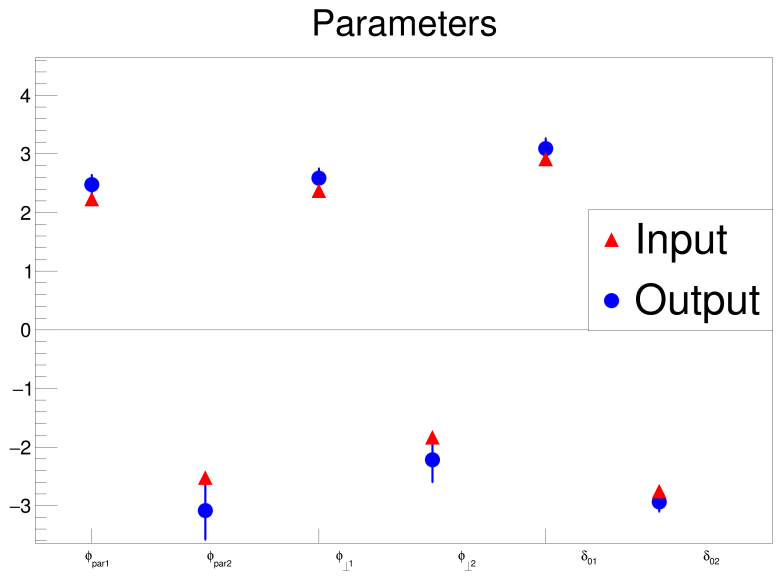

Figure 10.56: Angular fitter input and output parameters.

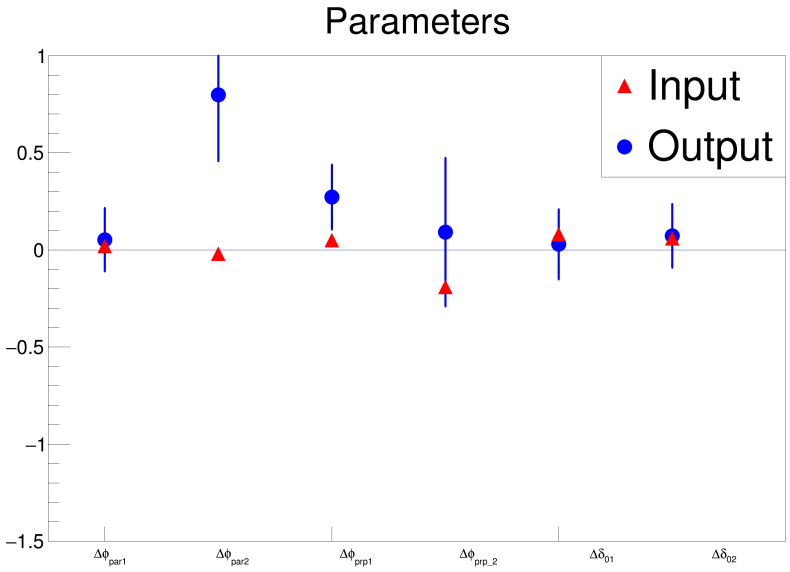

Figure 10.57: Difference in the angular parameters for fitter input and output.

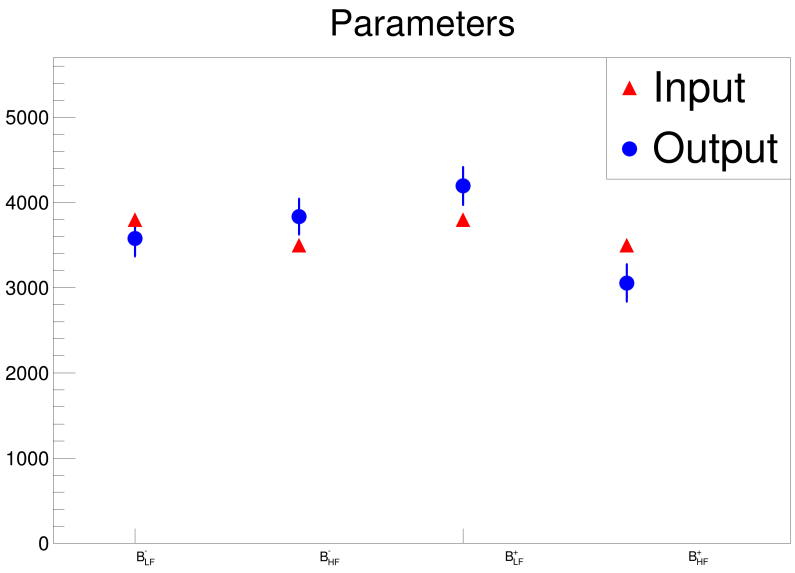

Figure 10.58: Input and output number of B^+ and B^- heavy flavor and light flavor backgrounds.

10.0.2 **Bias and Pulls for 1x Signal Data**

For each parameter to the fit, we created a bias plot and pull to describe one fit of 1x toy MC. The bias is defined as (output - input) for each parameter and the pull is defined as bias / (MINUIT error) for each parameter. Table 10.3 summarizes the bias mean and the pull RMS for 320 toy MC data outputs. All pulls have RMS close to 1 and there are no significant biases in the signal parameters (there is a bias in the background, but we do not worry about that).

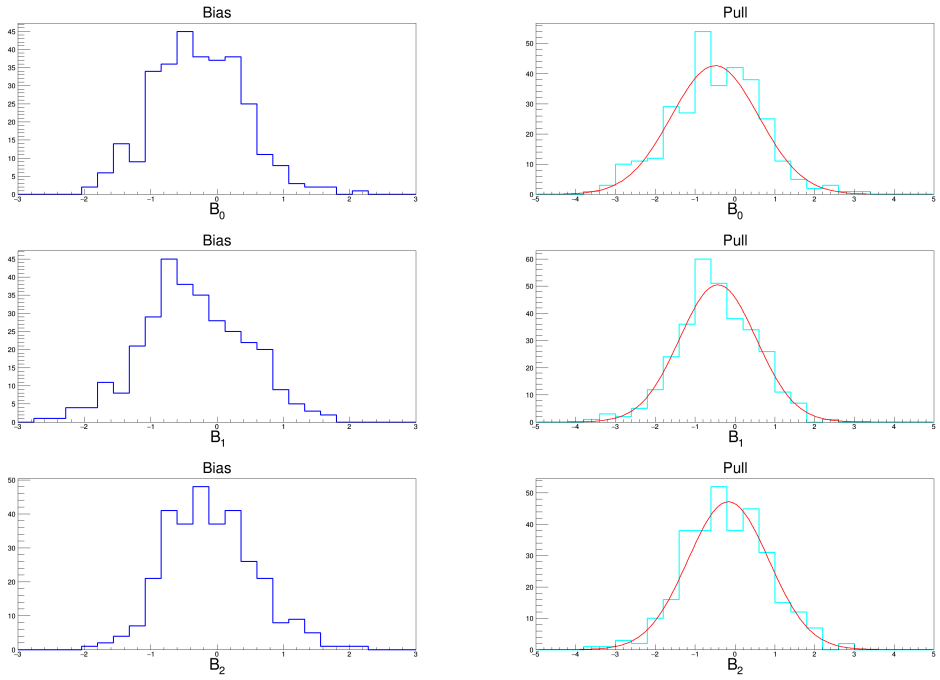

Figure 10.59: Bias and pull distributions for branching fractions with 1x the signal.

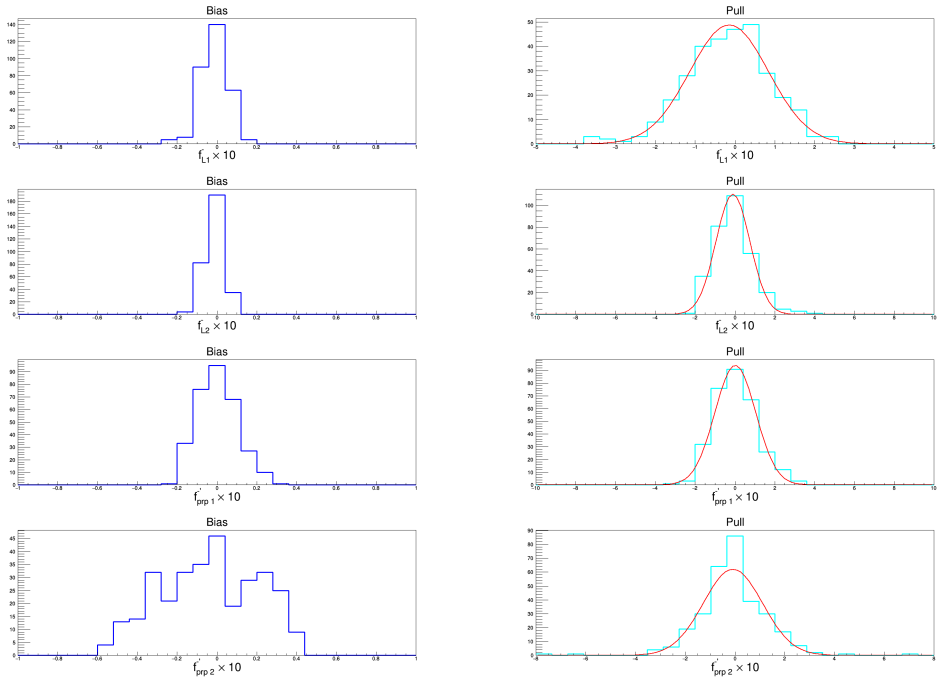

Figure 10.60: Bias and pull distributions for amplitude fractions for B^- with 1x the signal.

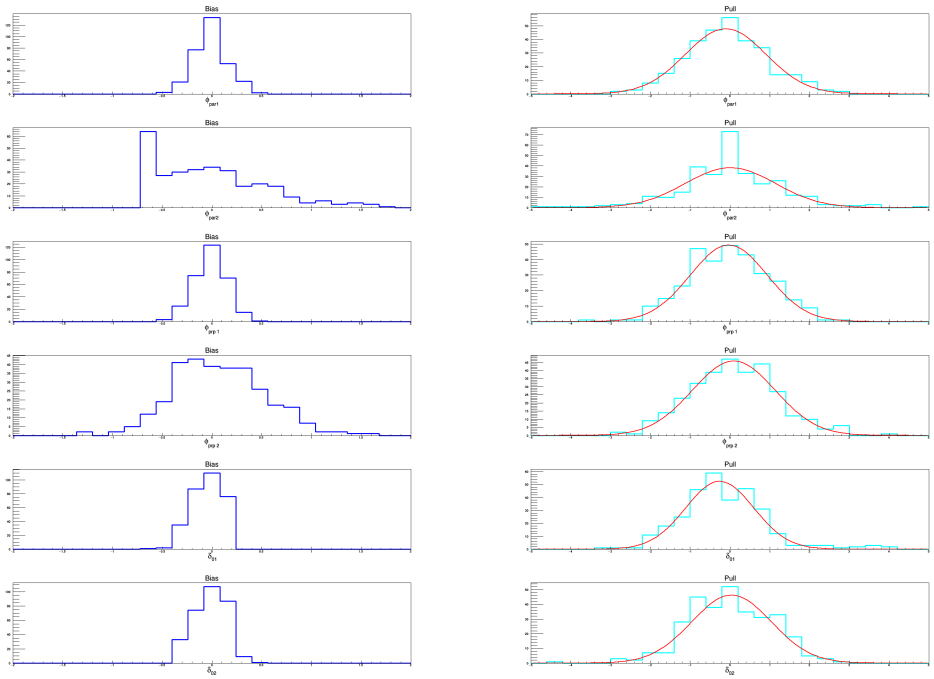

Figure 10.61: Bias and pull distributions for phases with 1x the signal.

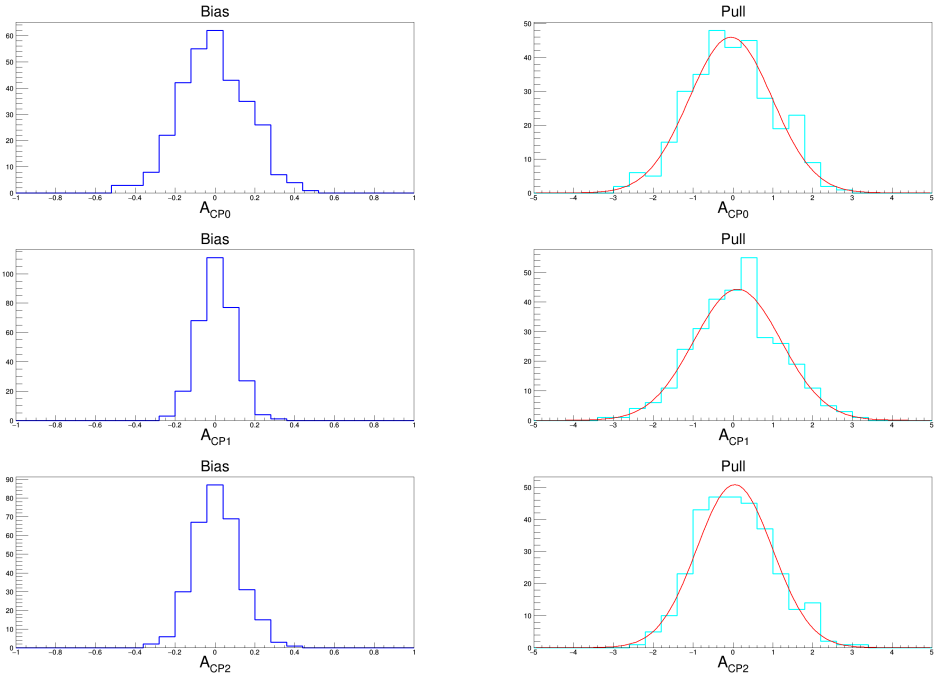

Figure 10.62: Bias and pull distributions for A_{CP} parameters with 1x the signal.

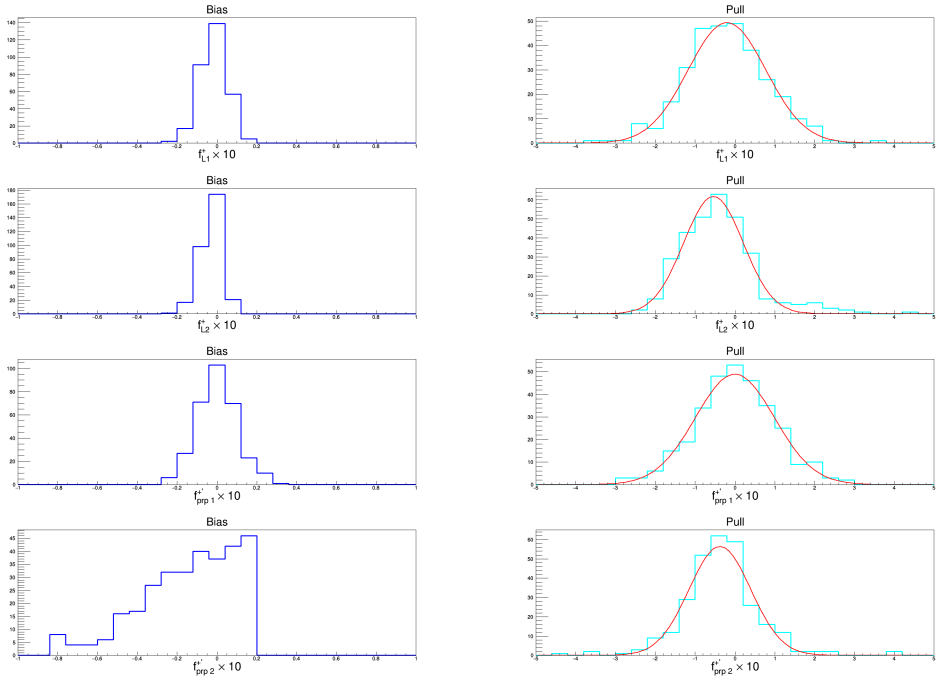

Figure 10.63: Bias and pull distributions for amplitude fractions for B^+ with 1x the signal.

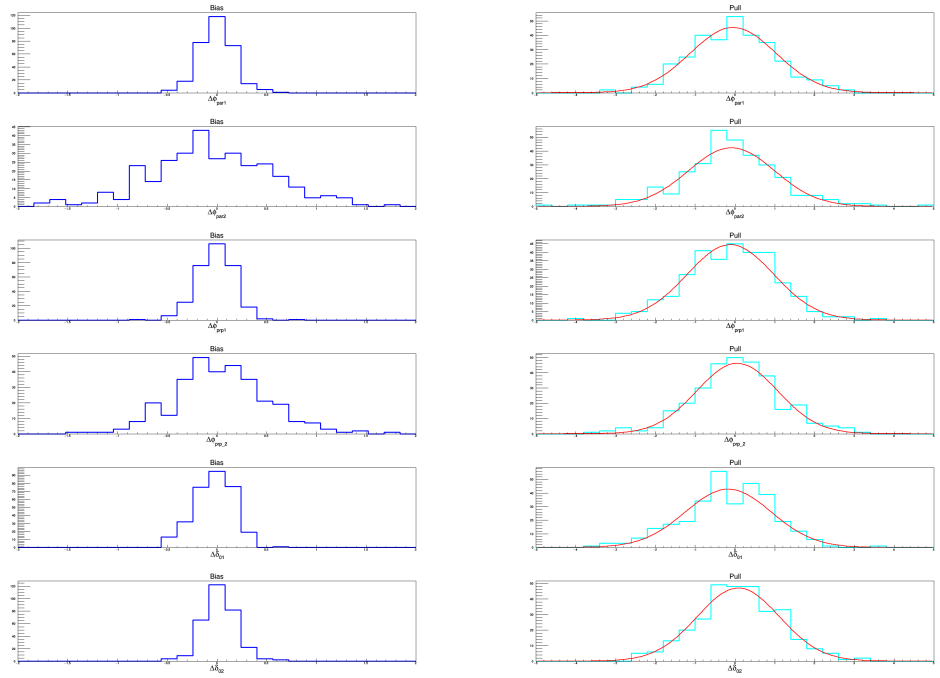

Figure 10.64: Bias and pull distributions for Δ parameters with 1x the signal.

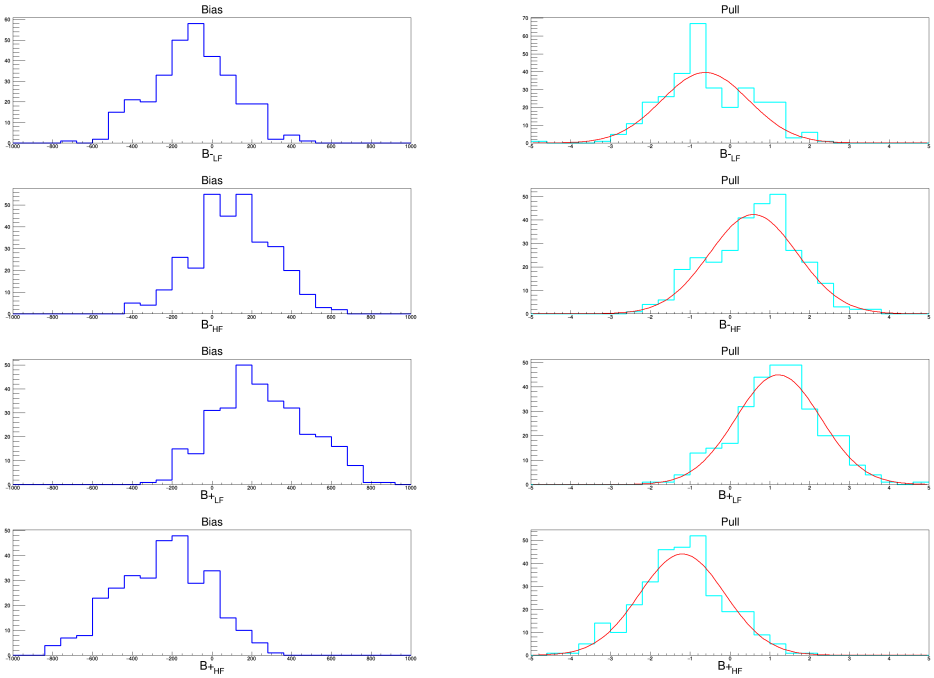

Figure 10.65: Bias and pull distributions for background parameters and 1x the signal.

10.0.3 **Full Unbinned Fits for 10x Signal Data**

In this section we present the results of the full unbinned fits for 10x signal using the Belle neutral mode parameters as shown in Figs. 10.66 through 10.101. As with the 1x fits, the 10x fits are very good. Both the input and output for each parameter are plotted in Figs. 10.102 through 10.106. In the pull and bias plots, the pull histograms are fit with a Gaussian, and fit reasonably well. From the 1x MC data sets, we get a total χ^2 of 482.2 for 403 bins (with non-zero entries). For the 10x MC data sets we get 396.6 for 380 bins with non-zero entries.

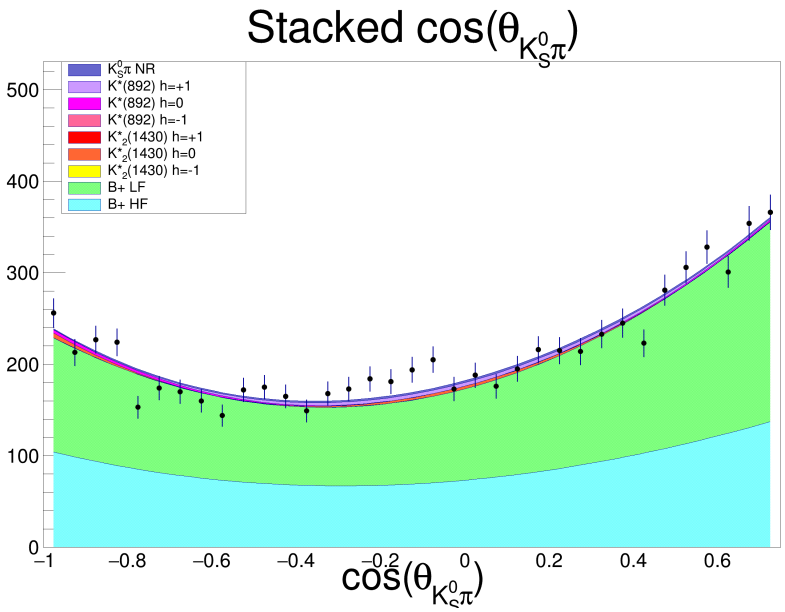

Figure 10.66: Fit to $cos(\theta_{K^0_S\pi})$ for B^+ signal and background.

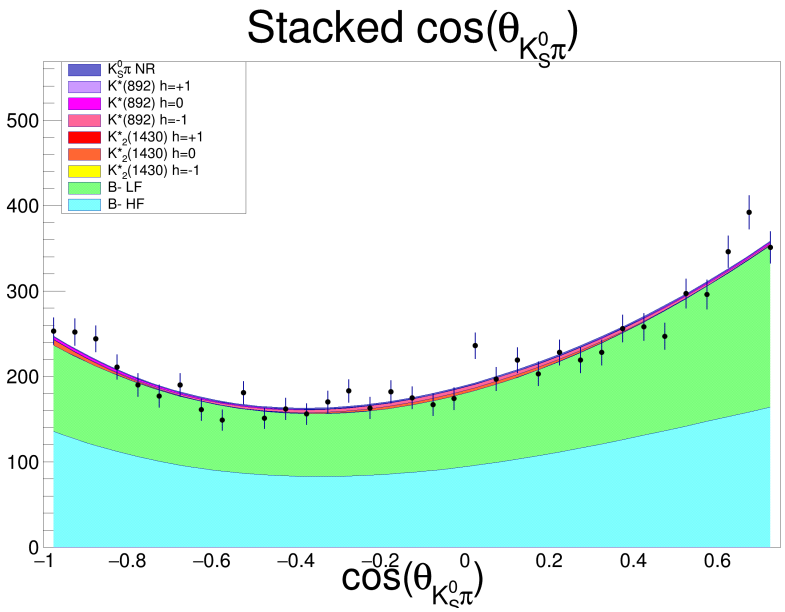

Figure 10.67: Fit to $cos(\theta_{K^0_S\pi})$ for B^- signal and background.

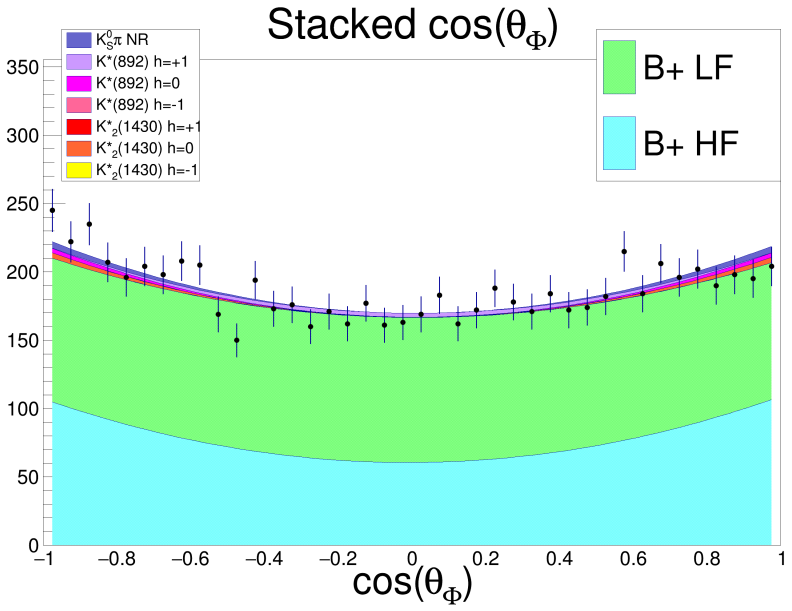

Figure 10.68: Fit to $cos(\theta_\Phi)$ for B^+ signal and background.

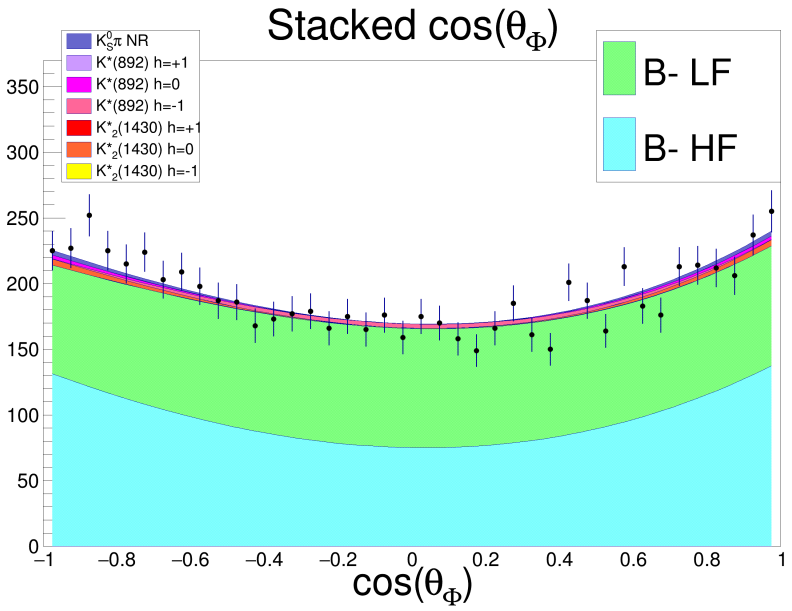

Figure 10.69: Fit to $cos(\theta_\Phi)$ for B^- signal and background.

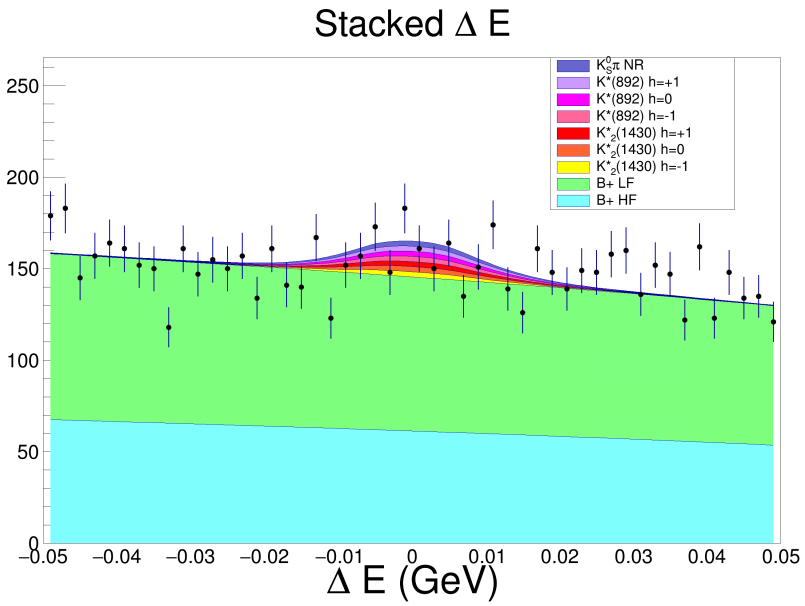

Figure 10.70: Fit to ΔE for B^+ signal and background.

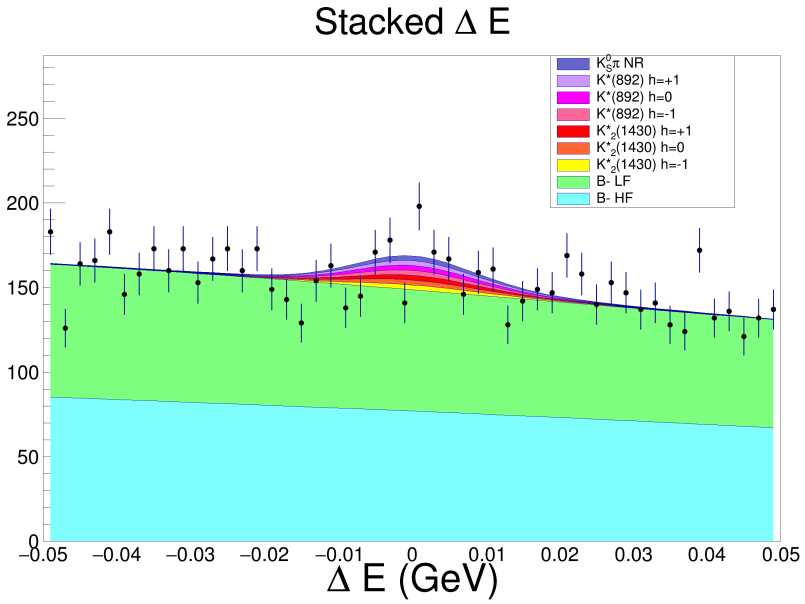

Figure 10.71: Fit to ΔE for B^- signal and background.

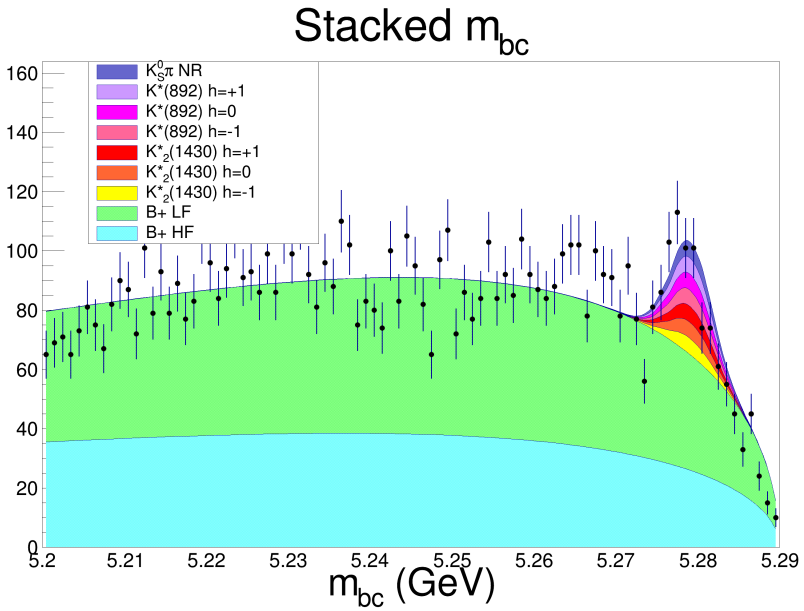

Figure 10.72: Fit to m_{bc} for B^+ signal and background.

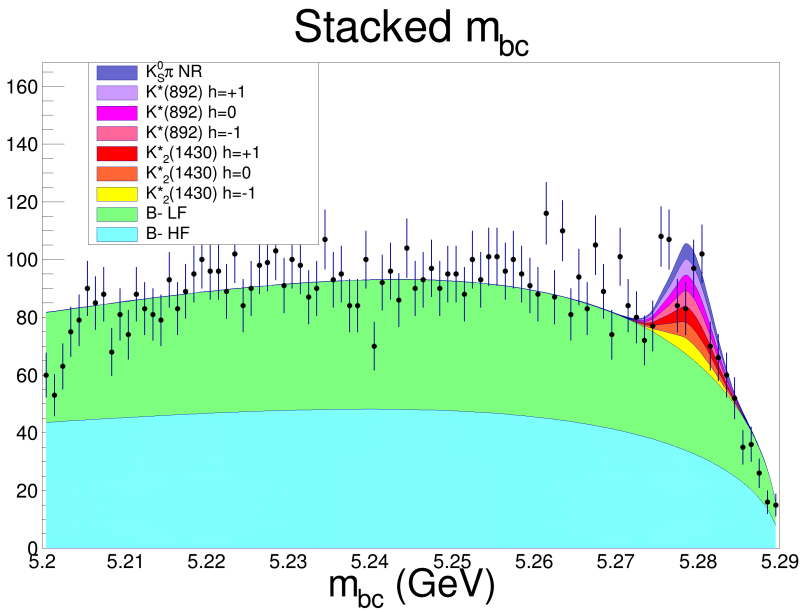

Figure 10.73: Fit to m_{bc} for B^- signal and background.

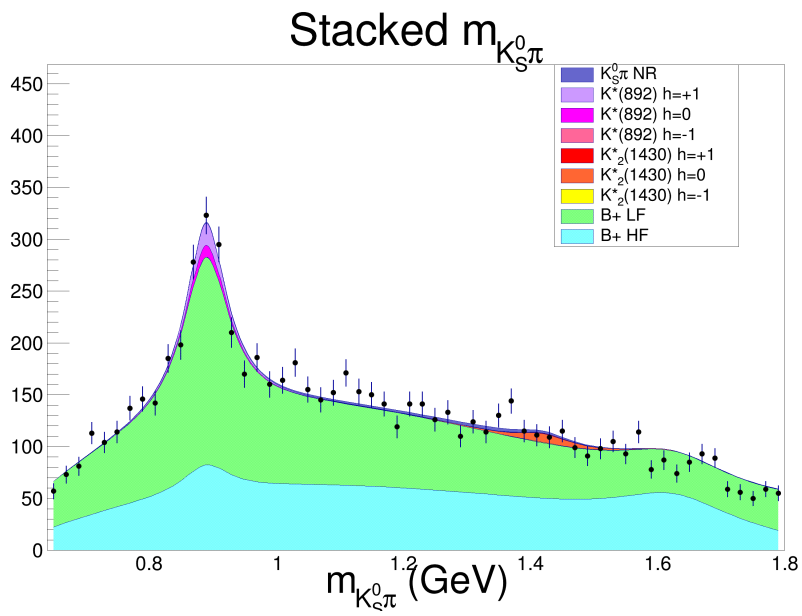

Figure 10.74: Fit to $m_{K^0_S\pi}$ for B^+ signal and background.

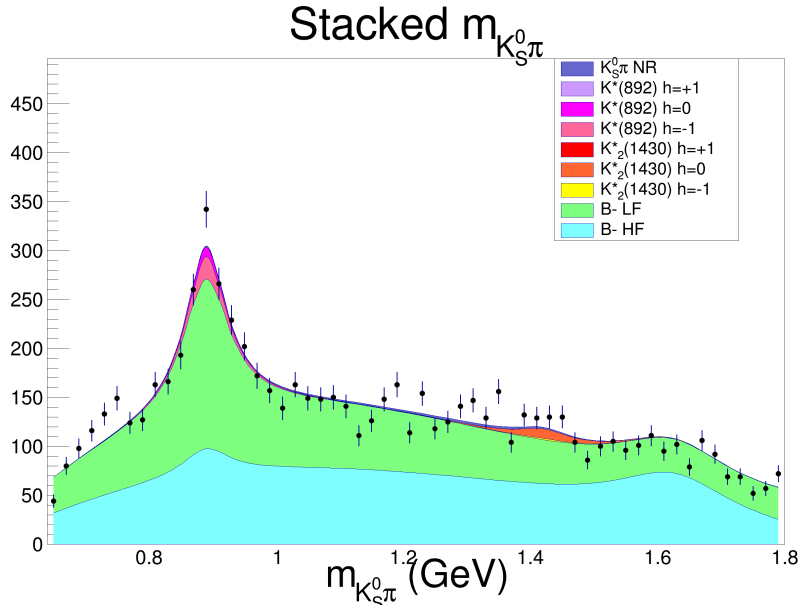

Figure 10.75: Fit to $m_{K^0_S\pi}$ for B^- signal and background.

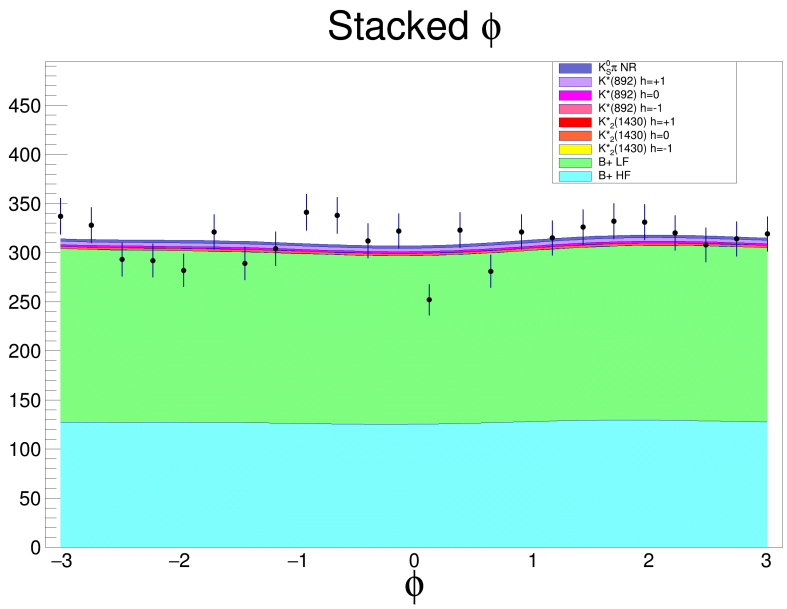

Figure 10.76: Fit to Φ for B^+ signal and background.

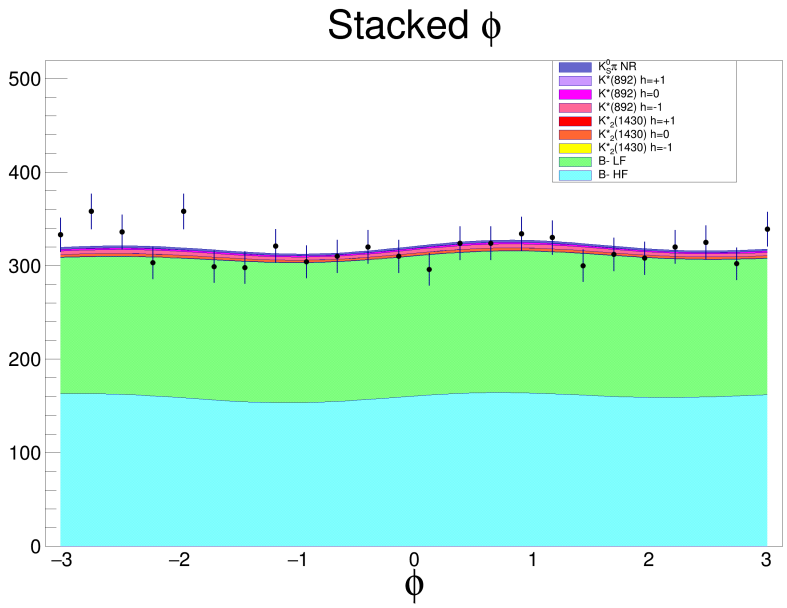

Figure 10.77: Fit to Φ for B^- signal and background.

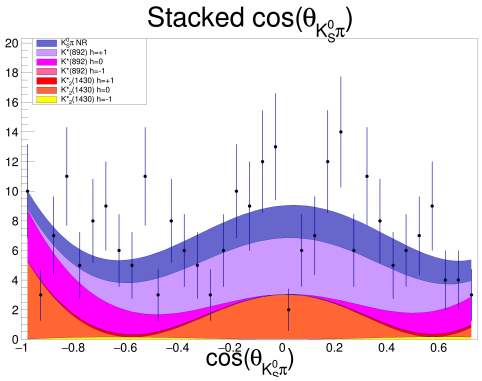

Figure 10.78: Fit to $cos(\theta_{K^0_S\pi})$ for B^+ signal.

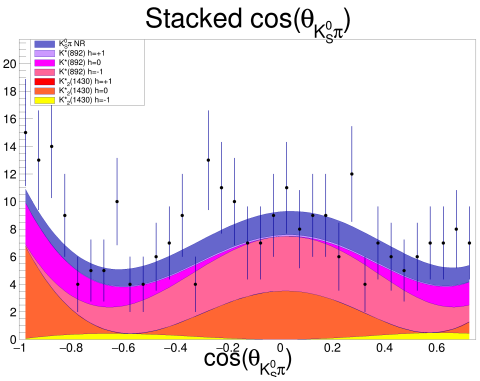

Figure 10.79: Fit to $cos(\theta_{K^0_S\pi})$ for B^- signal.

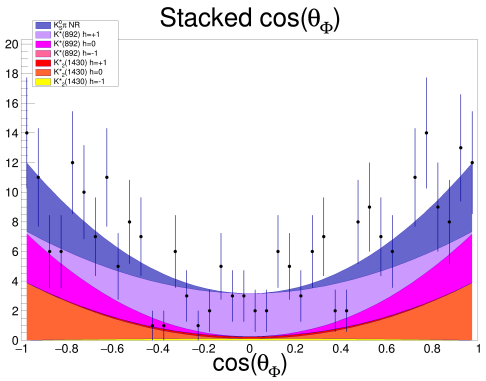

Figure 10.80: Fit to $cos(\theta_\Phi)$ for B^+ signal.

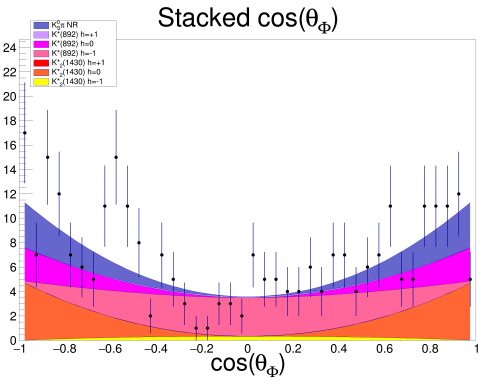

Figure 10.81: Fit to $cos(\theta_\Phi)$ for B^- signal.

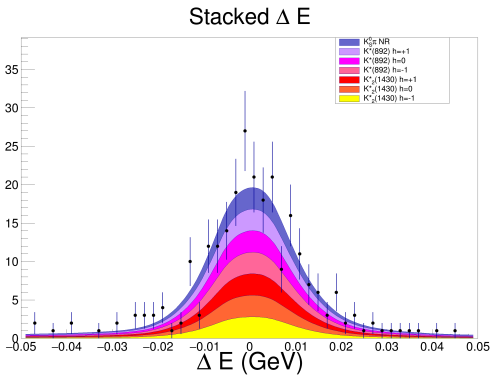

Figure 10.82: Fit to ΔE for B^+ signal.

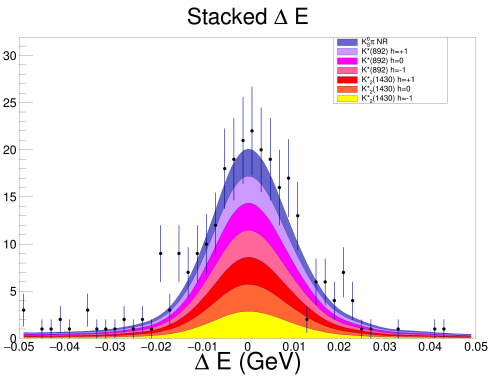

Figure 10.83: Fit to ΔE for B^- signal.

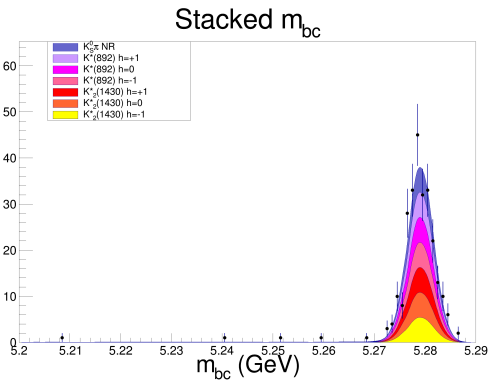

Figure 10.84: Fit to m_{bc} for B^+ signal.

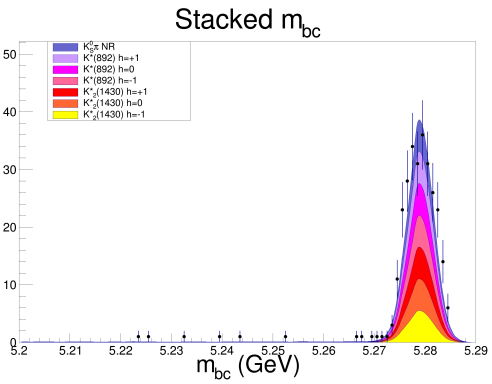

Figure 10.85: Fit to m_{bc} for B^- signal.

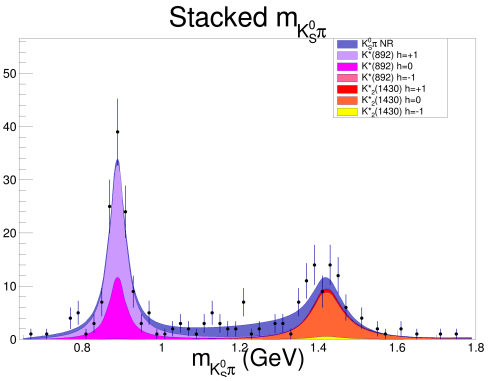

Figure 10.86: Fit to $m_{K^0_S\pi}$ for B^+ signal.

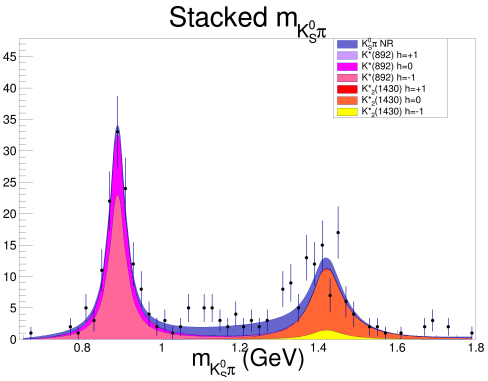

Figure 10.87: Fit to $m_{K^0_S\pi}$ for B^- signal.

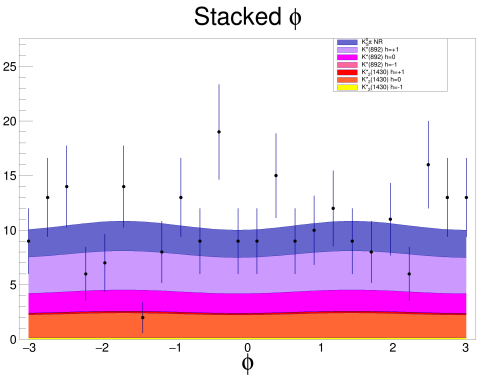

Figure 10.88: Fit to Φ for B^+ signal.

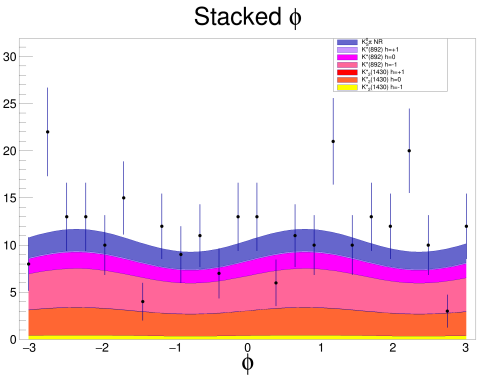

Figure 10.89: Fit to Φ for B^- signal.

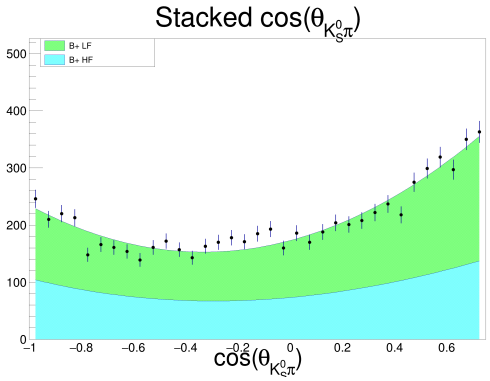

Figure 10.90: Fit to $cos(\theta_{K^0_S\pi})$ for B^+ background.

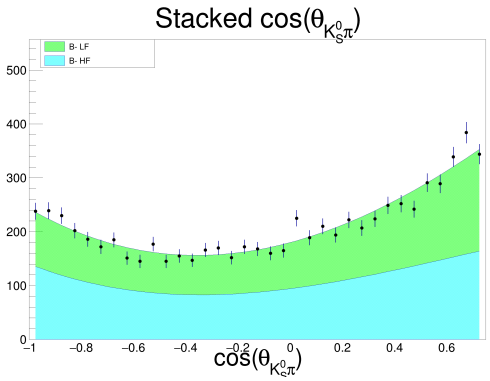

Figure 10.91: Fit to $cos(\theta_{K^0_S\pi})$ for B^- background.

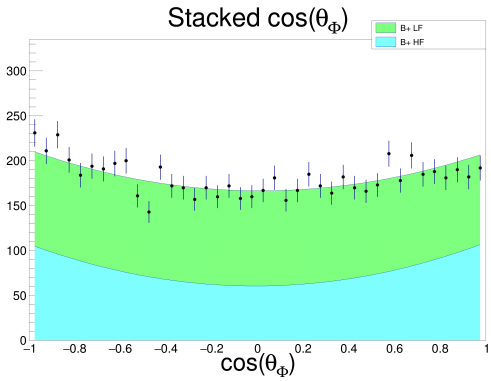

Figure 10.92: Fit to $cos(\theta_\Phi)$ for B^+ background.

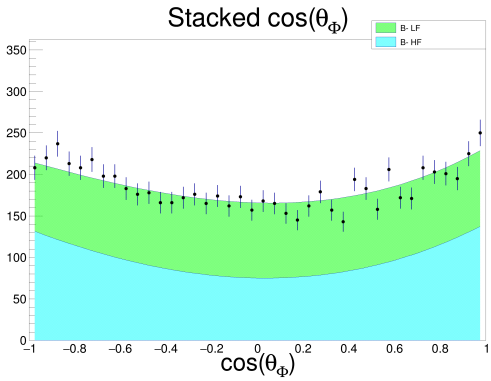

Figure 10.93: Fit to $cos(\theta_\Phi)$ for B^- background.

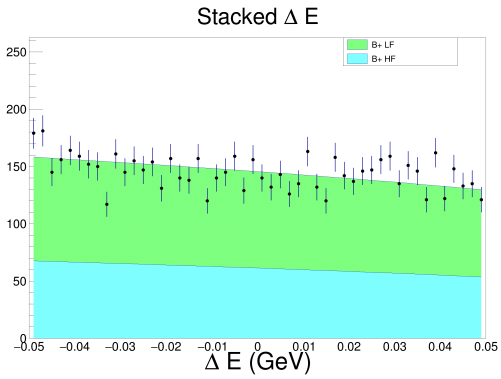

Figure 10.94: Fit to ΔE for B^+ background.

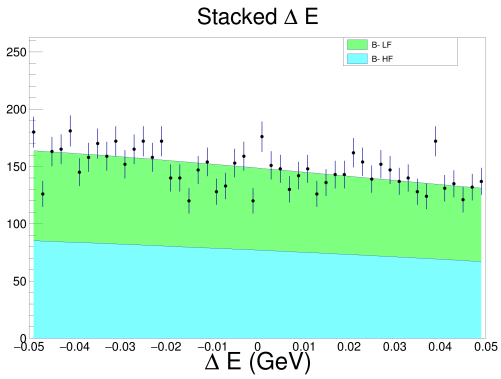

Figure 10.95: Fit to ΔE for B^- background.

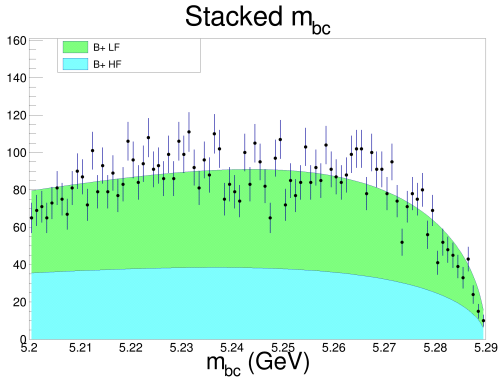

Figure 10.96: Fit to m_{bc} for B^+ background.

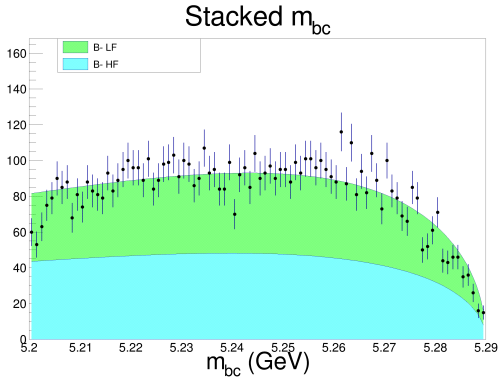

Figure 10.97: Fit to m_{bc} for B^- background.

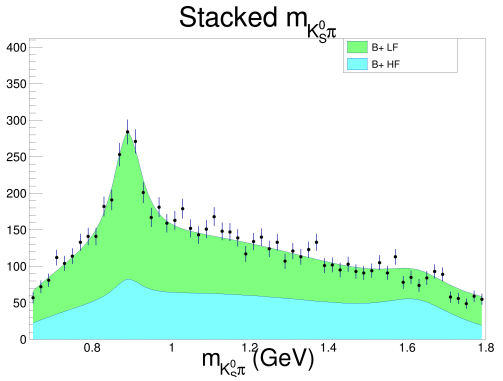

Figure 10.98: Fit to $m_{K_S^0\pi}$ for B^+ background.

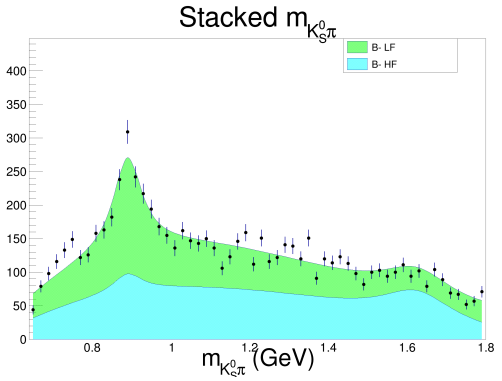

Figure 10.99: Fit to $m_{K_S^0\pi}$ for B^- background.

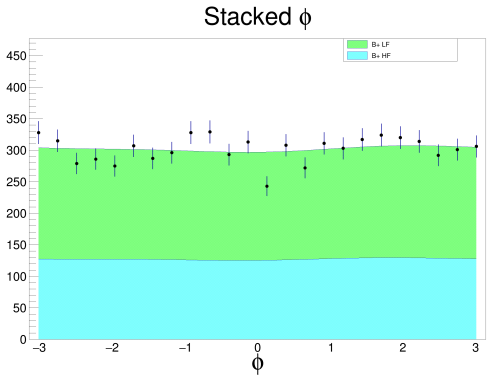

Figure 10.100: Fit to Φ for B^+ background.

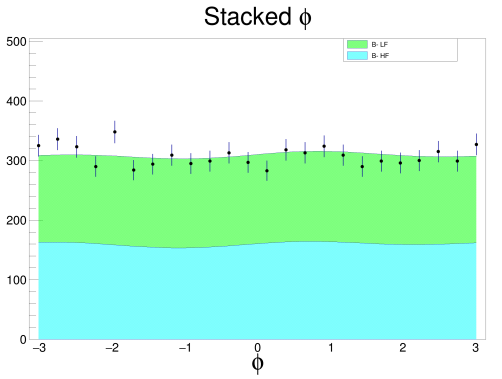

Figure 10.101: Fit to Φ for B^- background.

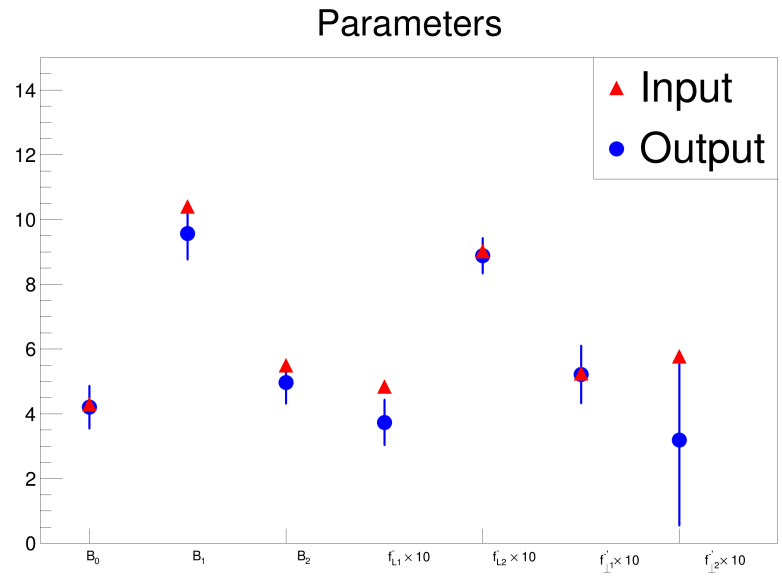

Figure 10.102: Branching fraction and f_L fitter input and output parameters

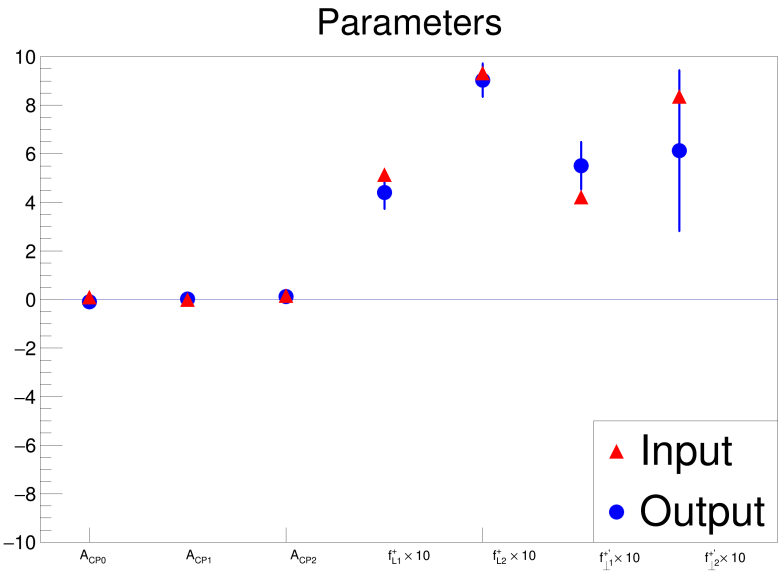

Figure 10.103: A_{CP} and f_L fitter input and output parameters.

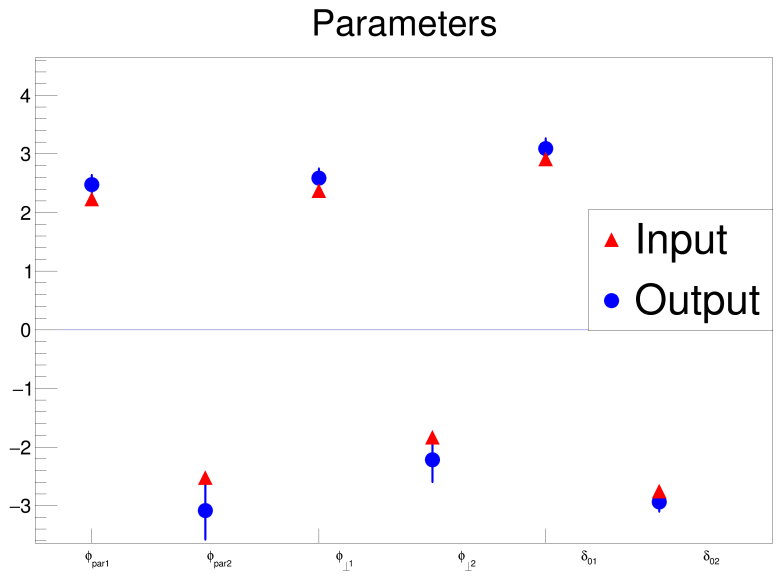

Figure 10.104: Angular fitter input and output parameters.

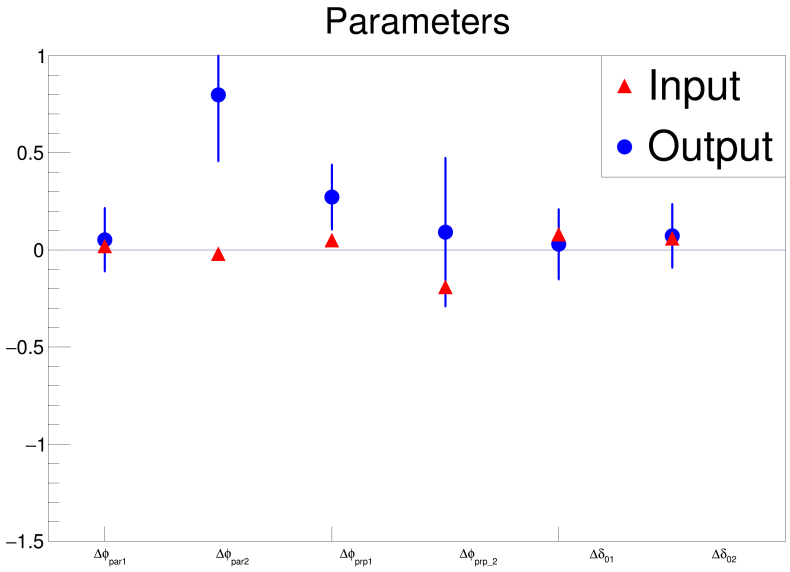

Figure 10.105: Difference in the angular parameters for fitter input and output.

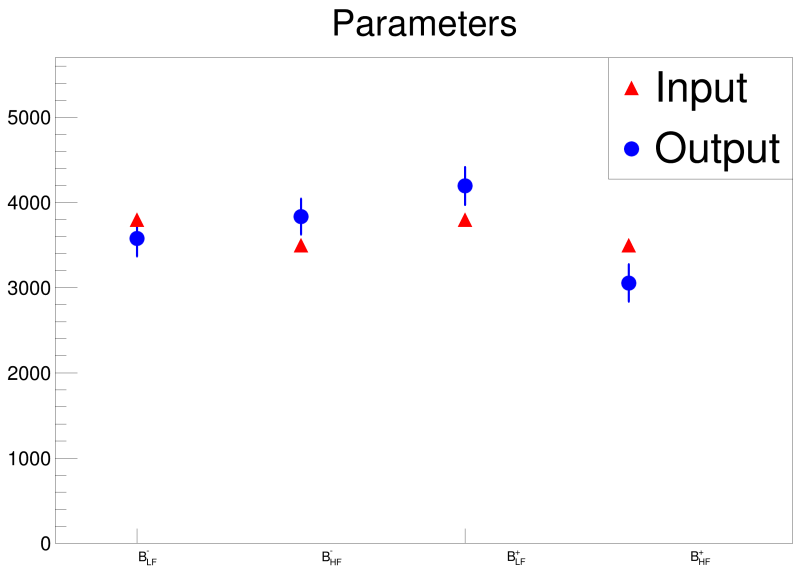

Figure 10.106: Input and output number of B^+ and B^- heavy flavor and light flavor backgrounds.

10.0.4 **Bias and Pulls for 10x Signal Data**

For each parameter to the fit, we created a bias plot and pull to describe one fit of 10x toy MC. The bias is defined as (output - input) for each parameter and the pull is defined as bias / (MINUIT error) for each parameter. Table 10.4 summarizes the bias mean and the pull RMS for 320 toy MC data outputs. All pulls have RMS close to 1 and there are no significant biases in the signal parameters.

Table 10.4 Input Values, Bias Means, and Pull RMS for 10x Signal Fits to 320 Toy MC Data Sets

	Parameter	Input	Bias Mean	Par Err	Pull RMS
1	$B_0(ppm)$	43.0000	-0.3458 ± 0.1033	1.8473	1.0452 ± 0.0413
2	$B_1(ppm)$	104.0000	-1.0059 ± 0.1432	2.5609	1.0866 ± 0.0429
3	$B_2(ppm)$	55.0000	-0.3974 ± 0.1084	1.9388	1.0447 ± 0.0413
4	$f_{L1}^{-} \times 10$	0.4840	-0.0028 ± 0.0010	0.0186	1.0012 ± 0.0396
5	$f_{L2}^{-} \times 10$	0.9030	-0.0014 ± 0.0007	0.0129	0.9891 ± 0.0391
6	$f_{\perp 1}^{-\prime} \times 10$	0.5250	0.0017 ± 0.0016	0.0278	1.0147 ± 0.0401
7	$f_{\perp 2}^{-\prime} \times 10$	0.5770	-0.0077 ± 0.0044	0.0790	1.0499 ± 0.0415
8	$\phi_{\parallel 1}$	2.2300	-0.0042 ± 0.0024	0.0432	1.0700 ± 0.0423
9	ϕ_{par2}	-2.5232	-0.0233 ± 0.0110	0.1969	1.0959 ± 0.0433
10	$\phi_{\perp 1}$	2.3700	-0.0006 ± 0.0026	0.0467	1.1084 ± 0.0438
11	$\phi_{\perp 2}$	-1.8332	0.0183 ± 0.0068	0.1213	1.0975 ± 0.0434
12	δ_{01}	2.9100	-0.0099 ± 0.0027	0.0477	1.0556 ± 0.0417
13	δ_{02}	-2.7532	-0.0017 ± 0.0025	0.0443	1.1198 ± 0.0443
14	A_{CP0}	0.0930	-0.0091 ± 0.0025	0.0441	1.0732 ± 0.0424
15	A_{CP1}	-0.0070	0.0020 ± 0.0013	0.0240	1.0527 ± 0.0416
16	A_{CP2}	0.1550	0.0011 ± 0.0019	0.0346	1.0301 ± 0.0407
17	$f_{L1}^{+} \times 10$	0.5140	-0.0029 ± 0.0010	0.0187	1.0344 ± 0.0409
18	$f_{L2}^{+} \times 10$	0.9330	-0.0036 ± 0.0007	0.0124	0.9357 ± 0.0370
19	$f_{\perp 1}^{+\prime} \times 10$	0.4220	0.0039 ± 0.0016	0.0280	1.0115 ± 0.0400
20	$f_{\perp 2}^{+\prime} \times 10$	0.8360	-0.0164 ± 0.0045	0.0797	1.0683 ± 0.0422
21	$\Delta\phi_{\parallel 1}$	0.0200	0.0071 ± 0.0023	0.0420	1.0361 ± 0.0410
22	$\Delta\phi_{\parallel 2}$	-0.0200	0.0091 ± 0.0107	0.1917	1.0648 ± 0.0421
23	$\Delta\phi_{\perp 1}$	0.0500	-0.0016 ± 0.0025	0.0442	1.0406 ± 0.0411
24	$\Delta\phi_{\perp 2}$	-0.1900	-0.0077 ± 0.0069	0.1243	1.1250 ± 0.0445
25	$\Delta\delta_{01}$	0.0800	-0.0011 ± 0.0025	0.0449	0.9969 ± 0.0394
26	$\Delta\delta_{02}$	0.0600	-0.0006 ± 0.0026	0.0456	1.1326 ± 0.0448
27	B_{LF}^{-}	3800	-88.63 ± 11.53	206.22	1.0939 ± 0.0432
28	B_{HF}^{-}	3500	113.73 ± 11.54	206.34	1.0368 ± 0.0410
29	B_{LF}^{+}	3800	266.79 ± 13.41	239.93	1.0743 ± 0.0425
30	B_{HF}^{+}	3500	-260.22 ± 13.26	237.16	1.0799 ± 0.0427

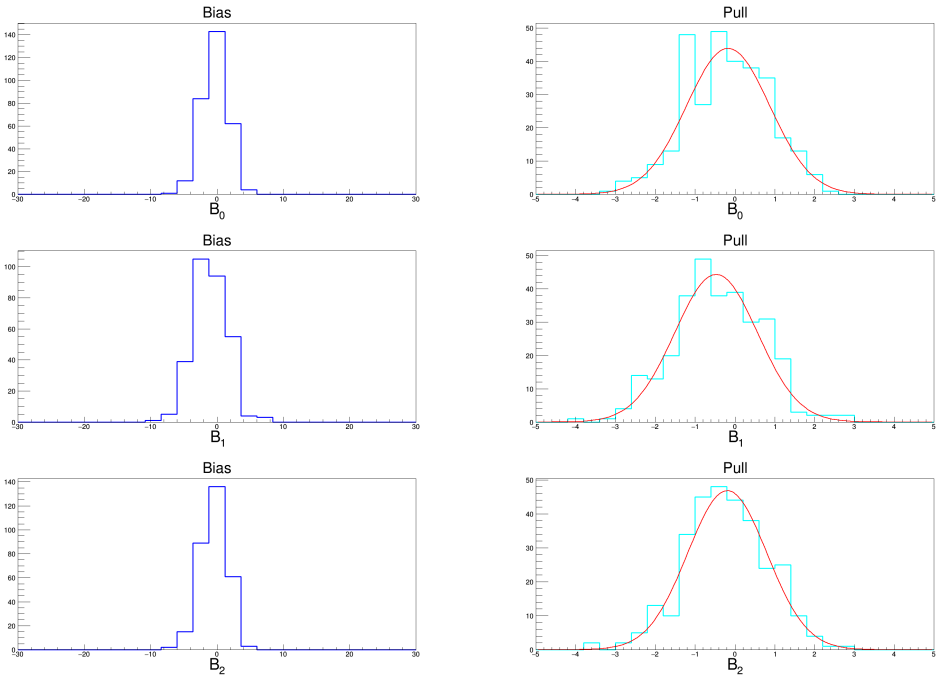

Figure 10.107: Bias and pull distributions for branching fractions with 10x the signal.

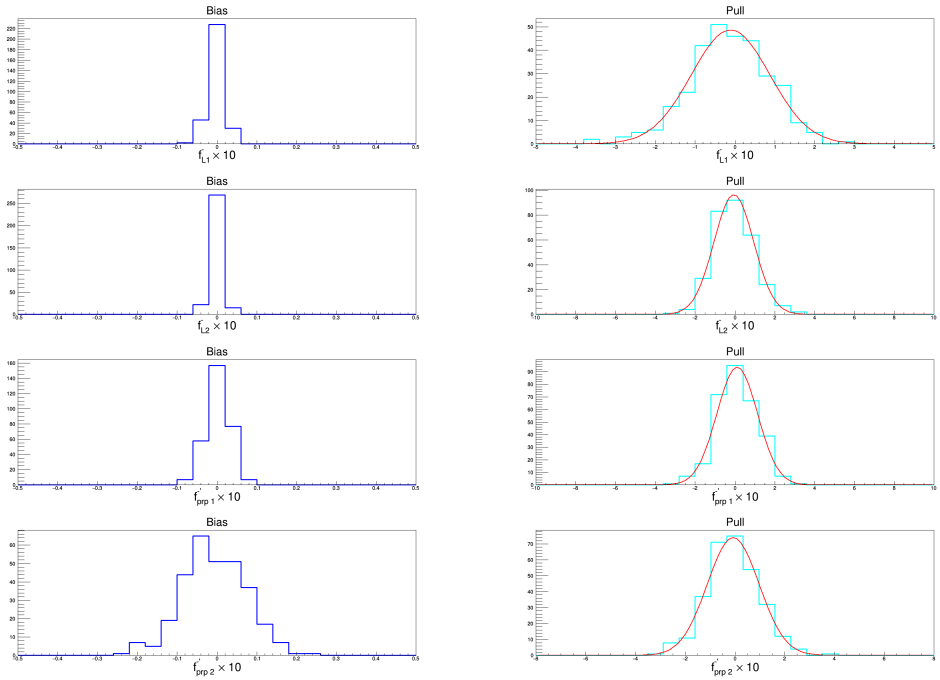

Figure 10.108: Bias and pull distributions for amplitude fractions for B^- with 10x the signal.

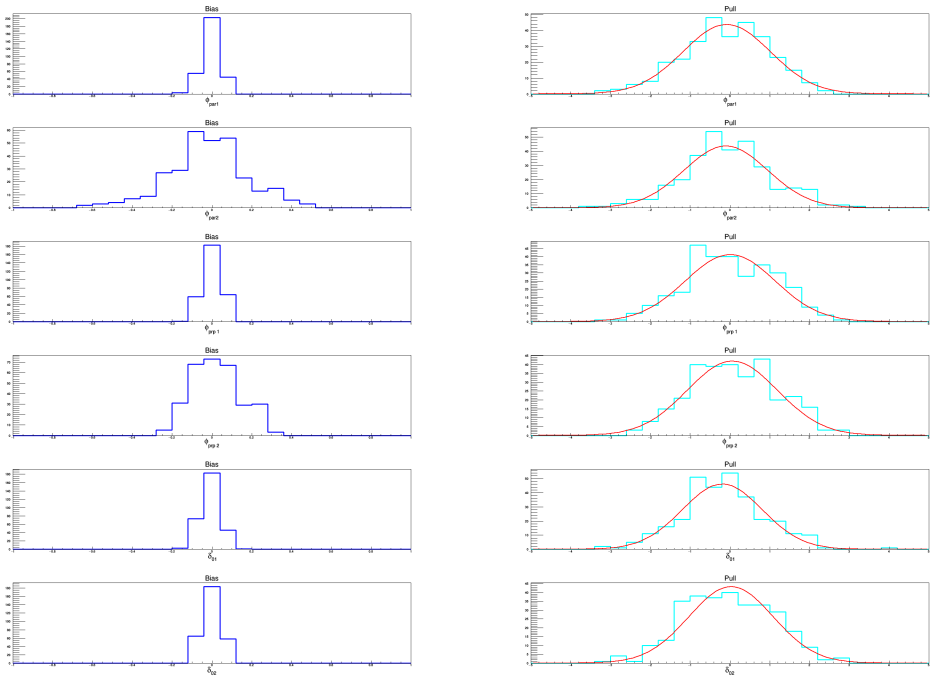

Figure 10.109: Bias and pull distributions for phases with 10x the signal.

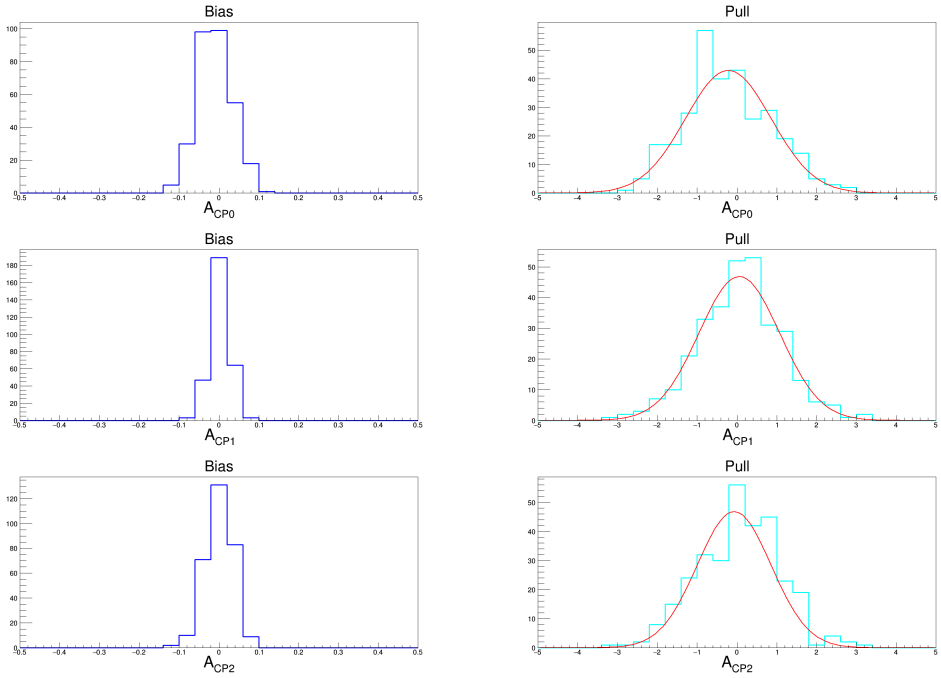

Figure 10.110: Bias and pull distributions for A_{CP} parameters with 10x the signal.

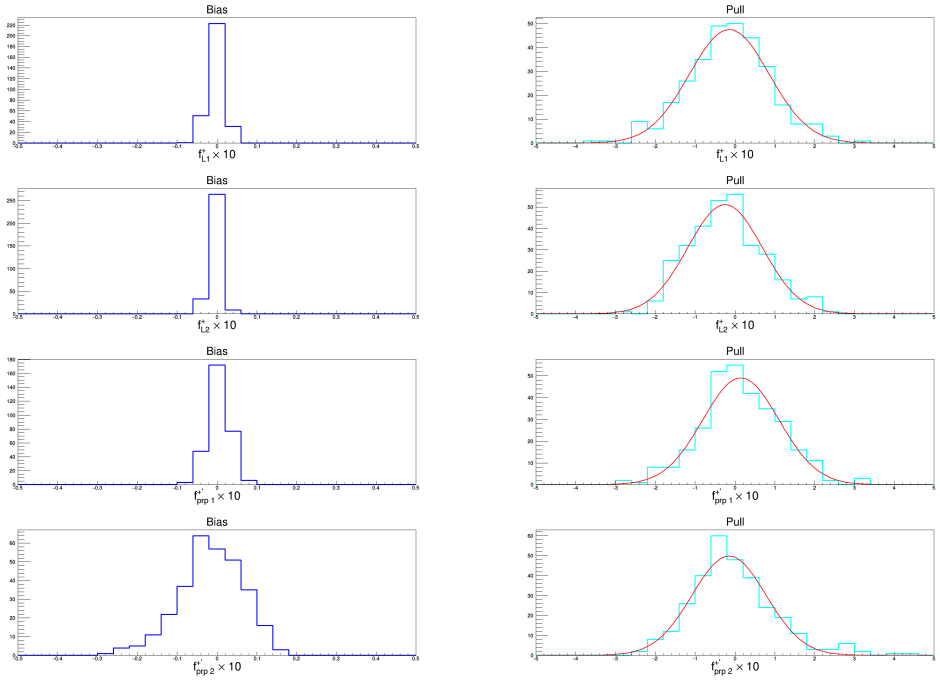

Figure 10.111: Bias and pull distributions for amplitude fractions for B^+ with 10x the signal.

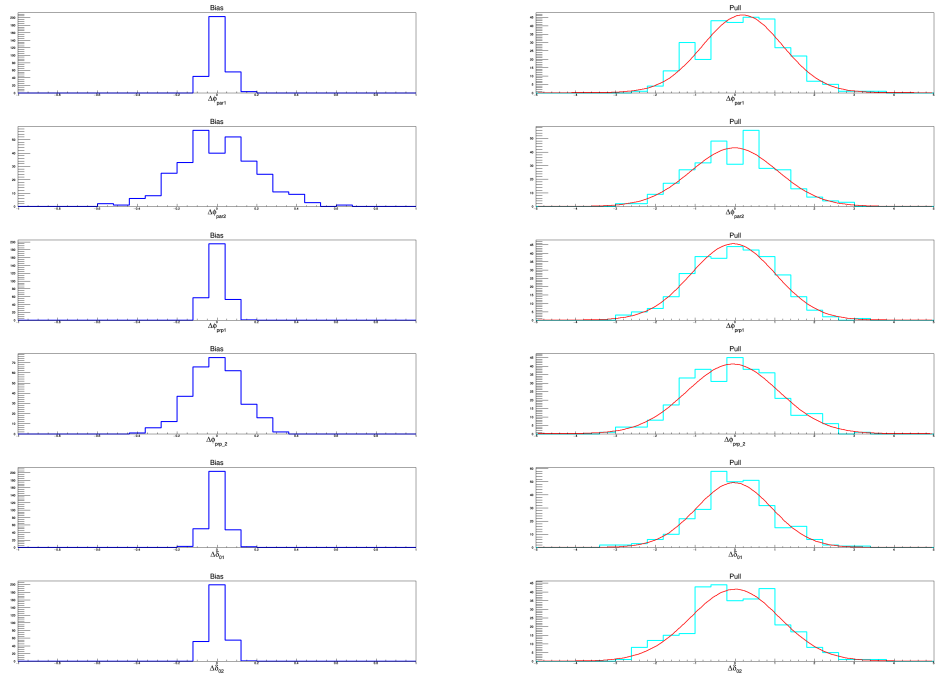

Figure 10.112: Bias and pull distributions for Δ parameters with 10x the signal.

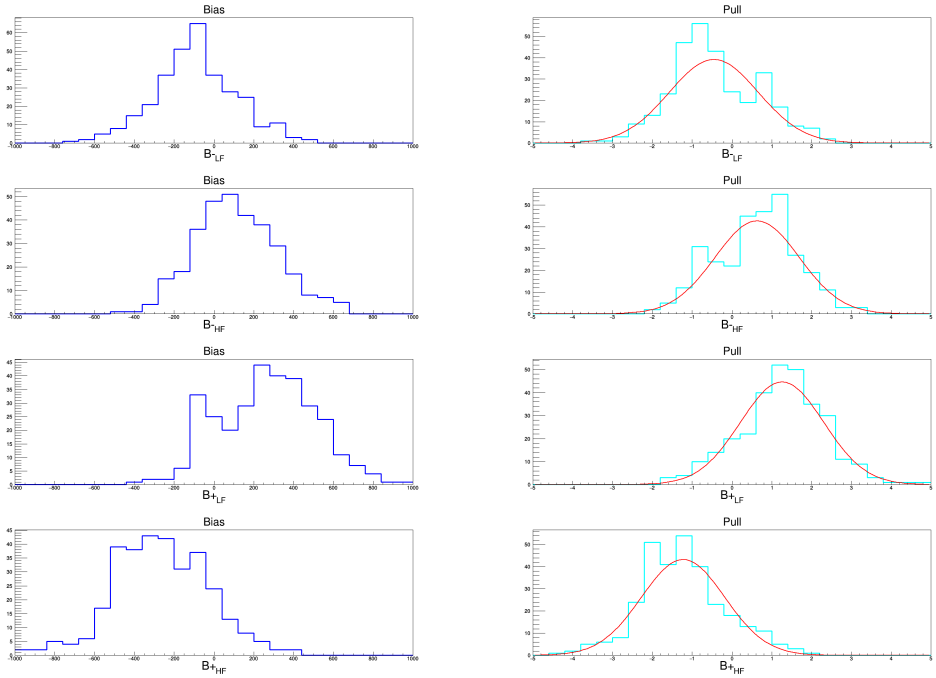

Figure 10.113: Bias and pull distributions for background parameters and 10x the signal.

Chapter 11

The Control Mode

In this chapter we explain our studies with our control mode, $B^+ \to \overline{D}^0\pi^+$ (and c.c.) where the neutral D-meson decays to $\overline{K}^0\pi^+\pi^-$, and the neutral K-meson becomes K^0_S which in turn decays to two charged pions. We use the control mode for three things. First, we check if our event shape discriminant, a'_1, distribution is modeled correctly by the MC. To do this we compare the MC distribution with data. Secondly, we compare the width of the ΔE distribution between MC and data. And lastly, we check if the the BF for the control mode agrees with the PDG value.

Fits to the control mode a'_1 distribution can be seen in Figs. 11.1 and 11.2. These plots show the widths are similar, and they display the MC signal fit. Note that the curve in Fig. 11.1 does not fit the data very well, which is why we measure the efficiency three different ways and take the spread in the values so obtained as a measure of systematic error. To repeat, we measure the efficiency three different ways: from the signal MC fit (red curve in Fig. 11.1), from the signal histogram (blue line in Fig. 11.1), and from the data fit (right blue curve in Fig. 11.2) and then take the systematic error to be 3%, the rough spread in the values. To find the efficiency of a cut on a'_1 distribution, we look at what fraction of event lie above the cut. Using an $ANN_1 > 0.2$ which is about $a'_1 > -0.22$, we find 91.8%, 88.7%, and (91.8 ± 0.6)% respectively for the signal MC, signal histogram, and data fits. [Note: two of the percentages have statistical uncertainty, however they are too small to even mention]. This means there is a 3% uncertainty in the ANN_1 cut efficiency.

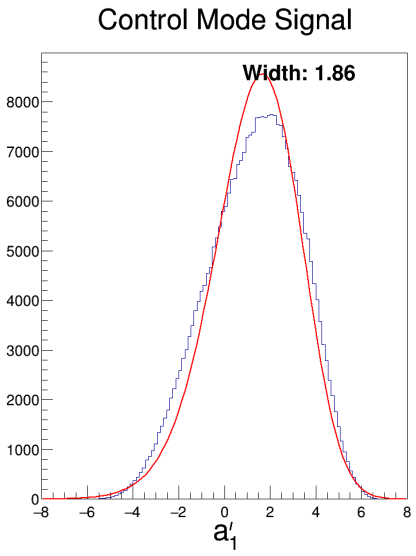

Figure 11.1: Fit to a_1' for $B^+ \to \overline{D}^0\pi^+$ MC events.

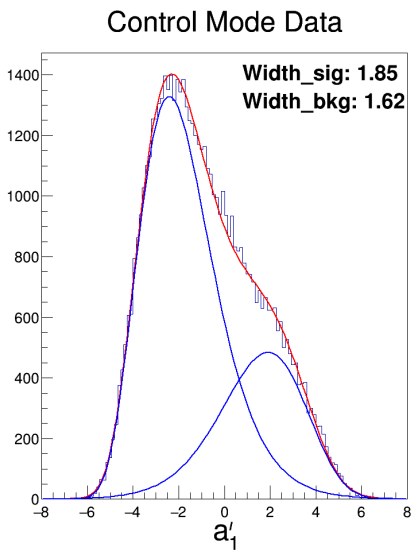

Figure 11.2: Fit to a_1' for $B^+ \to \overline{D}^0\pi^+$ data events.

Figs. 11.3 through 11.6 show the distributions for ΔE and m_{D^0} for control mode MC and data. Note we used m_{D^0} because the m_{bc} variable was not available for this mode. There is $\sim$20% difference between the MC and data distribution widths. It is important to note that we avoid the problem of data/ MC differences by fitting the data distributions in the signal and background discriminating variables m_{bc} and ΔE first and then use the result in our final fit.

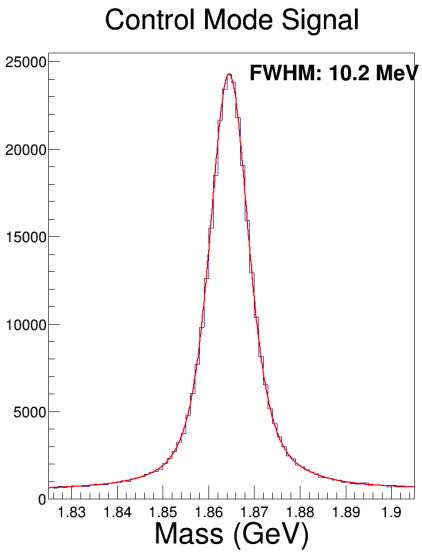

Figure 11.3: Fit to $m(D^0)$ for $B^+ \to \overline{D}^0\pi^+$ MC events.

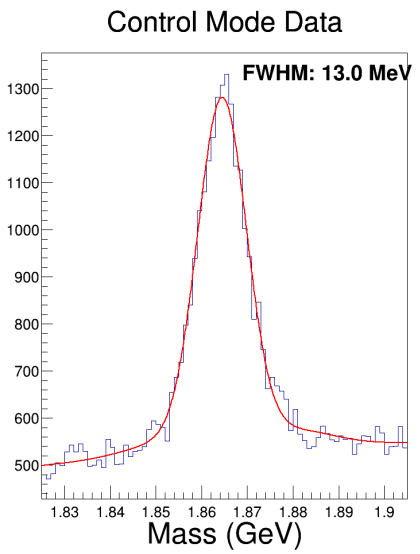

Figure 11.4: Fit to $m(D^0)$ for $B^+ \to \overline{D}^0\pi^+$ data events.

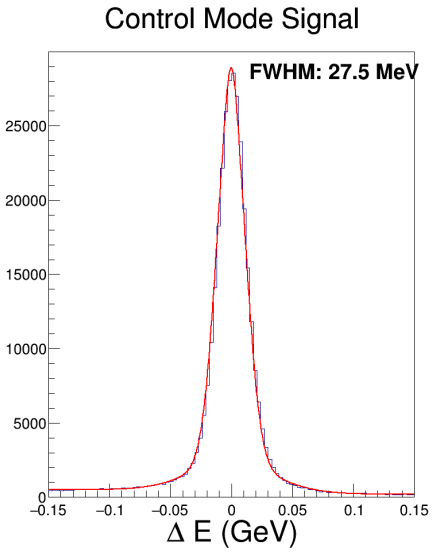

Figure 11.5: Fit to ΔE for $B^+ \to \overline{D}^0\pi^+$ MC events.

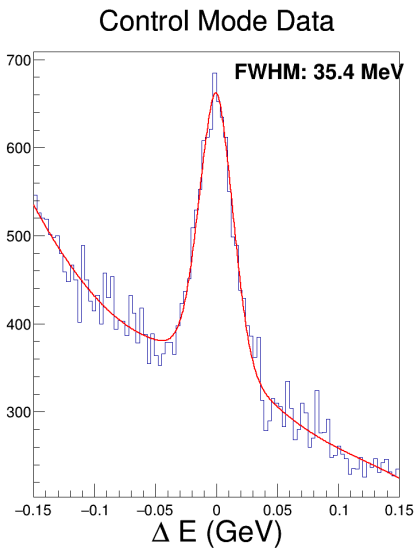

Figure 11.6: Fit to ΔE for $B^+ \to \overline{D}^0\pi^+$ data events.

For each of the Figs. 11.3 through 11.6 we find the number of signal and background events from the fit. These numbers can be seen in table 11.1. Using the number of $b\bar{b}$ pairs produced by Belle, $(771.581 \pm 10.566) \times 10^6$ [13], we find the BF for the control mode to be $(4.55 \pm 0.35) \times 10^{-3}$ using the ΔE fits, and $(5.12 \pm 0.38) \times 10^{-3}$

using the m_{D^0} fits. These numbers are in good agreement with the PDG value of $(4.80 \pm 0.15) \times 10^{-3}$. Our large errors, in comparison to the PDG error, come from the fact that the PDG uses a decay mode that is more copious in D^0's to measure its BF.

Table 11.1 Yields for Data and MC Signals from the Control Mode Study

	Number of Entries	N_S	N_B
m_{D0} data	53379	22143 ± 705	31170 ± 707
m_{D0} MC	301001	286459 ± 3191	14468 ± 3152
ΔE data	77673	19105 ± 709	58486 ± 736
ΔE MC	295447	278397 ± 556	16149 ± 216

Chapter 12

Systematics

12.0.1 **Radiative Corrections**

Kaons and pions radiate due to acceleration in strong fields as they emerge from the interaction region. We used 750,000 simulated events to study the energy radiated by a photon from kaons and pions. To do this we had a program sort through the truth tables of the signal decays to find when photons are emitted with a certain energy. We found that the average energy of a photon, with energy $E_\gamma > 10$ MeV, was radiated from a pion was 1.64 GeV. Approximately 1.2% of events had a radiated photon which would be lost down the beam-pipe and then the B decay cannot be reconstructed. The BF thus would have to be corrected upward of a value of 1.2%. This percentage is too small to study further. Only 198 events were found where kaons radiated a photon. The average radiated energy was 1.36 GeV. We expected that kaons radiate much less due to their higher mass (radiation of photons goes like the square of the acceleration (from the Larmor formula) and is thus much smaller for the higher mass kaons).

Figs. 12.1, 12.2 show distributions of the photon energy for the kaon and pion events.

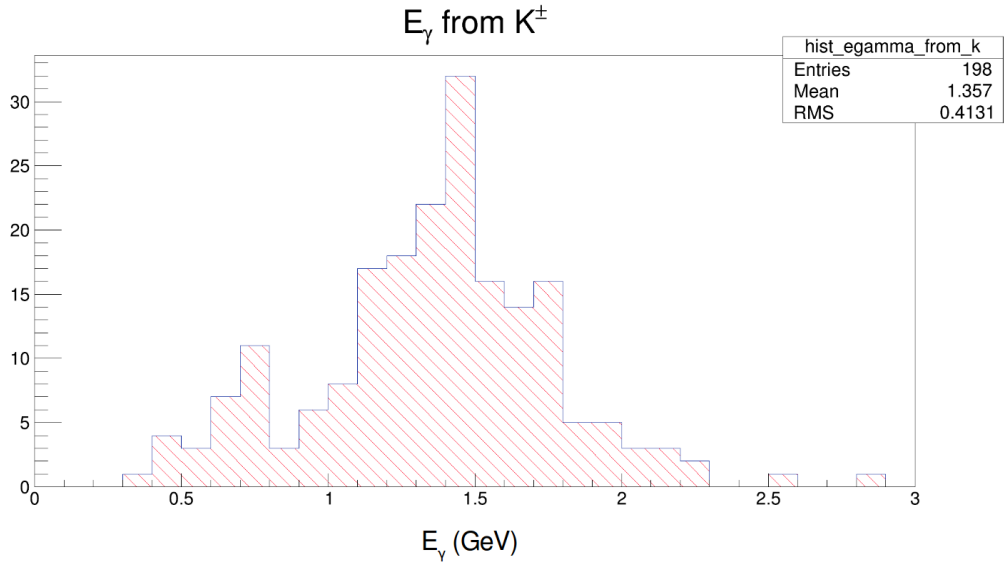

Figure 12.1: Energy of photons radiated from kaon decays.

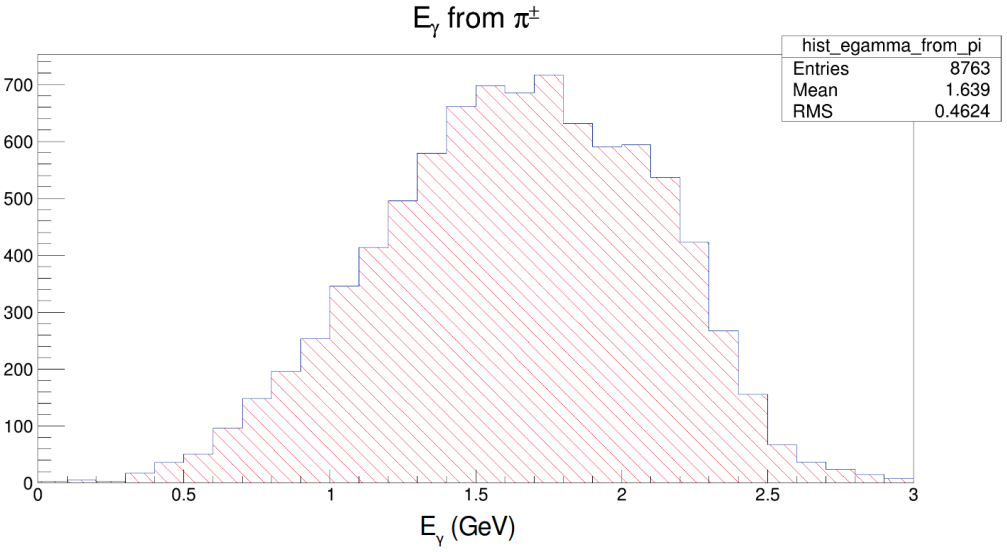

Figure 12.2: Energy of photons radiated from pion decays.

12.0.2 Systematic uncertainties that apply to Branching Fractions only

We have two classifications for our systematics: those that apply to the overall yields, i.e., to branching fractions only, and those that apply to all parameters. In this subsection, we will be addressing the systematic errors that effect our BF's.

From our 1x fake data sets, we expect statistical uncertainties on the order of 16%, 8%, and 12% respectively for the $J = 0$, $J = 1$, and $J = 2$ modes. Comparing our analysis with the Belle neutral mode, [13], we know that we will have a smaller PID systematic since the neutral mode has three charged kaons and we have two. We expect larger fractional statistical errors. This means that we can afford to be less concerned with the smaller systematic effects than the neutral mode analysis.

The Belle established tracking efficiency uncertainty is taken to be 0.35% for charged pions [13]. For the K^0_S's we take the Belle FindKs PID uncertainty algorithm result (weighting theirs to match our momentum spectrum), giving 0.83%, and similarly for the nisKsFinder which yields 0.94% [32] [33]. We use 0.94% for the K^0_S's, which is the larger of the two uncertainties obtained.

We took the charged kaon PID efficiency systematic to be 2.2%, which was derived from the neutral mode where the PID uncertainty of the three charged kaons taken together was taken assigned a value of 3.3% [13]. The uncertainty in the number of $B\overline{B}$ pairs is widely approximated in Belle papers [13] as 1.4%. The uncertainty on the K^*_2 and ϕ branching fractions are taken to be 2.4%, and 1.0% respectively [26]. As explained in the previous subsection, 11, we assumed an uncertainty of 3.0% in the ANN_1 cut efficiency.

12.0.3 Systematic uncertainties that apply to all parameters

In this subsection we are focusing less on the uncertainties in the BF. We are more concerned with the uncertainty in modeling the shapes of the distributions of variables. We are expecting major sources of uncertainties to be from the efficiency model

(such as dependence on cos(θ)) and due to the different modeling of signal and background pdfs in the S/B discrimination variables a_1', a_2', m_{bc}, and ΔE. To find these uncertainties, we replaced our pdf models for S/B variables with 1D models and we replaced our efficiency double-cubic function with a linear function of cos(θ) as shown in Eq. (12.1)

$$\epsilon = \begin{cases} 0.21 + \frac{0.06(cos(\theta_{K^0_S\pi})-0.15)}{1.15} & \text{for } cos\theta_{K^0_S\pi} < 0.15 \\ 0.2 & \text{for } cos\theta_{K^0_S\pi} > 0.15 \end{cases} \tag{12.1}$$

The results of these model changes are shown in tables 12.1 and 12.2. As described in the neutral mode analysis [13], the uncertainties due to the self-cross-feed (SCF), the interference with the ϕ, and due to the uncertainties in the shape of KK mass spectrum are all of the order of 1%. We neglect these. Further this analysis has shown that the heavy flavor backgrounds are dominated by $c\bar{c}$, which implies that the SCF effects are negligible. The neutral mode also showed that the charge asymmetry effects in the efficiency were negligible. The largest uncertainty due to CP asymmetry in efficiency assigned in the neutral mode was 1.2% . They in turn calculated these from an earlier Belle analysis [34] [35].

Table 12.1 Fit Parameters, and Their Input Values, Stat. Errors, and Systematic Shifts for 1x Signal Fits to 320 Toy MC Data Sets

#	Parameter	Input	Average Output	Bkgd Model	Effy Model
1	$B_0(ppm)$	4.3	4.017 ± 0.6307	-0.12	-0.07305
2	$B_1(ppm)$	10.4	10.05 ± 0.8192	-0.2811	0.02317
3	$B_2(ppm)$	5.5	5.405 ± 0.6469	-0.1838	0.03154
4	f_{L1}^{-}	0.484	0.4718 ± 0.06613	3.424e-05	-0.002089
5	f_{L2}^{-}	0.903	0.8904 ± 0.0503	-0.0006493	0.003898
6	$f_{\perp 1}^{-\prime}$	0.525	0.5264 ± 0.09737	0.0004239	-8.803e-05
7	$f_{\perp 2}^{-\prime}$	0.577	0.5375 ± 0.2589	-0.003382	-0.001718
8	$\phi_{\parallel 1}$	2.23	2.218 ± 0.1486	0.0005635	-0.003717
9	ϕ_{par2}	-2.523	-2.975 ± 1.187	0.0362	0.03776
10	$\phi_{\perp 1}$	2.37	2.355 ± 0.1556	-0.0008137	-0.004319
11	$\phi_{\perp 2}$	-1.833	-1.763 ± 0.5042	0.002363	0.02103
12	δ_{01}	2.91	3.09 ± 0.1915	-0.001751	-0.00665
13	δ_{02}	-2.753	-2.935 ± 0.2077	-0.0004753	-0.01929
14	A_{CP0}	0.093	0.08894 ± 0.1563	-0.01042	-0.0008546
15	A_{CP1}	-0.007	0.002183 ± 0.08082	-0.006482	0.000144
16	A_{CP2}	0.155	0.1619 ± 0.1178	-0.004084	-0.001214
17	f_{L1}^{+}	0.514	0.5011 ± 0.0648	-0.0008621	-0.002127
18	f_{L2}^{+}	0.933	0.8988 ± 0.0578	-0.002534	0.002373
19	$f_{\perp 1}^{+\prime}$	0.422	0.4258 ± 0.09838	1.451e-05	-7.579e-05
20	$f_{\perp 2}^{+\prime}$	0.836	0.6961 ± 0.3199	-0.004537	0.0008575
21	$\Delta\phi_{\parallel 1}$	0.02	0.01367 ± 0.1509	0.002369	-8.152e-05
22	$\Delta\phi_{\parallel 2}$	-0.02	-0.09923 ± 0.7687	0.007548	0.02172
23	$\Delta\phi_{\perp 1}$	0.05	0.03544 ± 0.1579	0.001122	-0.0001666
24	$\Delta\phi_{\perp 2}$	-0.19	-0.1427 ± 0.512	-0.00308	-0.004939
25	$\Delta\delta_{01}$	0.08	0.05052 ± 0.1756	0.0002469	9.573e-05
26	$\Delta\delta_{02}$	0.06	0.08436 ± 0.1618	-0.005437	0.0003668
27	B_{LF}^{-}	3800	3699.5 ± 169.46	-20.482	-1.25
28	B_{HF}^{-}	3500	3608.5 ± 169.32	30.052	1.531
29	B_{LF}^{+}	3800	4054.8 ± 198.24	-27.275	-0.83371
30	B_{HF}^{+}	3500	3250 ± 196.03	32.705	0.91883

Table 12.2 Fit Parameters, and their Input Values, Stat. Errors, and Systematic Shifts for 10x Signal Fits to 320 Toy MC Data Sets

#	Parameter	Input	Average Output	Bkgd Model	Effy Model
1	$B_0(ppm)$	43	42.41 ± 1.675	-1.578	-0.7709
2	$B_1(ppm)$	104	103.1 ± 2.353	-3	0.1812
3	$B_2(ppm)$	55	55.24 ± 1.837	-1.548	0.4344
4	f_{L1}^{-}	0.484	0.4829 ± 0.01864	0.001408	-0.002182
5	f_{L2}^{-}	0.903	0.9037 ± 0.01278	0.0005254	0.004509
6	$f_{\perp 1}^{-\prime}$	0.525	0.5228 ± 0.02719	-0.0001976	-0.0003503
7	$f_{\perp 2}^{-\prime}$	0.577	0.584 ± 0.07689	-0.0006922	0.0005416
8	$\phi_{\parallel 1}$	2.23	2.225 ± 0.03896	0.0007856	-0.005732
9	ϕ_{par2}	-2.523	-2.601 ± 0.2981	0.0028	0.01777
10	$\phi_{\perp 1}$	2.37	2.378 ± 0.04086	0.0001388	-0.005992
11	$\phi_{\perp 2}$	-1.833	-1.813 ± 0.1078	0.0008584	0.02231
12	δ_{01}	2.91	2.896 ± 0.04594	0.0003636	-0.006414
13	δ_{02}	-2.753	-2.745 ± 0.03891	-0.004338	-0.01734
14	A_{CP0}	0.093	0.0645 ± 0.04121	-0.002241	-0.0003489
15	A_{CP1}	-0.007	0.001981 ± 0.023	-0.003581	-0.0001835
16	A_{CP2}	0.155	0.1609 ± 0.03371	-0.003361	-0.001073
17	f_{L1}^{+}	0.514	0.5104 ± 0.01808	0.001662	-0.002196
18	f_{L2}^{+}	0.933	0.929 ± 0.01334	0.0006579	0.002969
19	$f_{\perp 1}^{+\prime}$	0.422	0.4166 ± 0.02767	6.468e-05	-0.0002462
20	$f_{\perp 2}^{+\prime}$	0.836	0.8276 ± 0.07993	-0.002434	0.006215
21	$\Delta\phi_{\parallel 1}$	0.02	0.04195 ± 0.03876	0.0001537	-0.0002918
22	$\Delta\phi_{\parallel 2}$	-0.02	0.02799 ± 0.2608	0.002315	-0.002222
23	$\Delta\phi_{\perp 1}$	0.05	0.06602 ± 0.04095	0.0001216	1.582e-05
24	$\Delta\phi_{\perp 2}$	-0.19	-0.2208 ± 0.1083	-0.001813	-0.001554
25	$\Delta\delta_{01}$	0.08	0.09154 ± 0.0453	0.0006237	0.001845
26	$\Delta\delta_{02}$	0.06	0.03602 ± 0.04011	0.0006077	-7.304e-05
27	B_{LF}^{-}	3800	3695.7 ± 183	23.348	-4.5352
28	B_{HF}^{-}	3500	3651.1 ± 183.15	68.985	5.6992
29	B_{LF}^{+}	3800	4087.1 ± 192.03	0.8728	-3.8588
30	B_{HF}^{+}	3500	3228 ± 188.76	66.497	4.5912

Chapter 13

Simulated Results

Since we do not have approval from the Belle community to try our fitter on real data gathered by the detector, we instead give sample results using our simulated data.

We created a fake data set based on the input parameters for the Belle neutral mode analysis [13]. Table 13.1 reports the results of a single set of toy MC data. Note that "ppm" refers to parts per million.

We found $B_0 = (3.60 \pm 0.53) \times 10^{-6}$, $B_1 = (10.79 \pm 0.84) \times 10^{-6}$, and $B_2 = (5.95 \pm 0.66) \times 10^{-6}$. Each of these branching fractions are consistent with expectations.

For the $J = 1$ mode we found $f_{L1}^{-} = 0.55 \pm 0.06$ for the B^- candidates and $f_{L1}^{+} = 0.47 \pm 0.06$ for the B^+ candidates. This means we have both tree diagrams and penguin diagrams competing with each other.

We found no evidence of CP violation with $A_{CP0} = -0.12 \pm 0.16$, $A_{CP1} = 0.06 \pm 0.08$, and $A_{CP2} = 0.19 \pm 0.11$. A_{CP0} and A_{CP1} are consistent with our expectation of zero. A_{CP2} is one σ out of expectation.

Table 13.1 Fit Parameters, and Their Toymc Input Values, Output Values and Errors for One Set of Toy MC Data

	Parameter	Input	Output	Uncertainty
1	$B_0(ppm)$	4.3	3.597	0.534
2	$B_1(ppm)$	10.4	10.790	0.836
3	$B_2(ppm)$	5.5	5.949	0.662
4	f_{L1}^{-}	0.484	0.554	0.060
5	f_{L2}^{-}	0.903	0.903	0.047
6	$f_{\perp 1}^{-'}$	0.525	0.415	0.095
7	$f_{\perp 2}^{-'}$	0.577	0.412	0.271
8	$\phi_{\parallel 1}$	2.23	1.992	0.142
9	ϕ_{par2}	-2.52319	-2.78	0.62
10	$\phi_{\perp 1}$	2.37	2.07	0.15
11	$\phi_{\perp 2}$	-1.83	-1.78	0.46
12	δ_{01}	2.91	2.856	0.186
13	δ_{02}	-2.75319	-2.75	0.14
14	A_{CP0}	0.093	-0.117	0.160
15	A_{CP1}	-0.007	0.057	0.077
16	A_{CP2}	0.155	0.188	0.111
17	f_{L1}^{+}	0.514	0.468	0.063
18	f_{L2}^{+}	0.933	0.928	0.045
19	$f_{\perp 1}^{+'}$	0.422	0.498	0.099
20	$f_{\perp 2}^{+'}$	0.836	0.882	0.225
21	$\Delta\phi_{\parallel 1}$	0.02	0.032	0.120
22	$\Delta\phi_{\parallel 2}$	-0.02	-0.130	0.672
23	$\Delta\phi_{\perp 1}$	0.05	0.146	0.132
24	$\Delta\phi_{\perp 2}$	-0.19	-0.424	0.453
25	$\Delta\delta_{01}$	0.08	0.051	0.165
26	$\Delta\delta_{02}$	0.06	-0.011	0.148
27	B_{LF}^{-}	3800	3656.5	203.4
28	B_{HF}^{-}	3500	3721.9	203.9
29	B_{LF}^{+}	3800	3921.8	151.1
30	B_{HF}^{+}	3500	3501.2	150.8

Chapter 14

Conclusion

Using the full data sample of 772×10^6 $B\bar{B}$ pairs collected at the $\Upsilon(4S)$ resonance with the Belle detector at the KEKB asymmetric-energy e^+e^- collider, we report the fits designed for the measurements of branching fractions and CP asymmetries in $B^\pm \to \phi K^{*\pm}$. For a sample set of toy MC data we found $B_0 = (3.60 \pm 0.53) \times 10^{-6}$, $B_1 = (10.79 \pm 0.84) \times 10^{-6}$, and $B_2 = (5.95 \pm 0.66) \times 10^{-6}$.

For the $J = 1$ mode we found $f_{L1}^- = 0.55 \pm 0.06$ for the B^- candidates and $f_{L1}^+ = 0.47 \pm 0.06$ for the B^+ candidates. We found no evidence of CP violation with $A_{CP0} = -0.12 \pm 0.16$, $A_{CP1} = 0.06 \pm 0.08$, and $A_{CP2} = 0.19 \pm 0.11$.

We hope to run our fitter on the Belle detector collected data in the near future.

Bibliography

[1] C. Patrignani et al., (Particle Data Group), Chin. Phys. C, **40**, 100001 (2016).

[2] A. D. Sakharov, "Violation of CP invariance, C Asymmetry, and Baryon Asymmetry of the Universe," Pisma Zh. Eksp. Teor. Fiz. 5, 32-35 (1967), JETP Lett. 5, 24-27 (1967), Sov. Phys. Usp. 34, 392-393 (1991), Usp. Fiz. Nauk 161, 61-64 (1991).

[3] "CP Violation and Heavy-Quark Physics", J. D. Richman, Lectures given at the XIII Mexican School of Particles and Fields.

[4] "The Physics of the B Factories", Ed. A.J. Bevan, B. Golob, Th. Mannel, S. Prell, and B.D. Yabsley, Eur. Phys. J. C74 (2014) 3026, SLAC-PUB-15968, KEK Preprint 2014-3.

[5] M. Beneke, Buchalla, Neubert, and Sachrajda, 1999, 2000, 2001. M. Beneke, G. Buchalla, M. Neubert and C. T. Sachrajda, "QCD factorization in $B \to \pi K$, $\pi\pi$ decays and extraction of Wolfenstein parameters," Nucl. Phys. B **6**06, 245 (2001).
M. Beneke, G. Buchalla, M. Neubert and C. T. Sachrajda, "QCD factorization for exclusive, nonleptonic B meson decays: General arguments and the case of heavy light final states," Nucl. Phys. B **5**91, 313 (2000).
M. Beneke, G. Buchalla, M. Neubert and C. T. Sachrajda, "QCD factorization for $B \to \pi\pi$ decays: Strong phases and CP violation in the heavy quark limit," Phys. Rev. Lett. **8**3, 1914 (1999).

[6] M. Beneke, J. Rohrer, and D. Yang, Nucl. Phys. **B**774, 64 (2007).
Update: M. Beneke, private communication; updated table 7 from above.

[7] K. F. Chen, "A Study of $B \to \phi K^{(*)}$ decays". Belle Note 625, unpublished (2003).

[8] K. F. Chen et al., "Measurement of Polarization and Triple-Product Correlations in $B \to \phi K^*$ Decays" . PRL 94, 221804 (2005).

[9] B. Aubert et al., "Observation and Polarization Measurements of $B^\pm \to \phi K_1^\pm$ and $B^\pm \to \phi K_2^{*\pm}$", PRL 101, 161801 (2008).

[10] B. Aubert et al., "Amplitude Analysis of the $B^{\pm} \to \phi K^*(892)^{\pm}$", PRL 99, 201802 (2007).

[11] B. Aubert et al., "Time-dependent and time-integrated angular analysis of $B \to \phi K_s^0 \pi^0$ and $\phi K^{\pm}\pi^{\mp}$". PRD 78, 092008 (2008).

[12] K.A. Olive et al., (Particle Data Group), Chin. Phys. C, 38, 090001 (2014) and 2015 update.

[13] M. Prim et al., "Angular analysis of $B^0 \to \phi K^*$ decays and search for CP violation at Belle", Phys. Rev. D 88, 072004 (2013).

[14] R. Aaij et al., (LHCb Collaboration) "Measurement of polarization amplitudes and CP asymmetries in $B^0 \to \phi K^*(892)^0$", JHEP **1**405, 069 (2014).

[15] R.A. Briere et al., (CLEO Collaboration), "Observation of $B \to \phi K$ and $B \to \phi K^*$", PRL **8**6 3718 (2001).

[16] T. Abe et al., Performance and Operation Results of the RF Systems for the KEK B-Factory, Progress of Theoretical and Experimental Physics, Volume 2013, Issue 3, 1 March 2013, 03A006.

[17] KEK B Factory Design Report (1995).

[18] "KEK Accelerator" 1997. http://belle.kek.jp/belle/transparency/accelerator1.html#1

[19] KEKB breaks luminosity record. Cern Courier. June 8th, 2009.

[20] A. Abashian et al., (Belle Collaboration), Nucl. Instrum. Methods Phys. Res. Sect. A **4**79, 117 (2002).

[21] J. Brodzicka et al., Physics achievements from the Belle experiment, Prog. Theor. Exp. Phys., 04D001 (2012).

[22] KEK News Vol. 1, No. 1. 1997. Published by High Energy Accelerator Research Orgainization. https://www2.kek.jp/proffice/archives/kek-news/vol1no1/news3.html

[23] Belle II Internal Note 26.

[24] Lange, D. J.,"The EvtGen particle decay simulation package", Nucl. Instrum. Methods Phys. Res. Sect. A **4**62, 152-155 (2001).

[25] "GEANT3", Brun, R. and Bruyant, F. and Maire, M. and McPherson, A.C. and Zanarini, P., 1987.

[26] C. Patrignani et al., (Particle Data Group), Chin. Phys. **C**, 40, 100001 (2016), and earlier versions.

[27] D. Aston et al., (LASS Collaboration), Nuclear Phys. B **2**96, 493 (1988).

[28] B. Aubert et al., (BaBar Collaboration), Phys. Rev. D **7**8, 092008 (2008).

[29] E. P. Wigner, Phys. Rev. **9**8, 145 (1955).

[30] "ROOT: An object oriented data analysis", by R. Brun and F. Rademakers, "Nucl. Instrum. Meth.", **A**389, 1997, 81-86.

[31] The Fox-Wolfram moments were introduced in G. C. Fox and S. Wolfram, Phys. Rev. Lett. 41, 1581 (1978); The Fisher discriminant used by Belle, based on modified Fox- Wolfram moments (SFW), is described in K. Abe et al. (Belle Collaboration), Phys. Rev. Lett. 87, 101801 (2001); K. Abe et al. (Belle Collaboration), Phys. Lett. B 511, 151 (2001).

[32] "Determination of the K^0_S reconstruction efficiency", K. Chilikin, Belle Note 1356, 2016.

[33] "Systematic uncertainty for the K^0_S reconstruction efficiency", N. Dash et al., Belle Note 1472, 2017.

[34] "Evidence for CP Violation in the Decay $D^+ \to K^0_S\pi^+$", B. R. Ko et al., Phys. Rev. Lett. **1**09 021601 (2012).

[35] "Search for CP Violation in the Decay $D^+ \to K^0_S K^+$", B. R. Ko et al., JHEP **0**2 098 (2013).

Appendix A

Event Processing Tables

Below are the tables obtained from processing data. The "Skim In" column refers to the number of events going into the skim process. The "Skim Out" column refers to the number of events that were obtained after the skimming process. There are similar columns for the reconstruction process. On the MC tables there is a column "Belle Doc." which refers to how many events the Belle experiment documented in their MC data.

Table A.1 Skim and Reconstruction Event Numbers From Real Data Processing

Exp	Skim In	Skim Out	Skim Ratio(%)	Reco In	SkimOut -RecoIn	Reco Out	Reco Ratio(%)
7	24891675	138428	0.556	138415	13	1180	0.853
9	18489854	108560	0.587	108547	13	946	0.872
11	34113689	207206	0.607	207173	33	1862	0.899
13	44914733	278538	0.620	278528	10	2479	0.890
15	53244815	309047	0.580	309113	-66	2730	0.883
17	46237211	272321	0.589	272358	-37	2658	0.976
19	103962996	601674	0.579	601768	-94	5609	0.932
21	18489106	105243	0.569	105258	-15	1033	0.981
23	26802068	155377	0.580	155414	-37	1520	0.978
25	110272393	634789	0.576	634904	-115	6105	0.962
27	109198061	631511	0.578	631591	-80	5978	0.946
31	78502039	670183	0.854	670257	-74	5969	0.891
33	77541248	648548	0.836	648594	-46	6164	0.950
35	73875887	636256	0.861	636300	-44	5798	0.911
37	265946423	2280233	0.857	2280369	-136	21037	0.923
39	180004692	1511630	0.840	1511711	-81	14062	0.930
41	256419928	2148467	0.838	2148568	-101	19976	0.930
43	245273504	2089861	0.852	2089963	-102	19255	0.921
45	57315483	478698	0.835	478723	-25	4569	0.954
47	165163809	1403375	0.850	1403425	-50	13298	0.948
49	119534708	1008981	0.844	1009049	-68	9404	0.932

Exp	Skim In	Skim Out	Skim Ratio(%)	Reco In	SkimOut -RecoIn	Reco Out	Reco Ratio(%)
51	172799727	1469662	0.851	1469774	-112	13769	0.937
55	321315022	2733804	0.851	2724925	8879	25370	0.931
61	154618685	1330798	0.861	1330910	-112	12437	0.934
63	146092280	1251098	0.856	1251173	-75	11857	0.948
65	167611001	1411036	0.842	1411110	-74	13629	0.966
SVD1	590616601	3442694	6.42	3443069	-375	32100	10.2
SDV2	2482014436	21072630	12.7	21064851	7779	196594	14.0
Total	3072631037	24515324	19.1	24507920	7404	228694	24.2

Table A.2 Skim and Reconstruction Event Numbers From Full Stream 1 uds Processing

Exp	Belle Doc.	Skim In	Skim Out	Skim Ratio	Reco In	Reco Out	Reco Ratio
7	12115359	12115359	103500	0.00854	103500	1099	0.0106
9	8603092	8603092	75008	0.00872	75008	793	0.0106
11	16086112	16086112	141504	0.00880	141504	1325	0.0094
13	22372593	22372593	196643	0.00879	196643	2106	0.0107
15	26514597	26514597	227454	0.00858	227454	2494	0.0110
17	19287346	19287346	166383	0.00863	166383	1816	0.0109
19	51465220	51465220	438085	0.00851	438085	4491	0.0103
21	9018475	9018475	76686	0.00850	76686	795	0.0104
23	13222444	13222444	113778	0.00860	113778	1164	0.0102
25	53265401	53265401	459972	0.00864	459972	4798	0.0104
27	52992758	52992758	455991	0.00860	455991	4814	0.0106
31	35582936	35582936	396736	0.0111	396736	4559	0.0115
33	36330562	36330562	406016	0.0112	406016	4722	0.0116
35	35258660	35258660	400993	0.0114	400993	4453	0.0111
37	127249999	127249999	1449588	0.0114	1449588	16051	0.0111
39	88523407	88523407	1004744	0.0114	1004744	11397	0.0113
41	119814238	119814238	1362046	0.0114	1362046	14924	0.0110
43	114139596	114139596	1300642	0.0114	1300642	14319	0.0110
45	26739289	26739289	303490	0.0113	303490	3246	0.0107
47	76758509	76758509	877442	0.0114	877442	9504	0.0108
49	55742786	55742786	635537	0.0114	635537	6953	0.0109

Exp	Belle Doc.	Skim In	Skim Out	Skim Ratio	Reco In	Reco Out	Reco Ratio
51	81031726	81031726	924391	0.0114	924391	10383	0.0112
55	148951973	148951973	1696894	0.0114	1696894	18793	0.0111
61	71425095	71425095	825675	0.0116	825675	9295	0.0113
63	67221743	67221743	771832	0.0115	771832	8554	0.0111
65	77692728	77692728	893175	0.0115	893175	9849	0.0110
SVD1	284943397	284943397	2455004	0.0949	2455004	25695	0.115
SVD2	1162463247	1162463247	13249201	0.171	13249201	147002	0.167
Total	1447406644	1447406644	15704205	0.266	15704205	172697	0.282

Table A.3 Skim and Reconstruction Event Numbers From Full Stream 1 Charm Processing

Exp	Belle Doc.	Skim In	Skim Out	Skim Ratio	Reco In	Reco Out	Reco Ratio
7	12115359	12115359	103500	0.00854	103500	1099	0.0106
9	8603092	8603092	75008	0.00872	75008	793	0.0106
11	16086112	16086112	141504	0.00880	141504	1325	0.0094
13	22372593	22372593	196643	0.00879	196643	2106	0.0107
15	26514597	26514597	227454	0.00858	227454	2494	0.0110
17	19287346	19287346	166383	0.00863	166383	1816	0.0109
19	51465220	51465220	438085	0.00851	438085	4491	0.0103
21	9018475	9018475	76686	0.00850	76686	795	0.0104
23	13222444	13222444	113778	0.00860	113778	1164	0.0102
25	53265401	53265401	459972	0.00864	459972	4798	0.0104
27	52992758	52992758	455991	0.00860	455991	4814	0.0106
31	35582936	35582936	396736	0.0111	396736	4559	0.0115
33	36330562	36330562	406016	0.0112	406016	4722	0.0116
35	35258660	35258660	400993	0.0114	400993	4453	0.0111
37	127249999	127249999	1449588	0.0114	1449588	16051	0.0111
39	88523407	88523407	1004744	0.0114	1004744	11397	0.0113
41	119814238	119814238	1362046	0.0114	1362046	14924	0.0110
43	114139596	114139596	1300642	0.0114	1300642	14319	0.0110
45	26739289	26739289	303490	0.0113	303490	3246	0.0107
47	76758509	76758509	877442	0.0114	877442	9504	0.0108
49	55742786	55742786	635537	0.0114	635537	6953	0.0109

Exp	Belle Doc.	Skim In	Skim Out	Skim Ratio	Reco In	Reco Out	Reco Ratio
51	81031726	81031726	924391	0.0114	924391	10383	0.0112
55	148951973	148951973	1696894	0.0114	1696894	18793	0.0111
61	71425095	71425095	825675	0.0116	825675	9295	0.0113
63	67221743	67221743	771832	0.0115	771832	8554	0.0111
65	77692728	77692728	893175	0.0115	893175	9849	0.0110
SVD1	284943397	284943397	2455004	0.0949	2455004	25695	0.115
SVD2	1162463247	1162463247	13249201	0.171	13249201	147002	0.167
Total	1447406644	1447406644	15704205	0.266	15704205	172697	0.282

Table A.4 Skim and Reconstruction Event Numbers From Full Stream 1 Mixed Processing

Exp	Belle Doc.	Skim In	Skim Out	Skim Ratio	Reco In	Reco Out	Reco Ratio
7	3158539	3158539	5358	0.00170	5358	24	0.00448
9	2243081	2243081	3870	0.00173	3870	12	0.00310
11	4194377	4194377	7195	0.00172	7195	27	0.00375
13	5833568	5833568	10427	0.00179	10427	32	0.00307
15	6913774	6913774	11840	0.00171	11840	43	0.00363
17	5029273	5029273	8597	0.00171	8597	24	0.00279
19	13419895	13419895	22773	0.00170	22773	98	0.00430
21	2351610	2351610	3990	0.00170	3990	18	0.00451
23	3447814	3447814	6059	0.00176	6059	22	0.00363
25	13889176	13889176	23915	0.00172	23915	92	0.00385
27	13818248	13818248	23852	0.00173	23852	86	0.00361
31	9278483	9278483	23952	0.00258	23952	67	0.00280
33	9473593	9473593	24657	0.00260	24657	72	0.00292
35	9194074	9194074	24318	0.00264	24318	87	0.00358
37	33181993	33181993	87710	0.00264	87710	310	0.00353
39	23083591	23083591	61389	0.00266	61389	195	0.00318
41	31243161	31243161	82987	0.00266	82987	281	0.00339
43	29763443	29763443	79147	0.00266	79147	279	0.00353
45	6972626	6972626	18167	0.00261	18167	61	0.00336
47	20015813	20015813	53287	0.00266	53287	169	0.00317
49	14535658	14535658	38336	0.00264	38336	101	0.00263

Exp	Belle Doc.	Skim In	Skim Out	Skim Ratio	Reco In	Reco Out	Reco Ratio
51	21130008	21130008	55889	0.00265	55889	181	0.00324
55	38841208	38841208	102892	0.00265	102892	326	0.00317
61	18624948	18624948	49496	0.00266	49496	186	0.00376
63	17528960	17528960	46471	0.00265	46471	192	0.00413
65	20259430	20259430	53152	0.00262	53152	182	0.00342
SVD1	74299355	74299355	127876	0.0189	127876	478	0.0407
SVD2	303126989	303126989	801850	0.0396	801850	2689	0.0498
Total	377426344	377426344	929726	0.0585	929726	3167	0.0905

Table A.5 Skim and Reconstruction Event Numbers From Full Stream 1 Charged Processing

Exp	Belle Doc.	Skim In	Skim Out	Skim Ratio	Reco In	Reco Out	Reco Ratio
7	3158539	3158539	8771	0.00278	8771	37	0.00422
9	2243082	2243082	6317	0.00282	6317	38	0.00602
11	4194377	4194377	12028	0.00287	12028	43	0.00357
13	5833568	5833568	16576	0.00284	16576	65	0.00392
15	6913772	6913772	19412	0.00281	19412	94	0.00484
17	5029273	5029273	14249	0.00283	14249	68	0.00477
19	13419896	13419896	37147	0.00277	37147	195	0.00525
21	2351610	2351610	6674	0.00284	6674	24	0.00360
23	3447814	3447814	9724	0.00282	9724	44	0.00452
25	13889176	13889176	39138	0.00282	39138	157	0.00401
27	13818245	13818245	39107	0.00283	39107	165	0.00422
31	9278486	9278486	36854	0.00397	36854	130	0.00353
33	9473597	9473597	37697	0.00398	37697	137	0.00363
35	9194075	9194075	37656	0.00410	37656	143	0.00380
37	33181995	33181995	134822	0.00406	134822	517	0.00383
39	23083585	23083585	93494	0.00405	93494	376	0.00402
41	31243163	31243163	127517	0.00408	127517	536	0.00420
43	29763451	29763451	121374	0.00408	121374	491	0.00405
45	6972626	6972626	28199	0.00404	28199	120	0.00426
47	20015809	20015809	81528	0.00407	81528	351	0.00431
49	14535659	14535659	59095	0.00407	59095	234	0.00396

Exp	Belle Doc.	Skim In	Skim Out	Skim Ratio	Reco In	Reco Out	Reco Ratio
51	21130003	21130003	86241	0.00408	86241	352	0.00408
55	38841213	38841213	156826	0.00404	156826	620	0.00395
61	18624949	18624949	76058	0.00408	76058	292	0.00384
63	17528959	17528959	71405	0.00407	71405	267	0.00374
65	20259429	20259429	82084	0.00405	82084	313	0.00381
SVD1	74299352	74299352	209143	0.0310	209143	930	0.0489
SVD2	303126999	303126999	1230850	0.0608	1230850	4879	0.0590
Total	377426351	377426351	1439993	0.0918	1439993	5809	0.1080

Table A.6 Skim and Reconstruction Event Numbers From Full Stream 2 uds Processing

Exp	Belle Doc.	Skim In	Skim Out	Skim Ratio	Reco In	Reco Out	Reco Ratio
7	12115355	12115355	102986	0.00850	102986	1098	0.0107
9	8603093	8603093	74764	0.00869	74764	812	0.0109
11	16086111	16086111	141443	0.00879	141443	1393	0.0098
13	22372594	22372594	197342	0.00882	197342	2051	0.0104
15	26514597	26514597	227497	0.00858	227497	2287	0.0101
17	19287346	19287346	166744	0.00865	166744	1716	0.0103
19	51465218	51465218	438123	0.00851	438123	4675	0.0107
21	9018476	9018476	76224	0.00845	76224	887	0.0116
23	13222446	13222446	113929	0.00862	113929	1159	0.0102
25	53265399	53265399	458994	0.00862	458994	4781	0.0104
27	52992755	52992755	458133	0.00865	458133	4856	0.0106
31	35582933	35582933	396703	0.0111	396703	4345	0.0110
33	36330562	36330562	405863	0.0112	405863	4555	0.0112
35	35258653	35258653	401582	0.0114	401582	4392	0.0109
37	127250003	127250003	1449098	0.0114	1449098	15871	0.0110
39	88523416	88523416	1004574	0.0113	1004574	10995	0.0109
41	119814233	119814233	1362205	0.0114	1362205	14909	0.0109
43	114139602	114139602	1300300	0.0114	1300300	14257	0.0110
45	26739293	26739293	303441	0.0113	303441	3457	0.0114
47	76758500	76758500	876398	0.0114	876398	9570	0.0109
49	55742786	55742786	634748	0.0114	634748	6951	0.0110

Exp	Belle Doc.	Skim In	Skim Out	Skim Ratio	Reco In	Reco Out	Reco Ratio
51	81031724	81031724	922535	0.0114	922535	10090	0.0109
55	148951993	148951993	1696711	0.0114	1696711	18948	0.0112
61	71425097	71425097	823122	0.0115	823122	9203	0.0112
63	67221744	67221744	772634	0.0115	772634	8604	0.0111
65	77692724	77692724	891877	0.0115	891877	9923	0.0111
SVD1	284943390	284943390	2456179	0.095	2456179	25715	0.116
SVD2	1162463263	1162463263	13241791	0.171	13241791	146070	0.166
Total	1447406653	1447406653	15697970	0.266	15697970	171785	0.281

Table A.7 Skim and Reconstruction Event Numbers From Full Stream 2 Charm Processing

Exp	Belle Doc.	Skim In	Skim Out	Skim Ratio	Reco In	Reco Out	Reco Ratio
7	7536264	7536264	69863	0.00927	69863	1027	0.0147
9	5351449	5351449	51149	0.00956	51149	731	0.0143
11	10005970	10005970	96423	0.00964	96423	1322	0.0137
13	13916305	13916305	134895	0.00969	134895	1971	0.0146
15	16492592	16492592	153946	0.00933	153946	2312	0.0150
17	11997075	11997075	113535	0.00946	113535	1716	0.0151
19	32012211	32012211	298675	0.00933	298675	4356	0.0146
21	5609656	5609656	52044	0.00928	52044	718	0.0138
23	8224605	8224605	77171	0.00938	77171	1054	0.0137
25	33132056	33132056	312401	0.00943	312401	4557	0.0146
27	32962344	32962344	311291	0.00944	311291	4519	0.0145
31	22133167	22133167	270155	0.0122	270155	4074	0.0151
33	22598087	22598087	276774	0.0122	276774	4066	0.0147
35	21931341	21931341	271758	0.0124	271758	4099	0.0151
37	79151020	79151020	984106	0.0124	984106	14749	0.0150
39	55062605	55062605	684431	0.0124	684431	10530	0.0154
41	74525780	74525780	923297	0.0124	923297	13757	0.0149
43	70996086	70996086	882073	0.0124	882073	13422	0.0152
45	16632143	16632143	207204	0.0125	207204	3167	0.0153
47	47744641	47744641	594168	0.0124	594168	9012	0.0152
49	34672639	34672639	432072	0.0125	432072	6692	0.0155

Exp	Belle Doc.	Skim In	Skim Out	Skim Ratio	Reco In	Reco Out	Reco Ratio
51	50402727	50402727	627745	0.0125	627745	9415	0.0150
55	92649827	92649827	1152666	0.0124	1152666	17485	0.0152
61	44427295	44427295	558632	0.0126	558632	8541	0.0153
63	41812686	41812686	524484	0.0125	524484	8096	0.0154
65	48325735	48325735	604240	0.0125	604240	9311	0.0154
SVD1	177240527	177240527	1671393	0.104	1671393	24283	0.159
SVD2	723065779	723065779	8993805	0.186	8993805	136416	0.228
Total	900306306	900306306	10665198	0.290	10665198	160699	0.386

Table A.8 Skim and Reconstruction Event Numbers From Full Stream 2 Mixed Processing

Exp	Belle Doc.	Skim In	Skim Out	Skim Ratio	Reco In	Reco Out	Reco Ratio
7	3158539	3158539	5375	0.00170	5375	21	0.00391
9	2243081	2243081	4018	0.00179	4018	16	0.00398
11	4194376	4194376	7509	0.00179	7509	31	0.00413
13	5833569	5833569	10215	0.00175	10215	45	0.00441
15	6913772	6913772	11621	0.00168	11621	56	0.00482
17	5029272	5029272	8655	0.00172	8655	33	0.00381
19	13419895	13419895	22996	0.00171	22996	76	0.00330
21	2351610	2351610	4067	0.00173	4067	15	0.00369
23	3447813	3447813	5988	0.00174	5988	22	0.00367
25	13889174	13889174	23807	0.00171	23807	93	0.00391
27	13818244	13818244	23980	0.00174	23980	90	0.00375
31	9278484	9278484	24044	0.00259	24044	70	0.00291
33	9473598	9473598	24722	0.00261	24722	92	0.00372
35	9194075	9194075	24459	0.00266	24459	71	0.00290
37	33181997	33181997	87528	0.00264	87528	308	0.00352
39	23083588	23083588	61064	0.00265	61064	204	0.00334
41	31243164	31243164	83137	0.00266	83137	290	0.00349
43	29763446	29763446	79061	0.00266	79061	280	0.00354
45	6972626	6972626	18479	0.00265	18479	66	0.00357
47	20015813	20015813	52893	0.00264	52893	173	0.00327
49	14535657	14535657	38499	0.00265	38499	134	0.00348

Exp	Belle Doc.	Skim In	Skim Out	Skim Ratio	Reco In	Reco Out	Reco Ratio
51	21130007	21130007	56166	0.00266	56166	188	0.00335
55	38841221	38841221	102950	0.00265	102950	346	0.00336
61	18624955	18624955	49511	0.00266	49511	152	0.00307
63	17528965	17528965	46299	0.00264	46299	147	0.00318
65	20259428	20259428	53734	0.00265	53734	198	0.00368
SVD1	74299345	74299345	128231	0.0191	128231	498	0.0434
SVD2	303127024	303127024	802546	0.0397	802546	2719	0.0504
Total	377426369	377426369	930777	0.0587	930777	3217	0.0938

Table A.9 Skim and Reconstruction Event Numbers From Full Stream 2 Charged Processing

Exp	Belle Doc.	Skim In	Skim Out	Skim Ratio	Reco In	Reco Out	Reco Ratio
7	3158539	3158539	8797	0.00279	8797	42	0.00477
9	2243082	2243082	6343	0.00283	6343	19	0.00300
11	4194376	4194376	12117	0.00289	12117	53	0.00437
13	5833569	5833569	16684	0.00286	16684	78	0.00468
15	6913774	6913774	19337	0.00280	19337	89	0.00460
17	5029272	5029272	14352	0.00285	14352	58	0.00404
19	13419895	13419895	37751	0.00281	37751	169	0.00448
21	2351610	2351610	6519	0.00277	6519	23	0.00353
23	3447814	3447814	9612	0.00279	9612	31	0.00323
25	13889175	13889175	39288	0.00283	39288	175	0.00445
27	13818246	13818246	38775	0.00281	38775	157	0.00405
31	9278484	9278484	36516	0.00394	36516	135	0.00370
33	9473591	9473591	37570	0.00397	37570	146	0.00389
35	9194074	9194074	37364	0.00406	37364	150	0.00401
37	33181989	33181989	134818	0.00406	134818	543	0.00403
39	23083584	23083584	93771	0.00406	93771	404	0.00431
41	31243172	31243172	126846	0.00406	126846	517	0.00408
43	29763451	29763451	121020	0.00407	121020	473	0.00391
45	6972624	6972624	28304	0.00406	28304	123	0.00435
47	20015819	20015819	82133	0.00410	82133	317	0.00386
49	14535654	14535654	59438	0.00409	59438	225	0.00379

Exp	Belle Doc.	Skim In	Skim Out	Skim Ratio	Reco In	Reco Out	Reco Ratio
51	21130008	21130008	85905	0.00407	85905	359	0.00418
55	38841224	38841224	157379	0.00405	157379	604	0.00384
61	18624953	18624953	76249	0.00409	76249	297	0.00390
63	17528965	17528965	71558	0.00408	71558	273	0.00382
65	20259430	20259430	82670	0.00408	82670	281	0.00340
SVD1	74299352	74299352	209575	0.0310	209575	894	0.0452
SVD2	303127022	303127022	1231541	0.0608	1231541	4847	0.0590
Total	377426374	377426374	1441116	0.0919	1441116	5741	0.104

Table A.10 Skim and Reconstruction Event Numbers From Full Stream 3 uds Processing

Exp	Belle Doc.	Skim In	Skim Out	Skim Ratio	Reco In	Reco Out	Reco Ratio
7	12115356	12115356	103000	0.00850	103000	1096	0.0106
9	8603092	8603092	74686	0.00868	74686	763	0.0102
11	16086112	16086112	142383	0.00885	142383	1448	0.0102
13	22372595	22372595	198014	0.00885	198014	2052	0.0104
15	26514598	26514598	226700	0.00855	226700	2414	0.0106
17	19287347	19287347	166531	0.00863	166531	1713	0.0103
19	51465218	51465218	437888	0.00851	437888	4527	0.0103
21	9018476	9018476	76412	0.00847	76412	798	0.0104
23	13222447	13222447	114216	0.00864	114216	1191	0.0104
25	53265400	53265400	459594	0.00863	459594	4895	0.0107
27	52992754	52992754	457154	0.00863	457154	4854	0.0106
31	35582930	35582930	397368	0.0112	397368	4421	0.0111
33	36330568	36330568	405861	0.0112	405861	4508	0.0111
35	35258659	35258659	401335	0.0114	401335	4378	0.0109
37	127250000	127250000	1448827	0.0114	1448827	15702	0.0108
39	88523399	88523399	1003697	0.0113	1003697	11366	0.0113
41	119814243	119814243	1360862	0.0114	1360862	14878	0.0109
43	114139599	114139599	1300734	0.0114	1300734	14243	0.0109
45	26739296	26739296	303308	0.0113	303308	3494	0.0115
47	76758506	76758506	875554	0.0114	875554	9735	0.0111
49	55742790	55742790	635096	0.0114	635096	7070	0.0111

Exp	Belle Doc.	Skim In	Skim Out	Skim Ratio	Reco In	Reco Out	Reco Ratio
51	81031726	81031726	922609	0.0114	922609	10416	0.0113
55	148951987	148951987	1698956	0.0114	1698956	18764	0.0110
61	71425109	71425109	822158	0.0115	822158	9478	0.0115
63	67221746	67221746	774052	0.0115	774052	8759	0.0113
65	77692728	77692728	891543	0.0115	891543	9901	0.0111
SVD1	284943395	284943395	2456578	0.0949	2456578	25751	0.115
SVD2	1162463286	1162463286	13241960	0.171	13241960	147113	0.167
Total	1447406681	1447406681	15698538	0.266	15698538	172864	0.282

Table A.11 Skim and Reconstruction Event Numbers From Full Stream 3 Charm Processing

Exp	Belle Doc.	Skim In	Skim Out	Skim Ratio	Reco In	Reco Out	Reco Ratio
7	7536266	7536266	69646	0.00924	69646	973	0.0140
9	5351448	5351448	50862	0.00950	50862	677	0.0133
11	10005969	10005969	96180	0.00961	96180	1324	0.0138
13	13916302	13916302	135111	0.00971	135111	1933	0.0143
15	16492591	16492591	154559	0.00937	154559	2290	0.0148
17	11997075	11997075	113667	0.00947	113667	1612	0.0142
19	32012210	32012210	298220	0.00932	298220	4337	0.0145
21	5609656	5609656	51916	0.00925	51916	745	0.0144
23	8224606	8224606	77486	0.00942	77486	1149	0.0148
25	33132059	33132059	312233	0.00942	312233	4484	0.0144
27	32962342	32962342	311538	0.00945	311538	4420	0.0142
31	22133167	22133167	269382	0.0122	269382	3995	0.0148
33	22598086	22598086	277091	0.0123	277091	4083	0.0147
35	21931344	21931344	273057	0.0125	273057	4144	0.0152
37	79151034	79151034	981595	0.0124	981595	14773	0.0150
39	55062614	55062614	683692	0.0124	683692	10165	0.0149
41	74525802	74525802	924543	0.0124	924543	13848	0.0150
43	70996073	70996073	883006	0.0124	883006	13276	0.0150
45	16632136	16632136	207402	0.0125	207402	3145	0.0152
47	47744646	47744646	596230	0.0125	596230	9104	0.0153
49	34672637	34672637	432660	0.0125	432660	6378	0.0147

Exp	Belle Doc.	Skim In	Skim Out	Skim Ratio	Reco In	Reco Out	Reco Ratio
51	50402721	50402721	628524	0.0125	628524	9557	0.0152
55	92649814	92649814	1153667	0.0125	1153667	17570	0.0152
61	44427292	44427292	558891	0.0126	558891	8607	0.0154
63	41812693	41812693	525046	0.0126	525046	8054	0.0153
65	48325737	48325737	605069	0.0125	605069	9302	0.0154
SVD1	177240524	177240524	1671418	0.104	1671418	23944	0.157
SVD2	723065796	723065796	8999855	0.187	8999855	136001	0.226
Total	900306320	900306320	10671273	0.290	10671273	159945	0.383

Table A.12 Skim and Reconstruction Event Numbers From Full Stream 3 Mixed Processing

Exp	Belle Doc.	Skim In	Extra Evnts	Skim Out	Skim Ratio	Reco In	Reco Out	Reco Ratio
7	3158539	3158539	0	5325	0.00169	5325	23	0.00432
9	2243082	2243082	0	3996	0.00178	3996	18	0.00450
11	4194376	4194376	0	7309	0.00174	7309	20	0.00274
13	5833569	5833569	0	10515	0.00180	10515	34	0.00323
15	6913773	6913773	0	12091	0.00175	12091	39	0.00323
17	5029271	5029271	0	8646	0.00172	8646	38	0.00440
19	13419897	13419897	0	22791	0.00170	22791	69	0.00303
21	2351609	2351609	0	4039	0.00172	4039	18	0.00446
23	3447814	3447814	0	5913	0.00171	5913	13	0.00220
25	13889176	13889176	0	23858	0.00172	23858	86	0.00360
27	13818247	13818247	0	23570	0.00171	23570	100	0.00424
31	9278486	9278486	0	23576	0.00254	23576	97	0.00411
33	9473596	9473596	0	24383	0.00257	24383	94	0.00386
35	9194073	9194073	0	24424	0.00266	24424	86	0.00352
37	33181996	33181996	0	88211	0.00266	88211	297	0.00337
39	23083586	23083586	0	61070	0.00265	61070	191	0.00313
41	31243169	31243169	0	82493	0.00264	82493	287	0.00348
43	29763456	29763456	0	78731	0.00265	78731	276	0.00351
45	6972625	6972625	0	18262	0.00262	18262	49	0.00268
47	20015818	20015818	0	53256	0.00266	53256	159	0.00299
49	14535650	14535650	0	38593	0.00266	38593	119	0.00308

Exp	Belle Doc.	Skim In	Extra Evnts	Skim Out	Skim Ratio	Reco In	Reco Out	Reco Ratio
51	21130008	21130008	0	56304	0.00266	56304	181	0.00321
55	38841220	38841220	0	103295	0.00266	103295	372	0.00360
61	18624952	18624952	0	49367	0.00265	49367	162	0.00328
63	17528961	17528962	1	46356	0.00264	46356	147	0.00317
65	20259432	20259432	0	53267	0.00263	53267	161	0.00302
SVD1	74299353	74299353	0	128053	0.0190	128053	458	0.0399
SVD2	303127028	303127029	1	801588	0.0395	801588	2678	0.0500
Total	377426381	377426382	1	929641	0.0586	929641	3136	0.0900

Table A.13 Skim and Reconstruction Event Numbers From Full Stream 3 Charged Processing

Exp	Belle Doc.	Skim In	Extra Evnts	Skim Out	Skim Ratio	Reco In	Reco Out	Reco Ratio
7	3158539	3158539	0	8641	0.00274	8641	30	0.00347
9	2243082	2243082	0	6301	0.00281	6301	24	0.00381
11	4194377	4194377	0	12002	0.00286	12002	54	0.00450
13	5833568	5833568	0	16819	0.00288	16819	91	0.00541
15	6913775	6913775	0	19254	0.00278	19254	72	0.00374
17	5029273	5029273	0	14162	0.00282	14162	66	0.00466
19	13419897	13419897	0	37428	0.00279	37428	181	0.00484
21	2351608	2351608	0	6455	0.00274	6455	31	0.00480
23	3447814	3447814	0	9834	0.00285	9834	42	0.00427
25	13889177	13889177	0	39136	0.00282	39136	157	0.00401
27	13818246	13818246	0	38903	0.00282	38903	183	0.00470
31	9278484	9278484	0	36646	0.00395	36646	150	0.00409
33	9473593	9473593	0	38024	0.00401	38024	137	0.00360
35	9194073	9194073	0	37206	0.00405	37206	156	0.00419
37	33181999	33181999	0	134837	0.00406	134837	572	0.00424
39	23083584	23083584	0	93880	0.00407	93880	385	0.00410
41	31243175	31243175	0	127246	0.00407	127246	480	0.00377
43	29763452	29763452	0	121464	0.00408	121464	461	0.00380
45	6972625	6972625	0	28128	0.00403	28128	106	0.00377
47	20015820	20015820	0	81804	0.00409	81804	343	0.00419
49	14535657	14535657	0	59191	0.00407	59191	223	0.00377

Exp	Belle Doc.	Skim In	Extra Evnts	Skim Out	Skim Ratio	Reco In	Reco Out	Reco Ratio
51	21130012	21130012	0	85994	0.00407	85994	337	0.00392
55	38841223	38841223	0	157520	0.00406	157520	602	0.00382
61	18624951	18624951	0	75934	0.00408	75934	299	0.00394
63	17528959	17528962	3	71580	0.00408	71580	286	0.00400
65	20259428	20259428	0	81914	0.00404	81914	319	0.00389
SVD1	74299356	74299356	0	208935	0.0309	208935	931	0.0482
SVD2	303127035	303127038	3	1231368	0.0608	1231368	4856	0.0591
Total	377426391	377426394	3	1440303	0.0917	1440303	5787	0.107

Table A.14 Skim and Reconstruction Event Numbers From Full Stream 4 uds Processing

Exp	Belle Doc.	Skim In	Skim Out	Skim Ratio	Reco In	Reco Out	Reco Ratio
7	12115358	12115358	102671	0.0085	102671	1085	0.0106
9	8603090	8603090	74729	0.0087	74729	762	0.0102
11	16086114	16086114	141888	0.0088	141888	1411	0.0099
13	22372594	22372594	198093	0.0089	198093	2176	0.0110
15	26514600	26514600	227392	0.0086	227392	2324	0.0102
17	19287345	19287345	166306	0.0086	166306	1795	0.0108
19	51465218	51465218	438158	0.0085	438158	4747	0.0108
21	9018476	9018476	76372	0.0085	76372	816	0.0107
23	13222447	13222447	113711	0.0086	113711	1206	0.0106
25	53265401	53265401	459333	0.0086	459333	4732	0.0103
27	52992755	52992755	457533	0.0086	457533	4672	0.0102
31	35582925	35582925	397032	0.0112	397032	4492	0.0113
33	36330569	36330569	407321	0.0112	407321	4733	0.0116
35	35258658	35258658	401529	0.0114	401529	4491	0.0112
37	127250005	127250005	1446117	0.0114	1446117	15808	0.0109
39	88523404	88523404	1006890	0.0114	1006890	10883	0.0108
41	119814227	119814227	1359108	0.0113	1359108	14827	0.0109
43	114139596	114139596	1300514	0.0114	1300514	14125	0.0109
45	26739290	26739290	304169	0.0114	304169	3483	0.0115
47	76758506	76758506	877053	0.0114	877053	9733	0.0111
49	55742788	55742788	635611	0.0114	635611	7202	0.0113

Exp	Belle Doc.	Skim In	Skim Out	Skim Ratio	Reco In	Reco Out	Reco Ratio
51	81031723	81031723	924123	0.0114	924123	10380	0.0112
55	148951983	148951983	1698295	0.0114	1698295	18837	0.0111
61	71425097	71425097	824569	0.0115	824569	9077	0.0110
63	67221739	67221739	772464	0.0115	772464	8910	0.0115
65	77692725	77692725	889752	0.0115	889752	10109	0.0114
SVD1	284943398	284943398	2456186	0.0949	2456186	25726	0.115
SVD2	1162463235	1162463235	13244547	0.171	13244547	147090	0.168
Total	1447406633	1447406633	15700733	0.266	15700733	172816	0.283

Table A.15 Skim and Reconstruction Event Numbers From Full Stream 4 Charm Processing

Exp	Belle Doc.	Skim In	Skim Out	Skim Ratio	Reco In	Reco Out	Reco Ratio
7	7536266	7536266	69471	0.00922	69471	991	0.0143
9	5351447	5351447	51009	0.00953	51009	795	0.0156
11	10005969	10005969	96290	0.00962	96290	1344	0.0140
13	13916305	13916305	134358	0.00965	134358	1892	0.0141
15	16492592	16492592	154673	0.00938	154673	2317	0.0150
17	11997073	11997073	113037	0.00942	113037	1668	0.0148
19	32012213	32012213	297109	0.00928	297109	4258	0.0143
21	5609656	5609656	51731	0.00922	51731	735	0.0142
23	8224604	8224604	77517	0.00943	77517	1089	0.0140
25	33132053	33132053	311865	0.00941	311865	4417	0.0142
27	32962344	32962344	311915	0.00946	311915	4368	0.0140
31	22133164	22133164	269762	0.0122	269762	4124	0.0153
33	22598080	22598080	277933	0.0123	277933	4260	0.0153
35	21931342	21931342	272836	0.0124	272836	4012	0.0147
37	79151024	79151024	983921	0.0124	983921	14922	0.0152
39	55062612	55062612	684377	0.0124	684377	10322	0.0151
41	74525791	74525791	924404	0.0124	924404	13758	0.0149
43	70996085	70996085	881552	0.0124	881552	13225	0.0150
45	16632144	16632144	206188	0.0124	206188	3055	0.0148
47	47744644	47744644	597192	0.0125	597192	9117	0.0153
49	34672639	34672639	431200	0.0124	431200	6550	0.0152

Exp	Belle Doc.	Skim In	Skim Out	Skim Ratio	Reco In	Reco Out	Reco Ratio
51	50402724	50402724	627907	0.0125	627907	9645	0.0154
55	92649821	92649821	1154647	0.0125	1154647	17403	0.0151
61	44427287	44427287	558563	0.0126	558563	8494	0.0152
63	41812693	41812693	523655	0.0125	523655	7875	0.0150
65	48325746	48325746	604037	0.0125	604037	9262	0.0153
SVD1	177240522	177240522	1668975	0.104	1668975	23874	0.158
SVD2	723065796	723065796	8998174	0.186	8998174	136024	0.227
Total	900306318	900306318	10667149	0.290	10667149	159898	0.385

Table A.16 Skim and Reconstruction Event Numbers From Full Stream 4 Mixed Processing

Exp	Belle Doc.	Skim In	Skim Out	Skim Ratio	Reco In	Reco Out	Reco Ratio
7	3158538	3158538	5448	0.00172	5448	21	0.00385
9	2243082	2243082	3926	0.00175	3926	19	0.00484
11	4194377	4194377	7522	0.00179	7522	30	0.00399
13	5833567	5833567	10465	0.00179	10465	39	0.00373
15	6913774	6913774	11769	0.00170	11769	38	0.00323
17	5029273	5029273	8763	0.00174	8763	36	0.00411
19	13419895	13419895	22912	0.00171	22912	70	0.00306
21	2351610	2351610	3980	0.00169	3980	10	0.00251
23	3447814	3447814	5927	0.00172	5927	22	0.00371
25	13889177	13889177	24196	0.00174	24196	114	0.00471
27	13818246	13818246	23974	0.00173	23974	84	0.00350
31	9278488	9278488	23903	0.00258	23903	99	0.00414
33	9473597	9473597	24630	0.00260	24630	97	0.00394
35	9194069	9194069	24321	0.00265	24321	72	0.00296
37	33181993	33181993	88172	0.00266	88172	338	0.00383
39	23083585	23083585	60705	0.00263	60705	216	0.00356
41	31243164	31243164	82385	0.00264	82385	285	0.00346
43	29763454	29763454	78875	0.00265	78875	295	0.00374
45	6972623	6972623	18273	0.00262	18273	49	0.00268
47	20015816	20015816	53236	0.00266	53236	177	0.00332
49	14535658	14535658	38213	0.00263	38213	115	0.00301

Exp	Belle Doc.	Skim In	Skim Out	Skim Ratio	Reco In	Reco Out	Reco Ratio
51	21130005	21130005	55971	0.00265	55971	169	0.00302
55	38841222	38841222	103016	0.00265	103016	357	0.00347
61	18624955	18624955	49646	0.00267	49646	188	0.00379
63	17528965	17528965	46394	0.00265	46394	157	0.00338
65	20259428	20259428	53457	0.00264	53457	183	0.00342
SVD1	74299353	74299353	128882	0.0191	128882	483	0.0412
SVD2	303127022	303127022	801197	0.0396	801197	2797	0.0517
Total	377426375	377426375	930079	0.0587	930079	3280	0.0930

Table A.17 Skim and Reconstruction Event Numbers From Full Stream 4 Charged Processing

Exp	Belle Doc.	Skim In	Extra Evnts	Skim Out	Skim Ratio	Reco In	Reco Out	Reco Ratio
7	3158538	3158538	0	8618	0.00273	8618	44	0.00511
9	2243082	2243082	0	6398	0.00285	6398	31	0.00485
11	4194377	4194377	0	12095	0.00288	12095	53	0.00438
13	5833569	5833569	0	17090	0.00293	17090	78	0.00456
15	6913775	6913775	0	19301	0.00279	19301	77	0.00399
17	5029272	5029272	0	14382	0.00286	14382	66	0.00459
19	13419896	13419896	0	37582	0.00280	37582	167	0.00444
21	2351609	2351609	0	6582	0.00280	6582	34	0.00517
23	3447813	3447813	0	9720	0.00282	9720	45	0.00463
25	13889176	13889176	0	38706	0.00279	38706	178	0.00460
27	13818248	13818248	0	38866	0.00281	38866	192	0.00494
31	9278484	9278484	0	36805	0.00397	36805	150	0.00408
33	9473593	9473593	0	38370	0.00405	38370	147	0.00383
35	9194074	9194074	0	37296	0.00406	37296	125	0.00335
37	33181993	33181993	0	134735	0.00406	134735	542	0.00402
39	23083580	23083580	0	93677	0.00406	93677	369	0.00394
41	31243165	31243165	0	126777	0.00406	126777	511	0.00403
43	29763453	29763453	0	121356	0.00408	121356	472	0.00389
45	6972622	6972622	0	28129	0.00403	28129	133	0.00473
47	20015814	20015814	0	81428	0.00407	81428	314	0.00386
49	14535657	14535657	0	59149	0.00407	59149	254	0.00429

Exp	Belle Doc.	Skim In	Extra Evnts	Skim Out	Skim Ratio	Reco In	Reco Out	Reco Ratio
51	21130009	21130009	0	86465	0.00409	86465	315	0.00364
55	38841224	38841224	0	157591	0.00406	157591	626	0.00397
61	18624956	18624956	0	76060	0.00408	76060	316	0.00415
63	17528939	17528955	16	70917	0.00405	70917	277	0.00391
65	20259428	20259428	0	82577	0.00408	82577	322	0.00390
SVD1	74299355	74299355	0	209340	0.0311	209340	965	0.0513
SVD2	303126991	303127007	16	1231332	0.0609	1231332	4873	0.0596
Total	377426346	377426362	16	1440672	0.0919	1440672	5838	0.111

Table A.18 Skim and Reconstruction Event Numbers From Full Stream 5 uds Processing

Exp	Belle Doc.	Skim In	Skim Out	Skim Ratio	Reco In	Reco Out	Reco Ratio
7	12115358	12115358	103136	0.00851	103136	1055	0.0102
9	8603091	8603091	74620	0.00867	74620	816	0.0109
11	16086114	16086114	141587	0.00880	141587	1316	0.0093
13	22372592	22372592	197309	0.00882	197309	2022	0.0102
15	26514597	26514597	227342	0.00857	227342	2384	0.0105
17	19287344	19287344	166451	0.00863	166451	1781	0.0107
19	51465220	51465220	437136	0.00849	437136	4555	0.0104
21	9018475	9018475	76161	0.00844	76161	814	0.0107
23	13222447	13222447	114077	0.00863	114077	1218	0.0107
25	53265405	53265405	458944	0.00862	458944	4916	0.0107
27	52992757	52992757	457723	0.00864	457723	4806	0.0105
31	35582931	35582931	397571	0.0112	397571	4423	0.0111
33	36330567	36330567	406048	0.0112	406048	4592	0.0113
35	35258657	35258657	401335	0.0114	401335	4433	0.0110
37	127250006	127250006	1446386	0.0114	1446386	16050	0.0111
39	88523413	88523413	1004424	0.0113	1004424	11165	0.0111
41	119814223	119814223	1359751	0.0113	1359751	14856	0.0109
43	114139590	114139590	1301555	0.0114	1301555	14371	0.0110
45	26739290	26739290	304255	0.0114	304255	3408	0.0112
47	76758511	76758511	877175	0.0114	877175	9724	0.0111
49	55742790	55742790	634119	0.0114	634119	7130	0.0112

Exp	Belle Doc.	Skim In	Skim Out	Skim Ratio	Reco In	Reco Out	Reco Ratio
51	81031721	81031721	923612	0.0114	923612	10365	0.0112
55	148951996	148951996	1697377	0.0114	1697377	18762	0.0111
61	71425104	71425104	824663	0.0115	824663	9097	0.0110
63	67221741	67221741	773812	0.0115	773812	8391	0.0108
65	77692720	77692720	891300	0.0115	891300	10003	0.0112
SVD1	284943400	284943400	2454486	0.0948	2454486	25683	0.115
SVD2	1162463260	1162463260	13243383	0.171	13243383	146770	0.167
Total	1447406660	1447406660	15697869	0.266	15697869	172453	0.281

Table A.19 Skim and Reconstruction Event Numbers From Full Stream 5 Charm Processing

Exp	Belle Doc.	Skim In	Skim Out	Skim Ratio	Reco In	Reco Out	Reco Ratio
7	7536264	7536264	70174	0.00931	70174	1020	0.0145
9	5351447	5351447	51201	0.00957	51201	773	0.0151
11	10005967	10005967	95572	0.00955	95572	1303	0.0136
13	13916303	13916303	135141	0.00971	135141	2014	0.0149
15	16492593	16492593	154754	0.00938	154754	2333	0.0151
17	11997074	11997074	113404	0.00945	113404	1618	0.0143
19	32012212	32012212	297626	0.00930	297626	4218	0.0142
21	5609656	5609656	51974	0.00927	51974	757	0.0146
23	8224605	8224605	77184	0.00938	77184	1105	0.0143
25	33132057	33132057	312695	0.00944	312695	4536	0.0145
27	32962343	32962343	311527	0.00945	311527	4592	0.0147
31	22133164	22133164	268833	0.0121	268833	3948	0.0147
33	22598083	22598083	277455	0.0123	277455	4175	0.0150
35	21931344	21931344	272781	0.0124	272781	3985	0.0146
37	79151035	79151035	982650	0.0124	982650	14489	0.0147
39	55062603	55062603	682930	0.0124	682930	10502	0.0154
41	74525788	74525788	921985	0.0124	921985	13690	0.0148
43	70996077	70996077	883592	0.0124	883592	13459	0.0152
45	16632143	16632143	207013	0.0124	207013	3081	0.0149
47	47744639	47744639	596382	0.0125	596382	9041	0.0152
49	34672640	34672640	431865	0.0125	431865	6584	0.0152

Exp	Belle Doc.	Skim In	Skim Out	Skim Ratio	Reco In	Reco Out	Reco Ratio
51	50402727	50402727	626885	0.0124	626885	9464	0.0151
55	92649822	92649822	1152172	0.0124	1152172	17192	0.0149
61	44427294	44427294	558037	0.0126	558037	8395	0.0150
63	41812688	41812688	524850	0.0126	524850	8364	0.0159
65	48325730	48325730	603366	0.0125	603366	9195	0.0152
SVD1	177240521	177240521	1671252	0.104	1671252	24269	0.160
SVD2	723065777	723065777	8990796	0.186	8990796	135564	0.226
Total	900306298	900306298	10662048	0.290	10662048	159833	0.386

Table A.20 Skim and Reconstruction Event Numbers From Full Stream 5 Mixed Processing

Exp	Belle Doc.	Skim In	Skim Out	Skim Ratio	Reco In	Reco Out	Reco Ratio
7	3158539	3158539	5440	0.00172	5440	21	0.00386
9	2243081	2243081	3890	0.00173	3890	14	0.00360
11	4194376	4194376	7320	0.00175	7320	27	0.00369
13	5833567	5833567	10482	0.00180	10482	46	0.00439
15	6913775	6913775	11793	0.00171	11793	46	0.00390
17	5029272	5029272	8679	0.00173	8679	19	0.00219
19	13419895	13419895	22856	0.00170	22856	72	0.00315
21	2351610	2351610	3986	0.00170	3986	14	0.00351
23	3447813	3447813	5908	0.00171	5908	21	0.00355
25	13889173	13889173	24050	0.00173	24050	98	0.00407
27	13818247	13818247	23701	0.00172	23701	107	0.00451
31	9278487	9278487	24115	0.00260	24115	80	0.00332
33	9473591	9473591	24679	0.00261	24679	84	0.00340
35	9194075	9194075	24355	0.00265	24355	78	0.00320
37	33181995	33181995	87553	0.00264	87553	302	0.00345
39	23083582	23083582	61214	0.00265	61214	207	0.00338
41	31243168	31243168	82933	0.00265	82933	296	0.00357
43	29763450	29763450	79530	0.00267	79530	271	0.00341
45	6972621	6972621	18152	0.00260	18152	46	0.00253
47	20015804	20015804	53501	0.00267	53501	205	0.00383
49	14535655	14535655	38428	0.00264	38428	136	0.00354

Exp	Belle Doc.	Skim In	Skim Out	Skim Ratio	Reco In	Reco Out	Reco Ratio
51	21130003	21130003	56402	0.00267	56402	180	0.00319
55	38841221	38841221	102796	0.00265	102796	334	0.00325
61	18624953	18624953	49539	0.00266	49539	160	0.00323
63	17528965	17528965	46298	0.00264	46298	165	0.00356
65	20259429	20259429	53446	0.00264	53446	165	0.00309
SVD1	74299348	74299348	128105	0.0190	128105	485	0.0404
SVD2	303126999	303126999	802941	0.0396	802941	2709	0.0500
Total	377426347	377426347	931046	0.0586	931046	3194	0.0904

Table A.21 Skim and Reconstruction Event Numbers From Full Stream 5 Charged Processing

Exp	Belle Doc.	Skim In	Extra Evnts	Skim Out	Skim Ratio	Reco In	Reco Out	Reco Ratio
7	3158538	3158538	0	8648	0.00274	8648	37	0.00428
9	2243082	2243082	0	6451	0.00288	6451	30	0.00465
11	4194376	4194376	0	11975	0.00286	11975	52	0.00434
13	5833569	5833569	0	16897	0.00290	16897	67	0.00397
15	6913775	6913775	0	19177	0.00277	19177	78	0.00407
17	5029273	5029273	0	14391	0.00286	14391	72	0.00500
19	13419895	13419895	0	37135	0.00277	37135	166	0.00447
21	2351610	2351610	0	6561	0.00279	6561	35	0.00533
23	3447814	3447814	0	9662	0.00280	9662	33	0.00342
25	13889176	13889176	0	39304	0.00283	39304	168	0.00427
27	13818247	13818247	0	39147	0.00283	39147	163	0.00416
31	9278486	9278486	0	36860	0.00397	36860	123	0.00334
33	9473597	9473597	0	37427	0.00395	37427	143	0.00382
35	9194072	9194072	0	37382	0.00407	37382	147	0.00393
37	33181997	33181997	0	135166	0.00407	135166	502	0.00371
39	23083591	23083591	0	94018	0.00407	94018	405	0.00431
41	31243167	31243167	0	127117	0.00407	127117	484	0.00381
43	29763452	29763452	0	121545	0.00408	121545	513	0.00422
45	6972625	6972625	0	28335	0.00406	28335	109	0.00385
47	20015802	20015802	0	82040	0.00410	82040	333	0.00406
49	14535655	14535655	0	59244	0.00408	59244	212	0.00358

Exp	Belle Doc.	Skim In	Extra Evnts	Skim Out	Skim Ratio	Reco In	Reco Out	Reco Ratio
51	21130007	21130007	0	85797	0.00406	85797	341	0.00397
55	38841218	38841218	0	157280	0.00405	157280	656	0.00417
61	18624952	18624952	0	76057	0.00408	76057	308	0.00405
63	17528936	17528942	6	71274	0.00407	71274	292	0.00410
65	20259431	20259431	0	82061	0.00405	82061	322	0.00392
SVD1	74299355	74299355	0	209348	0.0310	209348	901	0.0480
SVD2	303126988	303126994	6	1231603	0.0608	1231603	4890	0.0588
Total	377426343	377426349	6	1440951	0.0919	1440951	5791	0.107

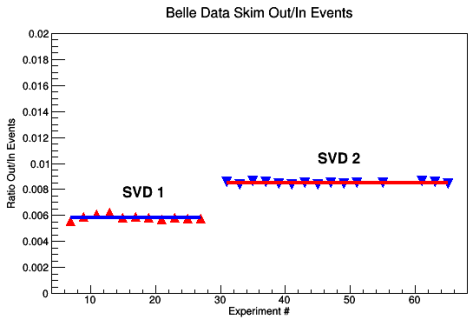

Figure A.1: Data Skim Out/In Ratio.

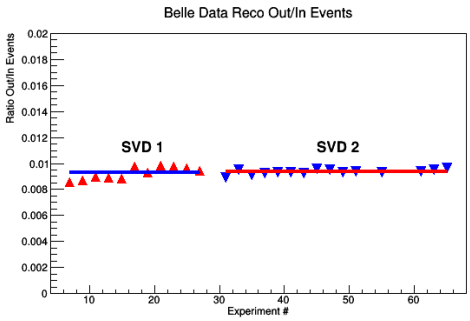

Figure A.2: Data Reco Out/In Ratio.

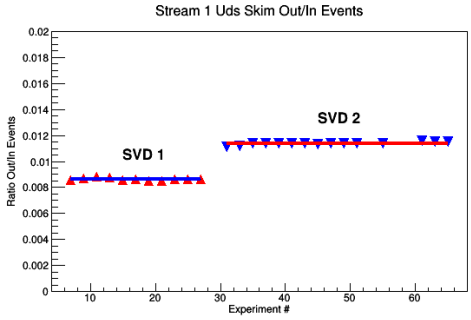

Figure A.3: Full stream 1 uds Skim Out/In Ratio.

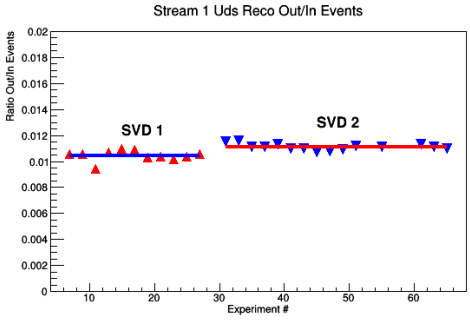

Figure A.4: Full stream 1 uds Reco Out/In Ratio.

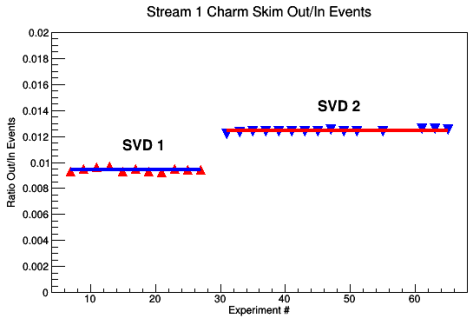

Figure A.5: Full stream 1 Charm Skim Out/In Ratio.

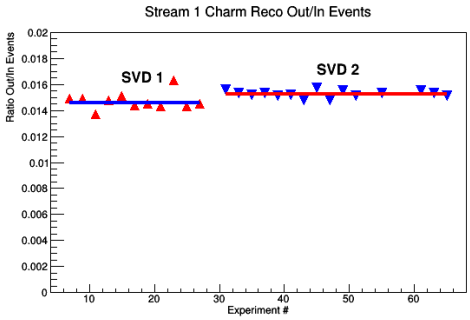

Figure A.6: Full stream 1 Charm Reco Out/In Ratio.

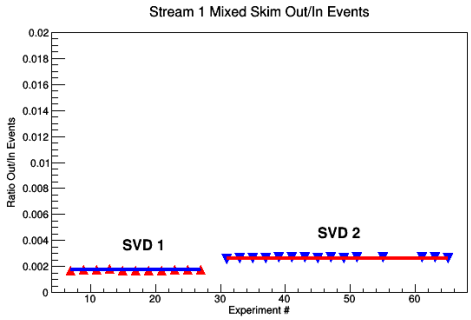

Figure A.7: Full stream 1 mixed Skim Out/In Ratio.

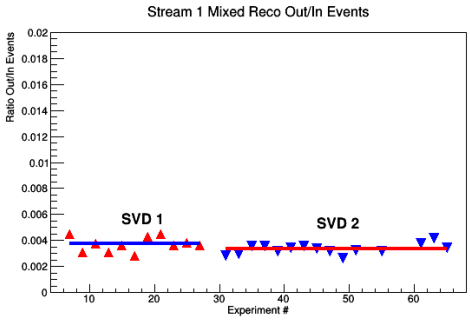

Figure A.8: Full stream 1 mixed Reco Out/In Ratio.

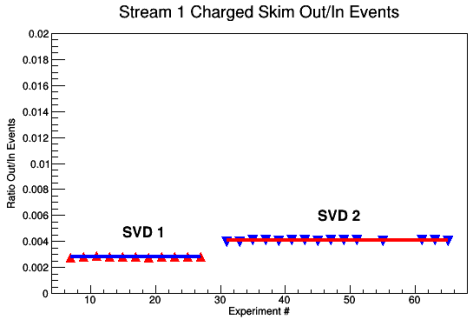

Figure A.9: Full stream 1 charged Skim Out/In Ratio.

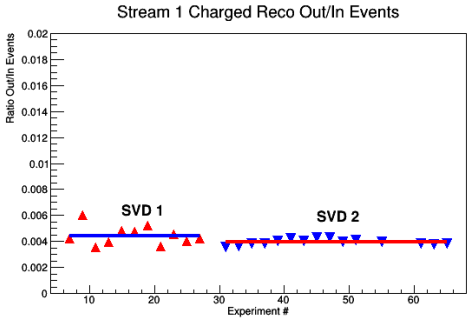

Figure A.10: Full stream 1 charged Reco Out/In Ratio.

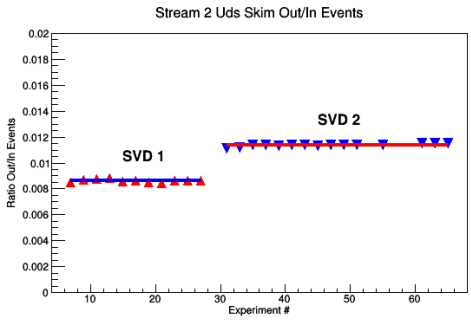

Figure A.11: Full stream 2 uds Skim Out/In Ratio.

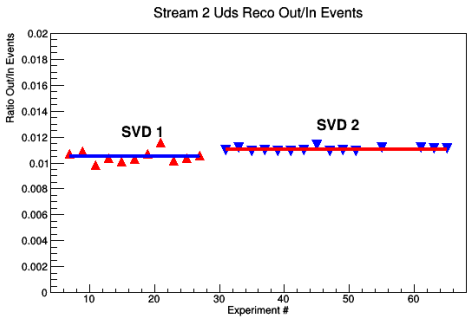

Figure A.12: Full stream 2 uds Reco Out/In Ratio.

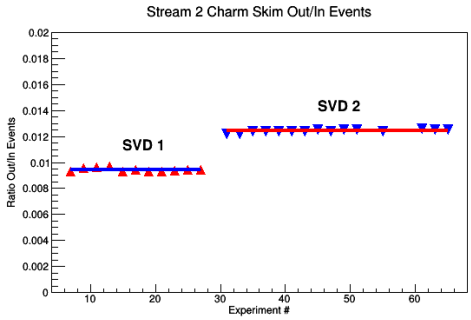

Figure A.13: Full stream 2 charm Skim Out/In Ratio.

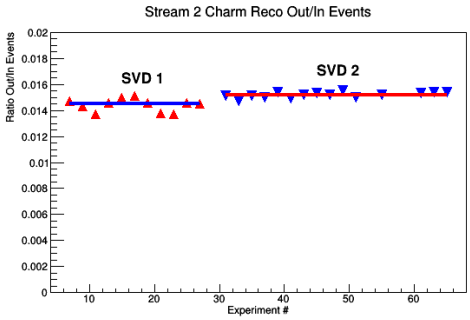

Figure A.14: Full stream 2 charm Reco Out/In Ratio.

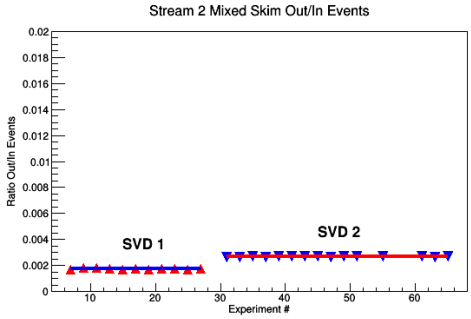

Figure A.15: Full stream 2 mixed Skim Out/In Ratio.

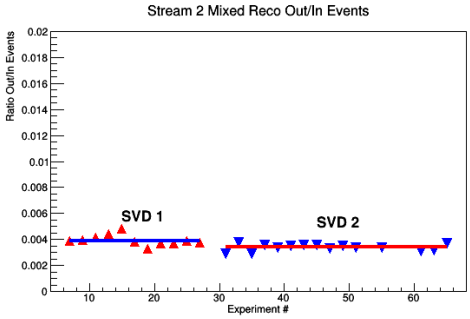

Figure A.16: Full stream 2 mixed Reco Out/In Ratio.

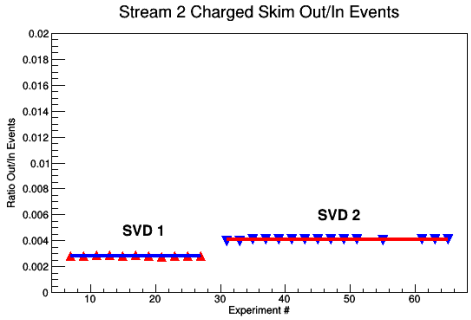

Figure A.17: Full stream 2 charged Skim Out/In Ratio.

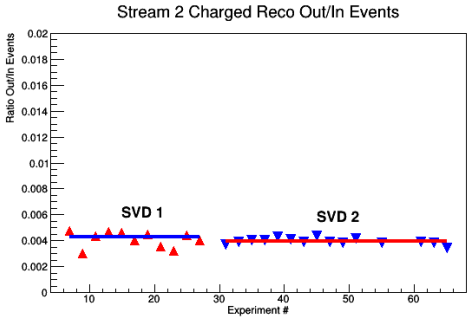

Figure A.18: Full stream 2 charged Reco Out/In Ratio.

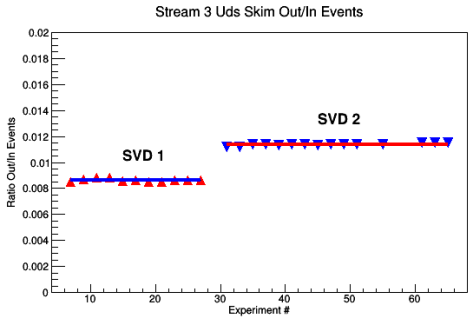

Figure A.19: Full stream 3 uds Skim Out/In Ratio.

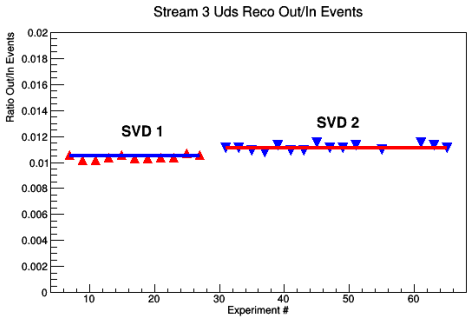

Figure A.20: Full stream 3 uds Reco Out/In Ratio.

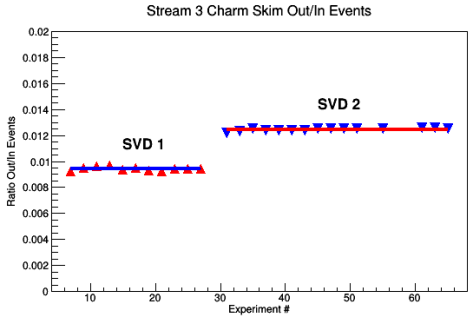

Figure A.21: Full stream 3 charm Skim Out/In Ratio.

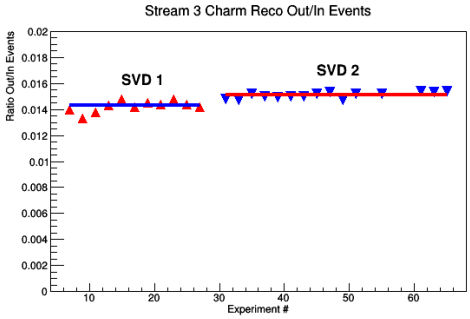

Figure A.22: Full stream 3 charm Reco Out/In Ratio.

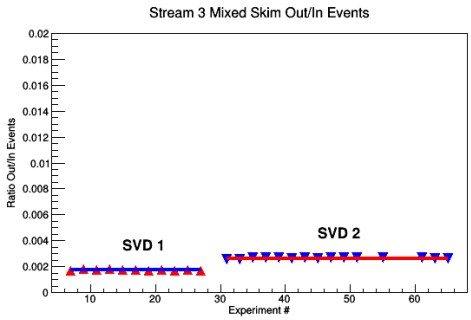

Figure A.23: Full stream 3 mixed Skim Out/In Ratio.

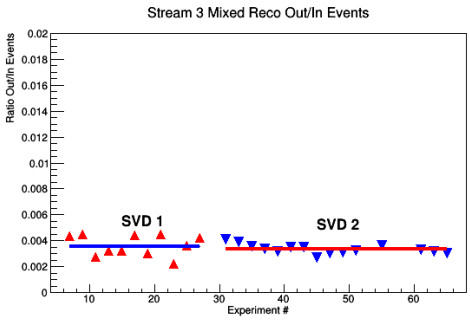

Figure A.24: Full stream 3 mixed Reco Out/In Ratio.

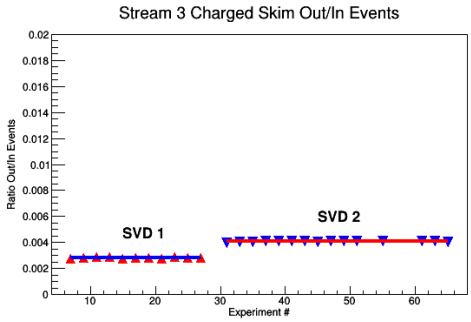

Figure A.25: Full stream 3 charged Skim Out/In Ratio.

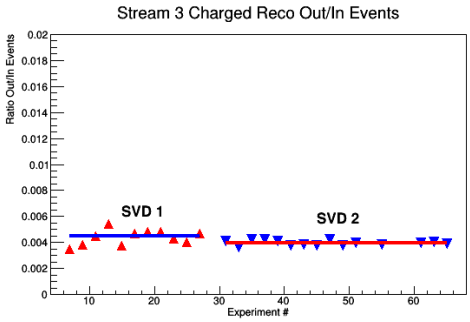

Figure A.26: Full stream 3 charged Reco Out/In Ratio.

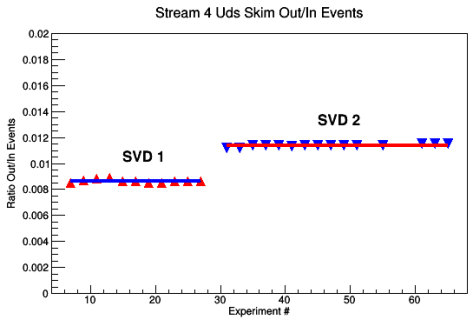

Figure A.27: Full stream 4 uds Skim Out/In Ratio.

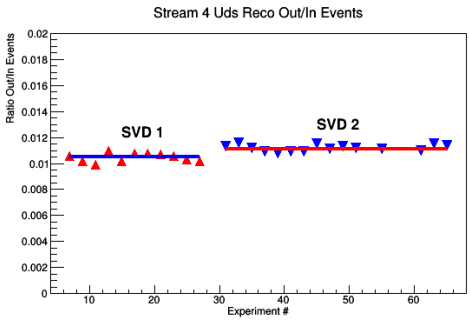

Figure A.28: Full stream 4 uds Reco Out/In Ratio.

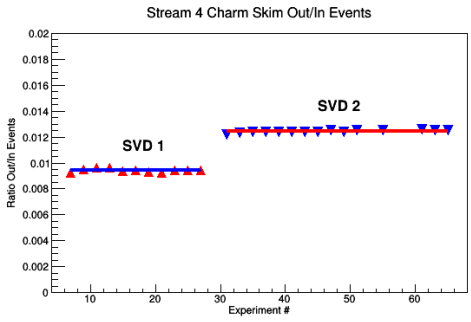

Figure A.29: Full stream 4 charm Skim Out/In Ratio.

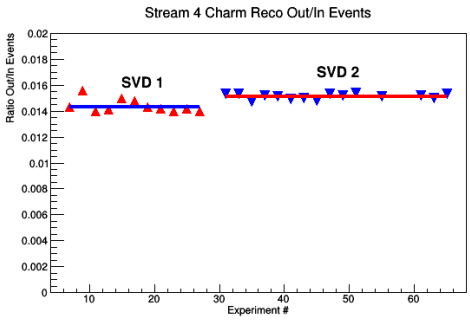

Figure A.30: Full stream 4 charm Reco Out/In Ratio.

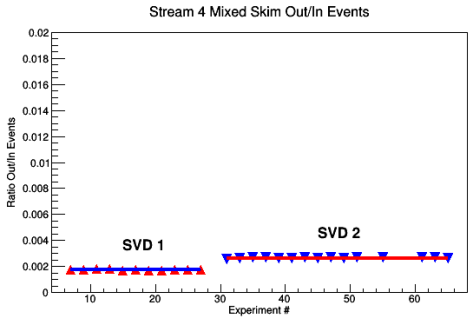

Figure A.31: Full stream 4 mixed Skim Out/In Ratio.

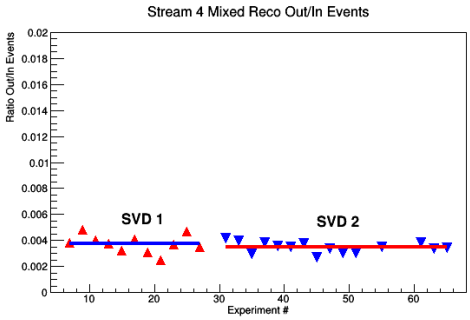

Figure A.32: Full stream 4 mixed Reco Out/In Ratio.

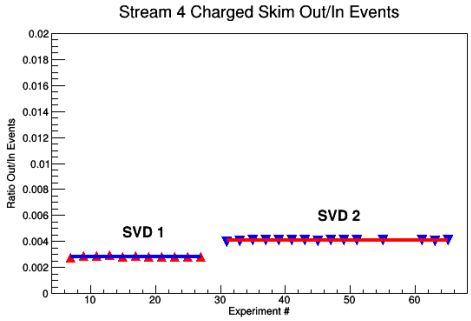

Figure A.33: Full stream 4 charged Skim Out/In Ratio.

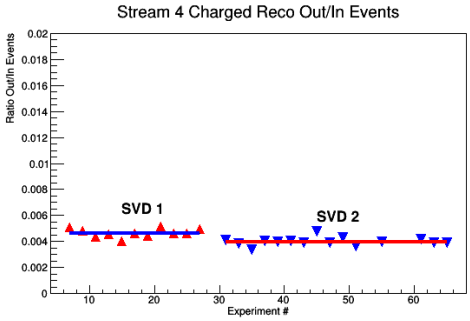

Figure A.34: Full stream 4 charged Reco Out/In Ratio.

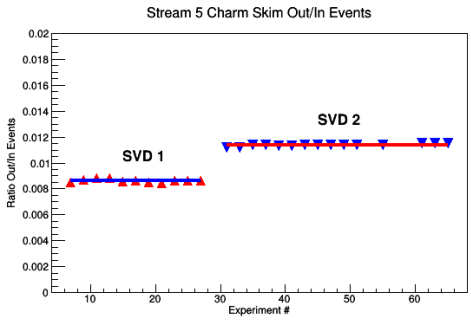

Figure A.35: Full stream 5 uds Skim Out/In Ratio.

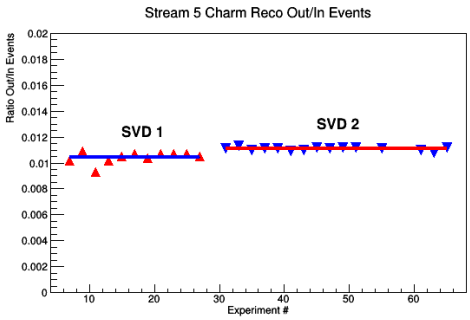

Figure A.36: Full stream 5 uds Reco Out/In Ratio.

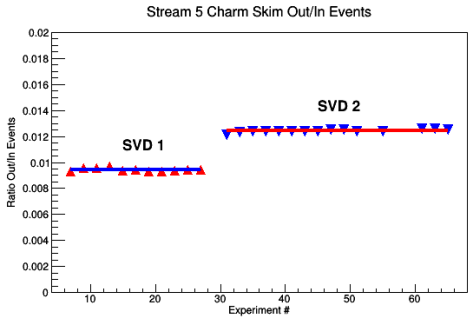

Figure A.37: Full stream 5 charm Skim Out/In Ratio.

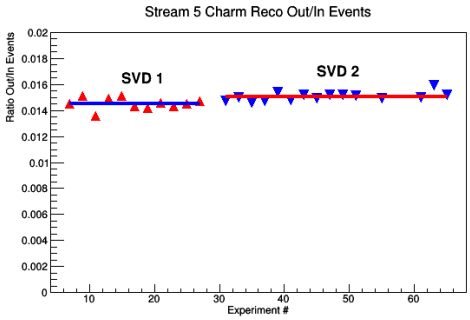

Figure A.38: Full stream 5 charm Reco Out/In Ratio.

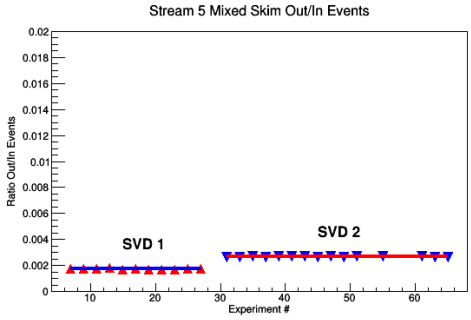

Figure A.39: Full stream 5 mixed Skim Out/In Ratio.

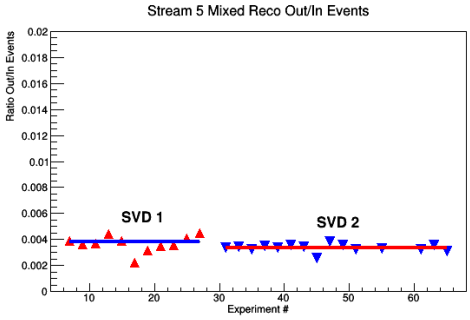

Figure A.40: Full stream 5 mixed Reco Out/In Ratio.

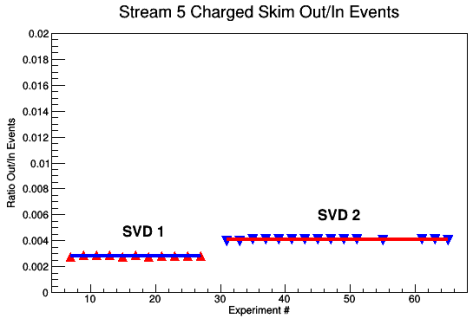

Figure A.41: Full stream 5 charged Skim Out/In Ratio.

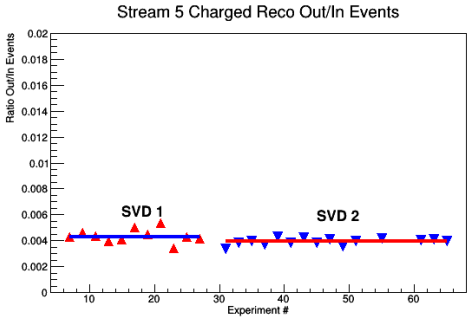

Figure A.42: Full stream 5 charged Reco Out/In Ratio.

Appendix B

Additional Efficiency Plots

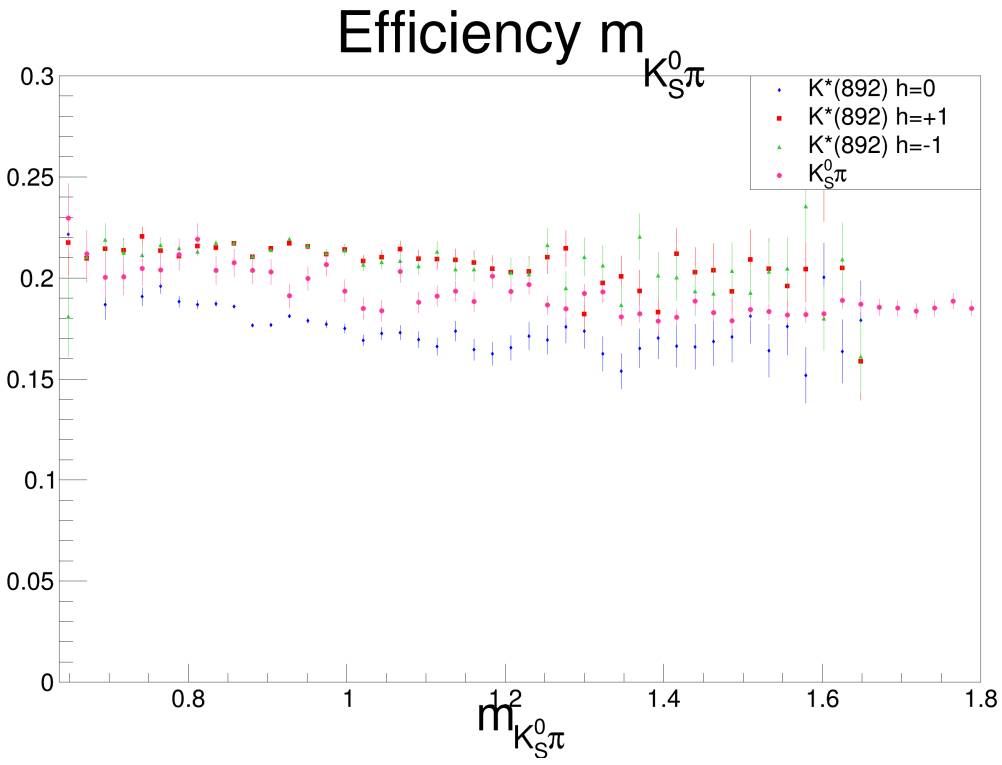

Figure B.1: Efficiency of $m_{K^0_S\pi}$ for different decay modes.

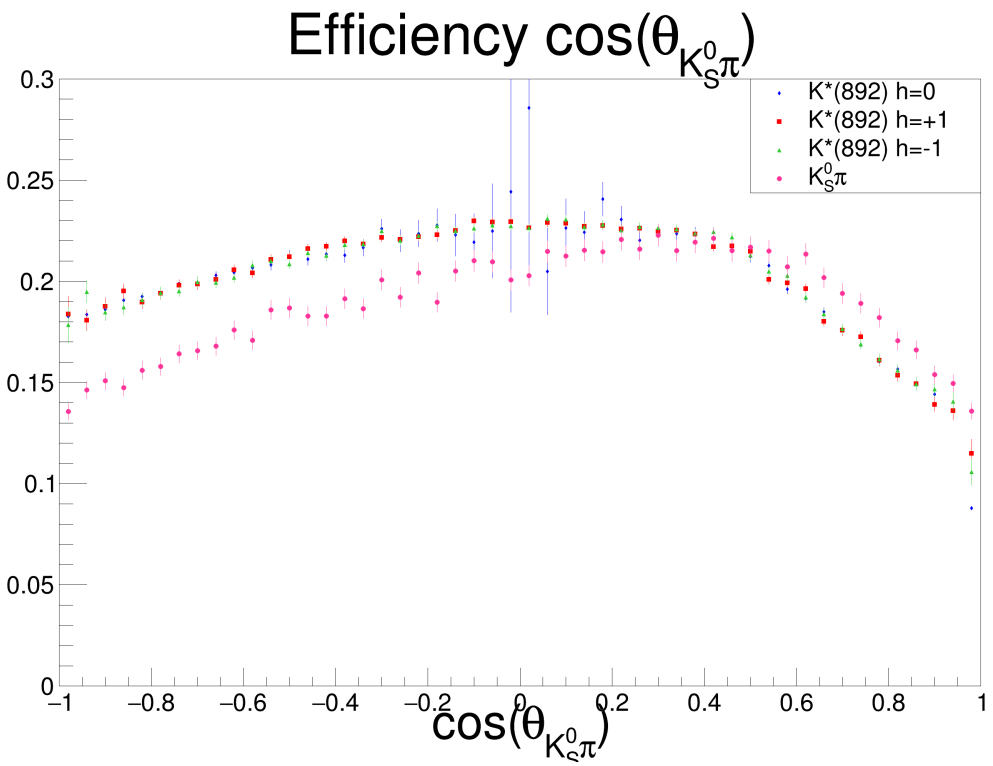

Figure B.2: Efficiency of $\cos(\theta_{K^0_S\pi})$ for different decay modes.

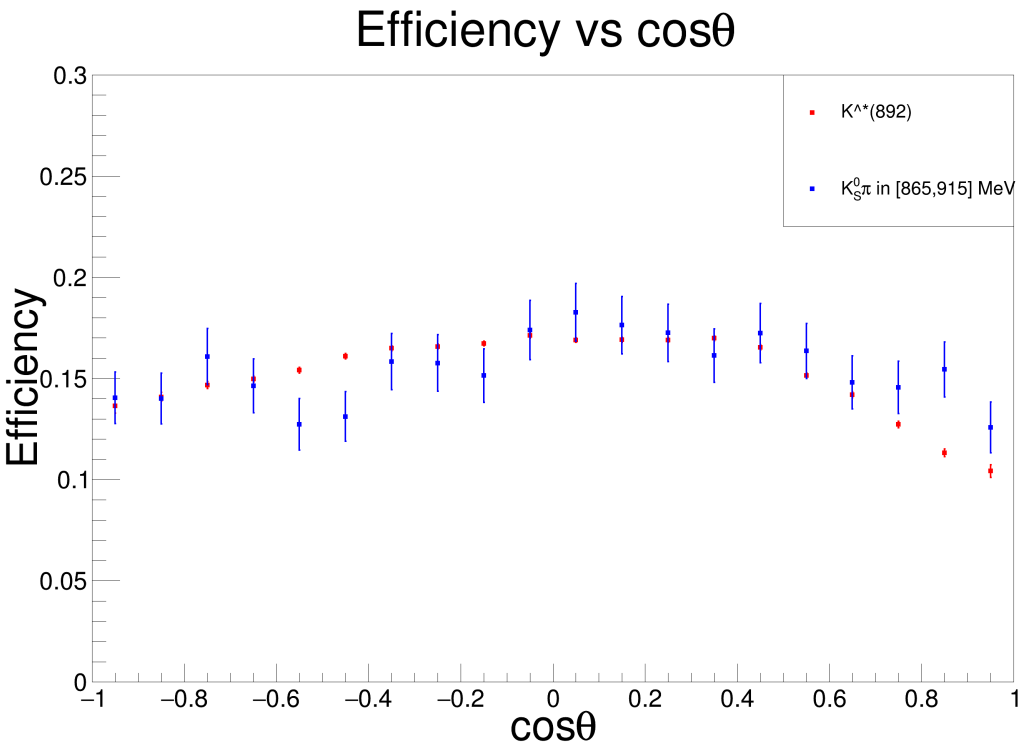

Figure B.3: Efficiency vs $\cos\theta_{K^0_S\pi}$ in the mass range [865, 915] MeV for K*(892) and $K^0_S\pi$ NR modes. The efficiencies are a lot closer when the mass range is restricted.

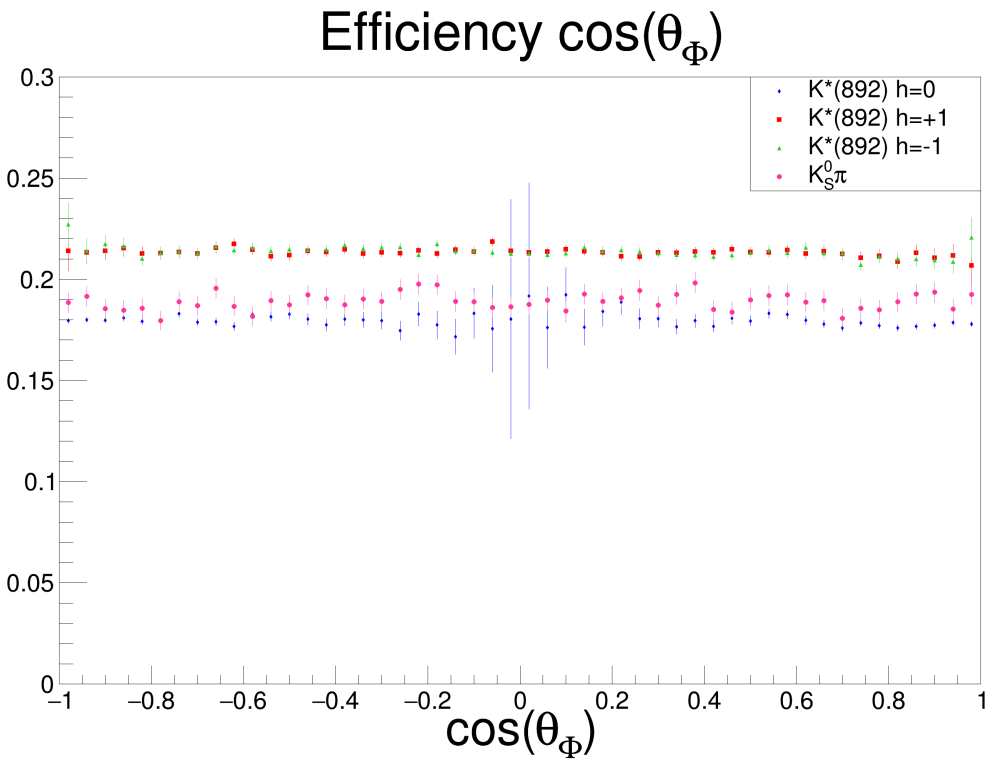

Figure B.4: Efficiency of $\cos(\theta_\Phi)$ for different decay modes.

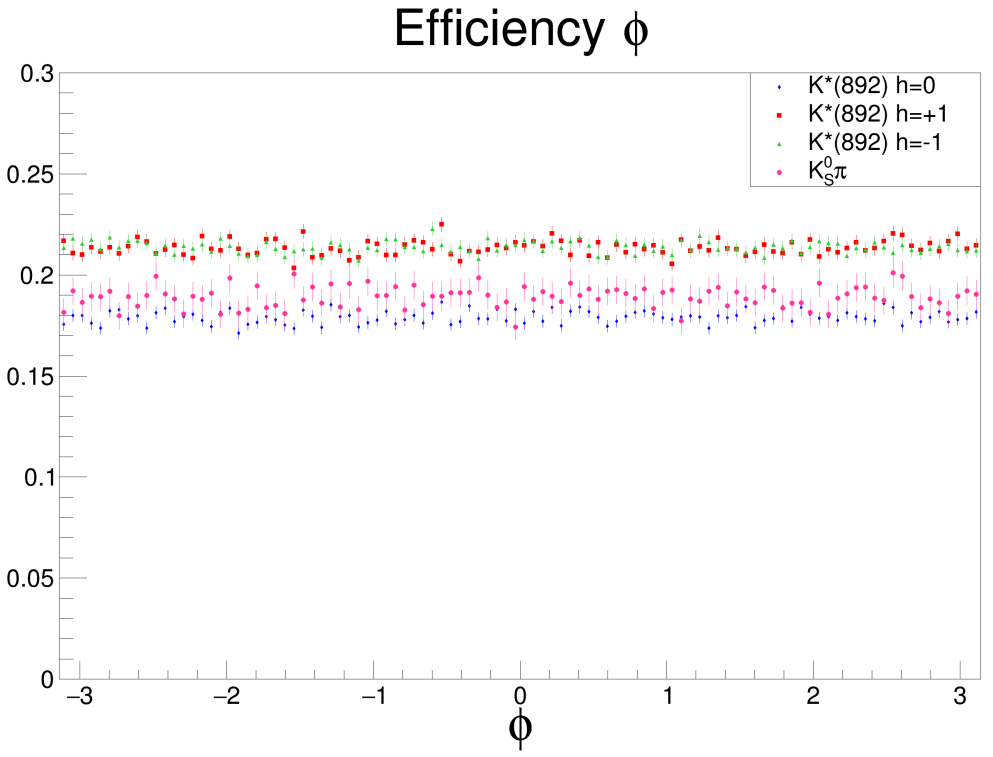

Figure B.5: Efficiency of ϕ for different decay modes.